Title
The Influence of Charged Species on the Phase Behavior, Self-Assembly, and Electrochemical Performance of Block Copolymer Electrolytes

Author
Thelen, Jacob Lloyd

Publication Date
2016

Peer reviewed|Thesis/dissertation

The Influence of Charged Species on the Phase Behavior, Self-Assembly, and Electrochemical Performance of Block Copolymer Electrolytes

By

Jacob Lloyd Thelen

A dissertation submitted in partial satisfaction of the

requirements for the degree of

Doctor of Philosophy

in

Chemical Engineering

in the

Graduate Division

of the

University of California, Berkeley

Committee in charge:

Professor Nitash P. Balsara, Chair
Professor Susan J. Muller
Professor Andrew M. Minor

Fall 2016

The Influence of Charged Species on the Phase Behavior, Self-Assembly, and Electrochemical Performance of Block Copolymer Electrolytes

Abstract

The Influence of Charged Species on the Phase Behavior, Self-Assembly, and Electrochemical Performance of Block Copolymer Electrolytes

by

Jacob Lloyd Thelen

Doctor of Philosophy in Chemical Engineering

University of California, Berkeley

Professor Nitash P. Balsara, Chair

One of the major barriers to expanding the capacity of large-scale electrochemical energy storage within batteries is the threat of a catastrophic failure. Catastrophic battery pack failure can be initiated by a defect within a single battery cell. If the failure of a defective battery cell is not contained, the damage can spread and subsequently compromise the integrity of the entire battery back, as well as the safety of those in its surroundings. Replacing the volatile, flammable liquid electrolyte components found in most current lithium ion batteries with a solid polymer electrolyte (SPE) would significantly improve the cell-level safety of batteries; however, poor ionic conductivity and restricted operating temperatures compared to liquid electrolytes have plagued the practical application of SPEs. Rather than competing with the performance of liquid electrolytes directly, our approach to developing SPEs relies on increasing electrolyte functionality through the use of block copolymer architectures.

Block copolymers, wherein two or more chemically dissimilar polymer chains are covalently bound, have a propensity to microphase separate into nanoscale domains that have physical properties similar to those of each of the different polymer chains. For instance, the block copolymer, polystyrene-*b*-poly(ethylene oxide) (SEO), has often been employed as a solid polymer electrolyte because the nanoscale domains of polystyrene (PS) can provide mechanical reinforcement, while the poly(ethylene oxide) microphases can solvate and conduct lithium ions. Block copolymer electrolytes (BCEs) formed from SEO/salt mixtures result in a material with the bulk mechanical properties of a solid, but with the ion conducting properties of a viscoelastic fluid. The efficacy SEO-based BCEs has been demonstrated; the enhanced mechanical functionality provided by the PS domains resist the propagation of dendritic lithium structures during battery operation, thus enabling the use of a lithium metal anode. The increase in the specific energy of a battery upon replacing a graphite anode with lithium metal can offset the losses in performance due to the poor ion conduction of SPEs. However, BCEs that enable the use of a lithium anode and have improved performance would represent a major breakthrough for the development of high capacity batteries.

The electrochemical performance of BCEs has a complex relationship with the nature of the microphase separated domains, which is not well-understood. The objective of this dissertation is to provide fundamental insight into the nature of microphase separation and self-assembly of block copolymer electrolytes. Specifically, I will focus on how the ion-polymer interactions within a diverse set of BCEs dictate nanostructure. Combining such insight with knowledge of how nanostructure influences ion motion will enable the rational design of new BCEs with enhanced performance and functionality.

In order to facilitate the study of BCE nanostructure, synchrotron-based X-ray scattering techniques were used to study samples over a wide range of length-scales (i.e., from Angstroms to hundreds of nanometers) under conditions relevant to the battery environment. The development of the experimental aspects of the X-ray scattering techniques, as well as an improved treatment of scattering data, played a pivotal role in the success of this work. The dissemination of those developments will be the focus of the first section.

The thermodynamic impact of adding salt to a neutral diblock copolymer was studied in a model BCE composed of a low molecular weight SEO diblock copolymer mixed with lithium bis(trifluoromethanesulfonyl)imide (LiTFSI), a common salt used in lithium batteries. In neutral block copolymers (BCPs), self-assembly is a thermodynamically driven process governed by a balance between unfavorable monomer contacts (i.e., the enthalpic contribution) and the entropy of mixing. When the enthalpic and entropic contributions to free energy are similar in magnitude, a block copolymer can undergo a thermally reversible phase transition from an ordered to a disordered nanostructure (i.e., the order-to-disorder transition (ODT). We used temperature-dependent small angle X-ray scattering (SAXS) to observe this transition in the model SEO/LiTFSI system. Unlike neutral BCPs, which to a first approximation are single component systems, the SEO/LiTFSI system demonstrated the thermodynamically stable coexistence phases of ordered lamellae and disordered polymer over a finite temperature window. Analysis of the lamellar domains revealed an increase in salt concentration during the ODT, indicating local salt partitioning due to the presence of nanostructure. While the Gibbs phase rule predicts this behavior, this was the first result demonstrating a direct connection between ion-polymer interactions and block copolymer nanostructure.

We found evidence of salt redistribution in BCEs wherein self-assembly has been kinetically arrested. Through the structural analysis of BCEs formed from a high molecular weight SEO sample over a wide range of LiTFSI concentrations, it was revealed that in some cases, coexisting nanostructures were stable. While it is likely that the stability of these nanostructures was kinetic in nature, the relationship between nanostructure and salt partitioning revealed previously indicates that the salt could redistribute between the nanostructures to achieve the lowest energetic state. Unusual trends in the ionic conductivity with respect to salt concentration support this hypothesis. In some cases, high salt concentrations lead to significant improvements in ionic conductivity, representing a strong departure from the behavior of standard SPEs, and a possible route to improving the performance of BCEs.

The performance of BCEs can also be improved by chemically functionalizing one of the polymer blocks by covalently attaching the salt anion. Since the cation is the only mobile species, these materials are coined single-ion conducting block copolymers. Single ion conduction can improve the efficiency of battery operation. In order for cation motion to occur in single-ion conducting block copolymers, it must dissociate from the backbone of the anion-containing polymer block. Through the structural and electrochemical characterization of poly(ethylene oxide)-*b*-poly[(styrene-4-sulfonyltrifluoromethylsulfonyl)imide] (PEO-P(STFSI))-based single-ion conductors, we found that ion dissociation significantly influences nanostructure: when a large amount of ions are dissociated, the polymer blocks tend to mix, thus precluding microphase separation and the formation of nanostructure. This direct coupling of ion dissociation (and hence conduction) and nanostructure has interesting implications for BCE performance. For instance, without discreet microphases, the single-ion conducting polymers cannot provide the enhanced mechanical properties like those obtained in SEO/LiTFSI electrolytes. Future development in single-ion conducting block copolymers should investigate polymer architectures where a third polymer block, such as PS, facilitates microphase separation and improved mechanical properties.

Additional analysis of the single-ion conducting block copolymers revealed that ion dissociation from the charge-containing backbone (P(STFSI)) could also influence the crystallization of the neutral polymer block (PEO). Interestingly, ion dissociation did not disrupt PEO crystallization by directly interfering with the PEO chains, rather the homogeneity of the polymer melt prior to PEO crystallization led to differences in crystallization behavior. In the cases where ion dissociation lead to significant mixing of the polymer block, PEO crystallites grew unimpeded and formed well-ordered lamellar structures. When ion dissociation did not occur, fluctuations in concentration due to the demixing of PEO and P(STFSI) interrupted the growth of PEO crystallites, slowing the crystallization process and leading to less-ordered nanostructures.

The final study in this work highlights the capability of utilizing *in situ* electrochemical characterization techniques while monitoring polymer microstructure using synchrotron X-ray scattering. We studied the electrochemical oxidation (doping) of poly(3-hexylthiophene) (P3HT) in a block copolymer of poly(3-hexylthiophene)-*b*-poly(ethylene oxide) (P3HT-PEO) mixed with LiTFSI. During the doping process, we monitored the charge mobility electrochemically and the crystalline structure of P3HT using wide angle X-ray scattering (WAXS). Combining the structural analysis with the transport measurements *in situ* allowed the observation of a clear correlation between doping-induced changes in the P3HT crystal lattice and improvements in charge mobility. Since the doping-induced structural changes involve the intercalation of a salt anion into the P3HT crystal lattice, tuning the nature of the anion present during electrochemical oxidation might provide a new route to improving hole mobility in P3HT.

“Stay handsome and don’t work too hard.”
-Ricardo Perez

Table of contents

List of figures

List of tables

Acknowledgments

While it's likely impossible to acknowledge all of the people that enabled my journey through grad school, hopefully I can at least scratch the surface here. Being part of the UC Berkeley ChemE department defined much of my grad school experience, so I first want to acknowledge those that directly influenced how I got here: Taylor Massey, Prof. Michael Dickey, Dr. Timothy Fornes, and the ChemE graduate student community in 2011. I've known Taylor for over ten years now (we were suitemates in the freshmen dorms at NC State). Taylor is one of the most thoughtful, generous people I have ever known. He has always been there for me, especially when I'm in need of whiskey and a Zachary's "Carne" pizza. Having preceded me by coming out to work in SF back in 2010, it was under Taylor's suggestion that I even look into UC Berkeley. Without Taylor's suggestion, I might not have even applied to Berkeley. Michael was my undergraduate research advisor and played an instrumental role in my development as a scientist. He was (and continues to be) an excellent mentor, who inspires creative thought and motivates students with his passion for teaching and seemingly unbounded enthusiasm. Tim, my project lead at Lord Corporation, recognized my potential to become an independent researcher and encouraged me to go to grad school even though it meant leaving his team. He was an excellent mentor and has continued to offer his support and advice during grad school, including providing recommendations for jobs and fellowships. (It seems clear that both Michael and Tim write excellent letters of recommendation, for which they have my gratitude). Finally, I want to thank the staff and ChemE graduate students who helped recruit our class back in February of 2011. The sense of community among the graduate students in the ChemE department was one of the deciding factors that brought me to Berkeley. My only opportunity to witness that community before making my decision about grad school was during the recruiting weekend, so I want acknowledge the efforts of those who helped make everything happen. In particular, I want to acknowledge Fred Deakin, Victor Ho, Ben Hsia, and the class of 2010.

Fortunately, my impression of the ChemE graduate student community at Berkeley was accurate. In particular, I want to acknowledge the entire ChemE 2011 class for being the most supportive, creative, intelligent, thoughtful, passionate, and all-around amazing classmates and friends that anyone could ask for. I can honestly say that this dissertation would not exist without all of you: Allie, Anna, Asmit, Bonnie, Brandon, Carly, Chaeyoung, Cynthia, Diesel, Eddie, Hilda, Kevin, Lin, Lunet, Melanie, Michele, Nikki, Norman, OJ, Pete, Rachel, Stan, Velencia, and Yi Pei. You were there for me (and each other) throughout all of the struggles: classes, prelims, post-beamtime slumps, existential crises, qualifying exam(s), job searching, and dissertation writing. You were also there to celebrate the good times at potlucks and house parties, birthday celebrations, ChemE kegs, the Halloween and holiday parties, post-exam celebrations, post-prelim celebrations, recruitment events, the graduation parties, Norman's last stand, post-qual celebrations, more birthday celebrations (thank you Rachel for all of the cakes!), post-colloquium celebrations, and whatever else we could find to celebrate. I am tempted to write something about each of you, because as some point you all made an impact on my

life, but for the sake of time and space, I'll just say that I'm proud of all of us, and I look forward to following everyone's journey from here.

In addition to the support I receive from my classmates, I am also fortunate to have the support of an amazing family. Specifically, I want to acknowledge all of my siblings. Josh, my older brother, somehow always finds time to call and check in with me, even though he's constantly working to take care of his nine children. I honestly don't know how he does it, but I'm grateful that he still finds the time to think of his younger brother amongst the chaos. My oldest sister, Holly, has been a rock for me. The way she handles the immense responsibility of raising and educating a family, while still constantly growing as an individual, truly inspires me. Also, I know I can always count on her to answer the phone when I'm struggling or need to vent. I've always looked up to my older sister, Valerie, and I can't begin to describe how proud I am of her. Since I started grad school, she has found an amazing partner, started a dog family, started and finished law school, passed the bar exam, and found a job that is perfectly suited to her many talents. Her ambition to improve herself and society has inspired me to both persist through grad school, as well as pursue a career path that might involve way more politics than I ever imagined. Mary, my younger sister, has truly taught me what it means to be brave. Since starting undergrad around the same time I came to grad school, she has courageously (and very successfully) pursued her interests and dreams. I'm proud of how she has grown into the amazing person she is, and I'm so glad for the opportunity to witness the happiness she has found in her life. My younger brother, Joe, has also come a long way during my time in grad school. What impresses me most about Joe is his ability to balance work and play, while persevering even when the cards don't fall his way. I'm glad I get to share the fun times with him. My youngest brother, James (yes, I have 6 siblings), is growing up entirely too fast. Although he generally prefers to spend his time online or playing video games with his friends, he still finds time to talk to me once in a while, haha. Apparently he has recently gotten serious about playing soccer…he's going to have to prove it next time we are together. Finally, I want to acknowledge my parents. My mom has dedicated nearly half of her life toward mine and my siblings' childhood education, and both of my parents have been supportive of my pursuit of higher education. I hope I will get to return the favor by teaching them about what I've learned over the course of all my time in college.

I also want to acknowledge my friends who have supported me and are like family in every way except DNA. Taylor, who I acknowledged earlier, is definitely in this category. I also want to acknowledge and thank Brady McReynolds and Daniel Sabo, my closest friends since high school, who both played an instrumental role in my decision to stick with grad school. Although it's strange to think of us as adults, I'm proud of the paths each of us has taken, and I look forward to our future adventures. Lastly, I want to acknowledge Will and Katherine McDanel, who both know the struggles of grad school all too well. Not only have they been there to support me, but they've also shown how hard work and perseverance during and after grad school can pay off. I'm proud of them and so excited for my future niece!

My housemates throughout the last 5.5 years have taught me so much, and truly made day-to-day life the best it could possibly be. I lived with John Alper for my first 4 years here. In addition to picking up some uniquely "John" quirks, I learned a ton about cooking while we lived together. John also helped inspire me to keep up with my photography hobby. I'm glad to see that he's continuing in his unique ways during his postdoc abroad. Meagan, Wes, and Kellie were also great to live with. Each of us had a very different grad school experience, so there was always something unique to complain about. The last year and a half living with Brandon and Melanie has also been great. Brandon has managed to fill any void that might have been created by the absence of John's quirkiness, and Melanie always provides some sanity. I also want to acknowledge the tremendous impact of my adopted housemates: Carly, Hilda, Lin, and Nico. Carly and Hilda are always willing to go on adventures, discuss life, or even sometimes talk science (mainly Hilda, haha). Carly's enthusiasm convinced me to finally start rock climbing, and Hilda's scolding continues to drive me to be my best. I want to thank Carly, Hilda, and Nico for putting up with my constant presence, while I eat of all their food and leave my bike in everyone's way. I know they don't deal with me solely through the goodness of their hearts, but rather because we all love Lin. Lin is truly one of the kindest, most intelligent, most talented, most generous, and most beautiful individuals I have ever known, and I don't know how I would have made it through the last 3.5 years of grad school without her. She continues to inspire me to grow into a better person every day.

Thus far I have focused mainly on acknowledging the people who supported my growth and development as an individual; however, working within Nitash Balsara's lab provided me with both the personal and intellectual support, as well as the resources necessary to perform high quality research. I want to thank Nitash for letting me be a part of his group and for being supportive when I was struggling to decide if I wanted to continue pursuing my PhD. Nitash is an intelligent and insightful scientist, and he truly cares about the well-being and success of his students. He seems to have a gift for attracting talented individuals, but more importantly, his leadership has fostered the development of a tight-knit community within the lab, where collaboration thrives and successes are shared by everyone. I can't imagine doing my PhD work anywhere else.

I've had the privilege of working with many amazing people during my time in the Balsara lab. When I first started grad school, there were a number of individuals from the Balsara lab, including Scott Mullin, Keith Beers, and Greg Stone, who were graduating soon, but still took time to meet with me and give their perspective on working for Nitash. I thank them for encouraging me to join the lab. I also want to thank David Wong for training me at the beamline and helping me consume a whole rotisserie chicken; Guilluame Sudre for being an X-ray scattering mentor and helping me write my first beamtime proposal; and Evren Ozcam for encouraging me to join the lab and assisting me during polymer synthesis. Dan Hallinan provided excellent training in general lab practice and how to maintain gloveboxes. He also helped me during polymer synthesis, provided many fruitful scientific discussions, and brought a general positivity to the lab that made adjusting to grad school much easier. Anna Javier provided me with materials to study and was instrumental in keeping the lab in shape, while Inna Gurevitch helped keep Anna in line. Alex Teran was responsible for most of my training when I joined the

lab, including block copolymer synthesis, X-ray scattering at the ALS, and how to perform electrochemical measurements. I am grateful for all of his help. Shrayesh Patel is a gentleman, a scholar, and a Chipotle aficionado. I am glad we got to work together, and I hope we will collaborate in the future. Nick Young is a true softball hero. He also provided me with sound life advice and a high quality desk-space in the basement of Tan Hall. Sebnem Inceoglu is like a sister to me. She was one of the first people I interacted with in the lab, and we were deskmates for my first couple of years. She is an amazingly talented chemist who I owe much of my success to, but she's also an amazing friend. I'm glad that I've been able to witness her happiness over the last few years. Pepa and Nikos are also very talented chemists, as well as masters of discretion. It was an honor to work on polymer synthesis with the "maestro". I am indebted to Chelsea Chen for her amazing electron microscopy work, as well as her critical analysis of my scientific explanations. Didier Devaux was responsible for bringing me up to speed on more advanced electrochemical characterization techniques. Although he hid his softball talent for many years, I still consider him an American Hero. I also want to acknowledge the excellent undergrads that have worked for me: Naveen Venkatesan, Andrew Wang, and Aditya Raguthanan. Naveen and I published a number of studies together, and now he has gone on to pursue his own PhD. Andrew and I are currently finishing up his first publication; I think he has a bright future as a researcher. Aditya and I only worked together for a short time before he decided to leave me and work for Kevin; however, I want to acknowledge that he is an excellent American citizen.

I couldn't have asked for a better set of people to join Nitash's lab when I did. Kevin is a champion of cornhole, softball, and the octagon. He is a master of the banana diet, the carillon, and handling sleep deprivation. He is also a brilliant researcher and a better friend. I truly believe that he will make fuels cells great again. Chaeyoung seems to be able to master whatever she puts her mind to. She is a brilliant musician, a creative researcher, and a great chauffeur. Katherine is a superb scientist who is passionate about everything in life. She is also an amazing singer. It was an honor singing together throughout the many lab ski trips (and whenever else Nitash decided we needed to play music, haha). Mahati is a potter extraordinaire and master of growing plants in the dungeon. She is a brilliant researcher, and I was lucky to be able to work with her on many projects. However, in terms of both of our productivities, she was a terrible desk mate.

I'm comforted to know that the Balsara lab is set to continue in its history of excellence. Alex, Doug, and Adri appear to be set to finish up their degrees in the near future. Alex is one of the kindest people I know. He is a diligent researcher, a great friend, and would be a better climber if he practiced more. Doug always brings energy and a new perspective to the lab. He excels at water sports (especially water-level control) and taking group selfies. Adri is a passionate (fierce?) researcher; her efforts have brought safety to a new level in our lab. She is also a brilliant cook. I'm glad we had opportunities to collaborate in the kitchen as well as the lab. It was a pleasure watching and helping all three of them grow into the researchers they are today. Irune and Mahesh also appear to be ready to move on to bigger and better things. Mahesh is calm, thoughtful, and literally always willing to help: his leadership will be sorely missed. Irune's creativity has inspired many

new research directions in the lab. It will be hard to replace her passion for discovery. Fortunately, Ksenia, Danielle, Rita, and Hee Jeung appear more than ready to take on the leadership roles within the lab. Ksenia is a brilliant scientist and an excellent softball captain. She is okay at cornhole… Danielle is an ambitious researcher who has bravely explored the realm of unknown (homo)polymers and the depths of electrochemistry. A softball hero…she is also okay at cornhole. Rita is a highly motivated researcher who gives her all in every project; her willingness to take on daunting tasks is inspiring. It has been a pleasure collaborating with Hee Jeung. She manages to bring energy to everything and everyone she works with, even when she's exhausted from synthesis. Whitney, Jackie, and Deep have progressed a lot in their first year in the lab. Whitney has been an excellent mentee, even though I've been slacking a bit in my mentorship. She is already a master of polymer synthesis and installing refrigerators, and she's well on her way to mastering X-ray scattering. I think she's well-prepared to uncover the mysteries of block copolymer electrolyte self-assembly. Jackie always brings energy to the lab (except maybe during synthesis). She is the destroyer of Polymer Source, master of group lunch organization, and a future cornhole champion. Deep is resilient researcher who is dedicated to getting the most out of grad school life. I wish I would have been as proactive as he has in taking advantage of life in the Bay area. He is also an extremely patient and generous GSI. From my few interactions with Gumi and Mike, I think the lab has a bright future ahead. Gumi is always cheerful and has great taste in group meeting snacks. Mike always seems calm and collected, but he still knows how to rock out during karaoke. I have complete faith that both the research and the culture of Balsara's lab will be in good hands, and I am excited to see what breakthroughs will develop in the next few years.

Lastly, I want to acknowledge all of the people at the synchrotron facilities that made my research possible. In particular, Eric Schaible was instrumental in providing a quality beamline setup at ALS beamline 7.3.3, where nearly all of my major experiments were performed. It was a pleasure working with him over the last five years. I also want to thank Chenhui Zhu and Polite Stewart for all of their help at beamline 7.3.3. I thank Chris Tassone for his work setting up beamline 1-5 at SSRL and for all of his help getting our heating stage to work there.

Chapter 1 – Introduction

The transition from a fossil fuel-based economy to an economy based on renewable energy sources will require significant improvements in energy storage technology.[1–3] While the performance of energy storage systems is typically on the forefront of research, safety remains a primary concern for the practical implementation of any high-capacity energy storage system.[4,5] The overarching goal of the research presented in this dissertation is the development of safe high-capacity battery technologies; the approach rests in developing a fundamental understanding of the performance of inherently safe battery electrolyte materials, in order to inform the rational design of improved battery technologies.

1.1 Solid Polymer Electrolytes (SPEs)

A major safety hazard in many high energy density battery technologies is the use of volatile, flammable solvents in the electrolyte formulation.[6–8] In the event of a cell failure, these volatile components can cause the battery cell to over-pressurize and rupture, whereupon the flammable vapors can ignite and induce the catastrophic failure of the entire energy storage system. While such failures might be viewed as a serious nuisance in small-scale storage such as that found in portable electronics, it can actually preclude the implementation of larger scale systems (e.g., electric transportation or electric grid storage) where failure would result in significant damages and the potential loss of human life. One of the primary approaches in the development of safer battery technologies is the elimination of all volatile components through the implementation of solid state electrolytes.

The coordination of alkali metal salts with the polymer, poly(ethylene oxide) (PEO), was first reported by Fenton, Park, and Wright in 1973[9]. It was soon revealed that PEO could not only solvate the ions, but also conduct them without any additional solvents (i.e., in the melt)[10], which quickly led to the development of solid polymer electrolytes (SPEs) for electrochemical cells[11]. The field of solid polymer electrolytes advanced rapidly[12], with one of the major breakthroughs being the development of highly delocalized salts, such as lithium bis(trifluoromethanesulfonyl)imide (LiTFSI)[13]. Nevertheless, application of solid polymer electrolytes in lithium ion battery technologies has been limited due mainly to low cation mobility and restricted operating temperature requirements relative to liquid electrolytes.[14,15]

One of the primary advantages offered by SPEs is their electrochemical stability against lithium metal, which is theoretically one of the highest energy density anodes available.[16] Due to the significant increase in capacity offered by the lithium anode, SPEs could find application even with their limited transport properties. Unfortunately, after repeated charge and discharge cycles, the stripping and plating of lithium metal at the anode of a solid polymer battery tends occur unevenly, leading to “dendritic” protrusions that can short circuit the cell and lead to premature failure.[8,16,17] Monroe and Newman have proposed that these “dendritic” structures can be suppressed if the battery electrolyte has a sufficiently high shear modulus[18]; however, the mobility of polymer chains, and hence the SPE mechanical properties, are strongly coupled (i.e.,

an increase in shear modulus results in a decrease in ion mobility)[12]. It is clear that SPEs formed from simple polymer/salt mixtures will not provide the electrical or mechanical properties necessary for most battery applications.

1.2 Block Copolymer Electrolytes (BCEs)

One route to increasing the functionality of SPEs is to utilize a block copolymer, i.e., the typical ion solvating/conducting polymer is covalently bound to another polymer chain that has additional functionality. In particular, block copolymer electrolytes (BCEs) that include a rigid polymer block have gained considerable attention due to their unique ability to decouple mechanical properties from electrochemical performance.[19] A number of studies utilizing BCEs made from the block copolymer polystyrene-*b*-poly(ethylene oxide) (SEO) mixed with lithium bis(trifluoromethanesulfonyl)imide (LiTFSI) salt have provided evidence supporting Monroe and Newman's ideas on mechanical suppression of dendrite growth.[20–23] These materials hold great promise for enabling the use of the lithium metal anode; however the added complexity of microphase separation and nanoscale self-assembly within these BCEs significantly complicates their characterization, making it difficult to develop design rules for improving performance.[24–33]

Another emerging class of BCE consists of an ion solvating/conducting block (e.g., PEO) that is covalently bound to a polyanionic block.[34–37] The unique advantage of these systems is that due to the immobilization of the salt anion onto the polymer backbone, they serve as single-ion conductors for the cation species, i.e., the ion involved in the electrochemical reactions inside of a battery (e.g., Li^+). Single-ion conductors have been predicted to improve the performance of lithium batteries under certain conditions[38], as well as potentially suppressing the growth of dendritic structures[39]. The seminal work of Bouchet and coworkers[35] has indicated that block copolymers composed of PEO and the polyanionic block poly(styrene-4-sulfonyltrifluoromethylsulfonyl)imide lithium (P[(STFSI)Li]) behave as efficient single-ion conductors that appear to provide improved performance within lithium batteries. The influence that tethering the anion to the backbone of the BCE has on polymer microstructure has just begun to be explored[36,37,40,41]; however, based on the extensive study if the SEO/LiTFSI system, one would anticipate a strong correlation be microstructure and electrochemical performance in single-ion conducting BCEs.

BCEs can also be derived from polymer blocks with additional functionality, such as electronic conductivity. For example, the block copolymer poly(3-hexylthiophene)-b-poly(ethylene oxide) (P3HT-PEO), wherein P3HT is a conjugated polymer capable of conducting electronic charge, can be mixed with LiTFSI in order to conduct both ionic and electronic current.[42–46] While this material cannot function as a the separating layer between battery electrode, its unique conductive properties make it an intriguing binder material for the cathode layer.[45,47] It has been shown that the conductive properties of the P3HT phase, which drastically influence battery performance[47], are strongly dependent on an electrochemical doping[48,49], which occurs *in situ* within the battery during the charging process[42]. Electrochemical doping of P3HT can be expected to influence the microstructure of P3HT-PEO, and hence the performance of a battery cathode during operation.

It is clear that block copolymers provide an almost limitless opportunity for the development of novel electrolyte materials; however, their utility depends strongly on our ability to understand their performance and intelligently design improved materials. A key feature in the development of any BCE material is determining how the interactions between the two dissimilar polymer blocks influence the polymer nanostructure, and in turn, how that nanostructure influences electrolyte performance. The general features of block copolymer microphase separation and concomitant self-assembled nanostructures are well-established[50–53], whereas there is still much to learn about the influence of nanostructure on ion conduction[54].

1.3 Studying the Impact of Ion-Polymer Interactions in BCEs

Perhaps the most interesting aspect of BCEs is the complex interplay between nanostructure and electrochemical performance. On one hand, the presence of nanoscale structures are thought to alter conductive pathways and significantly impact electrolyte performance[54], but on the other, the presence of ions tends to dictate what nanostructures are actually formed[24–28]. Thus, we often observe both the performance and nanostructure of a given BCE sample, yet gain little insight as to how we might control either property independently.

My approach to contributing to the development of safer battery technology is based on the idea that we need to better understand how ionic species influence block copolymer microphase separation and self-assembly before we can intelligently design any improvements to the current BCE state-of-the-art. My methodology has been to perform detailed and careful analysis of BCE microstructure under controlled conditions that are relevant to either the process of microphase separation and self-assembly, or the conditions expected to occur within a battery. Since the behavior of neutral block copolymers is well understood[50–53], I can use the predicted behavior for neutral block copolymers to reveal the deviations in polymer microstructure induced by the ionic species. Additional analysis of the electrochemical response of the BCEs under similar conditions often provides insight to the environment experienced by the ions, as well as serving as a reference for comparison with other studies.

In order to study the microstructure of BCEs under the various conditions of interest, I have heavily utilized synchrotron small and wide angle X-ray scattering techniques (SAXS and WAXS). X-ray scattering is particularly well-suited for the analysis of BCEs because it can provide bulk (average) structural information of samples that have been prepared in the same manner used in application. Furthermore, the high flux provided by the synchrotron source can facilitate real-time data collection, enabling *in situ* structural analysis during the application of perturbations to the system. Lastly, since X-ray scattering provides statistically-relevant structural averages, the data can easily be compared to structure models. Such analysis can be particularly powerful when the scattering intensity values have been calibrated (i.e., absolute intensity), thus providing bounds for the model parameters. A significant result of my thesis work was the development of an experimental methodology for quantitative X-ray scattering.

1.4 Outline of Dissertation

In the enclosed work, I use quantitative X-ray scattering, in conjunction with electron microscopy, thermal analysis, and electrochemical techniques to analyze the influence of charged species on the nanostructure, phase behavior, and electrochemical properties of a series of BCEs with different chemical architectures. In Chapter 2, I provide a comprehensive guide to the experimental methodology I developed to obtain quantitative X-ray scattering data (Appendix A1 provides a guide to analysis of such data). Chapters 3 and 4 focus on the impact of adding salt to a neutral polymer (i.e., binary electrolytes). Chapter 3 presents the analysis of a model SEO/LiTFSI BCE system, wherein a structural phase transition (order-to-disorder) is probed to explore the influence of charged species on the thermodynamics of block copolymer self-assembly. Chapter 4 highlights the impact of charged species on the self-assembly of a non-ideal ("practical") SEO/LiTFSI system, where kinetic limitations begin to play a major role in BCE nanostructure. Chapters 5 and 6 utilize a library of single-ion conducting block copolymers composed of PEO-*b*-P[(STFSI)X], where X represents the cation species, to explore the influence of cation identity on the nanostructure and electrochemical properties of single-ion conducting BCEs. Chapter 5 presents the analysis of the single-ion conducting BCEs in the melt state, directly relating their nanostructure and ionic conductivity to the degree of cation dissociation from the charged polyanionic backbone. Chapter 6 demonstrates the influence of cation species on the crystallization of the neutral PEO block in these systems. Chapter 7 deals with the electrochemical doping of the simultaneous electron/ion conductor, P3HT-PEO. The work in Chapter 7 combines *in situ* WAXS and *in situ* electrochemical analysis to understand the relationship between P3HT crystal structure, charge mobility, and doping level in these systems.

1.5 Abbreviations

BCE	Block copolymer electrolyte
FEP	Fluorinated ethylene propylene
LiTFSI	Lithium bis(trifluoromethanesulfonyl)imide
P[(STFSI)Li]	poly(styrene-4-sulfonyltrifluoromethylsulfonyl)imide lithium
P[(STFSI)X]	poly(styrene-4-sulfonyltrifluoromethylsulfonyl)imide - exchangeable cation
P3HT	Poly(3-hexylthiophene)
P3HT-PEO	Poly(3-hexylthiophene)-*b*-Poly(ethylene oxide)
PEO	Poly(ethylene oxide)
PS	Polystyrene
SAXS	Small angle X-ray scattering
SEO	Polystyrene-*b*-poly(ethylene oxide) diblock copolymer
SPE	Solid Polymer Electrolyte
WAXS	Wide angle X-ray scattering

Chapter 2 - An Experimenter's Guide to Quantitative X-Ray Scattering

2.1 Introduction

X-ray scattering techniques have been become well-established methods for determining the microstructures present in soft materials.[55] In particular, the advent of improved, accessible synchrotron X-ray sources has enabled the widespread application of small angle X-ray scattering (SAXS), where quality scattering profiles can now be collected with exposure times on the order of seconds (or less) compared to the minutes or even hours needed to achieve similar signal to noise on bench top instruments. The high quality (steady flux, well-collimated) radiation and improved detectors commonly employed at synchrotron scattering instruments is amenable to the collection of scattering data with quantitative intensity; however, due to the lack of widespread adoption of intensity calibration methods, most scattering data reported in literature are still provided with arbitrary intensity units (a.u.). There has recently been a push to implement the use of calibration standards to allow for the conversion of raw intensity values to absolute scattering units (cm^{-1}); yet to my knowledge, a clear guide to the experimental steps required to yield quantitative scattering intensity does not exist. The goal of this chapter is to provide such a guide.

There are many motivations for one to undertake the effort required to perform quantitative X-ray scattering measurements. For instance, from an experimental standpoint, determining absolute scattering intensities provides a robust route to detecting artifacts in scattering data, whether from the sample or due to the instrument. Furthermore, absolute scattering data can be combined from multiple experiments using different instrument configurations, allowing one to probe an increased range of structural length-scales without having to change the sample preparation methods or the sample environment. In regard to data analysis and interpretation, absolute scattering intensities enable quantitative parameter extraction using model-independent scaling laws, as well as a means to constrain fitting optimizations when utilizing structural models to interpret data. Two case studies on the application of absolute scattering data toward quantitative structural analysis are included in Appendix A1. This chapter focuses on obtaining quantitative scattering data, and is organized into the following sections: (2.2) Background: X-ray/Matter Interactions and Scattering "Techniques"; (2.3) Sample Preparation and Optimization; (2.4) Instrument Setup; (2.5) Image Analysis and Data Reduction; (2.6) Data Corrections and Intensity Calibration; and (2.7) Data Collection.

2.2 Background: X-ray/Matter Interactions and Scattering "Techniques"

Figure 2.1 schematically depicts the most relevant physical processes that occur when an object is irradiated during a typical "hard" (i.e. non-interacting) X-ray scattering experiment. The object is irradiated with an incident X-ray intensity (I_0), which is determined by the flux X-rays of wavelength λ from the monochromatic source ($\Phi(\lambda)$), the area of the X-ray beam (A), and the exposure time (t). At any position (x) within the object, the incident radiation can either be

transmitted, absorbed, or scattered by the material, yielding intensity due to scattering (I_s) at angle θ, and the transmitted incident beam, which are both attenuated by absorption within the object. The degree of intensity attenuation due to absorption is determined by the exponential terms in Figure 2.1, which contain the linear absorption coefficient of the material for that wavelength of radiation ($\mu(\lambda)$) and the radiation path length, which is given by the total thickness of the sample (z) for the transmitted beam, and $\left(\frac{(z-x)}{\cos\theta}\right)$ for the scattered beam. The $(z-x)$ term for the attenuate of scattered intensity accounts for the path length modification due to the position of scattering event within the thickness of the sample, while the $\cos\theta$ term accounts for the increased path length for a given scattering angle.[56,57] Since scattering events are rare, typically $I_0 >> I_s$ and the attenuation of the incident beam due to scattering can be neglected.[55]

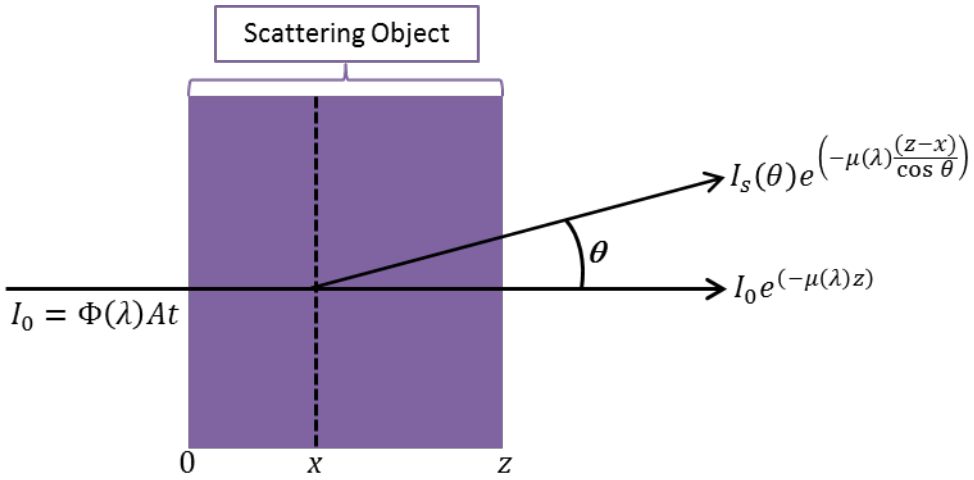

Figure 2.1: Simplified schematic of incident X-ray intensity (I_0) interacting with an object of thickness z.

Physically, X-rays interact with the electrons of the scattering object.[55,56] X-ray attenuation scales directly with the electron density; whereas scattering events occur due to fluctuations in electron density within the object. The detailed physics of matter-light interactions can be explored elsewhere.[55,56] Briefly, coherent scattering stems from the interaction between an X-ray and an electron, leading to the generation of a spherical wave of electromagnetic radiation with the same wavelength as the incident X-ray. Constructive and destructive interferences between these spherical waves lead to so-called scattered intensity at discreet angles relative to the incident radiation direction. The scattering angles are defined by the distance between spherical wave sources relative to the wavelength of the radiation. My goal here is to introduce various scattering "techniques" and provide some intuition for what processes lead to the experimentally observed scattering intensity at a given scattering angle θ. First, I define

$$q \equiv \frac{4\pi}{\lambda}\sin\frac{\theta}{2}\ [=]\ \mathrm{nm}^{-1} \tag{2.1}$$

where q is the magnitude of the scattering vector, which provides a measure of the scattering angle (θ) that is independent of the X-ray wavelength (λ) and scattering geometry used during the experiment. The relationship between q and the real-space Bragg's spacing (d) is simply $q = \frac{2\pi}{d}$. Thus large values of q correspond to large scattering angles (θ) and small Bragg's spacings (d). Likewise, small values of q relate small scattering angles (θ) and large Bragg's spacings (d).

Various scattering "techniques" are described by the range of q-values that are probed during an experiment; however, the experimental procedure in all cases is essentially identical. In Figure 2.2, I define three different scattering "regimes" based on the length-scales probed and the corresponding physical properties of the material that provide the fluctuations in electron density that lead to the scattering events. Small angle X-ray scattering (SAXS) typically refers to experiments that probe $q < 2$ nm^{-1} i.e. correlations larger than a couple of nanometers. At these length-scales, scattering events are induced by domains with different electron densities, and the total scattering intensity scales with the so-called scattering "contrast", which is defined as

$$\text{contrast} = v_{ref}(B_A - B_B)^2 \text{ [=] cm}^{-1} \tag{2.2}$$

where B_A and B_B are the scattering length densities of the two regions with differing electron density, and v_{ref} is an arbitrary reference volume. For modeling of polymer scattering, we typically use v_{ref} = 0.1 nm^3 = 1×10^{-22}cm^3. For hard X-ray experiments, the scattering length density (B_i) for a given phase can be approximated by

$$B_i \approx \frac{\mathrm{r}_e(\text{cm } [\mathrm{e}^-]^{-1})\eta_i([\mathrm{e}^-])\mathrm{N}_{AV}(\text{mol}^{-1})\rho_i(\text{g cm}^{-3})}{M_i(\text{g mol}^{-1})} \text{ [=] cm}^{-2} \tag{2.3}$$

where $\mathrm{r}_e = 2.81 \times 10^{-13}$ cm is the cross sectional scattering radius of a free electron[55]; η_i is the number of electrons per species i; N_{AV} is Avogadro's number (the product $\eta_i \mathrm{N}_{AV}$ represents the number of electrons in a mole of i); ρ_i is the density if phase i; and M_i is the molar mass of species i. It is important to reiterate that SAXS intensity stems from a *difference* in electron density (e.g. an interface, void, microphase, etc.); a completely homogeneous material will not exhibit small angle scattering. Conversely, the total intensity observed in wide angle X-ray scattering (WAXS), scales with the total electron density of the sample. WAXS experiments typical probe $q > 5$ nm^{-1} i.e. correlations between individual atoms/molecules. At these length-scales, fluctuations in electron density stem from the presence or absence of an atomic species, with electron depleted "voids" occupying the inter-atomic regions. Naturally, higher atomic mass atoms, which correspondingly have a larger local electron density, have a higher probability of interacting with X-rays and causing scattering events. Due to the scaling of WAXS intensity with the total number of electrons in the illuminated volume, some report absolute scattering intensity normalized by the number of electrons (i.e. electron units).[56] For simplicity, I will use the same intensity units (cm^{-1}) for scattering at all angles. At scattering angles between SAXS and WAXS exists a regime sometimes referred to as middle angle X-ray scattering (MAXS). Although experiments do not typically target solely this regime, it encompasses roughly $1 < q < 10$ nm^{-1} i.e. correlations on the order of 0.5 to 6 nm. At these length-scales, scattering can be caused by phases with different electron density, interfaces between those regions, as well as inter-

atom/molecule correlations. Thus the scaling of total scattering intensity is ill-defined, but can be strongly influenced by the total interfacial area between phases and the amount of density fluctuations or defects within an otherwise homogeneous phase.[55,58]

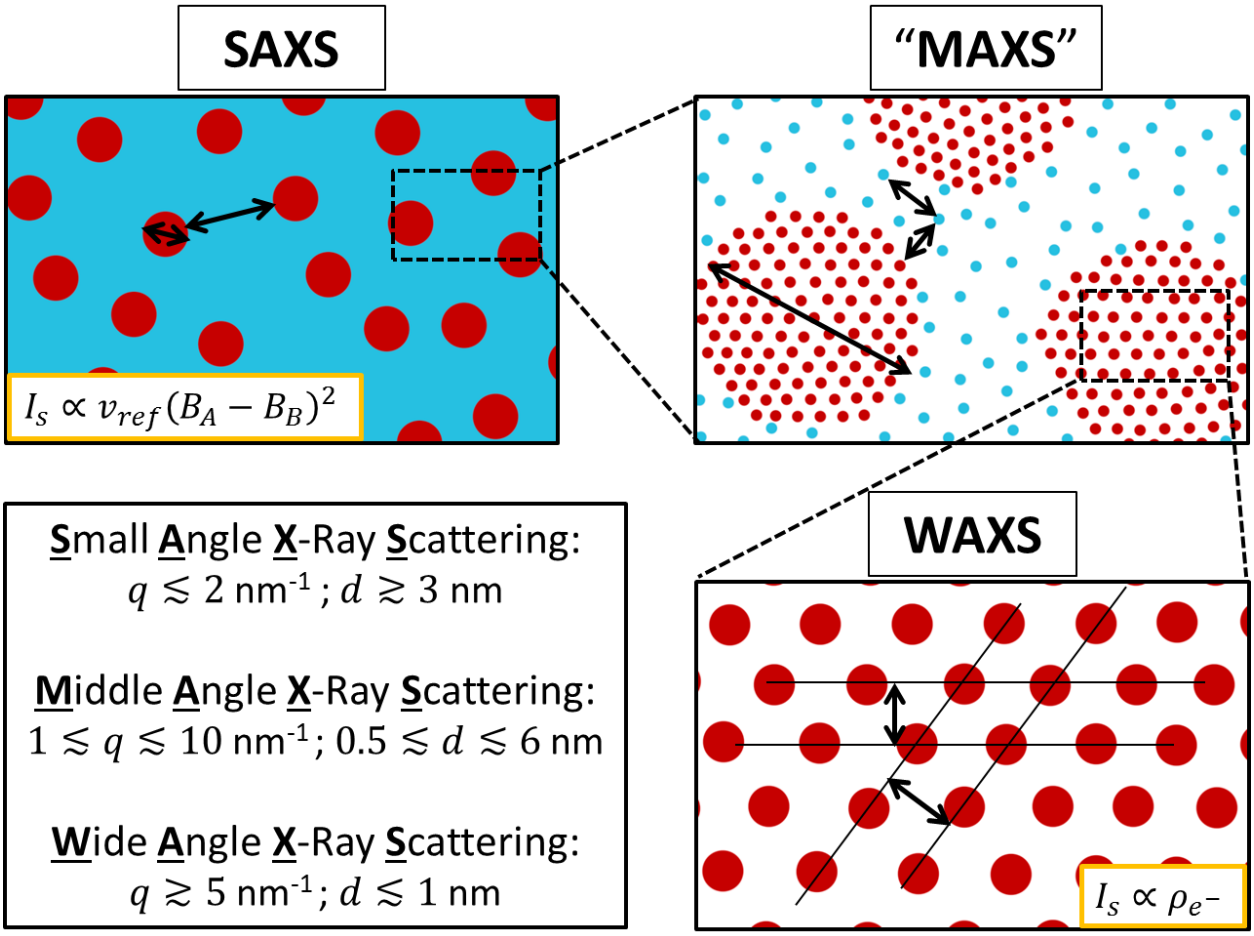

Figure 2.2: Qualitative definitions of the various scattering "techniques" based on the length-scales probed. The cartoons demonstrate a solution of ~5 nm nanoparticles (red) suspended in solvent (cyan). SAXS derives from intra- and inter-particle correlations; MAXS stems from intra-particle correlations, as well as fluctuations in density between and within homogeneous phases; and WAXS is due to inter-atomic/molecule correlations within the particle/solvent. The total scattering intensity for SAXS scales with scattering contrast i.e. the difference in scattering length density (B_A and B_B) between the two phases, whereas WAXS intensity scales with the total electron density (ρ_e-). The intensity scaling in MAXS is poorly defined due to the "grainy-ness" of the scattering objects i.e. intensity arises from both differences in scattering length density and molecular packing.

To better develop an intuitive understanding of the physical processes leading to scattering intensity observed in SAXS, MAXS, and WAXS, I find it useful to think in terms of modeling approaches. WAXS is analogous to a microscopic model, where the physics involved are perhaps a step higher than quantum physics (e.g. scattering from a single electron), but the treatment of inter-atomic correlation can technically describe the entire macroscopic system if propagated correctly. On the other hand, scattering in the SAXS regime is treated as a mean field model, where the many-bodied interactions within a given phase are averaged to a constant value in order to describe the larger-scale correlation between phases. Finally, MAXS occupies the

length-scales where both mean field and microscopic models begin to break down; local fluctuations in the mean-field averages become quite significant, but the problem is difficult to capture with the microscopic model due to the presence of interfaces, defects, multiple species, etc.

2.3 Sample Preparation and Optimization

In order to collect quality scattering data, some care needs to be taken during sample preparation. Ideally, samples will have flat surfaces and a uniform thickness over the entire area exposed to the X-ray beam. Furthermore, voids must be eliminated; the presence of voids will contribute a significant amount of SAXS intensity, and the measured thickness will not correspond to the actual amount of sample material. One must also consider the goal of the scattering experiment: if information about equilibrium structures is sought, appropriate annealing protocols need to be followed; whereas if the structure of a functional material is to be probed, samples should be prepared using the same methods as those used for the application. Lastly, the sample should be prepared such that a suitable signal to noise ratio is achieved during the scattering measurement.

The primary tool at the experimenter's disposal that can be used to yield optimal scattering results is controlling the sample thickness. As mentioned in Section 2.2, X-ray scattering events can occur at any point throughout the thickness of an object. While the inherent scattering power of the sample (i.e. the contrast in SAXS and electron density in WAXS) is fixed for a given material, the probability of a scattering event in an isotropic sample is independent of position; thus the total number of scattering events (i.e. the total scattering intensity) produced by an object is directly proportional to its thickness (assuming transmission geometry, as shown in Figure 2.1). However, the total attenuation of intensity (i.e. absorbance) within a sample is also dependent on sample thickness. X-ray transmission (T) is defined as

$$T \equiv \frac{I}{I_0} = e^{-\mu(\lambda)z} \tag{2.4}$$

where I is the total intensity exiting the sample (scattered and transmitted), I_0 is the incident intensity entering the sample, $\mu(\lambda)$ [=] cm^{-1} is the linear absorption coefficient, and z is the sample thickness. Since attenuation scales as a negative exponential of thickness and scattering scales linearly with thickness, there will naturally be an optimal thickness that yields the highest observed scattering intensity. In Figure 2.3 below, I plot the hypothetical observed scattering intensity (I_{obs}, left axis) versus the dimensionless quantity (μz), assuming a fixed value of μ. As anticipated, there is a clear maximum in I_{obs}, which corresponds to a value of roughly $\mu z = 1$, as demonstrated by the vertical dashed line in Figure 2.3. Also plotted in Figure 2.3 (right axis) is the corresponding transmission values (T) for each value of μz, which reveals that the maximum in I_{obs} occurs at roughly $T = 0.35$. Thus, for any sample, regardless of the absolute value of μ, the optimal sample thickness (z_{opt}) is related by

$$z_{opt} \approx \frac{1}{\mu} \tag{2.5}$$

Or equivalently, the optimal sample transmission (T_{opt}) value is

$$T_{opt} \approx 0.35 \tag{2.6}$$

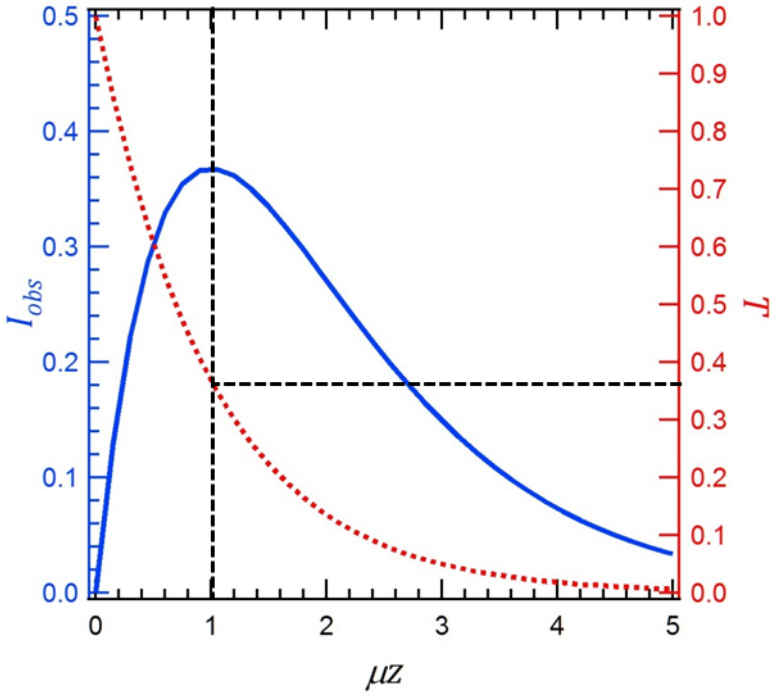

Figure 2.3: Example of the relationship between observed scattering intensity (solid blue curve, left axis), X-ray transmission (dashed red curve, right axis), and the absorption length (μz). Dashed black lines indicate the values of μz and T that yield the maximum observable scattering intensity (I_{obs}).

X-ray absorption at a given wavelength of radiation is determined by the atomic makeup of the object. Whereas the linear absorption coefficient (μ) can vary with the state of the system (phase, density, etc), the mass absorption coefficient, $^{\mu}/_{\rho}$ [=] $\mathrm{cm^2 g^{-1}}$, which is simply the linear absorption coefficient normalized by the density if the material, is independent of the chemical and physical state of the substance.[56] The mass absorption coefficients for all elements of interest are tabulated for a range of X-ray wavelengths.[59] Therefore, if the composition of a sample is known, one can approximate its mass absorption coefficient by

$$\frac{\mu}{\rho} = \sum_i w_i \left(\frac{\mu}{\rho}\right)_i \tag{2.7}$$

where *i* refers to each atomic species and *w* indicates its weight fraction within the sample. Thus, if the density of the sample compound is known (or can be approximated), then the linear absorption coefficient (μ) can be computed using Equation 2.7, and the optimal sample thickness can be approximated by Equation 2.5 prior to any X-ray scattering experiment. In practice, often either the sample thickness cannot be perfectly controlled, or the phase behavior (density) of the sample is unknown. In these circumstances, the measured X-ray transmission can either indicate whether the sample is an appropriate thickness for scattering (i.e. near T = 0.35), or be used to

calculate the optimal sample thickness for future measurements by combining Equations 2.4 and 2.5:

$$z_{opt} \approx \frac{-z_s}{ln(T_s)} \tag{2.8}$$

where the subscript *s* refers to the measured sample. As a point of reference, the block copolymer polystyrene-*b*-poly(ethylene oxide) (SEO), which will be discussed in depth later in this thesis, has a measured linear absorption coefficient of $\mu_{meas}^{SEO}(120℃) = 2.7$ cm^{-1} when the volume ratio of polystyrene (PS) and poly(ethylene oxide) (PEO) is roughly 50:50. Thus the optimal thickness of a sample of pure, symmetric SEO sample is $z_{opt} \approx 3.7$ mm.

The final means of improving scattering data on the sample preparation side of the experiment is to minimize unwanted (i.e. parastitic) scattering and absorption from sources other than the target material. Although some materials can be prepared and measured free-standing in ambient atmosphere, many samples are extremely sensitive to their environment and must be sealed within a container. In such cases, one should design the container so that the windows have high X-ray transmission and do not produce a significant amount of scattering intensity. Furthermore, in all cases where samples must be enclosed in a container, an empty container should be prepared in the same manner as the samples (ideally undergoing the sample thermal treatment). This blank sample, or "empty cell", will be used to correct for parasitic scattering and absorption, as described later in this chapter.

2.4 Instrument Setup

As mentioned in the background (Section 2.2), the actual experiments performed during SAXS, MAXS, or WAXS are essentially identical, even though the information provided by each measurement can be quite different. Figure 2.4 below demonstrates the geometry of a typical transmission X-ray scattering setup. In this geometry, the sample is irradiated by an X-ray source, producing scattered X-rays, as well as transmitting the intense direct beam. The intensity of the scattered X-rays is recorded on a 2D image detector at a distance (SD) away from the sample, while the transmitted beam is typically blocked by a physical barrier (i.e. the "beamstop") in order to preserve the integrity of the detector sensors. The scattering regime (SAXS/MAXS/WAXS) is denoted by the range of q-space probed during the experiment. As highlighted by the definition of q in Figure 2.4, one can change the q-space probed by either changing the X-ray wavelength (λ) or by moving the detector in order to observe different scattering angles (θ). Typically, the latter method is employed to switch between SAXS and WAXS by adjusting the sample to detector distance (SD). In some cases, the precise range of q-space probed for a given setup (SAXS or WAXS) can be adjusted by changing the X-ray wavelength (λ); however, most scattering instruments rely on a fixed wavelength for all setups. For a 10 keV ($\lambda = 1.24$ Å) X-ray source, a typical sample to detector distance for SAXS will be $SD_{SAXS} \geq 2$ m, while WAXS will typically utilize $SD_{WAXS} \leq 0.35$ m.

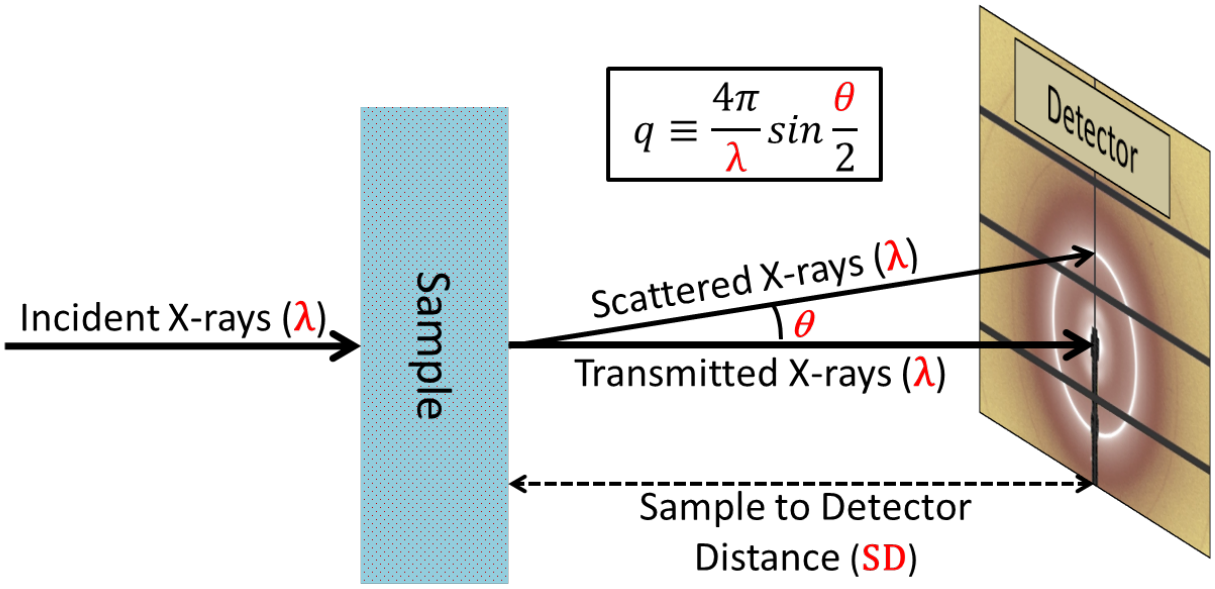

Figure 2.4: Schematic of a typical transmission X-ray scattering setup utilizing a 2D image detector.

It is instructive to derive how the observed scattering angle changes with the experimental setup, as well as how a q-value is assigned to each location of an image collected during an experiment. Figure 2.5 provides an image collected with the detector schematically demonstrated in Figure 2.4. This image provides a 2D map of the intensity observed at a distance (SD) from the scattered sample. Each pixel of the image was generated by a sensor that counts the number of photons striking a small area of the detector (0.172x0.172 mm). Thus, by knowing both the number of counts for each pixel and their position on the detector area, we can obtain the scattering intensity as a function of the scattering angle. The scattering angle (θ) associated with each pixel position on the image is determined from the scattering geometry, as portrayed schematically in Figure 2.5. We treat the image as a simple x-y coordinate plane, where the origin is defined as the location of the transmitted beam. For any point (x, y), the scattering angle can be determined from the length of the vector $\Delta(x, y)$ (i.e., $\|\Delta(x, y)\|$) and the sample to detector distance (SD) employed during the experiment by

$$\theta = \tan^{-1}\left(\frac{\|\Delta(x, y)\|}{SD}\right) \tag{2.9}$$

where $\|\Delta(x, y)\|$ is determined by the pixel size (P [=] mm) and the number of pixels away from the origin in the x- (n_x) and y-directions (n_y) using Equation 2.10.

$$\|\Delta(x, y)\| = \sqrt{(n_x P)^2 + \left(n_y P\right)^2} \tag{2.10}$$

Since the total detector area and pixel size are fixed for a given instrument, Equations 2.9 and 2.10 can be used to determine the total range of θ-values that will be observed for a given SD.

Furthermore, the effective angular resolution ($\Delta\theta$) between pixels for the detector can be determined by

$$\Delta\theta = \tan^{-1}\left(\frac{P}{\mathrm{SD}}\right) \tag{2.11}$$

I noted here the inverse relationship between $\Delta\theta$ and SD. Setting the detector distance further away from the sample provides a higher angular resolution; however, a smaller portion of θ-space will be probed for a given detector area.

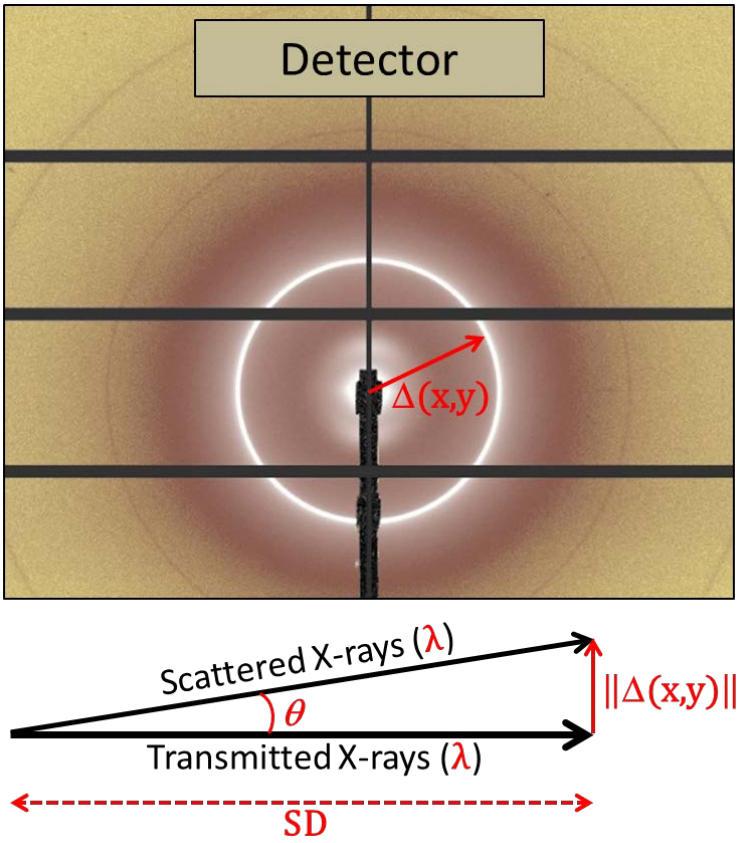

Figure 2.5: An example image from the detector during an X-ray scattering experiment. The scattering geometry schematic from Figure 2.4 is replicated below the image for reference.

The relations in Equations 2.9-2.11, combined with the definition of q (Equation 2.1), provide insight to the capabilities for a given instrument, allowing for the experimentalist to choose an appropriate setup to probe the structural length-scales they are interested in (through $d = \frac{2\pi}{q}$). Furthermore, as noted in the introduction, if the scattering intensity is known in absolute units, measurements from multiple setups (e.g. different detector distances, wavelengths, or instruments) can be combined in order to extend the range of length-scales probed. For Example, using the instrument at the Advanced Light Source (ALS) Beamline (BL) 7.3.3[60], I routinely measure samples using both a SAXS (SD ≈ 3.8 m) and WAXS (SD ≈ 0.3 m) in order to probe a

q-range of $0.035 < q < 35$ nm^{-1}, which corresponds to real-space length-scales from $180 > d > 0.18$ nm.

2.5 Image Analysis and Data Reduction

While it is important to discuss the experimental aspects of scattering data collection, it is perhaps be more instructive to first demonstrate the data processing procedures necessary to obtain absolute (quantitative) scattering intensity data. As noted in the previous section, the data obtained during a typical scattering experiment exists in the form of an image file. While there is utility in qualitatively analyzing the 2D scattering images (especially for anisotropic structures), in the majority of cases, bulk transmission X-ray scattering measurements yield isotropic 2D patterns (see Figure 2.5 for example). In such cases, quantitative analysis is simplified by obtaining a 1D data set of intensity (I) versus the magnitude of the scattering vector (q). In this section we briefly outline the procedure for obtaining 1D scattering profiles, and in the next section we detail how to correct the raw intensity values and calibrate I into absolute units.

The first step in processing any 2D scattering image is to eliminate artifacts within the image. While image processing can be performed using a number of programs, all of the work in this thesis was performed using the Nika[61] macro in Igor Pro, which was developed and is maintained by Jan Ilavsky (reference [61] provides an excellent description of the capabilities and operation of the program). In order to remove artifacts from a scattering image within Nika, one simply needs to create an image "mask", which effectively excludes the "highlighted pixels" from any processing steps. Figure 2.6a below shows an image collected during a WAXS experiment at ALS BL 7.3.3, wherein the detector was exposed to the X-ray beam for 5 seconds with no sample present; the color scale in the inset indicates pixel intensity. The Pilatus 2M detector used to capture the image in Figure 2.6a is composed of multiple rectangular sensor modules, hence the image appears tiled. Furthermore, the beamstop, which is used to physically block the high intensity transmitted X-ray beam, is creating an obvious shadow in the lower center of the image. These portions of the image are artifacts of the instrument and must be eliminated before converting the image into a 1D data set. The typical method used to obtain a 1D profile of I vs. q is to circularly average the intensity values for all pixels of the same distance from the origin (i.e. beam center), thus providing a robust intensity measure for each value of $\|\Delta(x,y)\|$, which through Equations 2.9-2.10 can be converted into q. Figure 2.6b demonstrates the outcome of circularly averaging the uncorrected image in Figure 2.6a, where the sharp drop in I as q approaches 0 (i.e. towards the beamstop) and the period dips in I throughout the profile reveal the influence of the image artifacts described above. In Figure 2.6c I show the same scattering image as in Figure 2.6a; however, this time the artifacts have been masked[61] (masked regions are highlighted in black). The corresponding 1D profile obtained by circularly averaging the image in Figure 2.6c is provided in Figure 2.6d. The smooth 1D profile indicates the image has been suitably masked over most of the image, although the decrease in intensity at low q-values indicates a small influence from the beamstop shadow remains. A new mask could be drawn (if necessary for the relevant analysis), but likely at the expense of a smaller q-range in the resulting 1D profile.

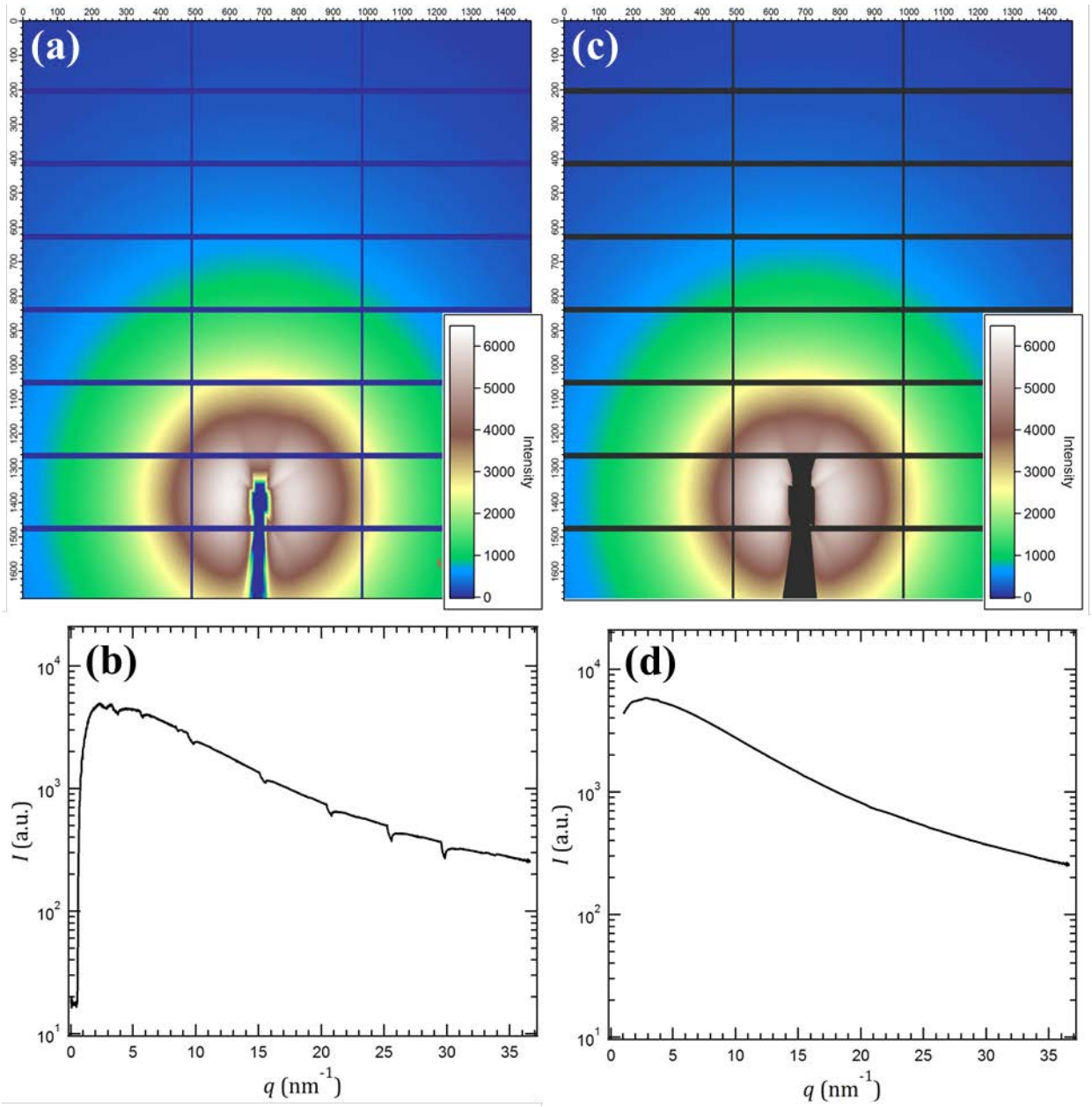

Figure 2.6: (a) 2D scattering image from the Pilatus 2M detector with no sample present. (b) The 1D scattering profile obtained from the image in (a). (c) A masked version of the 2D scattering image from (a), with the corresponding 1D profile (d).

Once a suitable image mask has been drawn in the Nika macro, it can be saved and applied to all subsequent images collected during that experiment. The next step in image processing is to determine an accurate value of SD for the instrument setup, as well as the position of the origin (i.e. the location of the transmitted beam) in the 2D images. These two values are determined simultaneously from an image obtained by scattering a sample with a known scattering pattern. In all the work described in this thesis, I use a silver behenate (AgB) calibration sample, whose 2D scattering pattern is shown in Figure 2.7 below. Since the scattering angles for each peak are well-known for AgB and the measured pattern is completely isotropic, one can iteratively match the measured 2D scattering pattern to a calculated pattern by

using Equation 2.9 with the known AgB scattering angles and varying SD and the origin location. The results of such an optimization (performed in Nika) are demonstrated by red and white concentric circles highlighting the first four rings of the AgB scattering pattern. The corresponding value for the sample to detector distance (SD) and location of the beam center can now be used with Equations 2.1 and 2.9 to assign a *q*-value for each $\|\Delta(x,y)\|$. Thus masked images from any measurement taken with that instrument setup can be radial averaged to obtain 1D profiles of *I* vs *q*.

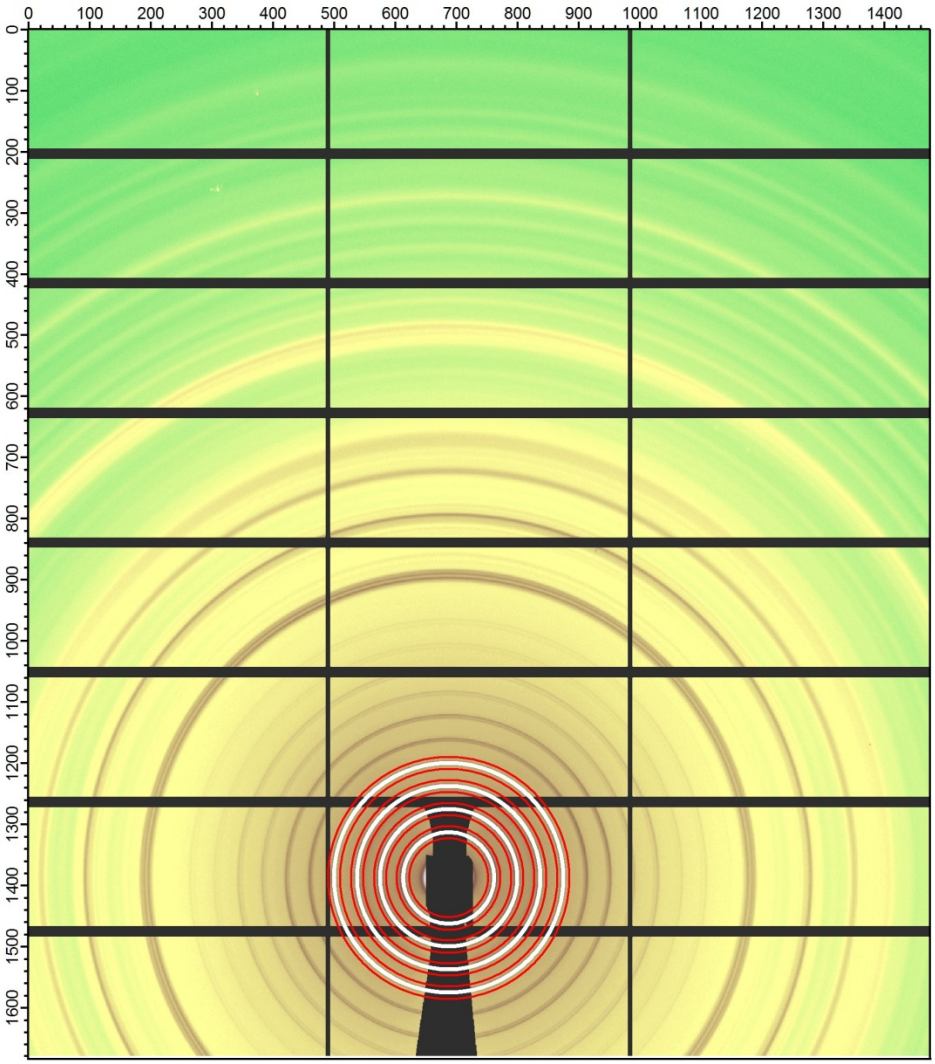

Figure 2.7: 2D scattering pattern collected by exposing an AgB calibration standard in a WAXS configuration. The red and white circles indicate regions where the scattering pattern was fitted and the predicted scattering ring locations, respectively.

A number of corrections can be applied to the data during the conversion from 2D images to 1D intensity profiles when using the Nika macro[61]. In order to apply the corrections and calibration procedure that will be described in the next section, the only corrections that should be applied (beyond the image mask) are “Geometry Corr” and “Polarization Corr”, which account for the fact that the detector is flat and synchrotron radiation is polarized, respectively.

The data may also be "Dezingered" in order to eliminate defective pixels. The Nika settings used to generate the *I* vs. *q* plots in Figure 2.6 are shown in Figure 2.8 below.

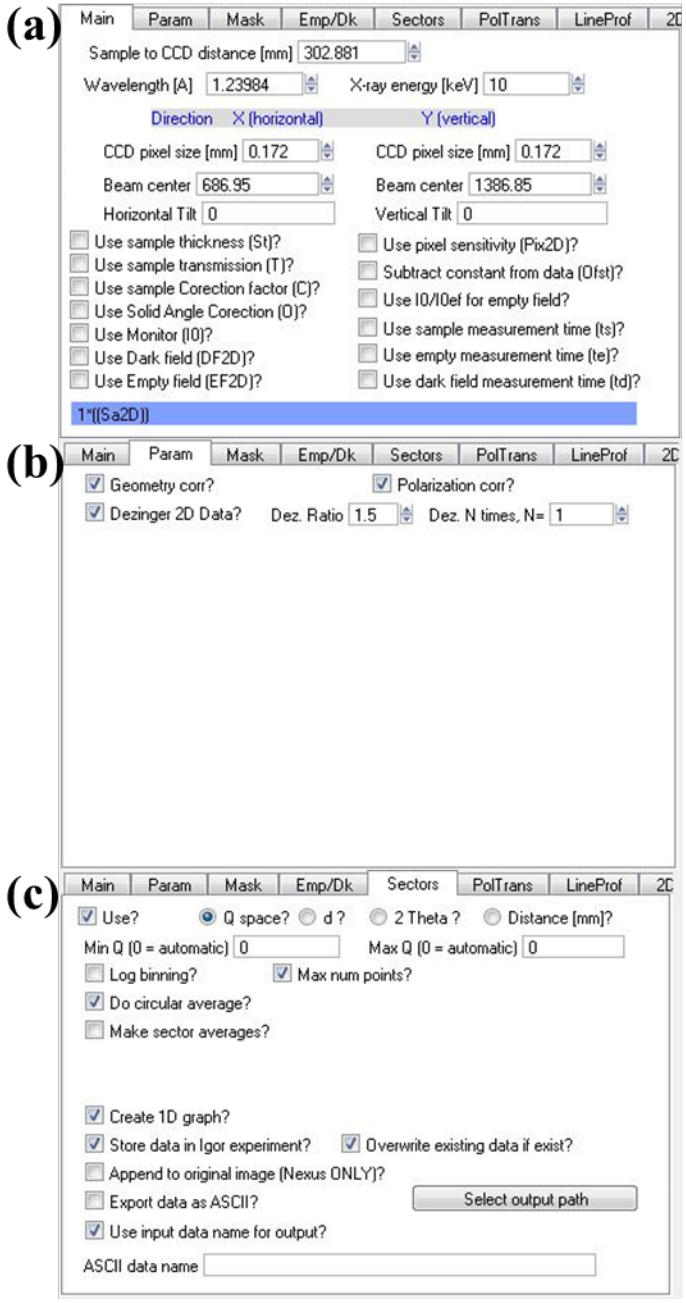

Figure 2.8: The settings used in the Nika (a) "Main" panel; (b) "Param" panel; and (c) "Sectors" panel when converting the WAXS image in Figure 2.6.

2.6 1D Data Corrections and Intensity Calibration

2.6.1 General Overview of Scattering Contributions

Before calibration to absolute units, the I vs. q data needs be corrected for sample absorption and the scattering from the empty cell. In the case of SAXS, where $\cos\theta \approx 1$ this correction is simply achieved by Equation 2.12:

$$I_{corr}(q) = \frac{\left[I_{sam,det}(q) - DC\right]}{T_{sam}} - \frac{\left[I_{ec,det}(q) - DC\right]}{T_{ec}} \tag{2.12}$$

where $I_{corr}(q)$ is the corrected scattering intensity, $I_{sam,det}(q)$ and $I_{ec,det}(q)$ are the measured scattering intensities from the sample and the empty sample holder, respectively, DC is the dark current/electronic noise from the detector readout, and T_{sam} and T_{ec} are the respective X-ray transmission values through the sample and the empty holder. However, when the assumption of $\cos\theta \approx 1$ no longer holds, such as with WAXS measurements, the absorption correction becomes more complex, as noted by Cotton and coworkers.[57] Following their approach for improving data treatment in neutron scattering, I have derived the angle-dependent correction factors for scattering from a free-standing object, as well as an object enclosed within a container.

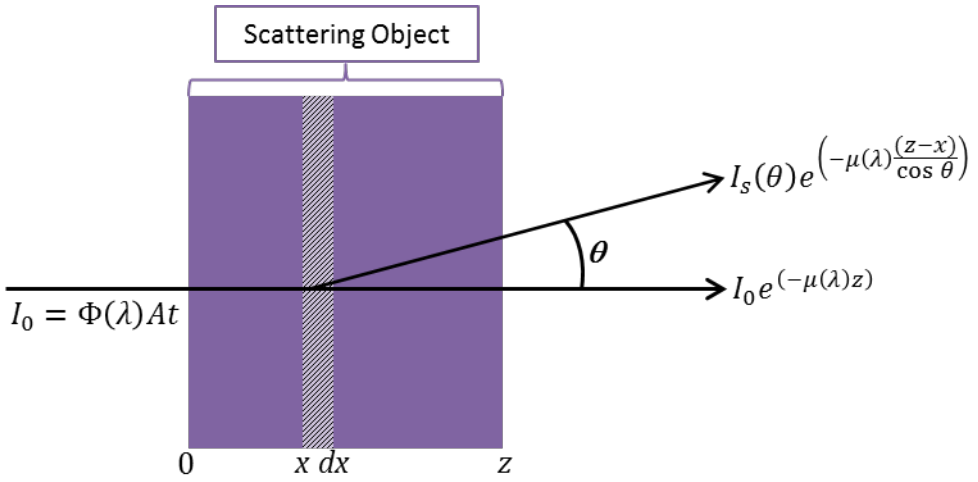

Figure 2.9: Schematic of scattering object where I_0 is the incident X-ray intensity, I_s is the scattered intensity at angle θ, z is the total sample thickness, and x is the location within the sample where the scattering event occurs.

To begin, we return back to our schematic from Figure 2.1; however, as shown in Figure 2.9, we will focus on a slice of thickness dx located at position x within the scattering material. As described in the earlier, any point throughout the thickness of the object, an incident X-ray has a probability to absorb or scatter. If we assume the frequency of multiple scattering is low i.e. scattered X-rays do not undergo additional scattering events, the total expected scattering intensity (I_s) detected from an object of thickness z is given by[57]

$$I_s(q) = \Phi(\lambda)\epsilon(\lambda)\Delta\Omega At \int_0^z \widetilde{\sigma_s}(q) e^{\left[-\mu\left(x+\frac{z-x}{\cos\theta}\right)\right]} dx \tag{2.13}$$

where $\Phi(\lambda)$ is the flux of incident x-rays per surface unit, $\epsilon(\lambda)$ is the detector efficiency, $\Delta\Omega$ is the solid angle of the detector element, A is the illuminated sample area, t is the measurement exposure time, $\widetilde{\sigma_s}(q)$ is the differential scattering cross section per unit volume of the sample, μ is the linear absorption coefficient of the sample, z is the sample thickness, θ is the scattering angle, and x is the position within the sample.[57] Evaluation of the integral in Equation 2.13 yields

$$I_s(q) = \Phi(\lambda)\epsilon(\lambda)\Delta\Omega A t\widetilde{\sigma_s}(q)\left(\frac{e^{\left(\frac{-\mu z}{\cos\theta}\right)} - e^{-\mu z}}{\mu\left(1-\frac{1}{\cos\theta}\right)}\right) \tag{2.14}$$

Using the relationship between the linear absorption coefficient and X-ray transmission in Equation 2.4, we can re-cast the term in parentheses (i.e. the attenuation term) in Equation 2.14 as

$$\left(\frac{e^{\left(\frac{-\mu z}{\cos\theta}\right)} - e^{-\mu z}}{\mu\left(1-\frac{1}{\cos\theta}\right)}\right) = \frac{T^{\frac{1}{\cos\theta}} - T}{\left(\frac{-\ln(T)}{z}\right)\left(1-\frac{1}{\cos\theta}\right)} = zT\left(\frac{T^{\left(\frac{1}{\cos\theta}-1\right)} - 1}{\ln(T)\left(\frac{1}{\cos\theta}-1\right)}\right) \tag{2.15}$$

and by defining the angle-dependent X-ray transmission, $T(\theta)$, as

$$T(\theta) \equiv T\left(\frac{T^{a(\theta)} - 1}{a(\theta)\ln(T)}\right); a(\theta) = \frac{1}{\cos\theta} - 1 \tag{2.16}$$

we can simplify Equation 2.14 into

$$I_s(q) = \Phi(\lambda)\epsilon(\lambda)\Delta\Omega A t\widetilde{\sigma_s}(q) zT(\theta) = C_{config}\widetilde{\sigma_s}(q) tzT(\theta) = ztT(\theta)F(q) \tag{2.17}$$

where we note that $\Phi(\lambda)$, $\epsilon(\lambda)$, $\Delta\Omega$, and A are instrument parameters that are constant (C_{config}) for a given experimental setup, which can be combined with $\widetilde{\sigma_s}(q)$ to yield the scattering intensity per unit thickness of the sample ($F(q)$). Thus for any scattering object, the observed intensity depends on the sample thickness (z), the exposure time (t), its angle-dependent X-ray transmission ($T(\theta)$), and $F(q)$, which can be thought of as the intrinsic scattering of the material. We note here that in the limit of small angle scattering ($\theta \to 0$) the attenuation term from Equation 2.14 becomes:

$$\lim_{\theta\to 0}\frac{e^{\left(\frac{-\mu z}{\cos\theta}\right)} - e^{-\mu z}}{\mu\left(1-\frac{1}{\cos\theta}\right)} = ze^{-\mu z} = zT \tag{2.18}$$

And thus for SAXS measurements, where $\cos\theta \approx 1$, the scattering intensity is scaled by the constant X-ray transmission factor T and is given by Equation 2.19:

$$I_s(q) = C_{config}\tilde{\sigma_s}(q)tzT = ztTF(q) \tag{2.19}$$

2.6.2 Attenuation of X-Rays by Absorbing/Scattering Objects, such as Windows or Air

In practice, the flux of X-rays entering a sample, as well as the subsequent scattered X-rays, are often attenuated by additional absorbing objects. An example of a possible scenario where the incident beam and scattered X-rays encounter absorbing objects is demonstrated schematically in Figure 2.10. In this scenario, the incident beam hitting the scattering object has already been attenuated by an absorbing object of thickness z_1 and transmission T_1. The subsequent scattered intensity is thus also scaled by a factor of T_1. The incident beam (attenuated by T_1 and T_s), as well as the scattered intensity (attenuated by T_1) then pass through an object of thickness z_2 and transmission T_2, where the incident beam gets attenuated by the usual factor, T_2, but due to a longer (angle-dependent) path length, the scattered intensity is attenuated by the factor T_2^{θ}, where T^{θ} accounts for the difference in path length and is defined as:

$$T^{\theta} \equiv e^{-\mu z(\theta)} = e^{\left(\frac{-\mu z}{\cos\theta}\right)} = T^{\frac{1}{\cos\theta}} \tag{2.20}$$

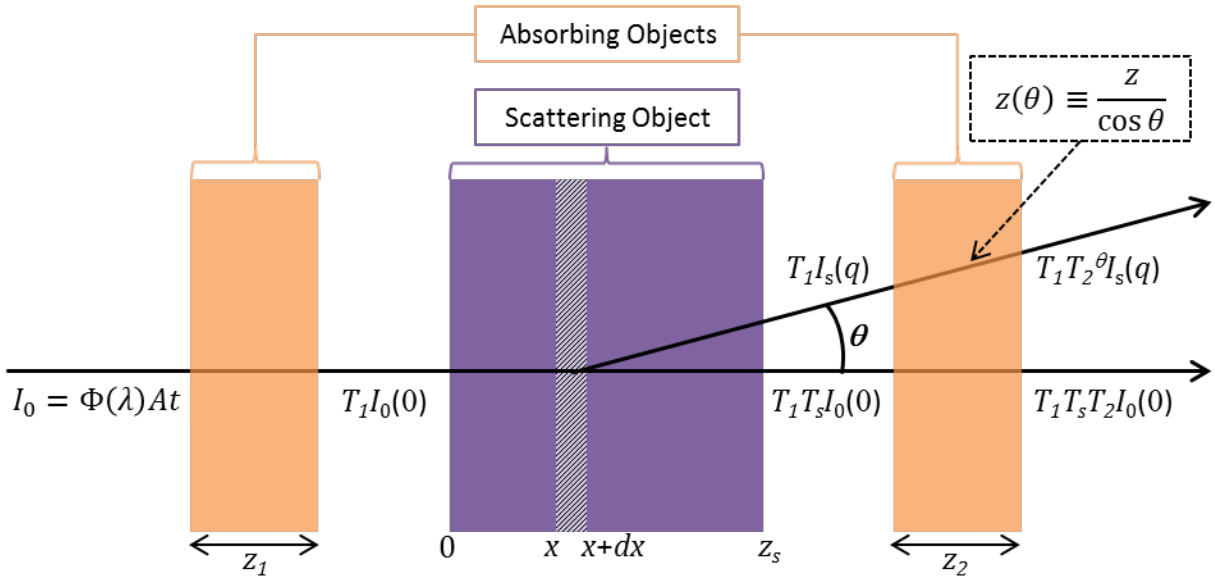

Figure 2.10: Schematic of a scattering object between two absorbing objects of thickness z_1 and z_2, where the incident intensity is attenuated by all three objects, and the scattered intensity is attenuated by the scattering object itself, as well as the second absorbing object.

Thus the angle-dependence of x-ray transmission not only applies to the attenuation from the scattering object itself, but also to any absorbing object in the path of the X-rays after the scattering object. In the following sections I demonstrate how to utilize the attenuation expressions in Equations 2.4, 2.16, and 2.20, along with scattering relationship in Equation 2.17 to extract the intrinsic scattering of a sample from experimental data.

2.6.3 Attenuation Correction for a Free-Standing Object

Utilizing the framework highlighted in (2.6.1) and (2.6.2), I now demonstrate how to extract the intrinsic scattering ($F(q)$) information from experimental data. First, I begin with a free-standing sample sitting a given distance (flight path, *fp*) from the detector, as shown in Figure 2.11 below. In the ideal case, the scattering from a free-standing object would be given by Equation 2.17, however, due to imperfect optics (beam spreading), X-ray absorption along the flight path after the scattering object, and electronic noise from the detection system itself, the recorded scattering pattern contains additional intensity that needs to be removed before interpretation.

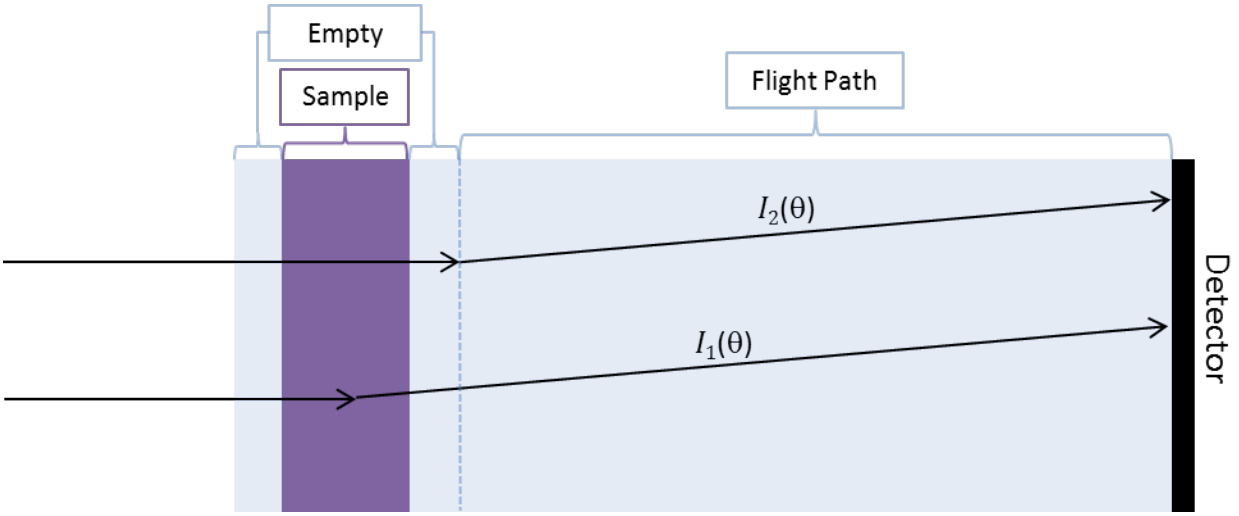

Figure 2.11: Schematic of a freestanding scattering sample. $I_1(\theta)$ represents detected intensity due to the sample, and $I_2(\theta)$ represents detected intensity due to parasitic scattering and beam spreading.

The two major contributions to the recorded scattering pattern for the sample in Figure 2.11 are the scattering from the sample itself ($I_1(\theta)$) and the additional intensity due to the incident beam spreading along the flight path and not being fully blocked by the beamstop ($I_2(\theta)$). Using the methodology described in (2.6.1), we can write the intensity recorded at the detector for a free-standing sample, $I_{sam,\,det}(q)$, as

$$I_{sam,\,det}(q) = I_1(\theta) + I_2(\theta) + DC = T_s(\theta)T_{fp}^{\theta}tz_sF_s(q) + T_sT_{fp}^{\theta}tF_b(\theta) + DC \qquad (2.21)$$

where the subscript *s* refers to the sample, the subscript *fp* corresponds to the flight path, $F_b(\theta)$ is the angle dependent intensity due to beamspreading, and DC is the electronic noise from the detector read-out. Since all of the structural information for the sample is contained in $F_s(q)$, t is chosen during the experiment, and z_s can be measured, the goal is to develop an expression for $tz_sF_s(q) \equiv I_{corr}(q)$. To begin, we isolate the $tz_sF_s(q)$ term yielding

$$tz_sF_s(q) = \frac{1}{T_s(\theta)T_{fp}^{\theta}}\left\{\left[I_{sam,\,det}(q) - DC\right] - T_sT_{fp}^{\theta}tF_b(\theta)\right\} \qquad (2.22)$$

The expression in Equation 2.22 reveals that one must measure the empty beam contribution ($F_b(\theta)$) independently in order to extract $tz_sF_s(q)$. To achieve this, one must measure the

scattering profile of the beam at the detector with no sample present ("empty beam", $I_{b,\,det}(q)$), as demonstrated in Figure 2.12 below. In this instance, the only contribution to the scattering is due to the imperfections in the beam and the beamstop. One can write the recorded intensity as

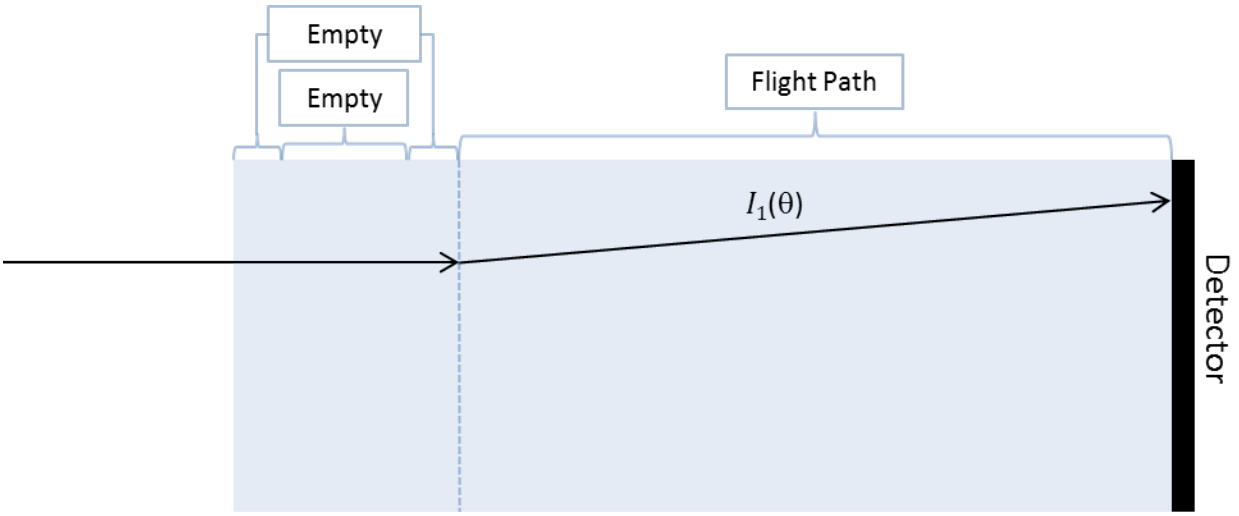

Figure 2.12: Schematic of scattering from the empty beam, where $I_1(\theta)$ represents detected intensity due to parasitic scattering and beam spreading.

$$I_{b,\,det}(q) = I_1(\theta) + DC = T_{fp}^{\theta} t F_b(\theta) + DC \tag{2.23}$$

which allows rearrangement to provide the following expression for $F_b(\theta)$

$$tF_b(\theta) = \frac{1}{T_{fp}^{\theta}}\left[I_{b,\,det}(q) - DC\right] \tag{2.24}$$

Thus, by measuring $I_{sam,\,det}(q)$ and $I_{b,\,det}(q)$ at the same exposure time, t, we can combine Equations 2.22 and 2.24 to yield

$$tz_s F_s(q) = \frac{1}{T_s(\theta) T_{fp}^{\theta}}\left\{\left[I_{sam,\,det}(q) - DC\right] - T_s\left[I_{b,\,det}(q) - DC\right]\right\} = I_{corr}(q) \tag{2.25}$$

which allows one to determine $I_{corr}(q)$ for a free-standing sample entirely from measured values.

2.6.4 Corrections for a Sample inside of a Container

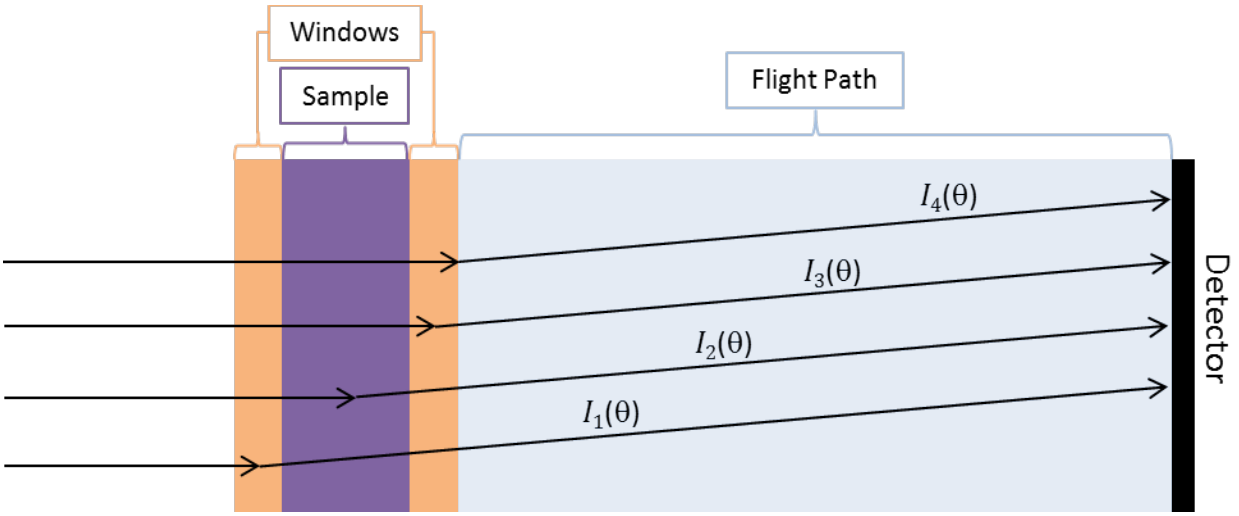

Figure 2.13: Schematic of a scattering sample within a container. $I_1(\theta)$ represents detected intensity due to the first container window, $I_2(\theta)$ represents detected intensity due to the sample, $I_3(\theta)$ represents detected intensity from the second container window, and $I_4(\theta)$ represents the detected intensity due to parasitic scattering and beam spreading.

The methodology used above to determine $I_{corr}(q)$ for a free-standing sample can also be applied to determine the corrections for a sample within a container. Here I treat the general case of a sample enclosed between two identical windows that both absorb and scatter X-rays, as shown in Figure 2.13 above. In this case there are 4 major contributions to the pattern recorded at the detector ($I_{sam,\,det}(q)$): Scattering from the container windows ($I_1(\theta)$ and $I_3(\theta)$), scattering from the sample ($I_2(\theta)$), and intensity due to beam spreading ($I_4(\theta)$). Accounting for attenuation of each layer, $I_{sam,\,det}(q)$ can be written in the same manner as Equation 2.21 to be:

$$\begin{aligned} I_{sam,\,det}(q) = {} & T_w(\theta)T_s^{\theta}T_w^{\theta}T_{fp}^{\theta}tz_wF_w(q) \\ & + T_wT_s(\theta)T_w^{\theta}T_{fp}^{\theta}tz_sF_s(q) \\ & + T_wT_sT_w(\theta)T_{fp}^{\theta}tz_wF_w(q) + T_wT_sT_wT_{fp}^{\theta}tF_b(\theta) + DC \end{aligned} \tag{2.26}$$

where the subscript w refers to the container windows and all other terms follow the nomenclature used for the free-standing sample. Again, our goal is to extract $tz_sF_s(q)$, thus we rearrange to yield Equation 2.27:

$$tz_sF_s(q) = \frac{1}{T_wT_s(\theta)T_w^{\theta}T_{fp}^{\theta}}\left\{\begin{array}{c}\left[I_{sam,\,det}(q) - DC\right] \\ -\left(T_w(\theta)T_s^{\theta}T_w^{\theta}T_{fp}^{\theta} + T_wT_sT_w(\theta)T_{fp}^{\theta}\right)tz_wF_w(q) \\ -T_wT_sT_wT_{fp}^{\theta}tF_b(\theta)\end{array}\right\} \tag{2.27}$$

As with the free-standing sample, one needs to make additional measurements in order to evaluate Equation 2.27. In this case, we need to measure the scattering of both the empty container ($I_{ec,\,det}(q)$, Figure 2.14) and the beam with no sample present ($I_{b,\,det}(q)$, Figure 2.12). One can write the scattering contributions from the empty container (Figure 2.14) in the usual way as

$$I_{ec,\,det}(q) = T_w(\theta)T_w^{\theta}T_{fp}^{\theta}tz_wF_w(q) + T_wT_w(\theta)T_{fp}^{\theta}tz_wF_w(q) + T_wT_wT_{fp}^{\theta}tF_b(\theta) + DC \tag{2.28}$$

which can be rearranged into

$$tz_wF_w(q) = \frac{1}{\left(T_w(\theta)T_w^{\theta}T_{fp}^{\theta} + T_wT_w(\theta)T_{fp}^{\theta}\right)}\left\{\left[I_{ec,\,det}(q) - DC\right] - T_wT_wT_{fp}^{\theta}tF_b(\theta)\right\} \tag{2.29}$$

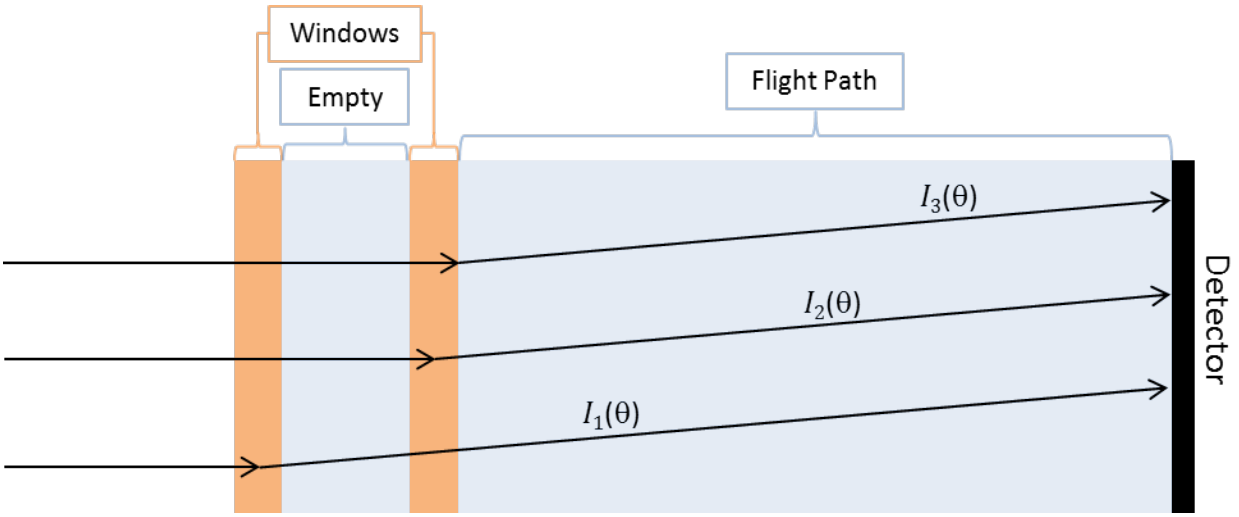

Figure 2.14: Schematic of scattering from the empty container. $I_1(\theta)$ represents detected intensity due to the first container window, $I_2(\theta)$ represents detected intensity from the second container window, and $I_3(\theta)$ represents the detected intensity due to parasitic scattering and beam spreading.

Substituting Equation 2.29 into Equation 2.27 yields

$$tz_sF_s(q) = \frac{1}{T_wT_s(\theta)T_w^{\theta}T_{fp}^{\theta}}\left\{\begin{array}{c}\left[I_{sam,\,det}(q) - DC\right] \\ -\dfrac{\left(T_s^{\theta}T_w^{\theta} + T_wT_s\right)}{\left(T_w^{\theta} + T_w\right)}\left[I_{ec,\,det}(q) - DC\right] \\ -\left[T_s - \dfrac{\left(T_s^{\theta}T_w^{\theta} + T_wT_s\right)}{\left(T_w^{\theta} + T_w\right)}\right]T_w^2T_{fp}^{\theta}tF_b(\theta)\end{array}\right\} \tag{2.30}$$

And finally substitution of Equation 2.24 from the empty beam into Equation 2.30 gives

$$tz_sF_s(q) = \frac{1}{T_wT_s(\theta)T_w^{\theta}T_{fp}^{\theta}}\left\{\begin{array}{c}\left[I_{sam,\,det}(q) - DC\right] \\ -\dfrac{\left(T_s^{\theta}T_w^{\theta} + T_wT_s\right)}{\left(T_w^{\theta} + T_w\right)}\left[I_{ec,\,det}(q) - DC\right] \\ -\left[T_s - \dfrac{\left(T_s^{\theta}T_w^{\theta} + T_wT_s\right)}{\left(T_w^{\theta} + T_w\right)}\right]T_w^2\left[I_{b,\,det}(q) - DC\right]\end{array}\right\} \tag{2.31}$$

where all quantities are measurable. The expression in Equation 2.31 can be used to correct the attenuation and scattering due to the sample container for arbitrary scattering angles. I note that in the limit of small scattering angles, the expression in Equation 2.31 simplifies to

$$\begin{aligned} tz_s F_s(q) &= \frac{1}{T_s T_w^2 T_{fp}} \{ [I_{sam,\,det}(q) - DC] - T_s [I_{ec,\,det}(q) - DC] \} \\ &= \frac{[I_{sam,\,det}(q) - DC]}{T_s T_w^2 T_{fp}} - \frac{[I_{ec,\,det}(q) - DC]}{T_w^2 T_{fp}} \\ &= \frac{[I_{sam,\,det}(q) - DC]}{T_{sam,det}} - \frac{[I_{ec,\,det}(q) - DC]}{T_{ec,det}} = I_{corr}(q) \end{aligned} \tag{2.32}$$

which is equivalent to Equation 2.12. The relative outcomes from Equations 2.12 and 2.31 depend strongly on the linear transmission (T) through the sample. For samples with high transmission values ($T \gtrsim 0.9$), the angle-dependent attenuation correction only significantly impacts scattering at very large angles ($q \gtrsim 30\ \mathrm{nm}^{-1}$). For samples that have been optimized, with $T \approx 0.35$, the angle-dependent correction becomes significant even for a free-standing samples (i.e. no additional attenuation from a container) around $q \approx 10\ \mathrm{nm}^{-1}$. In practice, I apply Equation 2.12 to all data collected with SAXS configurations, and Equation 2.31 to data collected using WAXS geometries.

2.6.5 Experimental Measurement of X-Ray Transmission

In order to apply the attenuation corrections derived above, one must know the X-ray transmission values for the sample, empty container, and beam without a sample present. These values are usually obtained during the experiment by measuring the X-ray flux before and after the sample position; however, the experimentally measured values of transmission need to be converted to the T_s, T_w, and T_{fp} values used in the derivations of the previous section. Below I describe how to calculate these terms based on the experimental values collected at the ALS BL 7.3.3 in both the SAXS and WAXS geometries, yet the methodology should apply generally to any scattering setup where the incident and transmitted X-ray fluxes are monitored.

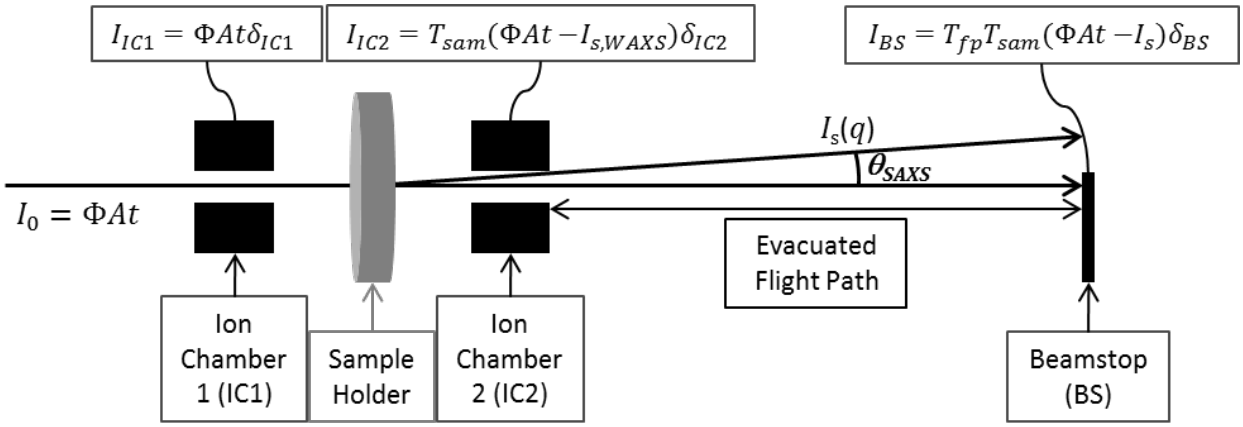

Figure 2.15: Schematic of the experimental setup for SAXS measurements at the Advanced Light Source Beamline 7.3.3.

Figure 2.15 above provides a schematic of the SAXS configuration at ALS BL 7.3.3 indicating where the X-ray flux is measured. The incident X-ray flux is measured by an ion chamber (IC1) immediately before the X-rays hit the sample target. The transmitted flux of X-rays is measured in two locations: (1) immediately after the sample by a second ion chamber (IC2) and (2) directly in front of the detector by a photodiode on the beamstop (BS) at the end of the evacuated flight tube. Thus the X-ray transmission can be calculated in two ways for every exposure as outlined below. I note that the flux measured at the second ion chamber excludes the X-rays scattered to wide angles, and that the beamstop diode only measured the flux at zero angle, thus the transmission values are calculated under the assumption that the scattered x-rays represent a very small portion of the total flux. Expressions defining experimental transmission values for a free-standing sample ($T_{sam,f}$), a sample within a container ($T_{sam,c}$), the empty container (T_{ec}), and the beam without sample (T_b) are given below. Superscript *IC* refers to values determined from the second ion chamber and superscript *BS* refers to those calculated using the beamstop diode.

$$\begin{aligned} T_{sam,f}^{IC} &\equiv \left(\frac{I_{IC2}}{I_{IC1}}\right)_{sam,f} = \frac{T_{s,f}(\Phi At - I_{s,WAXS})\delta_{IC2}}{\Phi At\delta_{IC1}} \cong \frac{T_s\delta_{IC2}}{\delta_{IC1}} \\ T_{sam,f}^{BS} &\equiv \left(\frac{I_{BS}}{I_{IC1}}\right)_{sam,f} = \frac{T_{s,f}T_{fp}(\Phi At - I_s)\delta_{BS}}{\Phi At\delta_{IC1}} \cong \frac{T_sT_{fp}\delta_{BS}}{\delta_{IC1}} \end{aligned} \tag{2.33}$$

$$\begin{aligned} T_{sam,c}^{IC} &\equiv \left(\frac{I_{IC2}}{I_{IC1}}\right)_{sam,c} = \frac{T_{s,c}(\Phi At - I_{s,WAXS})\delta_{IC2}}{\Phi At\delta_{IC1}} \cong \frac{T_wT_sT_w\delta_{IC2}}{\delta_{IC1}} \\ T_{sam,c}^{BS} &\equiv \left(\frac{I_{BS}}{I_{IC1}}\right)_{sam,c} = \frac{T_{s,c}T_{fp}(\Phi At - I_s)\delta_{BS}}{\Phi At\delta_{IC1}} \cong \frac{T_wT_sT_wT_{fp}\delta_{BS}}{\delta_{IC1}} \end{aligned} \tag{2.34}$$

$$\begin{aligned} T_{ec}^{IC} &\equiv \left(\frac{I_{IC2}}{I_{IC1}}\right)_{ec} = \frac{T_{ec}(\Phi At - I_{s,WAXS})\delta_{IC2}}{\Phi At\delta_{IC1}} \cong \frac{T_wT_w\delta_{IC2}}{\delta_{IC1}} \\ T_{ec}^{BS} &\equiv \left(\frac{I_{BS}}{I_{IC1}}\right)_{ec} = \frac{T_{ec}T_{fp}(\Phi At - I_s)\delta_{BS}}{\Phi At\delta_{IC1}} \cong \frac{T_wT_wT_{fp}\delta_{BS}}{\delta_{IC1}} \end{aligned} \tag{2.35}$$

$$\begin{aligned} T_b^{IC} &\equiv \left(\frac{I_{IC2}}{I_{IC1}}\right)_b = \frac{\Phi At\delta_{IC2}}{\Phi At\delta_{IC1}} = \frac{\delta_{IC2}}{\delta_{IC1}} \\ T_b^{BS} &\equiv \left(\frac{I_{BS}}{I_{IC1}}\right)_b = \frac{T_{fp}\Phi At\delta_{BS}}{\Phi At\delta_{IC1}} = \frac{T_{fp}\delta_{BS}}{\delta_{IC1}} \end{aligned} \tag{2.36}$$

where δ_{IC1}, δ_{IC2}, and δ_{BS} are the instrumental responses from Ion Chamber 1 (IC1), Ion Chamber 2 (IC2), and the Beamstop (BS), respectively. It is apparent from these expressions that without prior knowledge of the instrumental responses from the various flux gauges, the measured transmission values can only be compared on a relative scale; however, through proper normalization as shown below, one can calculate all relevant transmission values except for T_{fp}, which can either be predicted based on the path length, or in the case of the evacuated flight tube, we can safely assume $T_{fp} \approx 1$. T_s and T_w are calculated using the relations in Equations 2.33-2.36 by:

$$T_s = \frac{T_{sam,f}^{IC}}{T_b^{IC}} = \frac{T_{sam,f}^{BS}}{T_b^{BS}} = \frac{T_{sam,c}^{IC}}{T_{ec}^{IC}} = \frac{T_{sam,c}^{BS}}{T_{ec}^{BS}} \tag{2.37}$$

$$T_w = \left(\frac{T_{ec}^{IC}}{T_b^{IC}}\right)^{1/2} = \left(\frac{T_{ec}^{BS}}{T_b^{BS}}\right)^{1/2} \tag{2.38}$$

where the power of one-half in Equation 2.38 comes from the fact that the empty cell has two windows attenuating the beam.

The geometry of the transmission WAXS setup at ALS BL 7.3.3 is slightly different than that of the SAXS configuration described above. As shown in Figure 2.16 below, both the second ion chamber (IC2) and the evacuated flight tube are removed to make room for the detector. Thus for WAXS experiments, calculation of transmission must utilize the beamstop (BS) form of the expressions in Equations 2.33-2.36. Furthermore, the ambient air flight path cannot be assumed to have $T_{fp} \approx 1$. For example, if flight path has a length of 300mm, the transmission of 10 keV X-Rays through ambient air is predicted to be ~0.83 according to the NIST X-Ray Attenuation Database.[59] To account for this, T_{fp} for the WAXS setup at room temperature is approximated to be T_{fp}^{NIST}, which is calculated using the calibrated S-D distance as the attenuation thickness (z_{fp}) and the linear attenuation coefficient of ambient air provided by NIST ($\mu_{air}^{NIST} = 5.65 \times 10^{-3}$ cm^{-1})[59]. I note that the density of the air in the flight path near the sample stage can vary with the stage temperature, thus I typically use the following expression to approximate T_{fp} as a function of temperature (T)

$$T_{fp}(\mathrm{T}) \approx T_{fp}^{NIST}\left(\frac{T_b^{BS}(\mathrm{T})}{T_b^{BS}(25\ ^\circ\mathrm{C})}\right) \tag{2.39}$$

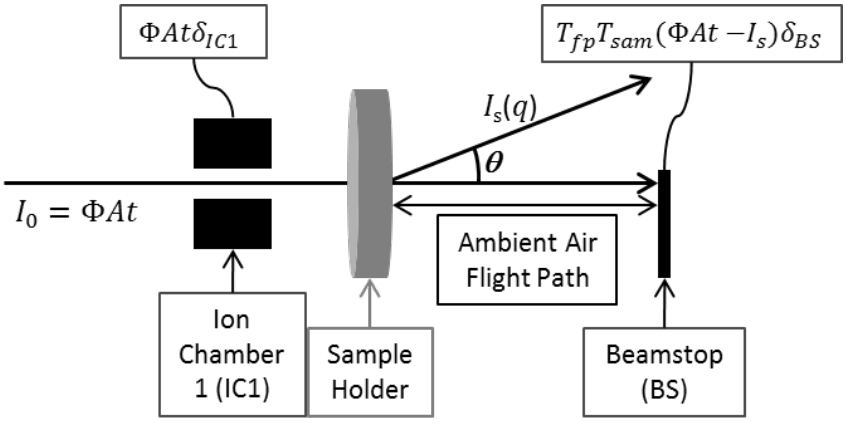

Figure 2.16: Schematic of the experimental setup for WAXS measurements at the Advanced Light Source Beamline 7.3.3.

where $T_b^{BS}(\mathrm{T})$ is the measured transmission of the empty beam at the temperature of interest, and $T_b^{BS}(25\ ℃)$ is the measured transmission at ambient temperature.

2.6.6 Calibration of I_{corr} to Absolute Units

In order to combine SAXS and WAXS data for a sample without arbitrary scaling factors, as well as to facilitate quantitative analysis of scattering intensity, $I_{corr}(q)$ needs to be further corrected to yield the intrinsic scattering of the sample (i.e. the differential scattering cross section per unit volume, $\widetilde{\sigma_s}(q)$ in absolute units (cm^{-1}). This can be achieved through a rearrangement of the expressions in Equation 2.17 into

$$\widetilde{\sigma_s}(q) = \frac{F(q)}{C_{config}} = \frac{I_{corr}(q)}{tz_s C_{config}}\ [=]\ \mathrm{cm}^{-1} \tag{2.40}$$

which can be evaluated using $I_{corr}(q)$ if the sample thickness (z_s) and the instrument configuration constant (C_{config}) are known. In all work within this thesis, I utilize a glassy carbon (GC) calibration sample from Jan Ilavsky (sample M13)[62] to determine C_{config} for each scattering geometry. To do this, one must measure the 2D scattering pattern of the GC sample and of the beam with no sample present. The isotropic 2D scattering patterns are then converted to 1D I vs q data sets and GC scattering must be corrected using the steps described in the previous section for a free-standing sample. One can then divide the resulting $I_{corr}(q)$ values for the GC sample by the exposure time and sample thickness ($z_{GC} = 0.10$ cm) to yield $F_{GC}(q)$. The actual differential scattering cross section per unit volume for the M13 glassy carbon sample ($\tilde{\sigma}_{GC}(q)$) was provided by Jan Ilavsky (as measured at The Advanced Photon Source, beamline 15ID). Thus the calibration constant (C_{config}) can be determined as the constant scaling factor required to equate the measured $F_{GC}(q)$ to the known $\tilde{\sigma}_{GC}(q)$ data. In Figure 2.17, I demonstrate the determination of C_{config} for data taken with a SAXS configuration ($C_{config}^{SAXS} = 4.03 \times 10^2\ \mathrm{s}^{-1}$) and a WAXS configuration ($C_{config}^{WAXS} = 7.75 \times 10^4\ \mathrm{s}^{-1}$) at ALS BL 7.3.3. The $\tilde{\sigma}_{GC}(q)$ and $F_{GC}(q)$ should overlap well in the q-range where the intensity begins to rapidly decay ($0.8 \leq q \leq 2\ \mathrm{nm}^{-1}$). **By convention, the differential scattering cross section per unit volume ($\widetilde{\sigma_s}(q)$) is often simply referred to as the "absolute scattering intensity" and is reported as I (cm^{-1})**. Thus, throughout the remainder of this work, any scattering data reported with units of cm^{-1} indicates that the "intensity" values correspond to the differential scattering cross section per unit volume of that sample.

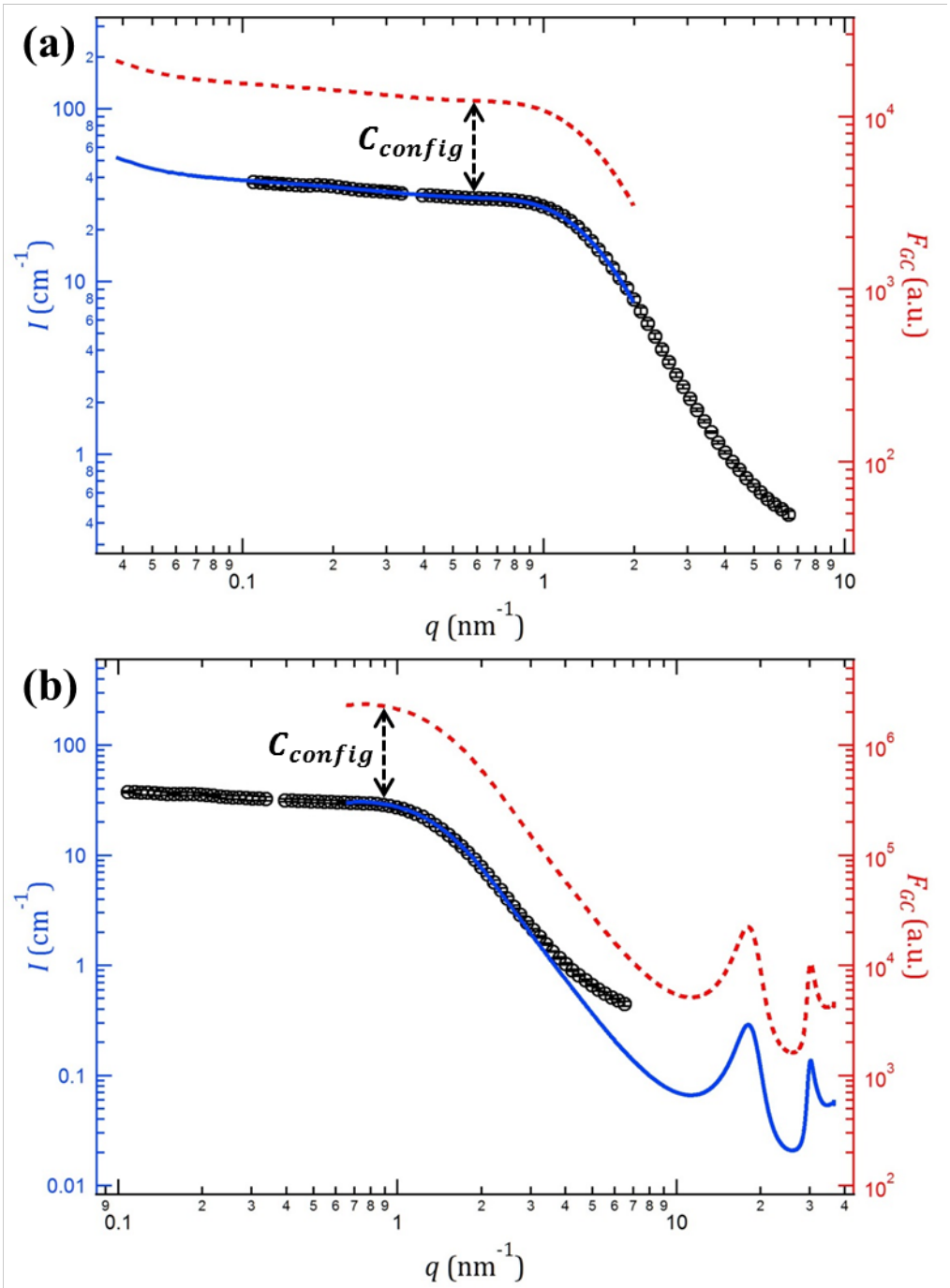

Figure 2.17: Demonstration of the scaling of $F_{GC}(q)$ (dashed red curves, right axis) to the $\tilde{\sigma}_{GC}(q)$ data (black circles, left axis), yielding the experimental absolute glassy carbon intensity (blue curve, left axis) and the calibration constants (C_{config}) for (a) SAXS and (b) WAXS configurations at ALS BL 7.3.3.

2.7 Data Collection

Going through the effort of obtaining absolute scattering data might appear to be a daunting task at this point; however, as long as the proper data is recorded, nearly all of the required steps can be performed after the experiment. To utilize the corrections described in

Sections 2.5 and 2.6, in addition to the measuring the scattering intensity of the sample itself ($I_{sam,\,det}(q)$), the experimenter needs to measure the thickness (z) of each sample, and make the following additional measurements during the X-ray scattering experiment:

1. *Calibrations*: To be performed at room temperature for each instrument configuration (i.e. SAXS vs. WAXS, or after any changes to the sample stage, detector distance, or in the X-ray beam)
    a. Scattering from silver behenate (AgB)
    b. Scattering from glassy carbon (GC)
    c. Scattering from air ("empty beam") at same exposure time as GC ($I_{b,\,det}(q)$)
    d. Dark current (DC) measurement – measure detector response with no X-rays present
2. *Sample Corrections*: To be performed at the same exposure times and temperatures as each sample measurement ($I_{sam,\,det}(q)$)
    a. Scattering from the empty beam ($I_{b,\,det}(q)$)
    b. Scattering from the empty cell ($I_{ec,\,det}(q)$)

If all of the above data is recorded, then image processing and intensity calibration can be implemented at the experimenter's leisure, and mistakes can be made and corrected without terribly detrimental effects.

In regard to sample measurement, one should attempt to measure a position on the sample that is of uniform thickness (if a perfectly planar sample cannot be obtained). If possible, measuring a few different locations on the sample can provide confidence that the scattering is representative of the material. The "optimal" exposure time for any scattering experiment is highly dependent on the sample. In general, for soft materials, one should use the shortest exposure time that provides a suitable number of counts, relative to the detector dark current (DC), to avoid the possibility of beam damage[63]. Finally, if the temperature or sample environment is to be changed during the experiment, leave plenty of time for sample equilibration; if beam damage is not a concern, it is good practice to make a few measurements over time to ensure the structure is time invariant.

2.8 Summary

The goal of this chapter has been to provide the information necessary to allow a novice X-ray scattering experimentalist to obtain quantitative scattering results. While there are many thorough resources available that discuss the theory of X-ray scattering, few directly address the questions an experimentalist might have when entering the field. I have sought to point out the essential details that will help the reader know what questions to ask and where to look in order efficiently solve many of the issues I faced when learning and applying X-ray scattering techniques during my thesis work. In Section 2.2, I provided a brief and largely qualitative overview of X-ray scattering in general, with the goal of allowing the reader to identify whether or not a particular scattering technique will a useful tool to study his or her system. I detailed the experimentally relevant aspects of sample preparation in Section 2.3, and provided insight as to how scattering instrument can be tuned in order to probe the desired length-scales for a given

experiment in Section 2.4. In Section 2.5 I described how to utilize the Nika[61] software package to convert scattering images into 1D scattering data sets, and in Section 2.6 I provided a detailed derivation of the corrections required to convert arbitrary scattering intensity values into absolute units. Finally, in Section 2.7 I highlighted the experimental requirements necessary to apply the methods described in Sections 2.5 and 2.6, and provided comments on good general practice during scattering experiments.

As a final note, there are three texts that I have found to be particularly useful within the field of X-ray scattering of polymers: Alexander[56], Vonk[58], and Roe[55].

2.9 Nomenclature

2.9.1 Abbreviations

AgB	Silver Behenate
BS	Beam Stop
DC	Dark Current
GC	Glassy Carbon
IC	Ion Chamber
MAXS	Middle Angle X-ray Scattering
SD	Sample to Detector Distance
SAXS	Small Angle X-ray Scattering
WAXS	Wide Angle X-ray Scattering

2.9.2 Subscripts

b	Empty beam
ec	Empty cell
fp	Flight path
s	Sample
sam,c	Measured sample, in container
sam,f	Measured sample, freestanding
w	Sample holder window

2.9.3 Superscripts

BS	Beam Stop
IC	Ion chamber

2.9.4 Symbols

A	Illuminated area of scattering object, cm^2
B_i	Scattering length density if phase i, cm^{-2}
C_{config}	Experimental X-ray calibration constant, s^{-1}
d	Bragg spacing, nm
$F_i(q)$	Intrinsic scattering function of object i, $cm^{-1}s^{-1}$
I_o	Incident X-ray intensity, a.u.
I_i	Scattered X-ray intensity from object i, a.u.
$I_{b,det}$	Measured scattering intensity from the empty beam, a.u.
I_{corr}	Scattering intensity - corrected for attenuation and parasitic scattering, a.u.

$I_{ec,det}$	Measured scattering intensity from the empty cell, a.u.
I_s	Scattered X-ray intensity, a.u.
$I_{sam,det}$	Measured scattering intensity from the sample, a.u.
M_i	Molar mass of species *i*, g mol^{-1}
n_{x}	Number of pixels from the origin in the x-direction, --
n_{y}	Number of pixels from the origin in the y-direction, --
P	Detector pixel size, mm
q	Magnitude of the scattering vector, nm^{-1}
t	Exposure time for scattering measurement, s
T_i	Zero-angle X-ray transmission through object *i*, --
$T_i(\theta)$	Angle-dependent X-ray transmission through scattering object *i*, --
T_i^{θ}	Angle-dependent X-ray transmission through absorbing object *i*, --
T_{ec}	Measured empty cell X-ray transmission, --
T_{opt}	Optimal sample transmission, --
T_{sam}	Measured sample X-ray transmission, --
v_{ref}	Reference volume, cm^3
w_i	Weight fraction of species *i*, --
x	Location within the thickness of a scattering object, cm
z_i	Thickness of object *i*, cm
z_{opt}	Optimal sample thickness, cm
$z(\theta)$	Effective thickness of object *i* through angle θ, cm

2.9.5 Greek

$\epsilon(\lambda)$	Detector efficiency, --
λ	Scattering wavelength, nm
μ	Linear X-ray absorption coefficient, cm^{-1}
μ_{air}^{NIST}	Linear X-ray absorption coefficient for air from the NIST database, cm^{-1}
η_i	Number of electrons in species *i*, --
ρ_i	Density if phase *i*, gcm^{-3}
θ	Scattering angle, rad
$\Delta\theta$	Detector pixel-to-pixel angular resolution, rad
$\widetilde{\sigma_s}(q)$	Differential scattering cross section, cm^{-1}
$\Phi(\lambda)$	X-ray flux, s^{-1}cm^{-2}
$\Delta\Omega$	Solid angle of the detector element, sr

Chapter 3 - Phase Behavior of a Block Copolymer/Salt Mixture Through the Order-to-Disorder Transition*

Abstract

Mixtures of block copolymers and lithium salts are promising candidates for lithium battery electrolytes. Structural changes that occur during the order-to-disorder transition (ODT) in a diblock copolymer/salt mixture were characterized by small angle X-ray scattering (SAXS). In salt-free block copolymers, the ODT is sharp, and the domain size of the ordered phase decreases with increasing temperature. In contrast, the ODT of the diblock copolymer/salt mixture examined here occurs gradually over an 11 ^{o}C temperature window, and the domain size of the ordered phase is a non-monotonic function of temperature. We present an approach to estimate the fraction of the ordered phase in the 11 ^{o}C window where ordered and disordered phases coexist. The domain spacing of the ordered phase increases with increasing temperature in the coexistence window. Both findings are consistent with the selective partitioning of salt into the ordered domains, as predicted by Nakamura et al., *ACS Macro Lett.* **2,** 478–481 (2013).

3.1 Introduction

Lithium metal batteries utilizing solid polymer electrolytes (SPEs) have recently gained considerable interest for use in electrified transportation applications.[64] In particular, block copolymer-based SPEs have demonstrated the remarkable ability to efficiently conduct lithium ions while preventing lithium dendritic growth[21], a problem that has plagued the implementation of lithium metal batteries since their initial commercial development in the 1980s[16]. Block copolymer electrolytes gain their unique properties by self-assembling into ordered arrays of hard, mechanically robust and soft, ion-conducting nano-scale domains.[29] At sufficiently high temperatures, entropy overcomes the repulsive forces between the chemically distinct polymer blocks and a homogeneous disordered phase is obtained. The transition from order to disorder is thus of considerable practical and fundamental significance.

The order-to-disorder transition (ODT) in neat *A*-*B* diblock copolymer melts is well understood. We restrict our attention to nearly monodisperse samples, which are, to a good approximation, one component systems. The mean field theory of Leibler predicts that for symmetric block copolymers wherein the volume fraction of the *A*-block (f_A) is 0.5, the ODT occurs at the temperature at which χN = 10.495, where χ is the temperature-dependent Flory-Huggins interaction parameter between segments *A* and *B*, and *N* is the number of segments per chain.[65] Small angle x-ray scattering (SAXS) has emerged as a powerful tool for studying the ODT in block copolymers. The disordered phase is characterized by a broad SAXS peak due to correlations between *A* and *B* segments enforced by connectivity, while the ordered phase is characterized by sharp peaks consistent with the symmetry of that phase. The SAXS signatures of the ODT have been reported in numerous publications.[66–72] Both the width and the height of the primary SAXS peak change discontinuously at the ODT. In contrast, the position of the

* This chapter was reported in *Macromolecules* **2014**, *47*, 2666–2673

primary peak (q^*) and the integrated scattering intensity (Q) decrease monotonically with increasing temperature with virtually no evidence of discontinuity at the ODT.

The mean field theory of Leibler predicts that the ODT of symmetric block copolymers is second-order.[65] Subsequent work by Fredrickson and Helfand[73] showed that fluctuations in the disordered state result in a change to a weakly first-order phase transition, consistent with a note in Leibler's original paper. The mean field limit is recovered in the limit of $N \to \infty$.

The effect of added salt on block copolymer thermodynamics is a relatively new and unexplored topic. Early experiments suggested that the thermodynamics of block copolymer/salt mixtures can be described by the same theories that were used to describe neat block copolymers except for the fact that χ must be replaced by an effective parameter (χ_{eff}) that now depends on salt concentration.[26,74–76] Generally speaking, with the notable exceptions[77,25], χ_{eff} was found to be larger than χ of the neat block copolymer, suggesting that the addition of salt stabilizes the ordered phase. The thermodynamic consequences of this were worked out by Nakamura et al.[75,76,78] They argued that as the ODT progressed, salt would partition preferentially into the ordered phase, leaving behind a disordered phase with lower salt concentration.[78] At equilibrium, the chemical potential of the salt in the two phases will be equal, dictating the compositions and morphologies of the coexisting disordered and ordered phases. This changes the order of the ODT and a first-order transition is obtained even in the mean field limit for any N, consistent with the Gibbs phase rule for binary mixtures.

The purpose of this paper is to report on the phase behavior of a block copolymer/salt mixture through the ODT using SAXS. We show that the SAXS signatures of the ODT of these systems are qualitatively different from those of neat diblock copolymers. The work presented here builds upon the results obtained by Wanakule et al.[74]

3.2 Experimental

3.2.1 Materials

The polystyrene-*b*-poly(ethylene oxide) (SEO) diblock copolymers used in this study were synthesized, purified, and characterized following the methods described in refs [79], [80], and [30]. The polymer characteristics are summarized in Table 3.1. The polymers were dried under vacuum at 90 °C for 24 hours before being stored in an argon-filled glovebox (MBraun) with sub ppm water and oxygen levels. Lithium bis(trifluoromethanesulfonyl)imide (LiTFSI) was obtained from Novolyte. The LiTFSI container was opened inside the glovebox, and then dried in a heated antechamber under vacuum for 3 days at 120 °C before being stored in the argon glovebox.

Table 3.1: Sample characteristics

Sample Name	M_{PS} (g mol^{-1})	M_{PEO} (g mol^{-1})	PDI	$f_{EO,eff}^*$ (140 °C)	T_g^{PS} (°C)	r ([Li$^+$][EO]$^{-1}$)
SEO(1.7-1.4)/LiTFSI (r=0.075)	1700	1400	1.05	0.50	30	0.075
SEO(6.4-7.3)	6400	7300	1.04	.52	80	0

*effective volume fraction of PEO/LiTFSI component based on calculation described in ref [25].

3.2.2 Sample Preparation

The polymer/salt mixture used in this study was prepared by mixing SEO(1.7-1.4)/benzene and LiTFSI/tetrahydrofuran (THF) solutions to obtain a salt concentration of r = 0.075 where r is the ratio of Li^+ ions to ethylene oxide monomer units. The SEO(1.7-1.4/LiTFSI(r=0.075) solution was freeze-dried in a Millrock LD85 lyophilizer to remove the solvent. The SEO(1.7-1.4/LiTFSI(r=0.075) mixture was returned to the glovebox antechamber without being exposed to air and dried under vacuum at 90 °C for 24 hours to remove any residual solvent.

Three *in situ* SAXS samples were prepared by melt forming the dried SEO(1.7-1.4)/LiTFSI(r=0.075) mixture into a 1/16 in. thick fiberglass reinforced silicone spacer with a diameter of 3/16 in. Both ends of the spacer were sealed with electrochemical grade aluminum foil electrodes, and then each sample was sealed in a vacuum pouch (Showa-Denka) with exposed aluminum tabs contacting each electrode. An empty pouch cell was also prepared in the same manner to serve as a blank reference for SAXS background subtraction. All of the samples were heated to 140°C to eliminate any strain induced during sample preparation and then cooled to and annealed at 70 °C for 20 hours and then at 50 °C for 20 hours before being stored at 30 °C. The *in situ* SAXS measurements were performed after two days of storage at 30 °C.

3.2.3 SAXS Measurements

SAXS measurements were performed at Lawrence Berkeley National Laboratory's Advance Light Source, beamline 7.3.3.[60] The sample-to-detector distance and beam center were calibrated using a silver behenate standard. The three SEO(1.7-1.4)/LiTFSI(r=0.075) samples and the empty cell were mounted onto a custom-built heating stage with thermocouples attached to both the front and back of each sample. An Omega OM-USB-TC data acquisition module was used to record each sample temperature every 10 seconds. The samples were connected to a Bio-Logic VMP3 potentiostat through the aluminum tabs contacting each electrode. Potentiostatic electrochemical impedance spectroscopy (PEIS) measurements were performed over a 1-10^6 Hz frequency range with 50 mV amplitude.

The samples were equilibrated at 30 °C for 1 hour in the SAXS instrument before beginning the heating scan. The heating scan was performed from 29-142 °C. 5 °C temperature steps were used for temperatures far from the ODT (29-78 °C and 107-142°C), and the samples were held at each temperature for a minimum of 30 minutes while PEIS and SAXS measurements were performed every 10 minutes. Smaller temperature steps were used near the ODT (78-91 °C). In this case, 2-3 °C steps were used and again the samples were held for a minimum of 30 minutes with PEIS and SAXS scans performed every 10 minutes. 1 °C temperature steps were used for the window of 93-104 °C and the samples were held at each temperature for at least 1 hour with PEIS and SAXS scans performed approximately every 10 minutes.

Each sample temperature was determined from the average of their front and back thermocouple readings during the scan; the back thermocouple was located adjacent to the heating element and it records the maximum possible sample temperature, while the front

thermocouple reading represents the minimum possible temperature. Sample temperatures are reported with error bars corresponding to these readings. The actual sample temperature was estimated by making separate electrolyte samples with a thermocouple running through the pouch. In all cases, the recorded sample temperature fell within the errors bars described above. The bulk electrolyte resistance was determined from the low frequency minimum of a Nyquist plot of the PEIS data. We found that the temperature- and microstructure-dependence of the ionic conductivity for SEO(1.7-1.4)/LiTFSI (r=0.075) qualitatively agreed with the published data of Teran et al[32]. The data are provided in Figure 3.S1 of the supporting information. This work is based exclusively on the SAXS data.

3.2.4 SAXS Data Reduction and Analysis

The raw SAXS patterns were reduced using the Nika macro for Igor Pro developed by Jan Ilavsky[61]. The scattering intensity (I) was averaged azimuthally and is reported as a function the magnitude of the scattering vector, $q = \frac{4\pi}{\lambda}\sin\left(\frac{\theta}{2}\right)$. Reduced SAXS data were further processed by subtracting the background scattering from the empty sample cell, and calibrated to a glassy carbon absolute intensity standard (sample M13, Jan Ilavsky)[62]. Standard deviation of the scattering intensity was approximated by the Nika reduction software and then propagated through the subsequent reduction steps with the assumption of uncorrelated random error.

Contributions to the absolute scattering intensity at each temperature were determined by nonlinear fitting of the scattering profiles. We utilized the built-in Levenberg-Marquardt nonlinear least-squares algorithm in Igor Pro with a user defined function to deconvolute the scattering into three components using Equation 3.1:

$$I_{tot}(q) = I_{ord}(q) + I_{dis}(q) + I_{bgd}(q) \tag{3.1}$$

where I_{tot} is the total measured scattering intensity, and I_{ord}, I_{dis}, and I_{bgd} are the scattering intensities due to the nano-structured ordered phase, the disordered phase, and the background, respectively. A Gaussian fuction was used to fit the primary ordered scattering peak:

$$I_{ord}(q) = y_0 e^{\left(-(q-q^*)^2\right)/2w^2} \tag{3.2}$$

Where y_0, w, and q^* are the primary scattering peak height, width, and position, respectively. The well-known Leibler structure factor[65] modified for polydispersity effects[69] was used to fit the broad disordered scattering peak:

$$I_{dis}(q) = C\left[\frac{S(q)}{W(q)} - 2\chi_{eff}\right]^{-1} \tag{3.3}$$

With

$$C = \nu_{ref}\left(\frac{b_A}{\nu_A} - \frac{b_B}{\nu_B}\right)^2_{eff} \tag{3.4}$$

$$S(q) = S_{AA}(q) + S_{BB}(q) + 2S_{AB}(q) \tag{3.5}$$

$$W(q) = S_{AA}(q)S_{BB}(q) - S_{AB}^2(q) \tag{3.6}$$

$$S_{AA}(q) = Ng(f_A) \tag{3.7}$$

$$S_{BB}(q) = Ng(1 - f_A) \tag{3.8}$$

$$S_{AB}(q) = \frac{N}{2}[g(1) - g(f_A) - g(1 - f_A)] \tag{3.9}$$

and

$$g(f) = 2\left({}^{1}/_{x^2}\right)\left\{fx - 1 + \left[{}^{k}/_{(k + fx)}\right]^k\right\} \tag{3.10}$$

where

$$x = q^2R_g^2 \tag{3.11}$$

and

$$k = \frac{1}{PDI - 1} \tag{3.12}$$

C is the effective scattering contrast from the difference in electron density between component A and component B, χ_{eff} is the effective interaction parameter, f_A is the volume fraction of block A, R_g is the radius of gyration, N is the number of polymer segments per chain, and PDI is the polydispersity index of the copolymer. The background scattering was fit with a decaying exponential function:

$$I_{bgd}(q) = y_1e^{({}^{y_2}/_{q})} \tag{3.13}$$

where y_1 and y_2 are constants. Fitting was performed with y_0, q^*, w, C, R_g, χ_{eff}, y_1, and y_2 as the adjustable parameters. Figure 3.1 shows a typical scattering profile and fit for a SEO(1.7-1.4)/LiTFSI(r=0.075) sample when both ordered and disordered phases coexist. The contributions from I_{ord}, I_{dis}, and I_{bgd} are also shown in Figure 3.1, offset by a decade for clarity. The fit parameters obtained for this scattering profile are given in Table 3.S1 of the supporting information, and those for all other temperatures are also provided in Table 3.S2-Table 3.S4 of the supporting information.

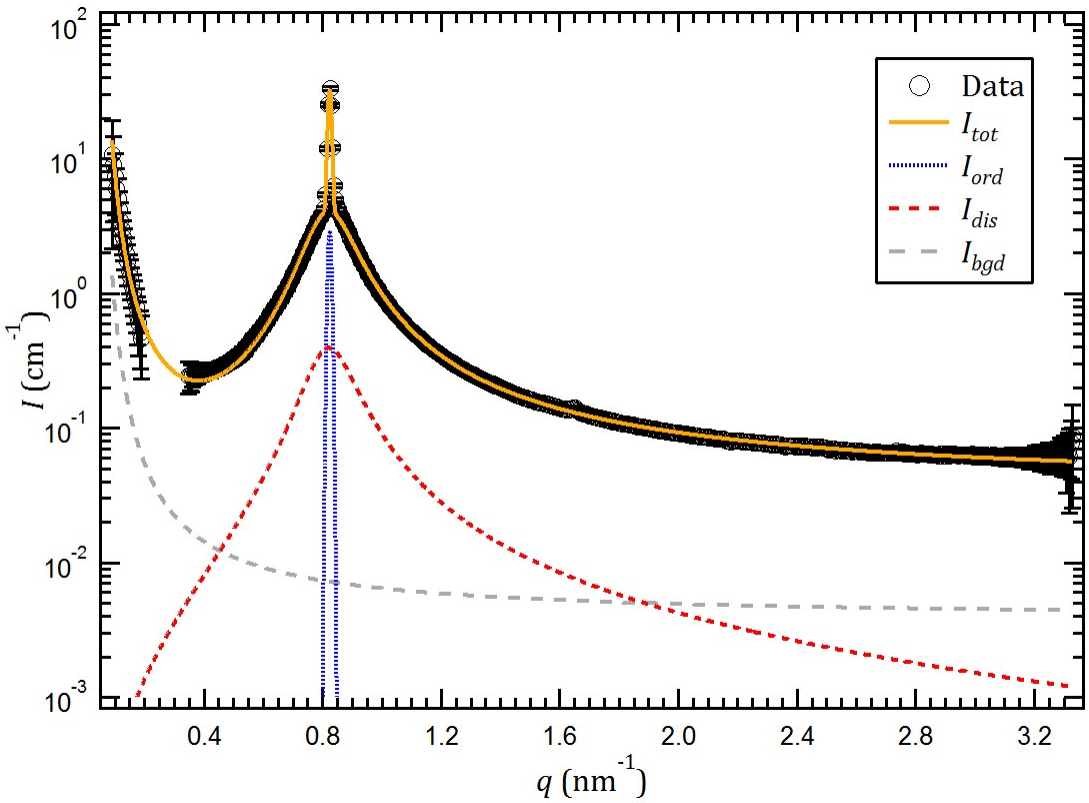

Figure 3.1: Example data and fitting for an SEO/LiTFSI sample during phase coexistence (97 °C). Experimental data are shown as discrete points with black circles and error bars corresponding to one standard deviation. The total fitting curve (I_{tot}) is plotted as a solid yellow line. The three contributions to the fit are shown as dashed lines offset by a decade with I_{ord} in blue, I_{dis} in red, and I_{bgd} in gray. Note: Data between q = 0.198 - 0.348 nm^{-1} correspond to a peak in the background (empty sample) scattering. Imperfect background subtraction resulted in negative and near zero intensity values within this range, and thus the data are not shown.

The fit parameters were used to calculate the characteristic domain spacing of the ordered phase, d_{ord},

$$d_{ord} = \frac{2\pi}{q^*} \tag{3.14}$$

and the characteristic length-scale of the disordered fluctuations, d_{dis},

$$d_{dis} = \frac{2\pi R_g}{\sqrt{3.6}} \tag{3.15}$$

where R_g is obtained by the fitting procedure (equ 1-13), and the factor $\sqrt{3.6}$ was determined using the methodology described by Teran et al[25]. The fitted curves were used to calculate the scattering invariant (Q_i), defined as

$$Q_i = \int I_i(q) q^2 \mathrm{d}q \;\; (i = ord \text{ or } dis) \tag{3.16}$$

For a heterogeneous system with two distinct phases separated by sharp interfaces, the invariant is independent of morphology and depends only on the volume of one of the phases.[55] In this case, $I \propto q^{-4}$ as $q \to \infty$ and the invariant is well-defined. It is well-known that $I_{dis} \propto q^{-2}$ as $q \to \infty$, and thus Q_{dis} is unbounded. We define ΔI_{dis} as

$$\Delta I_{dis} = I_{dis} - I_{dis,\chi=0} \tag{3.17}$$

where $I_{dis,\chi=0}$ is calculated by using the fit parameters determined for I_{dis}, but setting $\chi_{eff}=0$ in Equation 3.3. In Figure 3.2 we plot $\Delta I_{dis} q^2$ vs q for the data shown in Figure 3.1. The inset in Figure 3.2 shows the q-dependence of $I_{dis} q^2$ and $I_{dis,\chi=0} q^2$. It is clear from Figure 3.2 that ΔQ, defined as

$$\Delta Q = \int \Delta I_{dis}(q) q^2 \mathrm{d}q \tag{3.18}$$

is bounded.

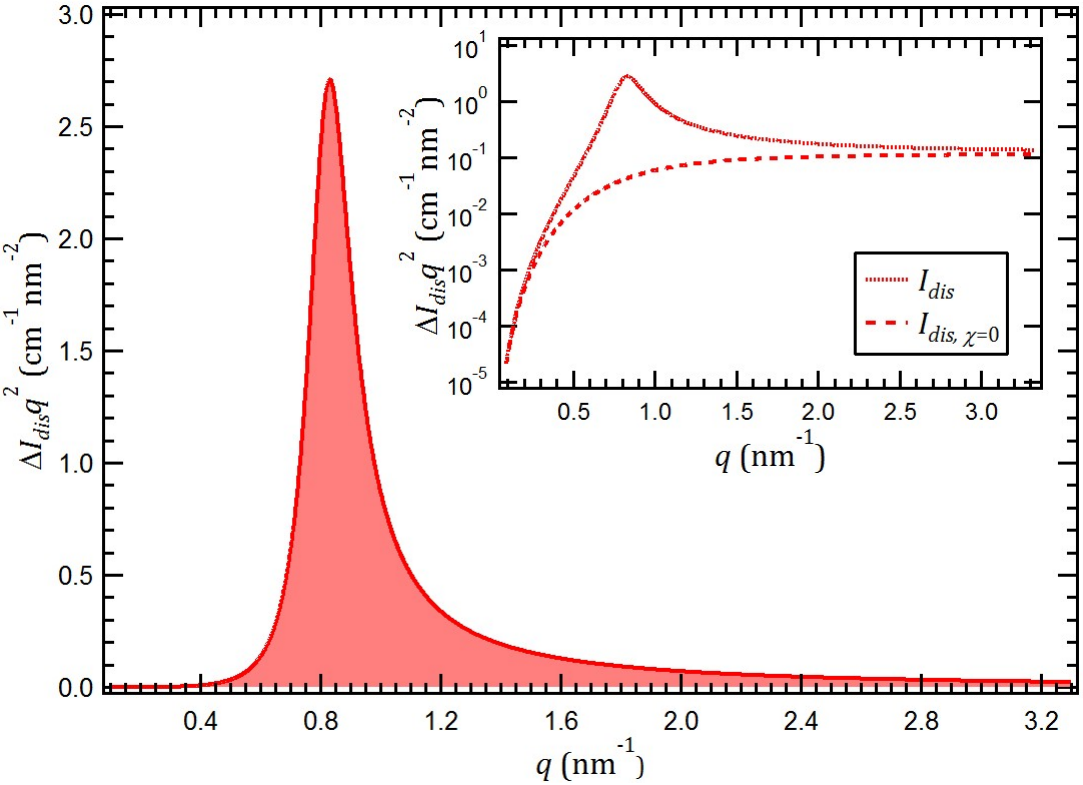

Figure 3.2: Graphical portrayal of the numerical integrations yielding the scattering invariant contributions from the disordered (red) polymer phase. Inset: Curves of $I_{dis} q^2$ and $I_{dis,\chi=0} q^2$ which were subtracted to yield $\Delta I_{dis} q^2$.

Because Q_{ord} and ΔQ depend only on the volumes of the ordered and disordered phases, respectively, we assume they are proportional to the volume of each phase, so that the volume fraction of the ordered phase (ϕ_{ord}) is given by

$$\phi_{ord} = \frac{Q_{ord}}{Q_{ord} + \Delta Q} \tag{3.19}$$

The values of Q_{ord} and ΔQ determined in this study were obtained from evaluating the integrals in Equations 3.16 and 3.18 between the limits q=0.09 and 3.3 nm^{-1}. Table 3.S5 of the supporting information provides the physically relevant values calculated from Equations 3.14-3.19 for one of the SEO(1.7-1.4)/LiTFSI(r=0.075) samples at all measured temperatures.

The data reduction and fitting analysis were performed on the SEO(1.7-1.4/LiTFSI(r=0.075) data gathered in the present study, as well as the scattering data collected from neat SEO(6.4-7.3) in the recently published work by Teran et al[25]. Whereas neat SEO (1.7-1.4) has a disordered morphology over all accessible temperatures, neat SEO(6.4-7.3) has a thermally accessible lamellar-to-disorder transition[25]. We compare the ODTs of SEO(1.7-1.4/LiTFSI(r=0.075) and neat SEO(6.4-7.3) because they both occur in a similar temperature window (90-105 °C). This temperature window is well above the glass transition temperature of the poly(styrene) block (T_g^{PS}) of each sample, thus the SAXS measurements made during each ODT should reflect thermodynamic structures.

3.3 Results and Discussion

Temperature-dependent SAXS profiles obtained from one of the SEO(1.7-1.4)/LiTFSI (r=0.075) samples are shown in Figure 3.3. At temperatures between 29 and 91 °C, the scattering profiles indicate the presence of a well-ordered lamellar morphology with sharp peaks at positions corresponding to q^*, $2q^*$, and $3q^*$ (blue curves in Figure 3.3). Data obtained in the 93-104 °C temperature range (yellow curves in Figure 3.3) are shown on an expanded scale in Figure 3.4a. Within this temperature range, even small increases (1 °C) in temperature result in large changes in the scattering profile. The general character of the SAXS profiles in this temperature range is clearly seen in the 102 °C data in Figure 3.4a. This SAXS profile is clearly a superposition of broad and narrow scattering peaks at q=0.82 nm^{-1}. We attribute this superposition to the coexistence of ordered and disordered phases within the polymer/salt sample. For temperatures above 107 °C, the SAXS profiles contain a single broad peak (red curves in Figure 3.3 and Figure 3.4a), characteristic of fully disordered samples. It is clear that ordered and disordered phases coexist in the polymer/salt sample at temperatures between 93 and 104 °C. In other words, the ODT occurs over a range of temperatures.

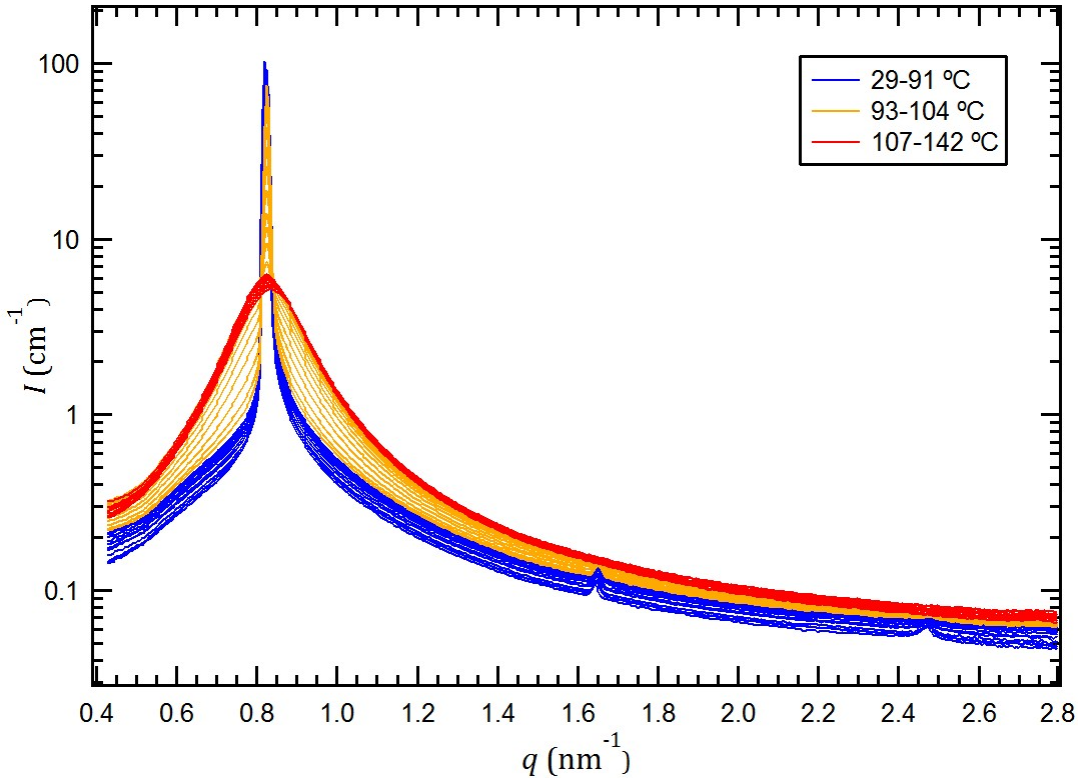

Figure 3.3: Absolute scattering intensities for SEO(1.7-1.4)/LiTFSI(*r*=0.075) from 29°C to 142°C. Blue traces denote well-ordered lamellar structures, yellow traces show coexistence of ordered lamellae and disordered phases, and red traces are fully disordered.

The data obtained from SEO(6.4-7.3) were very similar to data obtained from other neat block copolymers in the literature.[66,68,70,71] Temperature-dependent SAXS profiles obtained from the neat SEO(11) sample in the vicinity of the ODT are shown in Figure 3.4b. It is clear that an increase in temperature from 100 to 105 °C results in an abrupt transition from order to disorder.

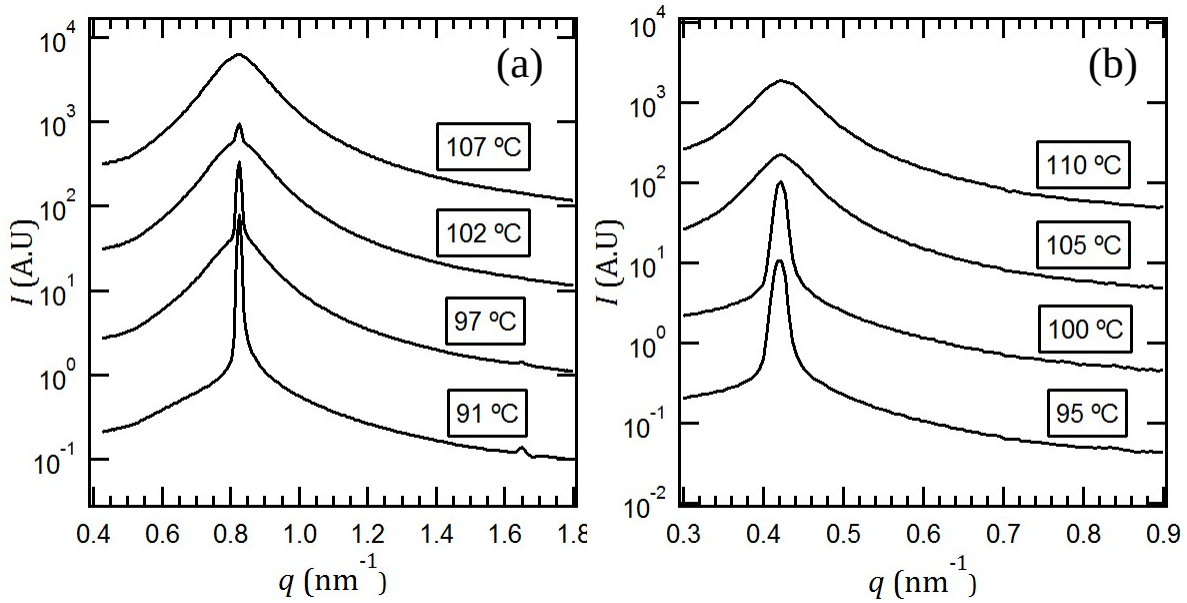

Figure 3.4: SAXS profiles for (a) SEO(1.7-1.4)/LiTFSI(*r*=0.075) through its ODT coexistence window, and (b) SEO(6.4-7.3) below and above its ODT. Profiles are offset by a decade for clarity.

The SAXS results described above were used to determine the temperature dependence of ϕ_{ord}, d_{dis}, and d_{ord}. Figure 3.5a shows the temperature dependence of ϕ_{ord} of the salt-containing block copolymer. The fraction of ordered lamellar phase (ϕ_{ord}) decreases gradually from 0.74 to 0.61 as temperature increases from 29 to 91 °C. At temperatures between 93 and 104 °C, ϕ_{ord} decreases rapidly from 0.59 to 0. Not surprisingly, ϕ_{ord} is identically 0 at temperatures above 107 °C in Figure 3.5a. The temperature dependence of ϕ_{ord} obtained from the neat block copolymer, shown in Figure 3.5b, exhibits a discontinuous jump from 0.61 to 0 as the temperature is increased from 100 to 105 °C. This is qualitatively different from the behavior of the salt-containing block copolymer. We note the value of ϕ_{ord} at temperatures well below the ODT is near 0.7 for both samples. One might expect a fully ordered lamellar sample at temperatures well below the ODT to yield ϕ_{ord}=1. It is well-known that block copolymer lamellae are not pure, i.e. there is a finite concentration of PS chains in the PEO-rich lamellae and vice-versa. We expect that scattering from such mixed microphases will be described by theory similar to the random phase approximation.[65,81] This effect results in contributions to I_{ord} that are not accounted for in our analysis. Our results suggest that the contribution from this effect to the overall disordered scattering is about 30 percent. In other words, we propose that our samples are fully ordered at temperatures well below the ODT temperature in spite of the fact that ϕ_{ord} is less than unity.

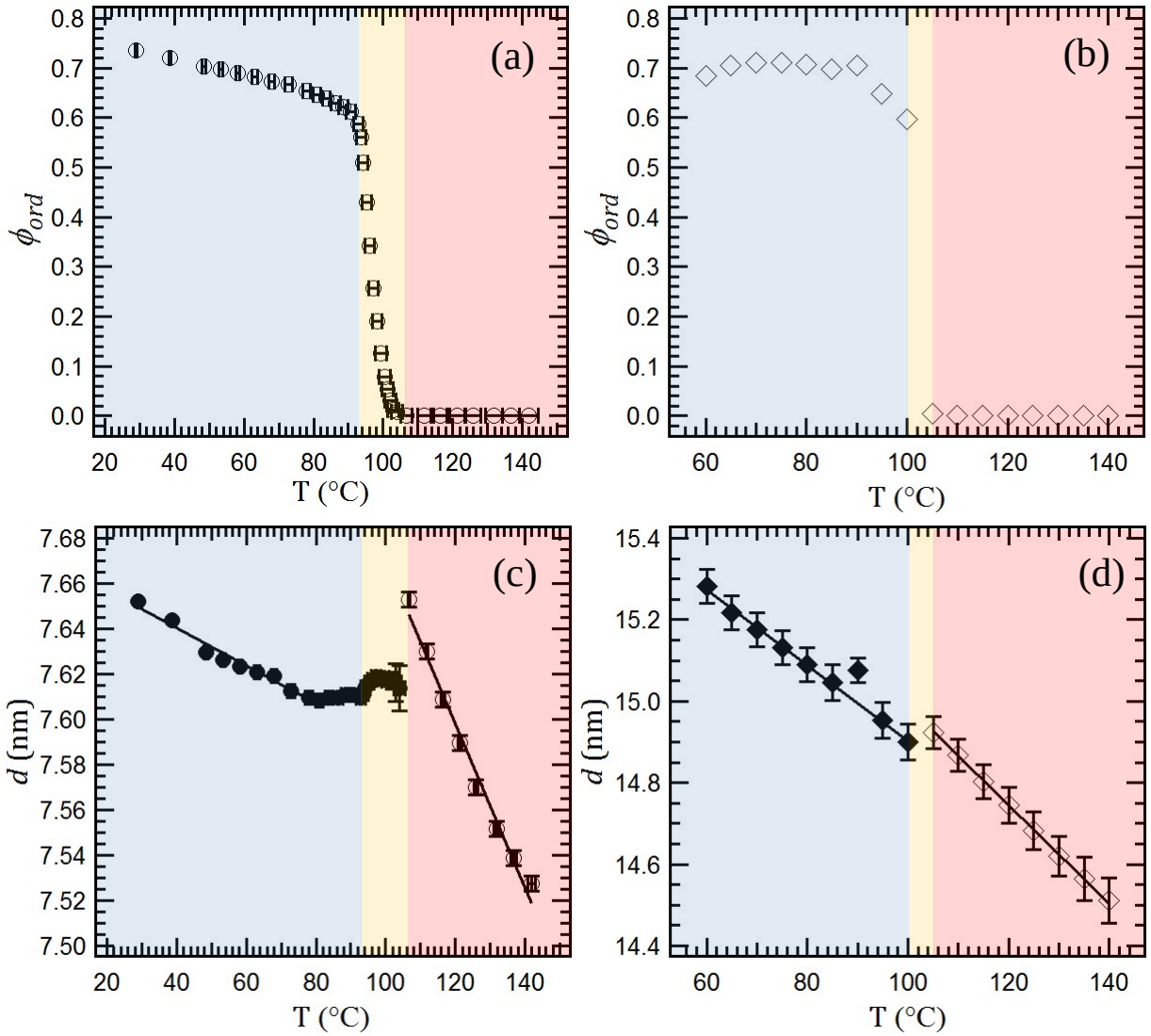

Figure 3.5: Temperature dependence of the calculated volume fraction of the ordered phase (ϕ_{ord}) for samples with (a) and without (b) LiTFSI salt added. The corresponding characteristic domain spacing as a function of temperature for the sample with (c) and without (d) salt added. In (c-d), filled symbols correspond to the ordered lamellar domain spacing, open symbols indicate the characteristic spacing from the disordered melt, and the solid lines represent linear fits to the *d* vs T data. In all graphs, regions shaded in blue indicate temperatures below the ODT, regions in yellow encompass the occurrence of an ODT, and regions in red correspond to a fully disordered polymer melt. X-axis error bars indicate the range of temperatures measured between the front and back of the sample, and y-axis error bars correspond to one standard deviation in the fitting of the SAXS profiles.

Additional information about phase behavior of the polymer melts can be gained by tracking the temperature dependence of the characteristic domain spacing. Figure 3.5c shows the data obtained from one of the SEO(1.7-1.4)/LiTFSI (r=0.075) polymer/salt mixtures, where filled symbols correspond to the lamellar spacing calculated from Equation 3.14 (d_{ord}), and open symbols are the characteristic length of the disordered phase calculated from Equation 3.15 (d_{dis}). The temperature dependence of the domain spacing for the polymer/salt mixture displays three distinct regimes, corresponding to the temperature windows for fully ordered, phase coexistence, and fully disordered states. Within the fully ordered temperature range, d_{ord} decreases gradually

with increasing temperature (T) between 29 and 81 °C; the slope, $\frac{d}{dT}(d_{ord})$, is -8.35x10^{-4} nmK^{-1}. d_{ord} is independent of temperature between 83 and 91 °C. The coexistence window (93-104 °C) is relatively narrow and it is not easy to discern the temperature dependence of d_{ord} in this temperature range from Figure 3.5c; we will soon show that d_{ord} increases with increasing temperature in the coexistence window. An abrupt change is seen in Figure 3.5c at 107 °C. At temperatures greater than 107 °C, d_{dis} decreases rapidly with increasing temperature; the slope $\frac{d}{dT}(d_{dis})$ is -3.61x10^{-3} nmK^{-1}, a factor of about 5 greater than $\frac{d}{dT}(d_{ord})$ in the ordered window. The temperature dependence of d_{ord} and d_{dis} of the neat SEO(6.4-7.3) polymer shown in Figure 3.5d is unremarkable. The domain spacings decrease monotonically with increasing temperature (except for one outlier). The slopes $\frac{d}{dT}(d_{ord})$ and $\frac{d}{dT}(d_{dis})$ are -9.2x10^{-3} and -1.2x10^{-2} nmK^{-1}, respectively, values within 30% of each other.

The data obtained from the salt-containing block copolymer sample in Figure 3.5a and 3.5c in the ordered and coexistence windows are combined in Figure 3.6, where d_{ord} is plotted as a function of ϕ_{ord}. The absolute magnitude of the changes in domain spacings reported in Figure 3.5c is small. To ensure the robustness of our conclusions we studied three independent salt-containing block copolymer mixtures. Figure 3.6a shows the results obtained from all of our samples. The coexistence temperature windows obtained from the independent samples differed by ~2-4 °C. Nevertheless, data obtained from these samples are quantitatively similar when plotted on a d_{ord} vesus ϕ_{ord} plot. A particular advantage of this format is that it enables an expanded view of the coexistence window. The decrease of domain spacing with temperature in the ordered phase followed by an increase of domain spacing with temperature in the coexistence window is observed in all samples. We propose that the increase in domain spacing with temperature in the coexistence window is a signature of salt partitioning predicted by Nakamura et al[78]. Their theory leads to the interesting conclusion that the order parameter of the ordered phase in the coexistence temperature window would be larger than that in the fully ordered temperature window. This is because the salt concentration in the ordered domains in the coexistence window is greater than the concentration in the fully ordered window. Our experiments do not enable determination of the order parameter. However, one might infer local salt concentration from the measured domain spacing of the ordered lamellae. Young and Epps first reported a power-law increase in the domain spacing of an ordered SEO block copolymer with increasing salt concentration.[24] Figure 3.6b shows an exaggerated pictorial representation of changes in the sample morphology of SEO(1.7-1.4)/LiTFSI(r=0.075) over the entire experimental temperature range. At low temperatures, the sample is fully ordered with large domain spacings that decrease with temperature. However, once the polymer begins to disorder within the coexistence window, the remaining lamellae become increasingly concentrated with salt. This partitioning of salt has two effects: it swells the lamellar domains by simple volume expansion, and the increased salt content in the lamellar phase increases the effective repulsion between the two blocks. It is important to note that stabilization of the ordered phase in the coexistence window is entirely due to salt partitioning, as noted by Nakamura et al[78]. At temperatures higher than the coexistence window, the salt concentration in the SEO(1.7-1.4)/LiTFSI(r=0.075) sample becomes spatially uniform and the temperature dependence of the domain spacing is similar to that seen in neat diblock copolymers (Figure 3.5d).

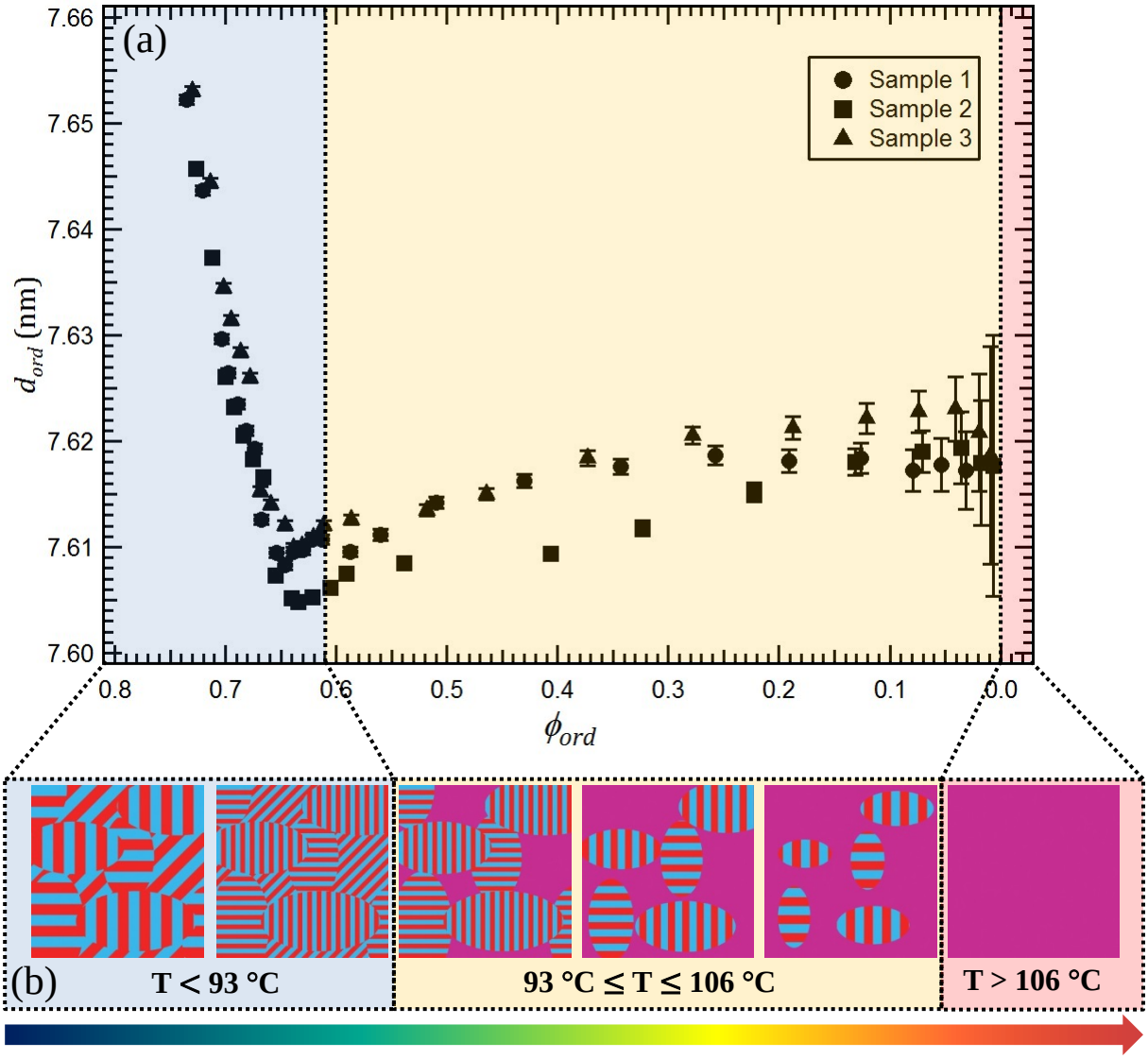

Figure 3.6: (a) $\phi_{ord}(T)$ and $d(T)$ data from Figures 3.4a and 3.4c, respectively, plotted as d vs. ϕ_{ord}. y-axis error bars correspond to one standard deviation in the fitting of the SAXS profiles. (b) Exaggerated pictorial representation of the phase behavior observed for SEO(1.7-1.4)/LiTFSI(r=0.075) throughout the experimental temperature range. Regions shaded in blue indicate temperatures below the ODT, regions in yellow encompass the coexistence region, and regions in red correspond to a fully disordered polymer melt.

The increase in d_{ord} with increasing temperature seen in the coexistence temperature window of the salt-containing block copolymer (Figure 3.6a) is a striking departure from the well-established behavior of neat block copolymers (Figure 3.5d). Most of the published literature on neat, nearly monodisperse block copolymers is consistent with the data presented in this paper.[68,70] A notable exception is the work of Koga et al. who reported a coexistence window of ~2 °C in a neat block copolymer and observed temperature-dependent domain spacings similar to the data obtained from the salt-containing block copolymer sample reported in this study.[67] Coexistence windows with widths of ~2 °C were also reported by Lee et al.[70]

3.4 Conclusions

We have studied the structural changes that occur in a blockcopolymer/salt mixture undergoing ODT using SAXS. In contrast to neat block copolymers, which show an abrupt change in SAXS scattering denoting the ODT, block copolymer/salt mixtures show a gradual transition from order to disorder over a finite temperature range. SAXS profiles within this temperature window appear to be the superposition of a sharp and a broad primary scattering peak, consistent with the coexistence of ordered and disordered phases. By fitting the scattering profiles and calculating the integrated scattering intensity contributions from each phase, we show that the ODT for block copolymer/salt mixtures is first order and occurs over a ~11 C° window.

We gained further insight into the nature of the ODT in block copolymer/salt mixtures by analyzing the characteristic domain spacings (d_{ord}, d_{dis}) obtained from the SAXS profiles. Whereas the domain spacings in the neat block copolymer decrease monotonically with temperature, the block copolymer/salt mixture demonstrated an increase in d_{ord} with temperature within the ODT temperature window. We attribute this swelling of the ordered domain to the partitioning of salt within the lamellar microdomains in the coexistence window, as predicted by Nakamura et al[78].

3.5 Acknowledgements

This work was supported by the National Science Foundation, DMR-0966626 and DMR-0966765. SAXS experiments were performed at Lawrence Berkeley National Laboratory's Advance Light Source, Beamline 7.3.3. Beamline 7.3.3 of the Advanced Light Source is supported by the Director of the Office of Science, Office of Basic Energy Sciences, of the U.S. Department of Energy under Contract No. DE-AC02-05CH11231.

3.6 Nomenclature

3.6.1 Abbreviations

LiTFSI	Lithium bis(trifluoromethanesulfonyl)imide
ODT	Order-Disorder Transition
PDI	Polydispersity Index
PEO	Poly(ethylene oxide)
PEIS	Potentiostatic Electrochemical Impedance Spectroscopy
PS	Polystyrene
SAXS	Small Angle X-ray Scattering
SEO	Polystyrene-*b*-poly(ethylene oxide) diblock copolymer
SPE	Solid Polymer Electrolyte
THF	Tetrahydrofuran

3.6.2 Symbols

A	Index for component one of *A*-*B* block copolymer
b_A	Scattering length of component *A*, cm

b_B	Scattering length of component *B*, cm
B	Index for component two of *A*-*B* block copolymer
C	Effective scattering contrast of disordered polymer or polymer/salt mixture, nm^{-1}
d	Characteristic domain spacing, nm
d_{dis}	Characteristic domain spacing of disordered phase, nm
d_{ord}	Characteristic domain spacing of ordered phase, nm
f_A	Volume fraction of block A in an *A*-*B* block copolymer, -
$f_{EO,eff}$	Effective volume fraction of poly(ethylene oxide) block and LiTFSI mixture, -
$g(f)$	Form factor for a Gaussian chain, -
I	Scattering intensity, cm^{-1}
$I_{bgd}(q)$	Fit background scattering intensity, cm^{-1}
$I_{dis}(q)$	Fit disordered phase scattering intensity, cm^{-1}
$I_{dis,\chi=0}(q)$	Fit disordered phase scattering intensity with χ_{eff}=0 in Eqn 3.3, cm^{-1}
$I_{ord}(q)$	Fit ordered phase scattering intensity, cm^{-1}
$I_{tot}(q)$	Fit total scattering intensity, cm^{-1}
$\Delta I_{dis}(q)$	Disordered phase scattering contribution, cm^{-1}
k	PDI correction factor constant, -
M_{PEO}	Number average molecular weight of PEO block, g mol^{-1}
M_{PS}	Number average molecular weight of PS block, g mol^{-1}
N	Number average degree of polymerization, sites $chain^{-1}$
q	Scattering vector, nm^{-1}
q^*	Primary ordered scattering peak, nm^{-1}
Q	Total integrated scattering intensity, $cm^{-1}nm^{-3}$
Q_i	Phase-specific integrated scattering intensity, $cm^{-1}nm^{-3}$
ΔQ	Disordered phase integrated scattering intensity, $cm^{-1}nm^{-3}$
r	Salt concentration, $[Li^+][EO]^{-1}$
R_g	Radius of gyration, nm
$S(q)$	Sum element of the structure factor matrix, -
$S_{AA}(q)$	*A*-*A* pairwise element of the structure factor matrix, -
$S_{AB}(q)$	*A*-*B* pairwise element of the structure factor matrix, -
$S_{BB}(q)$	*B*-*B* pairwise element of the structure factor matrix, -
T_g^{PS}	Glass transition temperature of the poly(styrene) block, °C
v_A	Monomer volume for component A, cm^3
v_B	Monomer volume for component B, cm^3
v_{ref}	Reference volume, cm^3
w	Gaussian peak width, nm^{-1}
$W(q)$	Determinant element of the structure matrix, -
x	Non-dimensional length, -
y_0	Constant in Eqn 3.2, cm^{-1}
y_1	Constant in Eqn 3.15, cm^{-1}

y_2 Constant in Eqn 3.15, nm^{-1}

3.6.3 Greek

χ Flory-Huggins interaction parameter, -

χ_{eff} Effective interaction parameter for copolymer/salt mixture, -

ϕ_{ord} Ordered phase volume fraction, -

λ Scattering wavelength, nm

θ Scattering angle, rad

σ Ionic conductivity, Scm^{-1}

3.7 Supporting Information

3.7.1 Electrochemical Impedance Spectroscopy

Recent work by Teran et al[32] demonstrated a correlation between the ionic conductivity and morphology in block copolymer salt mixtures. Their worked revealed a discontinuous increase in ionic conductivity as the sample transitioned from ordered lamellae to a disordered morphology. This work sought to gain insight into the ion transport behavior within coexistence window of the ODT. The temperature dependent ionic conductivity values of the three SEO(1.7-1.4)/LiTFI(r=0.075) samples measured in this study are shown in Figure 3.S1, where the coexistence window determined through SAXS is highlighted in yellow. All three samples demonstrate a discontinuous increase in ionic conductivity between the ordered lamellar and disordered phases present at low and high temperatures, respectively. The ionic conductivity within the coexistence temperature window is unremarkable and monotonically increases from the lower lamellar phase conductivity to the higher disordered phase conductivity.

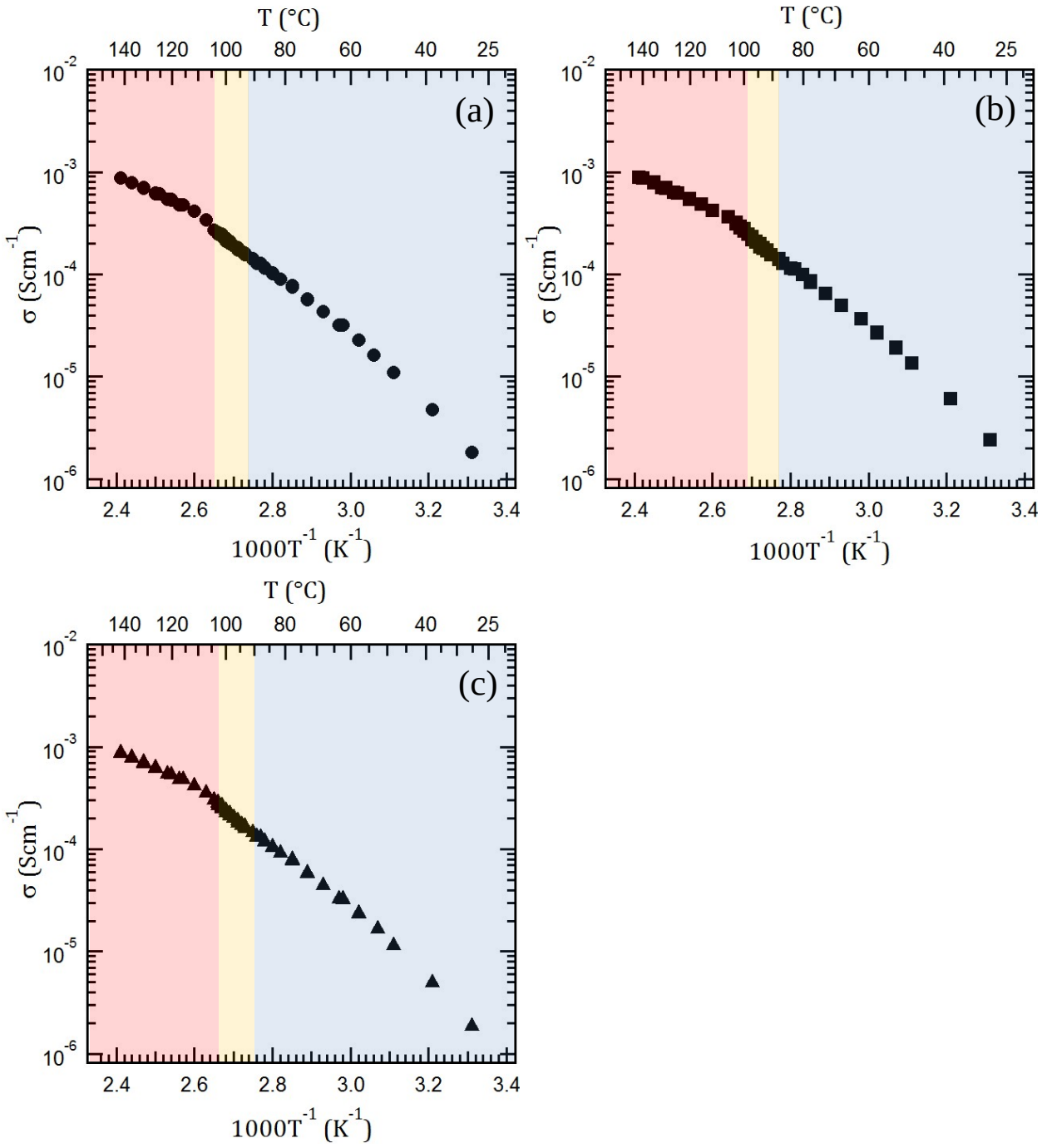

Figure 3.S1: Ionic conductivity for SEO(1.7-1.4)/LiTFSI(*r*=0.075) measured *in situ* during SAXS for (a) Sample 1, (b) Sample 2, and (c) Sample 3. Regions shaded in blue indicate temperatures below the ODT, regions in yellow encompass the occurrence of an ODT, and regions in red correspond to a fully disordered polymer melt.

3.7.2 SAXS Profile Fitting

The absolute SAXS intensity profiles obtained for the SEO(1.7-1.4)/LiTFSI(*r*=0.075) samples at all temperatures were fit with the functions described in Equations 3.1-3.13 of the main text. Table 3.S1 provides the fit parameters for the curve shown as an example in Figure 3.1 of the main text. The fit parameters for Sample 1 at the remaining temperatures are

organized into Table 3.S2-Table 3.S4. Table 3.S2 provides I_{ord} fit parameters, Table 3.S3 provides I_{dis} fit parameters, and Table 3.S4 provides I_{bgd} fit parameters. For consistency with the recent work by Teran et al[25], the PDI for all I_{dis} fitting was set to PDI = 1.035.

The SAXS profile fit parameters were used to calculate physically relevant quantities through Equations 3.14-3.19 of the main text. These values are summarized in Table 3.S5 for Sample 1 at all temperatures measured.

Table 3.S1：Fit parameters for the curve shown in Figure 3.1 of the main text. The measured sample temperature was 97.2 ± 1.5 °C. All reported errors represent one standard deviation of the fitting error.

Parameter	Value	(±)	Units
y_0	28.3	(0.7)	[cm^{-1}]
q^*	0.82471	(9E-05)	[nm^{-1}]
w	6.0E-03	(7.7E-05)	[nm^{-1}]
f	0.499	-	[-]
N	49.2	-	[sites $chain^{-1}$]
C	2.58E-02	(1.4E-04)	[cm^{-1}]
R_g	2.306	(1E-03)	[nm]
χ_{eff}	0.2049	(3.7E-05)	[-]
y_1	3.76E-02	(3.E-04)	[cm^{-1}]
y_2	0.54	(0.01)	[nm^{-1}]

Table 3.S2: Sample 1 fit parameters for I_{ord} at all measured temperatures. T_{set} represents the controller setpoint, $Time_{meas}$ is the cumulative experiemental time since the first scattering measurement, T_{meas} is the experimentally measured temperature, and y_0, q^*, w correspond to the constants in Equation 3.2 of the main text. All reported errors represent one standard deviation of the fitting error.

T_{set} [°C]	$Time_{meas}$ [hr:min]	T_{meas} (±) [°C]	y_0 (±) [cm^{-1}]	q^* (±) [nm^{-1}]	w (±) [nm^{-1}]
30	**0:00**	28.9 (0.1)	86.5 (1.8)	0.82109 (4E-05)	5.6E-03 (3.2E-05)
40	**0:42**	38.6 (0.3)	84.1 (1.8)	0.82213 (4E-05)	5.5E-03 (3.3E-05)
	0:52	38.6 (0.3)	83.2 (1.7)	0.82203 (4E-05)	5.5E-03 (3.3E-05)
	1:05	38.6 (0.3)	83.5 (1.8)	0.82202 (4E-05)	5.5E-03 (3.3E-05)
50	**1:21**	48.3 (0.5)	79.9 (1.7)	0.82318 (4E-05)	5.5E-03 (3.4E-05)
	1:31	48.3 (0.5)	79.2 (1.7)	0.82301 (4E-05)	5.5E-03 (3.4E-05)
	1:44	48.3 (0.5)	76.7 (1.6)	0.82352 (4E-05)	5.6E-03 (3.4E-05)
55	**1:59**	53.2 (0.6)	75.1 (1.6)	0.82405 (4E-05)	5.6E-03 (3.4E-05)
	2:09	53.2 (0.6)	74.4 (1.6)	0.82394 (4E-05)	5.5E-03 (3.4E-05)
	2:18	53.2 (0.5)	74.4 (1.6)	0.82387 (4E-05)	5.5E-03 (3.4E-05)
60	**2:35**	58.1 (0.7)	72.5 (1.5)	0.82439 (5E-05)	5.5E-03 (3.4E-05)
	2:44	58.1 (0.7)	71.8 (1.5)	0.82429 (5E-05)	5.5E-03 (3.4E-05)
	2:54	58.2 (0.7)	71.8 (1.5)	0.82419 (5E-05)	5.5E-03 (3.4E-05)
65	**3:15**	63.0 (0.8)	71.1 (1.5)	0.82468 (5E-05)	5.5E-03 (3.4E-05)
	3:24	63.0 (0.7)	70.9 (1.5)	0.82457 (5E-05)	5.5E-03 (3.4E-05)
	3:37	63.0 (0.7)	71.3 (1.5)	0.82446 (5E-05)	5.5E-03 (3.4E-05)
70	**3:52**	67.9 (0.9)	70.4 (1.5)	0.82492 (5E-05)	5.5E-03 (3.4E-05)
	4:02	67.9 (0.9)	70.7 (1.5)	0.82480 (5E-05)	5.6E-03 (3.4E-05)
	4:12	67.9 (0.8)	71.6 (1.5)	0.82465 (5E-05)	5.6E-03 (3.4E-05)
75	**4:28**	72.8 (1.0)	72.3 (1.5)	0.82563 (5E-05)	5.6E-03 (3.5E-05)
	4:39	72.7 (0.9)	72.5 (1.5)	0.82549 (5E-05)	5.6E-03 (3.5E-05)
	4:49	72.8 (0.9)	72.6 (1.5)	0.82537 (5E-05)	5.6E-03 (3.5E-05)
80	**5:12**	77.7 (1.1)	71.6 (1.5)	0.82586 (5E-05)	5.6E-03 (3.5E-05)
	5:20	77.8 (1.1)	70.9 (1.5)	0.82575 (5E-05)	5.6E-03 (3.5E-05)
	5:25	77.9 (1.1)	70.7 (1.5)	0.82571 (5E-05)	5.6E-03 (3.5E-05)
	5:35	78.3 (1.1)	71.1 (1.5)	0.82562 (5E-05)	5.6E-03 (3.5E-05)
83	**5:52**	81.1 (1.1)	69.1 (1.4)	0.82608 (5E-05)	5.7E-03 (3.6E-05)
	6:02	81.1 (1.1)	69.1 (1.4)	0.82597 (5E-05)	5.7E-03 (3.6E-05)
	6:12	81.0 (1.1)	69.0 (1.4)	0.82584 (5E-05)	5.7E-03 (3.6E-05)
86	**6:28**	83.9 (1.2)	68.4 (1.4)	0.82609 (5E-05)	5.7E-03 (3.7E-05)
	6:37	83.7 (1.2)	67.7 (1.4)	0.82582 (5E-05)	5.7E-03 (3.6E-05)
	6:48	83.6 (1.2)	67.8 (1.4)	0.82570 (5E-05)	5.7E-03 (3.6E-05)
89	**7:04**	86.5 (1.2)	67.3 (1.4)	0.82596 (5E-05)	5.7E-03 (3.7E-05)
	7:14	86.5 (1.2)	67.1 (1.4)	0.82586 (5E-05)	5.7E-03 (3.7E-05)
	7:24	86.4 (1.2)	67.1 (1.4)	0.82574 (5E-05)	5.7E-03 (3.7E-05)
	7:34	86.4 (1.2)	67.2 (1.4)	0.82567 (5E-05)	5.7E-03 (3.7E-05)

Table 3.S2 (continued)

T_{set} [°C]	$Time_{meas}$ [hr:min]	T_{meas} (±) [°C]	y_0 (±) [cm^{-1}]	q^* (±) [nm^{-1}]	w (±) [nm^{-1}]
91	7:49	88.4 (1.3)	66.5 (1.4)	0.82580 (5E-05)	5.7E-03 (3.7E-05)
	7:59	88.5 (1.3)	66.4 (1.4)	0.82570 (5E-05)	5.7E-03 (3.7E-05)
	8:09	88.6 (1.3)	66.3 (1.4)	0.82565 (5E-05)	5.7E-03 (3.7E-05)
	8:19	88.7 (1.3)	66.2 (1.4)	0.82557 (5E-05)	5.7E-03 (3.7E-05)
93	8:36	90.7 (1.3)	65.6 (1.4)	0.82574 (5E-05)	5.7E-03 (3.8E-05)
	8:46	90.7 (1.3)	65.1 (1.4)	0.82561 (5E-05)	5.7E-03 (3.7E-05)
	8:56	90.7 (1.3)	65.2 (1.4)	0.82557 (5E-05)	5.7E-03 (3.8E-05)
95	9:31	92.8 (1.4)	63.5 (1.3)	0.82582 (5E-05)	5.7E-03 (3.9E-05)
	9:42	92.7 (1.4)	63.3 (1.3)	0.82572 (5E-05)	5.7E-03 (3.9E-05)
	9:51	92.9 (1.4)	62.7 (1.3)	0.82570 (5E-05)	5.7E-03 (3.9E-05)
96	10:06	93.8 (1.4)	61.1 (1.3)	0.82573 (5E-05)	5.8E-03 (4.0E-05)
	10:16	93.8 (1.4)	60.4 (1.3)	0.82560 (5E-05)	5.8E-03 (4.1E-05)
	10:26	93.6 (1.4)	60.3 (1.3)	0.82553 (5E-05)	5.8E-03 (4.1E-05)
97	10:44	94.5 (1.4)	58.0 (1.2)	0.82557 (6E-05)	5.8E-03 (4.3E-05)
	10:54	94.5 (1.4)	57.1 (1.2)	0.82545 (6E-05)	5.8E-03 (4.3E-05)
	11:04	94.4 (1.4)	57.0 (1.2)	0.82542 (6E-05)	5.8E-03 (4.3E-05)
	11:14	94.3 (1.4)	56.8 (1.2)	0.82535 (6E-05)	5.8E-03 (4.4E-05)
	11:24	94.3 (1.4)	56.2 (1.2)	0.82528 (6E-05)	5.8E-03 (4.4E-05)
	11:32	94.3 (1.4)	55.5 (1.2)	0.82520 (6E-05)	5.8E-03 (4.4E-05)
98	11:48	95.3 (1.4)	52.0 (1.1)	0.82525 (6E-05)	5.8E-03 (4.7E-05)
	11:58	95.3 (1.4)	50.4 (1.1)	0.82517 (6E-05)	5.8E-03 (4.8E-05)
	12:08	95.3 (1.4)	49.4 (1.1)	0.82513 (6E-05)	5.8E-03 (4.9E-05)
	12:18	95.3 (1.4)	48.9 (1.1)	0.82510 (6E-05)	5.9E-03 (5.0E-05)
	12:29	95.3 (1.4)	48.2 (1.0)	0.82505 (7E-05)	5.8E-03 (5.0E-05)
	12:38	95.3 (1.4)	47.2 (1.0)	0.82497 (7E-05)	5.9E-03 (5.1E-05)
99	12:54	96.3 (1.4)	42.4 (0.9)	0.82502 (7E-05)	5.9E-03 (5.6E-05)
	13:04	96.2 (1.4)	41.5 (0.9)	0.82499 (7E-05)	5.9E-03 (5.7E-05)
	13:14	96.2 (1.4)	40.7 (0.9)	0.82492 (7E-05)	5.8E-03 (5.8E-05)
	13:24	96.3 (1.4)	39.4 (0.9)	0.82491 (8E-05)	5.9E-03 (5.9E-05)
	13:34	96.2 (1.4)	38.7 (0.9)	0.82487 (8E-05)	5.9E-03 (6.0E-05)
	13:45	96.2 (1.4)	37.6 (0.8)	0.82483 (8E-05)	5.9E-03 (6.1E-05)
100	14:01	97.2 (1.5)	31.9 (0.7)	0.82487 (9E-05)	6.0E-03 (7.0E-05)
	14:11	97.2 (1.5)	31.3 (0.7)	0.82482 (9E-05)	5.9E-03 (7.1E-05)
	14:21	97.2 (1.5)	30.4 (0.7)	0.82480 (9E-05)	6.0E-03 (7.3E-05)
	14:32	97.2 (1.5)	29.4 (0.7)	0.82478 (9E-05)	6.0E-03 (7.4E-05)
	14:42	97.2 (1.5)	28.8 (0.7)	0.82474 (9E-05)	6.0E-03 (7.6E-05)
	14:52	97.2 (1.5)	28.3 (0.7)	0.82471 (9E-05)	6.0E-03 (7.7E-05)

Table 3.S2 (continued)

T_{set} [°C]	$Time_{meas}$ [hr:min]	T_{meas} (±) [°C]	y_0 (±) [cm^{-1}]	q^* (±) [nm^{-1}]	w (±) [nm^{-1}]
101	**15:23**	98.2 (1.5)	23.4 (0.6)	0.82490 (1E-04)	6.0E-03 (8.9E-05)
	15:33	98.1 (1.5)	22.1 (0.6)	0.82483 (1E-04)	6.0E-03 (9.2E-05)
	15:41	98.1 (1.5)	21.7 (0.6)	0.82481 (1E-04)	6.0E-03 (9.3E-05)
	15:51	98.2 (1.5)	21.2 (0.6)	0.82481 (1E-04)	6.1E-03 (9.5E-05)
	15:58	98.2 (1.5)	21.0 (0.6)	0.82477 (1E-04)	6.0E-03 (9.6E-05)
102	**16:14**	99.2 (1.5)	16.8 (0.5)	0.82477 (1E-04)	6.1E-03 (1.1E-04)
	16:24	99.2 (1.5)	16.0 (0.5)	0.82474 (1E-04)	6.0E-03 (1.2E-04)
	16:34	99.2 (1.5)	14.8 (0.4)	0.82471 (1E-04)	6.1E-03 (1.2E-04)
	16:44	99.2 (1.5)	14.6 (0.4)	0.82470 (1E-04)	6.0E-03 (1.3E-04)
	16:54	99.3 (1.5)	14.2 (0.4)	0.82476 (1E-04)	6.2E-03 (1.3E-04)
	17:04	99.3 (1.5)	13.7 (0.4)	0.82474 (2E-04)	6.2E-03 (1.3E-04)
103	**17:21**	100.3 (1.5)	10.2 (0.4)	0.82484 (2E-04)	6.2E-03 (1.7E-04)
	17:31	100.3 (1.5)	9.0 (0.3)	0.82471 (2E-04)	6.1E-03 (1.8E-04)
	17:41	100.4 (1.5)	8.4 (0.3)	0.82476 (2E-04)	6.1E-03 (1.9E-04)
	17:51	100.3 (1.5)	8.3 (0.3)	0.82482 (2E-04)	6.2E-03 (2.0E-04)
	18:01	100.3 (1.5)	8.5 (0.3)	0.82486 (2E-04)	6.2E-03 (1.9E-04)
104	**18:27**	101.3 (1.6)	6.8 (0.3)	0.82484 (2E-04)	6.1E-03 (2.3E-04)
	18:37	101.2 (1.6)	6.3 (0.3)	0.82471 (3E-04)	5.9E-03 (2.4E-04)
	18:47	101.2 (1.6)	6.5 (0.3)	0.82488 (3E-04)	6.1E-03 (2.4E-04)
	18:57	101.2 (1.6)	5.9 (0.3)	0.82471 (3E-04)	5.9E-03 (2.5E-04)
	19:07	101.1 (1.6)	6.1 (0.3)	0.82488 (3E-04)	6.0E-03 (2.5E-04)
	19:17	101.2 (1.6)	5.9 (0.3)	0.82481 (3E-04)	6.0E-03 (2.6E-04)
105	**19:32**	102.1 (1.6)	4.5 (0.3)	0.82481 (3E-04)	5.9E-03 (3.2E-04)
	19:42	102.1 (1.6)	3.5 (0.2)	0.82462 (4E-04)	5.8E-03 (3.9E-04)
	19:52	102.0 (1.6)	3.3 (0.2)	0.82468 (4E-04)	5.7E-03 (4.1E-04)
	20:02	102.0 (1.6)	3.7 (0.2)	0.82489 (4E-04)	5.9E-03 (3.8E-04)
	20:03	101.9 (1.6)	3.7 (0.2)	0.82487 (4E-04)	5.9E-03 (3.7E-04)
	20:13	102.0 (1.6)	3.6 (0.2)	0.82487 (4E-04)	5.9E-03 (3.9E-04)
106	**20:30**	102.9 (1.6)	2.5 (0.2)	0.82486 (5E-04)	5.8E-03 (5.3E-04)
	20:40	102.9 (1.6)	2.2 (0.2)	0.82497 (6E-04)	5.7E-03 (5.8E-04)
	20:50	102.8 (1.6)	1.4 (0.2)	0.82498 (9E-04)	5.8E-03 (8.9E-04)
	21:17	102.9 (1.6)	1.4 (0.2)	0.82497 (9E-04)	5.7E-03 (9.0E-04)
107	**21:43**	103.8 (1.6)	1.4 (0.2)	0.82503 (8E-04)	5.3E-03 (8.4E-04)
	21:53	103.8 (1.6)	0.8 (0.2)	0.82494 (1E-03)	4.9E-03 (1.3E-03)
	22:03	103.8 (1.6)	1.1 (0.2)	0.82521 (1E-03)	5.2E-03 (1.0E-03)
	22:13	103.8 (1.6)	1.1 (0.2)	0.82517 (1E-03)	5.2E-03 (1.1E-03)
	22:23	103.8 (1.6)	1.0 (0.2)	0.82524 (1E-03)	5.1E-03 (1.1E-03)
	22:31	103.9 (1.6)	1.0 (0.2)	0.82524 (1E-03)	5.1E-03 (1.1E-03)

Table 3.S3: Sample 1 fit parameters for I_{dis} at all measured temperatures. T_{set} represents the controller setpoint, $Time_{meas}$ is the cumulative experiemental time since the first scattering measurement, T_{meas} is the experimentally measured temperature, and f, N, C, R_g, χ_{eff} correspond to the constants in Equations 3.3-3.12 of the main text. f and N were calculated based on the temperature depedence of the polymer block densities, as described in ref [25]. All reported errors represent one standard deviation of the fitting error.

T_{set} [°C]	$Time_{meas}$ [hr:min]	T_{meas} (±) [°C]	f -	N [sites chain^{-1}]	C (±) [cm^{-1}]	R_g (±) [nm]	χ_{eff} (±) -
30	**0:00**	28.9 (0.1)	0.500	47.2	1.41E-02 (1.4E-04)	2.264 (2E-03)	0.2086 (1.3E-04)
	0:42	38.6 (0.3)	0.500	47.5	1.50E-02 (1.5E-04)	2.263 (2E-03)	0.2069 (1.3E-04)
40	**0:52**	38.6 (0.3)	0.500	47.5	1.49E-02 (1.5E-04)	2.264 (2E-03)	0.2068 (1.3E-04)
	1:05	38.6 (0.3)	0.500	47.5	1.50E-02 (1.5E-04)	2.264 (2E-03)	0.2069 (1.3E-04)
	1:21	48.3 (0.5)	0.500	47.8	1.53E-02 (1.6E-04)	2.263 (2E-03)	0.2057 (1.3E-04)
50	**1:31**	48.3 (0.5)	0.500	47.8	1.53E-02 (1.6E-04)	2.263 (2E-03)	0.2056 (1.3E-04)
	1:44	48.3 (0.5)	0.500	47.8	1.51E-02 (1.6E-04)	2.262 (2E-03)	0.2055 (1.4E-04)
	1:59	53.2 (0.6)	0.500	47.9	1.49E-02 (1.5E-04)	2.261 (2E-03)	0.2053 (1.3E-04)
55	**2:09**	53.2 (0.6)	0.500	47.9	1.47E-02 (1.5E-04)	2.261 (2E-03)	0.2053 (1.3E-04)
	2:18	53.2 (0.5)	0.500	47.9	1.46E-02 (1.5E-04)	2.261 (2E-03)	0.2053 (1.3E-04)
	2:35	58.1 (0.7)	0.500	48.1	1.46E-02 (1.5E-04)	2.261 (2E-03)	0.2047 (1.3E-04)
60	**2:44**	58.1 (0.7)	0.500	48.1	1.46E-02 (1.5E-04)	2.261 (2E-03)	0.2047 (1.3E-04)
	2:54	58.2 (0.7)	0.500	48.1	1.46E-02 (1.5E-04)	2.262 (2E-03)	0.2047 (1.3E-04)
	3:15	63.0 (0.8)	0.500	48.2	1.49E-02 (1.5E-04)	2.262 (2E-03)	0.2041 (1.2E-04)
65	**3:24**	63.0 (0.7)	0.500	48.2	1.49E-02 (1.5E-04)	2.262 (2E-03)	0.2041 (1.2E-04)
	3:37	63.0 (0.7)	0.500	48.2	1.50E-02 (1.5E-04)	2.263 (2E-03)	0.2041 (1.2E-04)
	3:52	67.9 (0.9)	0.500	48.4	1.52E-02 (1.5E-04)	2.262 (2E-03)	0.2036 (1.2E-04)
70	**4:02**	67.9 (0.9)	0.500	48.4	1.55E-02 (1.5E-04)	2.263 (2E-03)	0.2035 (1.2E-04)
	4:12	67.9 (0.8)	0.500	48.4	1.57E-02 (1.5E-04)	2.264 (2E-03)	0.2035 (1.2E-04)
	4:28	72.8 (1.0)	0.499	48.5	1.61E-02 (1.6E-04)	2.261 (2E-03)	0.2031 (1.2E-04)
75	**4:39**	72.7 (0.9)	0.499	48.5	1.62E-02 (1.6E-04)	2.262 (2E-03)	0.2031 (1.2E-04)
	4:49	72.8 (0.9)	0.499	48.5	1.62E-02 (1.6E-04)	2.262 (2E-03)	0.2031 (1.2E-04)
	5:12	77.7 (1.1)	0.499	48.6	1.67E-02 (1.6E-04)	2.262 (2E-03)	0.2026 (1.1E-04)
80	**5:20**	77.8 (1.1)	0.499	48.7	1.67E-02 (1.6E-04)	2.263 (2E-03)	0.2025 (1.2E-04)
	5:25	77.9 (1.1)	0.499	48.7	1.68E-02 (1.6E-04)	2.263 (2E-03)	0.2025 (1.2E-04)
	5:35	78.3 (1.1)	0.499	48.7	1.69E-02 (1.6E-04)	2.264 (2E-03)	0.2025 (1.1E-04)
	5:52	81.1 (1.1)	0.499	48.8	1.70E-02 (1.6E-04)	2.263 (2E-03)	0.2021 (1.2E-04)
83	**6:02**	81.1 (1.1)	0.499	48.7	1.71E-02 (1.6E-04)	2.264 (2E-03)	0.2021 (1.2E-04)
	6:12	81.0 (1.1)	0.499	48.7	1.71E-02 (1.6E-04)	2.264 (2E-03)	0.2021 (1.2E-04)
	6:28	83.9 (1.2)	0.499	48.8	1.74E-02 (1.6E-04)	2.265 (2E-03)	0.2018 (1.1E-04)
86	**6:37**	83.7 (1.2)	0.499	48.8	1.74E-02 (1.6E-04)	2.265 (2E-03)	0.2017 (1.1E-04)
	6:48	83.6 (1.2)	0.499	48.8	1.75E-02 (1.6E-04)	2.266 (2E-03)	0.2018 (1.1E-04)
	7:04	86.5 (1.2)	0.499	48.9	1.78E-02 (1.6E-04)	2.267 (2E-03)	0.2015 (1.1E-04)
89	**7:14**	86.5 (1.2)	0.499	48.9	1.79E-02 (1.6E-04)	2.267 (2E-03)	0.2015 (1.1E-04)
	7:24	86.4 (1.2)	0.499	48.9	1.79E-02 (1.6E-04)	2.267 (2E-03)	0.2015 (1.1E-04)
	7:34	86.4 (1.2)	0.499	48.9	1.79E-02 (1.6E-04)	2.268 (2E-03)	0.2015 (1.1E-04)

Table 3.S3 (Continued).

T_{set} [°C]	$Time_{meas}$ [hr:min]	T_{meas} (±) [°C]	f -	N [sites chain^{-1}]	C (±) [cm^{-1}]	R_g (±) [nm]	χ_{eff} (±) -
91	**7:49**	88.4 (1.3)	0.499	49.0	1.81E-02 (1.6E-04)	2.268 (2E-03)	0.2013 (1.1E-04)
	7:59	88.5 (1.3)	0.499	49.0	1.82E-02 (1.6E-04)	2.269 (2E-03)	0.2013 (1.1E-04)
	8:09	88.6 (1.3)	0.499	49.0	1.82E-02 (1.6E-04)	2.269 (2E-03)	0.2013 (1.1E-04)
	8:19	88.7 (1.3)	0.499	49.0	1.83E-02 (1.6E-04)	2.269 (2E-03)	0.2013 (1.1E-04)
93	**8:36**	90.7 (1.3)	0.499	49.0	1.85E-02 (1.6E-04)	2.270 (2E-03)	0.2011 (1.1E-04)
	8:46	90.7 (1.3)	0.499	49.0	1.84E-02 (1.6E-04)	2.270 (2E-03)	0.2012 (1.1E-04)
	8:56	90.7 (1.3)	0.499	49.0	1.85E-02 (1.6E-04)	2.271 (2E-03)	0.2012 (1.1E-04)
95	**9:31**	92.8 (1.4)	0.499	49.1	1.89E-02 (1.6E-04)	2.274 (2E-03)	0.2014 (9.9E-05)
	9:42	92.7 (1.4)	0.499	49.1	1.89E-02 (1.6E-04)	2.275 (2E-03)	0.2015 (9.8E-05)
	9:51	92.9 (1.4)	0.499	49.1	1.90E-02 (1.6E-04)	2.276 (2E-03)	0.2016 (9.5E-05)
96	**10:06**	93.8 (1.4)	0.499	49.1	1.94E-02 (1.5E-04)	2.279 (2E-03)	0.2021 (8.6E-05)
	10:16	93.8 (1.4)	0.499	49.1	1.95E-02 (1.5E-04)	2.281 (2E-03)	0.2023 (8.3E-05)
	10:26	93.6 (1.4)	0.499	49.1	1.95E-02 (1.5E-04)	2.282 (2E-03)	0.2023 (8.3E-05)
97	**10:44**	94.5 (1.4)	0.499	49.2	2.00E-02 (1.5E-04)	2.285 (2E-03)	0.2028 (7.4E-05)
	10:54	94.5 (1.4)	0.499	49.2	2.00E-02 (1.5E-04)	2.286 (2E-03)	0.2029 (7.2E-05)
	11:04	94.4 (1.4)	0.499	49.2	2.02E-02 (1.5E-04)	2.287 (2E-03)	0.2030 (7.0E-05)
	11:14	94.3 (1.4)	0.499	49.2	2.03E-02 (1.5E-04)	2.288 (2E-03)	0.2031 (6.9E-05)
	11:24	94.3 (1.4)	0.499	49.2	2.04E-02 (1.5E-04)	2.288 (1E-03)	0.2032 (6.8E-05)
	11:32	94.3 (1.4)	0.499	49.2	2.04E-02 (1.5E-04)	2.289 (1E-03)	0.2033 (6.7E-05)
98	**11:48**	95.3 (1.4)	0.499	49.2	2.12E-02 (1.4E-04)	2.292 (1E-03)	0.2037 (5.9E-05)
	11:58	95.3 (1.4)	0.499	49.2	2.14E-02 (1.4E-04)	2.294 (1E-03)	0.2038 (5.7E-05)
	12:08	95.3 (1.4)	0.499	49.2	2.16E-02 (1.4E-04)	2.294 (1E-03)	0.2039 (5.5E-05)
	12:18	95.3 (1.4)	0.499	49.2	2.18E-02 (1.4E-04)	2.295 (1E-03)	0.2040 (5.4E-05)
	12:29	95.3 (1.4)	0.499	49.2	2.19E-02 (1.4E-04)	2.296 (1E-03)	0.2041 (5.3E-05)
	12:38	95.3 (1.4)	0.499	49.2	2.21E-02 (1.4E-04)	2.297 (1E-03)	0.2041 (5.2E-05)
99	**12:54**	96.3 (1.4)	0.499	49.2	2.29E-02 (1.4E-04)	2.299 (1E-03)	0.2044 (4.7E-05)
	13:04	96.2 (1.4)	0.499	49.2	2.32E-02 (1.4E-04)	2.300 (1E-03)	0.2044 (4.6E-05)
	13:14	96.2 (1.4)	0.499	49.2	2.34E-02 (1.4E-04)	2.300 (1E-03)	0.2045 (4.5E-05)
	13:24	96.3 (1.4)	0.499	49.2	2.36E-02 (1.4E-04)	2.301 (1E-03)	0.2046 (4.4E-05)
	13:34	96.2 (1.4)	0.499	49.2	2.37E-02 (1.4E-04)	2.301 (1E-03)	0.2046 (4.4E-05)
	13:45	96.2 (1.4)	0.499	49.2	2.39E-02 (1.4E-04)	2.302 (1E-03)	0.2047 (4.3E-05)
100	**14:01**	97.2 (1.5)	0.499	49.2	2.49E-02 (1.4E-04)	2.303 (1E-03)	0.2048 (3.9E-05)
	14:11	97.2 (1.5)	0.499	49.2	2.51E-02 (1.4E-04)	2.304 (1E-03)	0.2048 (3.9E-05)
	14:21	97.2 (1.5)	0.499	49.2	2.54E-02 (1.4E-04)	2.304 (1E-03)	0.2049 (3.8E-05)
	14:32	97.2 (1.5)	0.499	49.2	2.56E-02 (1.4E-04)	2.305 (1E-03)	0.2049 (3.8E-05)
	14:42	97.2 (1.5)	0.499	49.2	2.57E-02 (1.4E-04)	2.305 (1E-03)	0.2049 (3.7E-05)
	14:52	97.2 (1.5)	0.499	49.2	2.58E-02 (1.4E-04)	2.306 (1E-03)	0.2049 (3.7E-05)

Table 3.S3 (Continued).

T_{set} [°C]	$Time_{meas}$ [hr:min]	T_{meas} (±) [°C]	f -	N [sites chain^{-1}]	C (±) [cm^{-1}]	R_g (±) [nm]	χ_{eff} (±) -
101	**15:23**	98.2 (1.5)	0.499	49.3	2.70E-02 (1.4E-04)	2.306 (1E-03)	0.2050 (3.5E-05)
	15:33	98.1 (1.5)	0.499	49.3	2.71E-02 (1.4E-04)	2.306 (1E-03)	0.2050 (3.4E-05)
	15:41	98.1 (1.5)	0.499	49.3	2.71E-02 (1.4E-04)	2.307 (1E-03)	0.2050 (3.4E-05)
	15:51	98.2 (1.5)	0.499	49.3	2.73E-02 (1.4E-04)	2.307 (1E-03)	0.2050 (3.4E-05)
	15:58	98.2 (1.5)	0.499	49.3	2.74E-02 (1.4E-04)	2.308 (1E-03)	0.2050 (3.4E-05)
102	**16:14**	99.2 (1.5)	0.499	49.3	2.83E-02 (1.4E-04)	2.308 (1E-03)	0.2050 (3.2E-05)
	16:24	99.2 (1.5)	0.499	49.3	2.84E-02 (1.4E-04)	2.308 (1E-03)	0.2051 (3.2E-05)
	16:34	99.2 (1.5)	0.499	49.3	2.86E-02 (1.4E-04)	2.309 (1E-03)	0.2051 (3.1E-05)
	16:44	99.2 (1.5)	0.499	49.3	2.87E-02 (1.4E-04)	2.309 (1E-03)	0.2051 (3.1E-05)
	16:54	99.3 (1.5)	0.499	49.3	2.88E-02 (1.4E-04)	2.309 (1E-03)	0.2051 (3.1E-05)
	17:04	99.3 (1.5)	0.499	49.3	2.89E-02 (1.4E-04)	2.310 (1E-03)	0.2051 (3.1E-05)
103	**17:21**	100.3 (1.5)	0.499	49.3	2.97E-02 (1.5E-04)	2.310 (1E-03)	0.2050 (3.0E-05)
	17:31	100.3 (1.5)	0.499	49.3	2.98E-02 (1.5E-04)	2.310 (1E-03)	0.2051 (3.0E-05)
	17:41	100.4 (1.5)	0.499	49.3	3.00E-02 (1.5E-04)	2.310 (1E-03)	0.2051 (3.0E-05)
	17:51	100.3 (1.5)	0.499	49.3	3.00E-02 (1.5E-04)	2.311 (1E-03)	0.2051 (3.0E-05)
	18:01	100.3 (1.5)	0.499	49.3	3.01E-02 (1.5E-04)	2.311 (1E-03)	0.2051 (3.0E-05)
104	**18:27**	101.3 (1.6)	0.499	49.4	3.04E-02 (1.5E-04)	2.311 (1E-03)	0.2050 (2.9E-05)
	18:37	101.2 (1.6)	0.499	49.4	3.04E-02 (1.5E-04)	2.311 (1E-03)	0.2050 (2.9E-05)
	18:47	101.2 (1.6)	0.499	49.4	3.04E-02 (1.5E-04)	2.311 (1E-03)	0.2050 (2.9E-05)
	18:57	101.2 (1.6)	0.499	49.4	3.05E-02 (1.5E-04)	2.311 (1E-03)	0.2050 (2.9E-05)
	19:07	101.1 (1.6)	0.499	49.4	3.05E-02 (1.5E-04)	2.312 (1E-03)	0.2050 (2.9E-05)
	19:17	101.2 (1.6)	0.499	49.4	3.06E-02 (1.5E-04)	2.312 (1E-03)	0.2050 (2.9E-05)
105	**19:32**	102.1 (1.6)	0.499	49.4	3.09E-02 (1.5E-04)	2.312 (1E-03)	0.2049 (2.9E-05)
	19:42	102.1 (1.6)	0.499	49.4	3.11E-02 (1.5E-04)	2.312 (1E-03)	0.2049 (2.8E-05)
	19:52	102.0 (1.6)	0.499	49.4	3.11E-02 (1.5E-04)	2.313 (1E-03)	0.2049 (2.8E-05)
	20:02	102.0 (1.6)	0.499	49.4	3.12E-02 (1.5E-04)	2.313 (1E-03)	0.2049 (2.8E-05)
	20:03	101.9 (1.6)	0.499	49.4	3.10E-02 (1.5E-04)	2.313 (1E-03)	0.2049 (2.8E-05)
	20:13	102.0 (1.6)	0.499	49.4	3.11E-02 (1.5E-04)	2.313 (1E-03)	0.2049 (2.8E-05)
106	**20:30**	102.9 (1.6)	0.499	49.4	3.14E-02 (1.5E-04)	2.313 (1E-03)	0.2048 (2.8E-05)
	20:40	102.9 (1.6)	0.499	49.4	3.13E-02 (1.5E-04)	2.313 (1E-03)	0.2048 (2.8E-05)
	20:50	102.8 (1.6)	0.499	49.4	3.15E-02 (1.5E-04)	2.314 (1E-03)	0.2048 (2.8E-05)
	21:17	102.9 (1.6)	0.499	49.4	3.16E-02 (1.5E-04)	2.314 (1E-03)	0.2048 (2.8E-05)
107	**21:43**	103.8 (1.6)	0.499	49.4	3.17E-02 (1.5E-04)	2.314 (1E-03)	0.2047 (2.8E-05)
	21:53	103.8 (1.6)	0.499	49.4	3.17E-02 (1.5E-04)	2.314 (1E-03)	0.2047 (2.7E-05)
	22:03	103.8 (1.6)	0.499	49.4	3.17E-02 (1.5E-04)	2.314 (1E-03)	0.2047 (2.7E-05)
	22:13	103.8 (1.6)	0.499	49.4	3.17E-02 (1.5E-04)	2.314 (1E-03)	0.2047 (2.7E-05)
	22:23	103.8 (1.6)	0.499	49.4	3.17E-02 (1.5E-04)	2.314 (1E-03)	0.2047 (2.7E-05)
	22:31	103.9 (1.6)	0.499	49.4	3.17E-02 (1.5E-04)	2.314 (1E-03)	0.2047 (2.7E-05)

Table 3.S3(Continued).

T_{set} [°C]	$Time_{meas}$ [hr:min]	T_{meas} (±) [°C]	f -	N [sites chain^{-1}]	C (±) [cm^{-1}]	R_g (±) [nm]	χ_{eff} (±) -
	23:00	106.7 (1.7)	0.499	49.5	3.20E-02 (1.5E-04)	2.311 (1E-03)	0.2043 (2.4E-05)
110	**23:10**	106.8 (1.7)	0.499	49.5	3.19E-02 (1.5E-04)	2.311 (1E-03)	0.2043 (2.4E-05)
	23:19	106.7 (1.7)	0.499	49.5	3.18E-02 (1.5E-04)	2.311 (1E-03)	0.2043 (2.4E-05)
	23:40	111.6 (1.8)	0.499	49.7	3.18E-02 (1.5E-04)	2.307 (1E-03)	0.2037 (2.4E-05)
115	**23:50**	111.6 (1.8)	0.499	49.7	3.16E-02 (1.4E-04)	2.306 (1E-03)	0.2037 (2.4E-05)
	24:00	111.8 (1.8)	0.499	49.7	3.15E-02 (1.4E-04)	2.304 (1E-03)	0.2037 (2.4E-05)
	24:18	116.6 (2.0)	0.499	49.8	3.15E-02 (1.5E-04)	2.300 (1E-03)	0.2030 (2.4E-05)
120	**24:29**	116.9 (1.9)	0.499	49.9	3.12E-02 (1.4E-04)	2.298 (1E-03)	0.2030 (2.4E-05)
	24:39	116.4 (1.9)	0.499	49.8	3.13E-02 (1.4E-04)	2.298 (1E-03)	0.2031 (2.4E-05)
	24:57	120.9 (2.1)	0.499	50.0	3.14E-02 (1.5E-04)	2.294 (1E-03)	0.2024 (2.5E-05)
125	**25:07**	121.5 (2.1)	0.499	50.0	3.10E-02 (1.5E-04)	2.293 (1E-03)	0.2023 (2.5E-05)
	25:17	121.3 (2.0)	0.499	50.0	3.11E-02 (1.5E-04)	2.292 (1E-03)	0.2024 (2.5E-05)
	25:34	126.2 (2.2)	0.499	50.1	3.11E-02 (1.5E-04)	2.288 (1E-03)	0.2017 (2.5E-05)
130	**25:45**	126.8 (2.2)	0.499	50.2	3.10E-02 (1.5E-04)	2.286 (1E-03)	0.2016 (2.5E-05)
	25:54	126.0 (2.2)	0.499	50.1	3.10E-02 (1.5E-04)	2.286 (1E-03)	0.2017 (2.5E-05)
	26:10	130.9 (2.3)	0.499	50.3	3.10E-02 (1.5E-04)	2.282 (1E-03)	0.2010 (2.6E-05)
135	**26:21**	131.3 (2.3)	0.499	50.3	3.08E-02 (1.5E-04)	2.281 (1E-03)	0.2009 (2.6E-05)
	26:31	131.8 (2.3)	0.499	50.3	3.08E-02 (1.5E-04)	2.280 (1E-03)	0.2009 (2.6E-05)
	26:47	136.4 (2.5)	0.499	50.5	3.10E-02 (1.5E-04)	2.277 (1E-03)	0.2002 (2.7E-05)
140	**26:58**	136.4 (2.5)	0.499	50.5	3.08E-02 (1.5E-04)	2.277 (1E-03)	0.2002 (2.7E-05)
	27:07	136.6 (2.5)	0.499	50.5	3.09E-02 (1.5E-04)	2.277 (1E-03)	0.2002 (2.7E-05)
	27:23	141.3 (2.6)	0.499	50.6	3.10E-02 (1.6E-04)	2.274 (1E-03)	0.1995 (2.8E-05)
145	**27:34**	141.6 (2.6)	0.499	50.6	3.07E-02 (1.5E-04)	2.273 (1E-03)	0.1994 (2.8E-05)
	27:43	142.0 (2.6)	0.499	50.6	3.08E-02 (1.6E-04)	2.273 (1E-03)	0.1994 (2.8E-05)

Table 3.S4: Sample 1 fit parameters for I_{bdg} at all measured temperatures. T_{set} represents the controller setpoint, $Time_{meas}$ is the cumulative experiemental time since the first scattering measurement, T_{meas} is the experimentally measured temperature, and y_1, y_2 correspond to the constants in Equation 3.13 of the main text. All reported errors represent one standard deviation of the fitting error.

T_{set} [°C]	$Time_{meas}$ [hr:min]	T_{meas} (±) [°C]	y_1 (±) [cm^{-1}]	y_2 (±) [nm^{-1}]
30	**0:00**	28.9 (0.1)	3.57E-02 (3.E-04)	0.36 (0.02)
40	**0:42**	38.6 (0.3)	7.23E-02 (3.E-04)	0.33 (0.01)
	0:52	38.6 (0.3)	7.18E-02 (3.E-04)	0.32 (0.01)
	1:05	38.6 (0.3)	7.19E-02 (3.E-04)	0.32 (0.01)
50	**1:21**	48.3 (0.5)	7.30E-02 (3.E-04)	0.33 (0.01)
	1:31	48.3 (0.5)	7.26E-02 (3.E-04)	0.33 (0.01)
	1:44	48.3 (0.5)	7.38E-02 (3.E-04)	0.32 (0.01)
55	**1:59**	53.2 (0.6)	3.80E-02 (3.E-04)	0.37 (0.02)
	2:09	53.2 (0.6)	3.72E-02 (3.E-04)	0.36 (0.02)
	2:18	53.2 (0.5)	3.68E-02 (3.E-04)	0.35 (0.02)
60	**2:35**	58.1 (0.7)	3.71E-02 (3.E-04)	0.36 (0.02)
	2:44	58.1 (0.7)	3.66E-02 (3.E-04)	0.36 (0.02)
	2:54	58.2 (0.7)	3.65E-02 (3.E-04)	0.36 (0.02)
65	**3:15**	63.0 (0.8)	3.71E-02 (3.E-04)	0.37 (0.02)
	3:24	63.0 (0.7)	3.70E-02 (3.E-04)	0.38 (0.02)
	3:37	63.0 (0.7)	3.74E-02 (3.E-04)	0.39 (0.01)
70	**3:52**	67.9 (0.9)	3.77E-02 (3.E-04)	0.39 (0.01)
	4:02	67.9 (0.9)	3.80E-02 (3.E-04)	0.40 (0.01)
	4:12	67.9 (0.8)	3.88E-02 (3.E-04)	0.42 (0.01)
75	**4:28**	72.8 (1.0)	3.94E-02 (3.E-04)	0.38 (0.02)
	4:39	72.7 (0.9)	3.97E-02 (3.E-04)	0.39 (0.01)
	4:49	72.8 (0.9)	3.95E-02 (3.E-04)	0.39 (0.01)
80	**5:12**	77.7 (1.1)	4.04E-02 (3.E-04)	0.40 (0.01)
	5:20	77.8 (1.1)	3.99E-02 (3.E-04)	0.40 (0.01)
	5:25	77.9 (1.1)	3.99E-02 (3.E-04)	0.41 (0.01)
	5:35	78.3 (1.1)	4.04E-02 (3.E-04)	0.42 (0.01)
83	**5:52**	81.1 (1.1)	4.19E-02 (3.E-04)	0.40 (0.01)
	6:02	81.1 (1.1)	4.19E-02 (3.E-04)	0.41 (0.01)
	6:12	81.0 (1.1)	4.17E-02 (3.E-04)	0.41 (0.01)
86	**6:28**	83.9 (1.2)	4.23E-02 (3.E-04)	0.42 (0.01)
	6:37	83.7 (1.2)	4.16E-02 (3.E-04)	0.41 (0.01)
	6:48	83.6 (1.2)	4.18E-02 (3.E-04)	0.42 (0.01)
89	**7:04**	86.5 (1.2)	4.23E-02 (3.E-04)	0.43 (0.01)
	7:14	86.5 (1.2)	4.22E-02 (3.E-04)	0.43 (0.01)
	7:24	86.4 (1.2)	4.21E-02 (3.E-04)	0.43 (0.01)
	7:34	86.4 (1.2)	4.23E-02 (3.E-04)	0.44 (0.01)

Table 3.S4 (Continued).

T_{set} [°C]	$Time_{meas}$ [hr:min]	T_{meas} (±) [°C]	y_1 (±) [cm^{-1}]	y_2 (±) [nm^{-1}]
91	7:49	88.4 (1.3)	4.24E-02 (3.E-04)	0.44 (0.01)
	7:59	88.5 (1.3)	4.22E-02 (3.E-04)	0.44 (0.01)
	8:09	88.6 (1.3)	4.23E-02 (3.E-04)	0.45 (0.01)
	8:19	88.7 (1.3)	4.24E-02 (3.E-04)	0.45 (0.01)
93	8:36	90.7 (1.3)	4.22E-02 (3.E-04)	0.46 (0.01)
	8:46	90.7 (1.3)	4.19E-02 (3.E-04)	0.46 (0.01)
	8:56	90.7 (1.3)	4.20E-02 (3.E-04)	0.46 (0.01)
95	9:31	92.8 (1.4)	4.24E-02 (3.E-04)	0.46 (0.01)
	9:42	92.7 (1.4)	4.24E-02 (3.E-04)	0.46 (0.01)
	9:51	92.9 (1.4)	4.24E-02 (3.E-04)	0.47 (0.01)
96	10:06	93.8 (1.4)	4.25E-02 (3.E-04)	0.47 (0.01)
	10:16	93.8 (1.4)	4.24E-02 (3.E-04)	0.47 (0.01)
	10:26	93.6 (1.4)	4.22E-02 (3.E-04)	0.47 (0.01)
97	10:44	94.5 (1.4)	4.24E-02 (3.E-04)	0.48 (0.01)
	10:54	94.5 (1.4)	4.18E-02 (3.E-04)	0.48 (0.01)
	11:04	94.4 (1.4)	4.20E-02 (3.E-04)	0.48 (0.01)
	11:14	94.3 (1.4)	4.21E-02 (3.E-04)	0.49 (0.01)
	11:24	94.3 (1.4)	4.20E-02 (3.E-04)	0.49 (0.01)
	11:32	94.3 (1.4)	4.17E-02 (3.E-04)	0.49 (0.01)
98	11:48	95.3 (1.4)	4.14E-02 (3.E-04)	0.50 (0.01)
	11:58	95.3 (1.4)	4.10E-02 (3.E-04)	0.50 (0.01)
	12:08	95.3 (1.4)	4.09E-02 (3.E-04)	0.50 (0.01)
	12:18	95.3 (1.4)	4.10E-02 (3.E-04)	0.50 (0.01)
	12:29	95.3 (1.4)	4.09E-02 (3.E-04)	0.51 (0.01)
	12:38	95.3 (1.4)	4.06E-02 (3.E-04)	0.51 (0.01)
99	12:54	96.3 (1.4)	4.00E-02 (3.E-04)	0.51 (0.01)
	13:04	96.2 (1.4)	3.99E-02 (3.E-04)	0.51 (0.01)
	13:14	96.2 (1.4)	3.96E-02 (3.E-04)	0.51 (0.01)
	13:24	96.3 (1.4)	3.95E-02 (3.E-04)	0.52 (0.01)
	13:34	96.2 (1.4)	3.91E-02 (3.E-04)	0.52 (0.01)
	13:45	96.2 (1.4)	3.90E-02 (3.E-04)	0.52 (0.01)
100	14:01	97.2 (1.5)	3.82E-02 (3.E-04)	0.52 (0.01)
	14:11	97.2 (1.5)	3.80E-02 (3.E-04)	0.53 (0.01)
	14:21	97.2 (1.5)	3.80E-02 (3.E-04)	0.53 (0.01)
	14:32	97.2 (1.5)	3.78E-02 (3.E-04)	0.53 (0.01)
	14:42	97.2 (1.5)	3.77E-02 (3.E-04)	0.53 (0.01)
	14:52	97.2 (1.5)	3.76E-02 (3.E-04)	0.54 (0.01)

Table 3.S4 (Continued).

T_{set} [°C]	$Time_{meas}$ [hr:min]	T_{meas} (±) [°C]	y_1 (±) [cm^{-1}]	y_2 (±) [nm^{-1}]
101	**15:23**	98.2 (1.5)	3.70E-02 (3.E-04)	0.54 (0.01)
	15:33	98.1 (1.5)	3.65E-02 (3.E-04)	0.54 (0.01)
	15:41	98.1 (1.5)	3.64E-02 (3.E-04)	0.55 (0.01)
	15:51	98.2 (1.5)	3.62E-02 (3.E-04)	0.55 (0.01)
	15:58	98.2 (1.5)	3.63E-02 (3.E-04)	0.55 (0.01)
102	**16:14**	99.2 (1.5)	3.57E-02 (3.E-04)	0.55 (0.01)
	16:24	99.2 (1.5)	3.53E-02 (3.E-04)	0.56 (0.01)
	16:34	99.2 (1.5)	3.51E-02 (3.E-04)	0.56 (0.01)
	16:44	99.2 (1.5)	3.49E-02 (3.E-04)	0.56 (0.01)
	16:54	99.3 (1.5)	3.49E-02 (3.E-04)	0.56 (0.01)
	17:04	99.3 (1.5)	3.48E-02 (3.E-04)	0.57 (0.01)
103	**17:21**	100.3 (1.5)	3.45E-02 (3.E-04)	0.57 (0.01)
	17:31	100.3 (1.5)	3.39E-02 (3.E-04)	0.57 (0.01)
	17:41	100.4 (1.5)	3.38E-02 (3.E-04)	0.58 (0.01)
	17:51	100.3 (1.5)	3.39E-02 (3.E-04)	0.58 (0.01)
	18:01	100.3 (1.5)	3.41E-02 (3.E-04)	0.58 (0.01)
104	**18:27**	101.3 (1.6)	3.37E-02 (3.E-04)	0.58 (0.01)
	18:37	101.2 (1.6)	3.33E-02 (3.E-04)	0.58 (0.01)
	18:47	101.2 (1.6)	3.32E-02 (3.E-04)	0.59 (0.01)
	18:57	101.2 (1.6)	3.31E-02 (3.E-04)	0.59 (0.01)
	19:07	101.1 (1.6)	3.30E-02 (3.E-04)	0.59 (0.01)
	19:17	101.2 (1.6)	3.30E-02 (3.E-04)	0.59 (0.01)
105	**19:32**	102.1 (1.6)	3.30E-02 (3.E-04)	0.59 (0.01)
	19:42	102.1 (1.6)	3.27E-02 (3.E-04)	0.60 (0.01)
	19:52	102.0 (1.6)	3.26E-02 (3.E-04)	0.60 (0.01)
	20:02	102.0 (1.6)	3.29E-02 (3.E-04)	0.60 (0.01)
	20:03	101.9 (1.6)	3.26E-02 (3.E-04)	0.60 (0.01)
	20:13	102.0 (1.6)	3.24E-02 (3.E-04)	0.60 (0.01)
106	**20:30**	102.9 (1.6)	3.25E-02 (3.E-04)	0.60 (0.01)
	20:40	102.9 (1.6)	3.21E-02 (3.E-04)	0.60 (0.01)
	20:50	102.8 (1.6)	3.20E-02 (3.E-04)	0.61 (0.01)
	21:17	102.9 (1.6)	3.20E-02 (3.E-04)	0.61 (0.01)
107	**21:43**	103.8 (1.6)	3.23E-02 (3.E-04)	0.61 (0.01)
	21:53	103.8 (1.6)	3.18E-02 (3.E-04)	0.62 (0.01)
	22:03	103.8 (1.6)	3.19E-02 (3.E-04)	0.62 (0.01)
	22:13	103.8 (1.6)	3.19E-02 (3.E-04)	0.62 (0.01)
	22:23	103.8 (1.6)	3.19E-02 (3.E-04)	0.62 (0.01)
	22:31	103.9 (1.6)	3.18E-02 (3.E-04)	0.62 (0.01)

Table 3.S4 (Continued).

T_{set} [°C]	$Time_{meas}$ [hr:min]	T_{meas} (±) [°C]	y_1 (±) [cm^{-1}]	y_2 (±) [nm^{-1}]
	23:00	106.7 (1.7)	3.25E-02 (3.E-04)	0.61 (0.01)
110	**23:10**	106.8 (1.7)	3.26E-02 (3.E-04)	0.61 (0.01)
	23:19	106.7 (1.7)	3.25E-02 (3.E-04)	0.60 (0.01)
	23:40	111.6 (1.8)	3.37E-02 (3.E-04)	0.58 (0.01)
115	**23:50**	111.6 (1.8)	3.38E-02 (3.E-04)	0.57 (0.01)
	24:00	111.8 (1.8)	3.43E-02 (3.E-04)	0.56 (0.01)
	24:18	116.6 (2.0)	3.55E-02 (3.E-04)	0.55 (0.01)
120	**24:29**	116.9 (1.9)	3.54E-02 (3.E-04)	0.53 (0.01)
	24:39	116.4 (1.9)	3.57E-02 (3.E-04)	0.53 (0.01)
	24:57	120.9 (2.1)	3.71E-02 (3.E-04)	0.52 (0.01)
125	**25:07**	121.5 (2.1)	3.67E-02 (3.E-04)	0.51 (0.01)
	25:17	121.3 (2.0)	3.71E-02 (3.E-04)	0.51 (0.01)
	25:34	126.2 (2.2)	3.83E-02 (3.E-04)	0.49 (0.01)
130	**25:45**	126.8 (2.2)	3.83E-02 (3.E-04)	0.48 (0.01)
	25:54	126.0 (2.2)	3.86E-02 (3.E-04)	0.47 (0.01)
	26:10	130.9 (2.3)	4.00E-02 (3.E-04)	0.44 (0.01)
135	**26:21**	131.3 (2.3)	4.00E-02 (4.E-04)	0.42 (0.02)
	26:31	131.8 (2.3)	4.04E-02 (4.E-04)	0.42 (0.02)
	26:47	136.4 (2.5)	4.16E-02 (4.E-04)	0.42 (0.02)
140	**26:58**	136.4 (2.5)	4.11E-02 (4.E-04)	0.43 (0.02)
	27:07	136.6 (2.5)	4.16E-02 (4.E-04)	0.42 (0.02)
	27:23	141.3 (2.6)	4.28E-02 (4.E-04)	0.41 (0.02)
145	**27:34**	141.6 (2.6)	4.24E-02 (4.E-04)	0.41 (0.02)
	27:43	142.0 (2.6)	4.28E-02 (4.E-04)	0.40 (0.02)

Table 3.S5: Sample 1 calculated quantities. T_{set} represents the controller setpoint, $Time_{meas}$ is the cumulative experiemental time since the first scattering measurement, T_{meas} is the experimentally measured temperature, and Q_{ord}, ΔQ, ϕ_{ord}, d_{ord}, d_{dis} correspond to the values in Equations 3.14-3.19 of the main text. All reported errors represent the propagation of one standard deviation of the fitting error through the subsequent calculations.

T_{set} [°C]	$Time_{meas}$ [hr:min]	T_{meas} (±) [°C]	$Q_{ord}+\Delta Q$ [$cm^{-1}nm^{-3}$]	ϕ_{ord} -	d_{ord} (±) [nm]	d_{dis} (±) [nm]
30	**0:00**	28.9 (0.1)	1.103	0.735	7.652 (4E-04)	7.496 (7E-03)
40	**0:42**	38.6 (0.3)	1.091	0.722	7.643 (4E-04)	7.495 (7E-03)
	0:52	38.6 (0.3)	1.079	0.721	7.644 (4E-04)	7.497 (7E-03)
	1:05	38.6 (0.3)	1.082	0.721	7.644 (4E-04)	7.497 (7E-03)
50	**1:21**	48.3 (0.5)	1.065	0.707	7.633 (4E-04)	7.493 (7E-03)
	1:31	48.3 (0.5)	1.055	0.706	7.634 (4E-04)	7.495 (7E-03)
	1:44	48.3 (0.5)	1.033	0.704	7.630 (4E-04)	7.492 (7E-03)
55	**1:59**	53.2 (0.6)	1.023	0.697	7.625 (4E-04)	7.486 (7E-03)
	2:09	53.2 (0.6)	1.009	0.697	7.626 (4E-04)	7.486 (7E-03)
	2:18	53.2 (0.5)	1.005	0.697	7.626 (4E-04)	7.487 (7E-03)
60	**2:35**	58.1 (0.7)	0.989	0.690	7.622 (4E-04)	7.487 (7E-03)
	2:44	58.1 (0.7)	0.979	0.689	7.623 (4E-04)	7.488 (7E-03)
	2:54	58.2 (0.7)	0.978	0.689	7.623 (4E-04)	7.489 (7E-03)
65	**3:15**	63.0 (0.8)	0.980	0.682	7.619 (4E-04)	7.490 (7E-03)
	3:24	63.0 (0.7)	0.977	0.681	7.620 (4E-04)	7.491 (7E-03)
	3:37	63.0 (0.7)	0.986	0.682	7.621 (4E-04)	7.493 (7E-03)
70	**3:52**	67.9 (0.9)	0.986	0.674	7.617 (4E-04)	7.492 (7E-03)
	4:02	67.9 (0.9)	0.995	0.673	7.618 (4E-04)	7.495 (7E-03)
	4:12	67.9 (0.8)	1.009	0.673	7.619 (4E-04)	7.498 (7E-03)
75	**4:28**	72.8 (1.0)	1.036	0.667	7.610 (4E-04)	7.488 (7E-03)
	4:39	72.7 (0.9)	1.041	0.667	7.611 (4E-04)	7.490 (7E-03)
	4:49	72.8 (0.9)	1.042	0.667	7.613 (4E-04)	7.491 (7E-03)
80	**5:12**	77.7 (1.1)	1.045	0.657	7.608 (4E-04)	7.492 (6E-03)
	5:20	77.8 (1.1)	1.038	0.656	7.609 (4E-04)	7.494 (7E-03)
	5:25	77.9 (1.1)	1.040	0.654	7.609 (4E-04)	7.495 (6E-03)
	5:35	78.3 (1.1)	1.046	0.654	7.610 (4E-04)	7.496 (6E-03)
83	**5:52**	81.1 (1.1)	1.034	0.646	7.606 (4E-04)	7.495 (7E-03)
	6:02	81.1 (1.1)	1.035	0.646	7.607 (4E-04)	7.497 (7E-03)
	6:12	81.0 (1.1)	1.034	0.646	7.608 (4E-04)	7.498 (7E-03)
86	**6:28**	83.9 (1.2)	1.039	0.639	7.606 (4E-04)	7.500 (6E-03)
	6:37	83.7 (1.2)	1.030	0.639	7.608 (4E-04)	7.502 (7E-03)
	6:48	83.6 (1.2)	1.035	0.638	7.610 (4E-04)	7.504 (7E-03)
89	**7:04**	86.5 (1.2)	1.039	0.631	7.607 (5E-04)	7.506 (6E-03)
	7:14	86.5 (1.2)	1.039	0.630	7.608 (5E-04)	7.507 (6E-03)
	7:24	86.4 (1.2)	1.038	0.630	7.609 (5E-04)	7.508 (6E-03)
	7:34	86.4 (1.2)	1.040	0.630	7.610 (5E-04)	7.509 (6E-03)

Table 3.S5(Continued).

T_{set} [°C]	$Time_{meas}$ [hr:min]	T_{meas} (±) [°C]	$Q_{ord}+\Delta Q$ [$cm^{-1}nm^{-3}$]	ϕ_{ord} -	d_{ord} (±) [nm]	d_{dis} (±) [nm]
91	7:49	88.4 (1.3)	1.041	0.624	7.609 (5E-04)	7.511 (6E-03)
	7:59	88.5 (1.3)	1.040	0.623	7.610 (5E-04)	7.512 (6E-03)
	8:09	88.6 (1.3)	1.041	0.622	7.610 (5E-04)	7.514 (6E-03)
	8:19	88.7 (1.3)	1.042	0.622	7.611 (5E-04)	7.515 (6E-03)
93	8:36	90.7 (1.3)	1.044	0.615	7.609 (5E-04)	7.517 (6E-03)
	8:46	90.7 (1.3)	1.040	0.614	7.610 (5E-04)	7.517 (6E-03)
	8:56	90.7 (1.3)	1.043	0.613	7.611 (5E-04)	7.520 (6E-03)
95	9:31	92.8 (1.4)	1.047	0.595	7.608 (5E-04)	7.530 (6E-03)
	9:42	92.7 (1.4)	1.048	0.593	7.609 (5E-04)	7.533 (6E-03)
	9:51	92.9 (1.4)	1.049	0.588	7.610 (5E-04)	7.537 (6E-03)
96	10:06	93.8 (1.4)	1.061	0.567	7.609 (5E-04)	7.548 (6E-03)
	10:16	93.8 (1.4)	1.062	0.561	7.610 (5E-04)	7.553 (5E-03)
	10:26	93.6 (1.4)	1.062	0.560	7.611 (5E-04)	7.555 (5E-03)
97	10:44	94.5 (1.4)	1.073	0.534	7.611 (5E-04)	7.566 (5E-03)
	10:54	94.5 (1.4)	1.070	0.527	7.612 (5E-04)	7.570 (5E-03)
	11:04	94.4 (1.4)	1.077	0.523	7.612 (5E-04)	7.573 (5E-03)
	11:14	94.3 (1.4)	1.081	0.519	7.613 (5E-04)	7.575 (5E-03)
	11:24	94.3 (1.4)	1.083	0.514	7.613 (5E-04)	7.578 (5E-03)
	11:32	94.3 (1.4)	1.080	0.509	7.614 (5E-04)	7.581 (5E-03)
98	11:48	95.3 (1.4)	1.093	0.473	7.614 (6E-04)	7.591 (5E-03)
	11:58	95.3 (1.4)	1.090	0.459	7.614 (6E-04)	7.595 (5E-03)
	12:08	95.3 (1.4)	1.095	0.451	7.615 (6E-04)	7.598 (4E-03)
	12:18	95.3 (1.4)	1.098	0.445	7.615 (6E-04)	7.601 (4E-03)
	12:29	95.3 (1.4)	1.098	0.437	7.616 (6E-04)	7.603 (4E-03)
	12:38	95.3 (1.4)	1.099	0.430	7.616 (6E-04)	7.606 (4E-03)
99	12:54	96.3 (1.4)	1.106	0.386	7.616 (7E-04)	7.612 (4E-03)
	13:04	96.2 (1.4)	1.110	0.376	7.616 (7E-04)	7.615 (4E-03)
	13:14	96.2 (1.4)	1.109	0.366	7.617 (7E-04)	7.617 (4E-03)
	13:24	96.3 (1.4)	1.111	0.357	7.617 (7E-04)	7.619 (4E-03)
	13:34	96.2 (1.4)	1.108	0.351	7.617 (7E-04)	7.621 (4E-03)
	13:45	96.2 (1.4)	1.109	0.343	7.618 (7E-04)	7.623 (4E-03)
100	14:01	97.2 (1.5)	1.115	0.294	7.617 (8E-04)	7.627 (4E-03)
	14:11	97.2 (1.5)	1.116	0.284	7.618 (8E-04)	7.629 (4E-03)
	14:21	97.2 (1.5)	1.121	0.276	7.618 (8E-04)	7.631 (4E-03)
	14:32	97.2 (1.5)	1.122	0.268	7.618 (8E-04)	7.633 (4E-03)
	14:42	97.2 (1.5)	1.122	0.262	7.618 (9E-04)	7.634 (4E-03)
	14:52	97.2 (1.5)	1.122	0.257	7.619 (9E-04)	7.636 (4E-03)

Table 3.S5(Continued).

T_{set} [°C]	$Time_{meas}$ [hr:min]	T_{meas} (±) [°C]	$Q_{ord}+\Delta Q$ [$cm^{-1}nm^{-3}$]	ϕ_{ord} -	d_{ord} (±) [nm]	d_{dis} (±) [nm]
101	**15:23**	98.2 (1.5)	1.135	0.212	7.617 (1E-03)	7.636 (4E-03)
	15:33	98.1 (1.5)	1.128	0.200	7.618 (1E-03)	7.638 (4E-03)
	15:41	98.1 (1.5)	1.128	0.199	7.618 (1E-03)	7.639 (4E-03)
	15:51	98.2 (1.5)	1.129	0.195	7.618 (1E-03)	7.641 (4E-03)
	15:58	98.2 (1.5)	1.133	0.191	7.618 (1E-03)	7.642 (4E-03)
102	**16:14**	99.2 (1.5)	1.140	0.153	7.618 (1E-03)	7.643 (4E-03)
	16:24	99.2 (1.5)	1.136	0.145	7.618 (1E-03)	7.644 (4E-03)
	16:34	99.2 (1.5)	1.136	0.135	7.619 (1E-03)	7.646 (4E-03)
	16:44	99.2 (1.5)	1.135	0.133	7.619 (1E-03)	7.647 (4E-03)
	16:54	99.3 (1.5)	1.137	0.131	7.618 (1E-03)	7.648 (4E-03)
	17:04	99.3 (1.5)	1.137	0.126	7.618 (1E-03)	7.649 (4E-03)
103	**17:21**	100.3 (1.5)	1.141	0.094	7.617 (2E-03)	7.648 (3E-03)
	17:31	100.3 (1.5)	1.137	0.082	7.619 (2E-03)	7.649 (3E-03)
	17:41	100.4 (1.5)	1.137	0.077	7.618 (2E-03)	7.650 (3E-03)
	17:51	100.3 (1.5)	1.138	0.078	7.618 (2E-03)	7.651 (3E-03)
	18:01	100.3 (1.5)	1.141	0.079	7.617 (2E-03)	7.652 (3E-03)
104	**18:27**	101.3 (1.6)	1.141	0.062	7.617 (2E-03)	7.652 (3E-03)
	18:37	101.2 (1.6)	1.136	0.056	7.619 (2E-03)	7.653 (3E-03)
	18:47	101.2 (1.6)	1.135	0.059	7.617 (2E-03)	7.654 (3E-03)
	18:57	101.2 (1.6)	1.136	0.052	7.619 (2E-03)	7.654 (3E-03)
	19:07	101.1 (1.6)	1.135	0.055	7.617 (2E-03)	7.656 (3E-03)
	19:17	101.2 (1.6)	1.135	0.053	7.618 (2E-03)	7.657 (3E-03)
105	**19:32**	102.1 (1.6)	1.137	0.040	7.618 (3E-03)	7.656 (3E-03)
	19:42	102.1 (1.6)	1.135	0.030	7.619 (4E-03)	7.657 (3E-03)
	19:52	102.0 (1.6)	1.134	0.028	7.619 (4E-03)	7.658 (3E-03)
	20:02	102.0 (1.6)	1.138	0.032	7.617 (4E-03)	7.659 (3E-03)
	20:03	101.9 (1.6)	1.134	0.033	7.617 (4E-03)	7.659 (3E-03)
	20:13	102.0 (1.6)	1.132	0.032	7.617 (4E-03)	7.660 (3E-03)
106	**20:30**	102.9 (1.6)	1.134	0.022	7.617 (5E-03)	7.660 (3E-03)
	20:40	102.9 (1.6)	1.129	0.019	7.616 (5E-03)	7.660 (3E-03)
	20:50	102.8 (1.6)	1.130	0.012	7.616 (8E-03)	7.661 (3E-03)
	21:17	102.9 (1.6)	1.133	0.012	7.616 (8E-03)	7.663 (3E-03)
107	**21:43**	103.8 (1.6)	1.137	0.011	7.616 (8E-03)	7.662 (3E-03)
	21:53	103.8 (1.6)	1.131	0.006	7.617 (1E-02)	7.663 (3E-03)
	22:03	103.8 (1.6)	1.132	0.009	7.614 (9E-03)	7.663 (3E-03)
	22:13	103.8 (1.6)	1.132	0.008	7.614 (1E-02)	7.663 (3E-03)
	22:23	103.8 (1.6)	1.132	0.008	7.614 (1E-02)	7.664 (3E-03)
	22:31	103.9 (1.6)	1.132	0.008	7.614 (1E-02)	7.664 (3E-03)

Table 3.S5(Continued).

T_{set} [°C]	$Time_{meas}$ [hr:min]	T_{meas} (±) [°C]	$Q_{ord}+\Delta Q$ [$cm^{-1}nm^{-3}$]	ϕ_{ord} -	d_{ord} (±) [nm]	d_{dis} (±) [nm]
	23:00	106.7 (1.7)	1.138	0.000	- -	7.654 (3E-03)
110	**23:10**	106.8 (1.7)	1.139	0.000	- -	7.653 (3E-03)
	23:19	106.7 (1.7)	1.137	0.000	- -	7.653 (3E-03)
	23:40	111.6 (1.8)	1.136	0.000	- -	7.640 (3E-03)
115	**23:50**	111.6 (1.8)	1.134	0.000	- -	7.635 (3E-03)
	24:00	111.8 (1.8)	1.139	0.000	- -	7.630 (3E-03)
	24:18	116.6 (2.0)	1.136	0.000	- -	7.616 (3E-03)
120	**24:29**	116.9 (1.9)	1.129	0.000	- -	7.611 (3E-03)
	24:39	116.4 (1.9)	1.135	0.000	- -	7.609 (3E-03)
	24:57	120.9 (2.1)	1.134	0.000	- -	7.596 (3E-03)
125	**25:07**	121.5 (2.1)	1.121	0.000	- -	7.592 (3E-03)
	25:17	121.3 (2.0)	1.128	0.000	- -	7.590 (3E-03)
	25:34	126.2 (2.2)	1.123	0.000	- -	7.576 (3E-03)
130	**25:45**	126.8 (2.2)	1.116	0.000	- -	7.572 (3E-03)
	25:54	126.0 (2.2)	1.121	0.000	- -	7.570 (3E-03)
	26:10	130.9 (2.3)	1.115	0.000	- -	7.557 (3E-03)
135	**26:21**	131.3 (2.3)	1.109	0.000	- -	7.554 (3E-03)
	26:31	131.8 (2.3)	1.109	0.000	- -	7.552 (3E-03)
	26:47	136.4 (2.5)	1.109	0.000	- -	7.541 (3E-03)
140	**26:58**	136.4 (2.5)	1.103	0.000	- -	7.540 (3E-03)
	27:07	136.6 (2.5)	1.106	0.000	- -	7.539 (3E-03)
	27:23	141.3 (2.6)	1.098	0.000	- -	7.529 (4E-03)
145	**27:34**	141.6 (2.6)	1.089	0.000	- -	7.528 (4E-03)
	27:43	142.0 (2.6)	1.092	0.000	- -	7.527 (4E-03)

Chapter 4 - Phase Coexistence in a Strongly-Segregated Block Copolymer Electrolyte at High Salt Concentrations

Abstract

The relationships between chain characteristics, self-assembled nanostructure, and ion conduction are strongly coupled to salt concentration in block copolymer electrolytes (BCEs). In this work, we explore the influence of a wide range of salt concentrations on the self-assembly and ionic conductivity of BCEs derived from a strongly-segregated (i.e., high molecular weight) polystyrene-*b*-poly(ethylene oxide) (SEO) block copolymer. Structural analysis of well-annealed samples revealed that self-assembly is kinetically limited in all cases, including the salt-free polymer. It is thus apparent that processing conditions for BCEs will strongly influence their nanostructure and performance. At high salt concentrations (i.e., $r \geq 0.15$, where $r \equiv [Li]/[EO]$), the BCEs show evidence of coexisting nanostructures: disordered ellipsoids and self-assembled lamellae. The presence of lamellae is correlated with the formation of crystalline PEO/salt complexes; however, the nanostructures are stable above the melting temperature of any PEO crystal phases, as well as above the glass transition of the polystyrene phase. Salt-induced short-range correlations observed in the wide angle X-ray scattering of molten samples suggest a possible driving force for self-assembly, but the nature of these correlations and their influence on self-assembly remains unclear. Regardless of formation mechanism, the presence of coexisting phases allows for the possibility of salt partitioning within the BCE sample. We observe evidence of such partitioning in the salt concentration-dependence of the PEO glass transition temperature, as well as the concentration-dependence of ionic conductivity. Interestingly, at high salt concentrations the BCEs exhibit ionic conductivities approaching those of homopolymer PEO, suggesting a potential route to improving the performance of solid-state battery electrolytes.

4.1 Introduction

Solid-state block copolymer electrolytes (BCEs) have garnered significant interest due to their unique ability to decouple mechanical properties from electrochemical performance through nanoscale self-assembly.[19] It has been predicted[18] and experimentally verified[20–23] that the mechanical properties of an electrolyte separator can influence the formation/propagation of "dendritic" structures that can short-circuit a battery cell. Developing a mechanically rigid electrolyte that maintains suitable electrochemical properties represents one route to enabling next generation high energy density batteries that utilized metal foil anode materials (e.g., the lithium metal anode).

A well-studied BCE system consists of the block copolymer polystyrene-*b*-poly(ethylene oxide) (SEO) mixed with lithium bis(trifluoromethanesulfonyl)imide (LiTFSI) salt, wherein the polystyrene (PS) block provides mechanical rigidity, and the poly(ethylene oxide) (PEO) block solvates and conducts the LiTFSI salt ions. In this system, ionic conductivity has been characterized as a function of SEO molecular weight[29,30], BCE nanostructure[31–33], and salt concentration[28,29]. The general conclusions from these studies indicate that ion conduction depends on all three factors. To complicate matters further, many studies have revealed a strong

coupling between nanoscale self-assembly, a thermodynamically driven process, and salt concentration within BCEs.[24–28]

The thermodynamic underpinnings of self-assembly in neutral block copolymers is well-established[52,53,65,82]; microphase separation is driven by repulsive interactions between dissimilar monomers, and self-assembly is governed by balancing the number of unfavorable monomer-monomer contacts with the entropic penalty due to increasing the order within the system. Attempts have been made to extend the theory developed for neutral block copolymers to characterize the self-assembly within BCEs.[24–26] Each of these studies focused on the influence of salt on the driving force for micro-phase separation, i.e., the Flory-Huggins interaction parameter (χ). In all cases, the addition of salt to a neutral block copolymer was found to increase the observed repulsion between the dissimilar polymer blocks, which was accounted for by an increase in the so-called effective interaction parameter (χ_{eff}). While this approach successfully captured the general behavior observed for the self-assembly of BCEs at that time, recent work[27,28] has demonstrated that additional factors need to be taken into account in order to describe the relationship between self-assembly and salt concentration. Namely, due to the multicomponent nature of BCEs (i.e., they are mixtures of salt and polymer), their phase behavior cannot be predicted by the results derived from the single-component theory for neat diblock copolymers. For example, a thermodynamically stable coexistence between microphase separated structures is allowed if the salt can partition between the two phases of different chemical potential[27]. Furthermore, while salt addition might increase χ_{eff}, we show in ref [28] that high salt concentrations can effectively inhibit the self-assembly of well-ordered nanostructures. Our working hypothesis is that the large increase in χ_{eff} at high salt concentration hinders the rearrangement of polymer chains (i.e., defect annihilation) necessary to achieve thermodynamically favorable self-assembled structures. Thus the kinetic aspects of self-assembly can significantly influence nanostructure, and hence the electrochemical performance of BCEs.

We propose that using a strongly segregated (i.e. high molecular weight) block copolymer to form BCEs will amplify the kinetic limitations to self-assembly and result in poorly ordered nanostructures, which have been shown to improve ionic conductivity in lower molecular weight systems.[28,33] In fact, past studies have shown that BCEs derived from high molecular weight SEO do have improved ionic conductivity[29,83]; however, the higher conductivities were previously attributed to the presence of more pure PEO microphases[29,30]. Furthermore, no previous work on high molecular weight SEO has extended analysis to the high salt concentration limit.[28] In the present work, we systematically investigate the influence of salt concentration on the self-assembly and ion conducting properties of BCEs derived from a strongly segregated (and entangled) SEO diblock copolymer over a wide salt concentration range. We use combined small- and wide-angle X-ray scattering (SAXS/WAXS), in conjunction with scanning transmission electron microscopy (STEM), to study BCE microstructure in both the semi crystalline and molten states. At low salt concentrations, it is apparent that self-assembly is kinetically limited; however, at high salt concentrations, we find the coexistence of self-assembled lamellae and a poorly ordered nanostructure similar to that seen at low salt concentrations. Changes in the amorphous WAXS profiles with salt concentration suggest that short-range specific interaction might drive self-assembly at these salt concentrations. Thermal analysis reveals that the glass transition (T_g) temperature of the PEO/LiTFSI phase at these

concentrations is different than in equivalent homopolymer PEO/LiTFSI samples. We suggest this difference is due to the partitioning of salt between the different nanostructures.[27] The ionic conductivity of SEO/LiTFSI at high salt concentrations was found to approach that of homopolymer PEO/LiTFSI, despite presence of the non-conducting PS phase. Our approach of making BCEs from a high molecular weight SEO in the high salt concentration limit has indeed provided improved ionic conductivity; however, the unexpected observation of phase coexistence in such a strongly segregated system reaffirms how little is understood about the relationship between salt concentration and self-assembly in BCEs.

4.2 Experimental

4.2.1 Materials

The polystyrene-*b*-poly(ethylene oxide) (SEO) diblock copolymer used in this study was synthesized using sequential anionic polymerization, as described in refs [79], [80], and [30]. Details about the purification and characterization can be found in the supporting information. The polymer has the following characteristics: $M_{n,PS}$ = 52 kgmol^{-1}, $M_{n,PEO}$ = 55 kgmol^{-1}, PDI = 1.1, and $\phi_{PEO} = 0.50$ at 90 °C. We will refer to the polymer as SEO(52-55) for the remainder of this work. The polymer was dried under vacuum at 90 °C for 24 hours before being stored in an argon-filled glovebox (MBraun) with sub ppm water and oxygen levels. Lithium bis(trifluoromethanesulfonyl)imide (LiTFSI) was obtained from Novolyte. The LiTFSI container was opened inside of the glovebox, and then dried in a heated antechamber under vacuum for 3 days at 120 °C before use.

The block copolymer electrolytes (BCEs) used in this study were prepared in the same manner as ref [28] by mixing solutions of SEO(52-55)/benzene and LiTFSI/THF in ratios that provided the desired salt concentration. In total, 20 solutions were prepared with salt concentrations ranging from r = 0.000 (neat) to r = 0.550, where $r \equiv \frac{[\mathrm{Li}]}{[\mathrm{EO}]}$ is the ratio of lithium to ethylene oxide (EO) moieties. The solutions were subsequently lyophilized in a Millrock LD85 lyophilizer using a custom air-free transfer stage. The lyophilized samples were transferred back into the glovebox antechamber and dried under vacuum for 12 hours at 90 °C before use. All subsequent sample preparation was performed within the argon glovebox.

4.2.2 Small and Wide Angle X-Ray Scattering (SAXS/WAXS)

The lyophilized SEO(52-55)/LiTFSI BCE samples were generally fluffy white powders, although at the highest salt concentrations they formed a more dense porous solid. X-ray scattering samples were prepared by packing the SEO(52-55)/LiTFSI BCE powder into 1/8 inch inner diameter spacer made of chemically resistant and thermally stable Aflas® rubber. The polymer-filled spacer was placed between two sheets of fluorinated ethylene-propylene (FEP) Teflon® and hot pressed at ~130 °C with a hand-held press. After several rounds of adding polymer and hot-pressing, the Aflas spacer was filled with a solid disc of BCE. The BCE/spacers were then covered on both sides with 1 mil Kapton® films and assembled into custom hermetically sealed aluminum sample holders. An empty sample was also prepared using the same protocol for use as a blank reference during the scattering measurements. The hermetically-sealed samples (including the blank) were removed from the glovebox and annealed under

vacuum at 140 °C for one week. After annealing, the oven heater was turned off and the samples were allowed to slowly cool in a nitrogen-purged atmosphere at -6 mmHg for 72 hours.

X-ray scattering measurements were performed in transmission geometry at the Advanced Light Source (ALS) Beamline (BL) 7.3.3[60] and the Stanford Synchrotron Radiation Laboratory (SSRL) BL 1-5 using a custom heating stage designed to hold the hermetically sealed aluminum sample holders. Each experiment was replicated using first a small angle (SAXS) configuration, and then a wide angle (WAXS) setup [the samples were re-annealed for 24 hours and allowed to slowly cool for 72 hours, as described above, between SAXS and WAXS experiments]. SAXS from SEO(52-55)/LiTFSI samples with $r = 0.000 - 0.350$ were measured using a ~3.8 m detector distance, 10keV X-rays, and a Pilatus 2M (Dectris) detector at ALS BL 7.3.3; while SAXS from SEO(52-55)/LiTFSI samples with $r = 0.400 - 0.550$ were measured at SSRL BL 1-5 using a ~3 m detector distance, 10 keV X-rays, and a Rayonix 165 CCD Camera. All WAXS measurements were performed at ALS 7.3.3 using a ~0.3 m detector distance, 10 keV X-rays, and the Pilatus 2M detector. In all cases, the actual sample to detector distance (SD) was determined from the scattering pattern of a silver behenate (AgB) calibration standard.

Each scattering experiment followed the same general protocol. First, the scattering for each sample was measured at 30 °C. The sample stage was then heated directly to 70 °C, where samples were allowed to equilibrate for at least 40 minutes before recording any scattering measurements. From 70 °C, a heating scan was performed in 10 °C intervals up to 120 °C, waiting at least 30 minutes at each temperature before making measurements. The samples were held for an additional 30 minutes at 120 °C to ensure the samples were equilibrated. When beamtime was available, a subsequent cooling scan was performed back down to 70 °C. It was found during these experiments that sample structure had a slight temperature-dependence during heating, but was essentially temperature-independent upon cooling. Thus, in order to compare all of the samples, only the scattering results from 30 °C (after controlled annealing) and 120 °C will be discussed in this work. After the final scattering measurements, the samples were returned to the glovebox and were disassembled in order to measure each sample thickness.

The 2D scattering images were processed as described in Chapter 2, using the Nika[61] macro in Igor Pro. 1D intensity (I) versus q profiles were obtained by azimuthally averaging the images; $q \equiv \frac{4\pi}{\lambda}\sin\left(\frac{\theta}{2}\right)$ represents the magnitude of the scattering vector, where λ is the X-ray wavelength and θ is the scattering angle. The 1D profiles were corrected for attenuation and scattering from the blank reference (empty cell) using Equations 2.12 (SAXS) and 2.31 (WAXS). All corrected intensity profiles were then calibrated to absolute units using the scattering from a glassy carbon reference[62] (sample M13 - obtained from Jan Ilavsky).

4.2.3 Thermal Analysis

After the scattering measurements, the thermal properties for each SEO(52-55)/LiTFSI BCE sample were measured using differential scanning calorimetry (DSC). About half (3 to 6 mg) of each X-ray scattering sample was placed in a TZero aluminum pan and sealed with a TZero hermetic lid (T.A. Inc) inside of the argon glovebox. The samples were removed from the glovebox and re-annealed in the vacuum oven for 24 hours before being slowly cooled for 72 hours, as described earlier. The thermal properties of the samples were then measured using a

heat-quench-heat method: the samples were equilibrated at 30 °C, heated at 5 °C/min up to 130 °C, held isothermally for 20 min, quenched to -80 °C, and then heated back up to 130 °C at 10 °C/min. Analysis was performed using the TA Instruments Universal Analysis 2000 software: melting transitions were analyzed from the first heating scan using the "Peak Integrate Linear" function, while glass transitions were analyzed from the second heating scan using the "Glass/Step Transition" function. Melting temperatures (T_m's) are reported from the peak temperature values, and glass transition temperatures (T_g's) are taken as the inflection temperature during the glass transition.

4.2.4 Scanning Transmission Electron Microscopy (STEM)

For selected BCE concentrations, the second half of the X-ray scattering sample (not used for thermal analysis) was further analyzed using STEM. These bulk electrolyte pieces were cryo-microtomed at −90 °C in a Leica FC6. Sections with thicknesses of approximately 100 nm were obtained using a diamond knife and picked up onto lacey carbon-coated copper grids (Electron Microscopy Sciences). STEM Samples were stained in ruthenium tetroxide vapor for 30 min prior to experiments. STEM experiments were performed on an FEI Titan microscope operated at 200kV at the National Center for Electron Microscopy of the Molecular Foundry, Lawrence Berkeley National Lab. The microscope is equipped with a high angle annular dark field detector (HAADF).

4.2.5 Electrochemical Characterization

The ionic conductivity (σ) of each SEO(52-55)/LiTFSI electrolyte was measured in triplicate. Samples were prepared by placing pellet of the lyophilized SEO(52-55)/LiTFSI sample in the center of a fiberglass spacer (Garolite G10, 5 mil thickness) with an inner diameter of 6.35 mm. The polymer-filled spacer was placed between two sheets of FEP Teflon® and pressed in a pneumatic hot press at 130 °C and 40 psi for 30 seconds. The sample was subsequently flipped and pressed again to achieve a uniform polymer disc within the G10 spacer. Two pieces of 0.0175 mm thick electrode-grade aluminum foil was placed on both sides of the polymer-filled spacer to serve as electrodes. The sample was hot pressed again at 130 °C and 40 psi for 30 seconds to ensure good contact between the electrodes and the BCE. The thickness of each sample was measured using a micrometer, and then aluminum current collector tabs were placed on the electrodes and the cell was vacuum sealed in an air-free pouch material (Showa Denko).

The ionic conductivities were determined using potentiostatic electrochemical impedance spectroscopy (PEIS) and the sample geometry. PEIS measurements were made using a Biologic VMP3 potentiostat. Sample temperature was maintained using a custom-built programmable heating stage. During each experiment, the as-prepared samples were initially heated to and held isothermally at 130 °C for 3 hours. Subsequently, their impedance was measured at 130 °C, and then a cooling scan to 70 °C was performed with 10 °C increments. The samples were held at each temperature for 1 hour before measurement. The PEIS measurements utilized a 50 mV excitation voltage with a frequency range from 1 MHz to 1 Hz. The dc resistance (R) of the electrolyte was determined from a Bode plot of the data, where it was interpreted as the plateau impedance value at the frequency where the maximum phase angle was observed. After PEIS measurements, the samples were disassembled in order to measure their final thickness. Ionic

conductivity (σ) was then calculated from $\sigma = \frac{L}{RA}$ where L is the sample thickness, R is the dc resistance, and A is the sample area.

4.3 Results and Discussion

The combined SAXS/WAXS profiles for all twenty SEO(52-55)/LiTFSI electrolyte concentrations at room temperature (after annealing) are provided in Figure 4.1 and Figure 4.2. Unlike lower molecular weight symmetric volume fraction SEO/LiTFSI samples, which typically exhibit strong Bragg diffraction peaks indicating lamellar nanostructures[28,27,25], the SAXS region of the scattering profiles in Figure 4.1 and Figure 4.2 generally do not contain any well-defined scattering peaks. In most cases, the SAXS profiles exhibit periodic oscillations in intensity reminiscent of the form factor scattering seen for isolated particles.[55] Two notable exceptions are the SEO(52-55)/LiTFSI(r = 0.150) profile in Figure 4.1, wherein there appears to be a primary scattering peak centered around q = 0.064 nm^{-1}, and the profile for SEO(52-55)/LiTFSI(r = 0.450) in Figure 4.2, where a primary scattering peaks is centered at q = 0.052 nm^{-1}. The existence of a primary scattering peak in these samples indicates periodic correlations on the order of 100-120 nm, however, the lack of well-defined higher-order reflections preclude the determination of nanoscale morphology from SAXS alone.

The WAXS profiles, conversely, demonstrate rich behavior as a function of salt concentration. In Figure 4.1, the WAXS from samples with r = 0.000-0.075 indicate the presence of crystalline PEO domains, with the level of Bragg peak intensity decreasing as salt concentration increases. No Bragg reflections are seen in the SEO(52-55)/LiTFSI(r = 0.100) sample. At salt concentrations of r = 0.125-0.150, a new set of Bragg scattering peaks is observed, which we attribute to the so-called 6:1 PEO/LiTFSI crystal complex (C_6)[84–87]. As the salt concentration is increased from r = 0.150, the C_6 complex is no longer observed, and the WAXS profiles only portray amorphous halos. At r = 0.250 in Figure 4.2, another set of Bragg peaks emerge, which we attribute to the formation of the 3:1 PEO/LiTFSI crystal complex (C_3)[84–87]. The C_3 complex is seen in the WAXS profiles of r = 0.250-0.300, whereupon further salt addition generates amorphous WAXS profiles again. For $r \geq$ 0.400 in Figure 4.2, Bragg peaks indicative of the 2:1 PEO/LiTFSI complex (C_2) are observed[84–87].

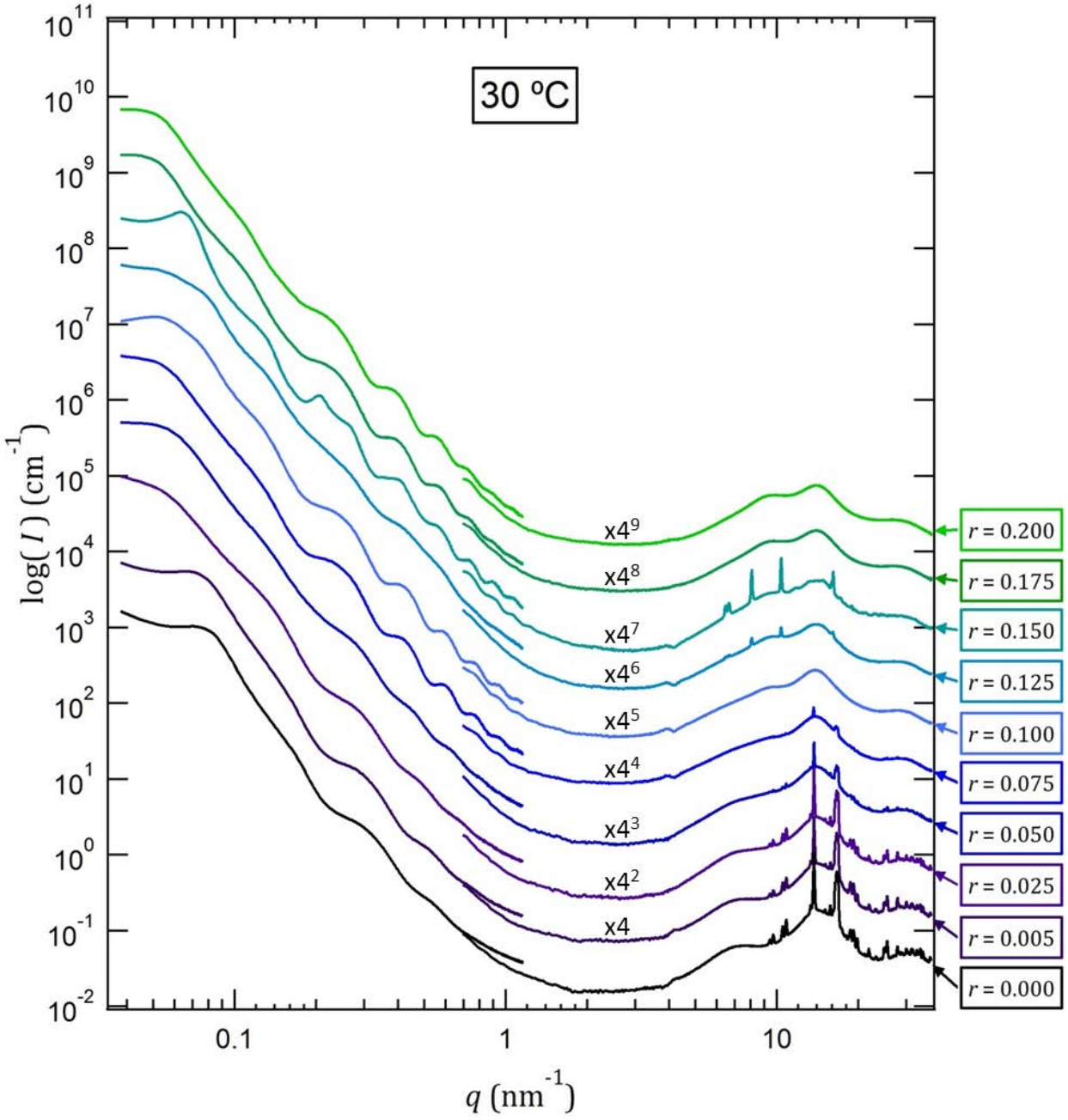

Figure 4.1: Combined SAXS/WAXS profiles for SEO(52-55)/LiTFSI with r = 0 – 0.200 at 30 °C. Each salt concentration is indicated by a data tag. Intensities are absolute, but offset by the factors indicated on the plot for clarity.

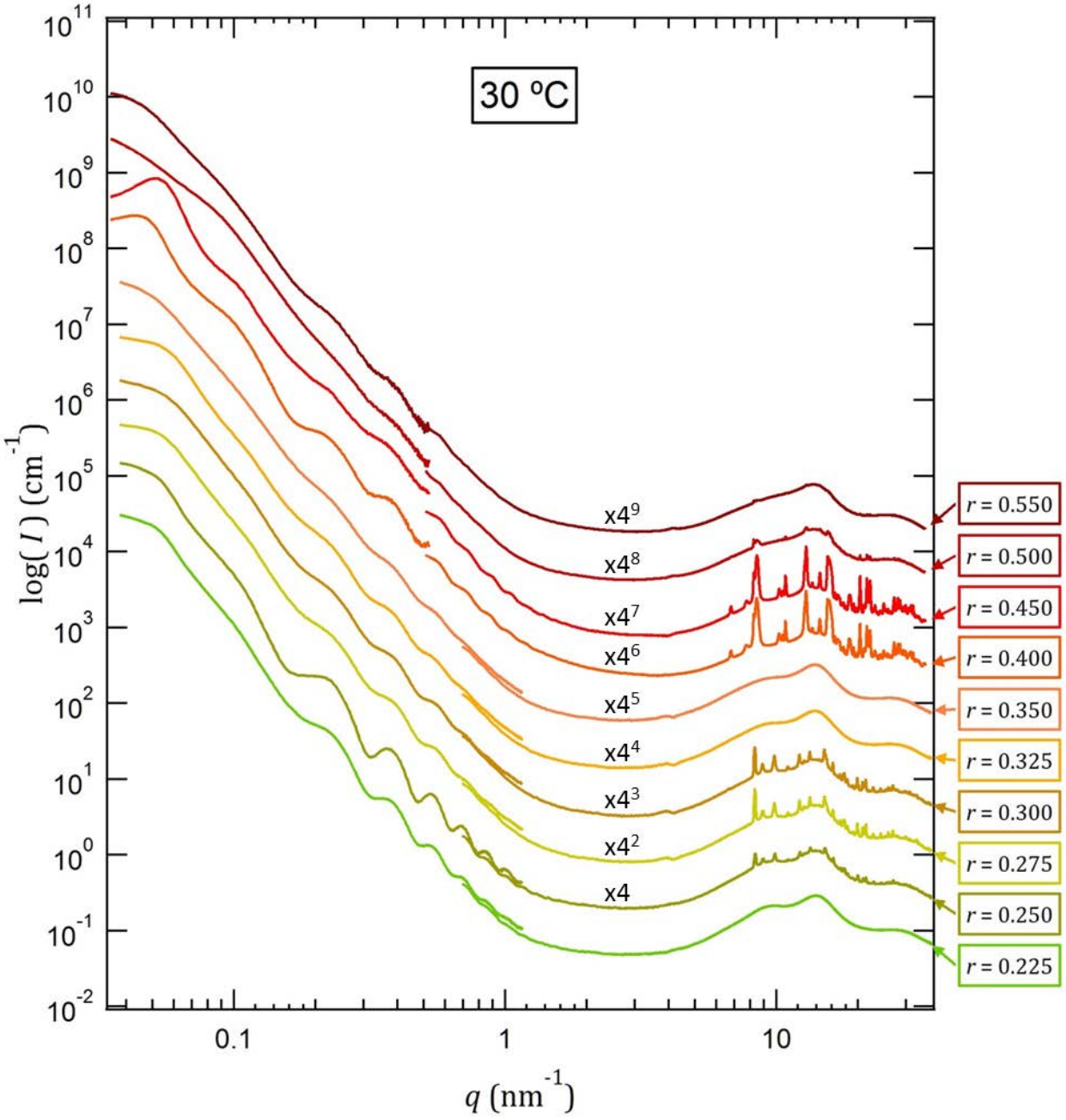

Figure 4.2: Combined SAXS/WAXS profiles for SEO(52-55)/LiTFSI with r = 0.225 – 0.550 at 30 °C. Each salt concentration is indicated by a data tag. Intensities are absolute, but offset by the factors indicated on the plot for clarity.

The presence of semicrystalline PEO and PEO/LiTFSI complexes in the annealed SEO(52-55)/LiTFSI BCEs was confirmed through DSC thermal analysis. In Figure 4.3 we provide a phase diagram summarizing the observations of crystallinity from both DSC and WAXS. While all samples that showed Bragg scattering in WAXS also exhibited melting transitions in DSC, a number of electrolytes indicated weak melting transitions in DSC, but did not portray Bragg scattering. Such samples are indicated with open symbols in Figure 4.3. In many respects, the phase diagram in Figure 4.3 is similar to those of PEO/LiTFSI[84] and

SEO/LiTFSI[28] determined previously; however, it is perhaps notable that none of the SEO(52-55)/LiTFSI concentrations exhibited coexisting C_6 and C_3 complexes as seen previously[28,84], nor was the coexistence of the C_3 and C_2 complexes observed in WAXS. The vertical dashed lines in Figure 4.3 indicate the location of the stoichiometric concentrations for each PEO/LiTFSI complex. Interestingly, the samples with the strongest Bragg intensities due to the PEO/LiTFSI complexes always occur at concentrations below the stoichiometric ratio. One potential cause of the discrepancies observed in PEO/LiTFSI phase behavior is the presence of the PS domains, which we note are in the glassy state for all of the observed melting transitions (purple crosses in Figure 4.3). Thus PEO and PEO/LiTFSI complex crystallization must occur in confinement[88,89] in all cases. To our knowledge, the interplay between PEO/salt complex crystallization microphase separation has never been investigated.

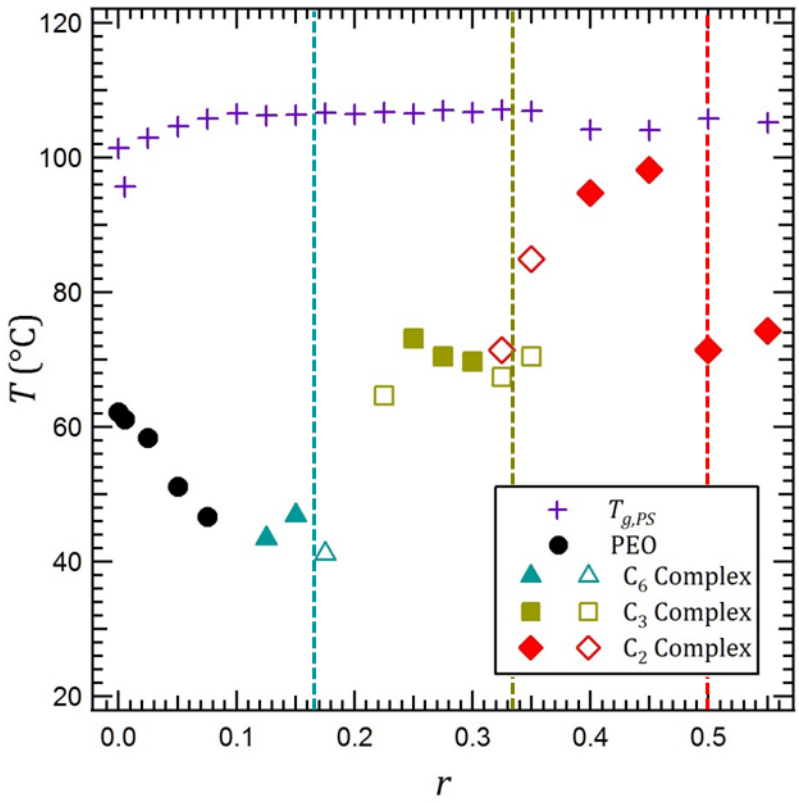

Figure 4.3: Thermal transition temperatures relevant to structure formation observed through DSC analysis of the thermally pre-treated SEO(52-55)/LiTFSI samples. The glass transition temperature for PS is shown as purple crosses, while all other data correspond to melting transitions that are attributed to: pure PEO crystals (black circles); the C_6 complex (turquoise triangles); the C_3 complex (earth-green squares); and the C_2 complex (red diamonds). Filled symbols indicate that the crystal structure was observed with WAXS, while open symbols indicate that only a weak thermal transition was observed that was not confirmed by WAXS. The vertical dashed lines indicate the stoichiometric concentrations for each PEO/LiTFSI complex.

In Figure 4.4 we provide the real-space STEM micrographs of the nanostructures observed in selected SEO(52-55)/LiTFSI electrolytes. In these micrographs, the bright regions indicate the PEO phase. In most cases, the STEM micrographs affirm our observation of SAXS profiles resembling particle form factor scattering by demonstrating the predominant motif of disordered ellipsoidal nanostructures. The micrograph of neat SEO(52-55) in Figure 4.4a

demonstrates local regions of lamellar-like order, which is the expected nanostructure for a symmetric diblock copolymer; however, the overall structure does not exhibit the well-defined periodic structures typical of self-assembled systems. Thus, even without the presence of LiTFSI salt, the self-assembly of SEO(52-55) appears to be kinetically limited. We note that the ellipsoidal PEO microdomains likely derive from the solution structure of the polymer before the solvent was lyophilized (micelles with PEO cores would be expected for SEO dissolved in benzene). In Figure 4.4b, the STEM micrograph for SEO(52-55)/LiTFSI(r = 0.100) contains only ellipsoidal nanostructures, suggesting that although it may induce microphase separation, salt addition hinders the self-assembly of long-range order, as noted previously[28]. However, at even higher salt concentrations, Figure 4.4c reveals a drastic departure from such behavior. In this case, STEM micrographs taken from different regions of the SEO(52-55)/LiTFSI(r = 0.150) sample indicate the coexistence of two distinct nanostructures: self-assembled lamellae and the disordered ellipsoids. The coexistence of these nanostructures is consistent with the SAXS profile in Figure 4.1, wherein the primary scattering peak is consistent with the lamellar spacing and the decaying oscillations at high q are consistent with the form factor scattering of the ellipsoidal phase. At a salt concentration of r = 0.450, the micrograph in Figure 4.4d provides evidence for what appears to be self-assembled cylinders, consistent with the defined primary peak in Figure 4.3. In this case, the structures appear to be well-distributed, with no clear evidence of coexisting microphases. We note all samples exhibiting defined nanostructures also contain crystalline PEO or PEO/LiTFSI-complex domains. While it is unlikely that the crystallization of PEO or PEO/LiTFSI complexes could induce such well-defined nanostructures at temperatures below the T_g of polystyrene, if the specific interactions (polymer-polymer, polymer-ion, etc) that lead to crystallization persist at temperatures above the T_g of polystyrene, then it may be possible that those interactions induce the formation of the nanostructures seen in Figure 4.4.

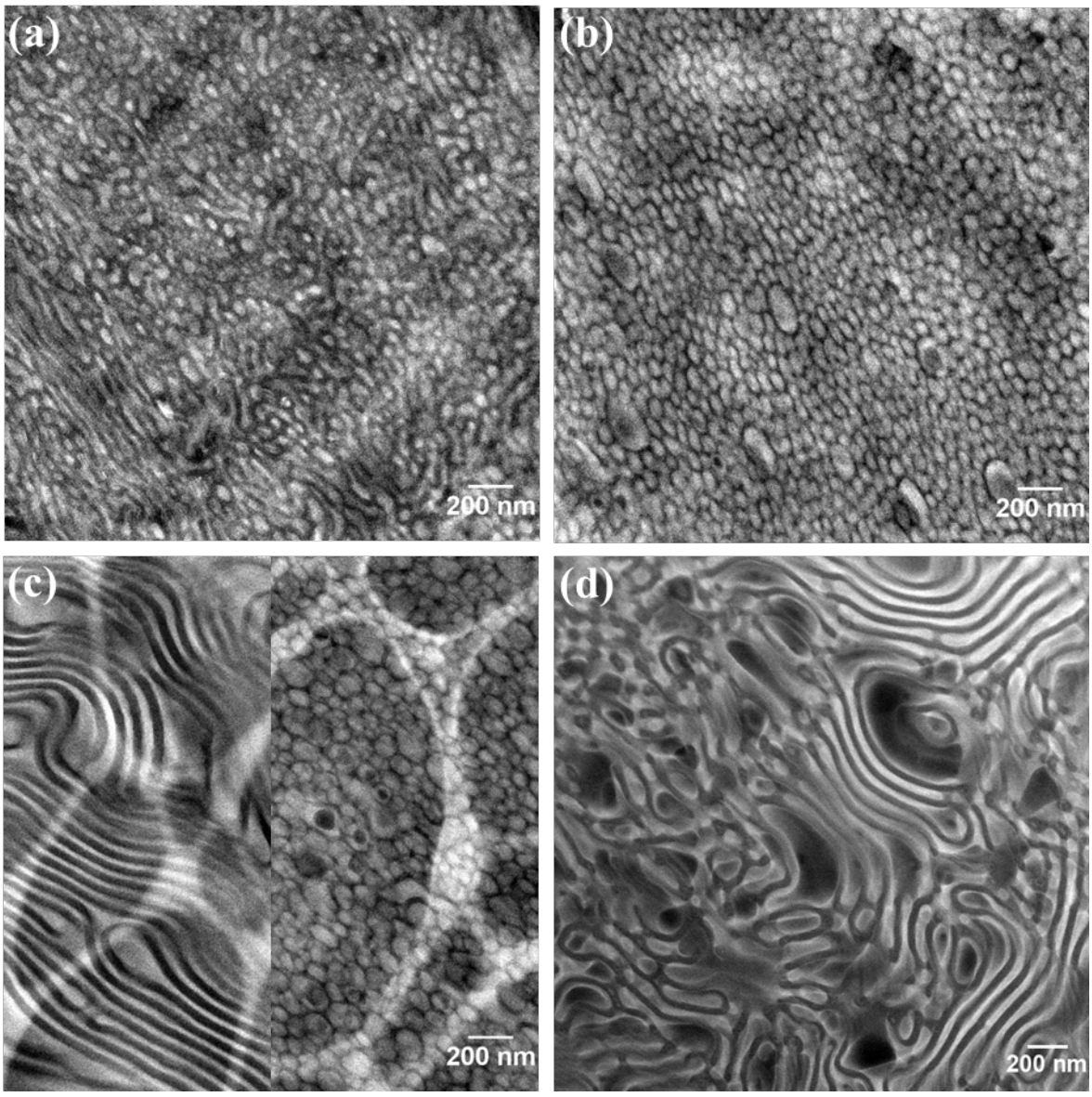

Figure 4.4: STEM micrographs of selected electrolyte concentrations. (a) SEO(52-55)/LiTFSI(r = 0.000); (b) SEO(52-55)/LiTFSI(r = 0.100); (c) SEO(52-55)/LiTFSI(r = 0.150); and (d) SEO(52-55)/LiTFSI(r = 0.450). Bright regions indicate PEO-rich phases. The micrograph in (c) is a composite of two separate images taken from difference regions of the sample; the scale bar applies to both images. Note: the micrograph in (d) was collected during a separated STEM session with a slightly different magnification, hence the slightly smaller scale bar.

In Figure 4.5 and Figure 4.6 we provide the combined SAXS/WAXS profiles for all of the samples at 120 °C, which is above the T_g of PS as well as melting point of all crystal complexes. Other than slight changes in overall intensity, due to the scattering contrast change upon melting of the crystalline domains, the SAXS profiles are essentially identical to those in Figure 4.1 and Figure 4.2. The only noticeable difference is seen in the SEO(52-55)/LiTFSI(r = 0.150) sample, where we observe a sharpening of the higher order peaks due to the lamellar microdomains. The fact that the SAXS profiles do not change at temperatures above the T_g of PS indicates that the nanostructures are at least kinetically stable, which is to be expected after the extensive annealing process described in the experimental section. The disappearance of all

Bragg peaks from the WAXS profiles confirms that all PEO and PEO/LiTFSI complex crystals have melted. Figure 4.5 reveals that the amorphous WAXS profiles undergo systematic changes with increasing salt concentration. The WAXS profile for neat (i.e., r = 0.000) SEO(52-55) contains three broad peaks, centered at approximately q = 7.3 nm^{-1}, q = 14.0 nm^{-1}, and q = 29.2 nm^{-1}. The peak at q = 7.3 nm^{-1} stems from correlations in the polystyrene domains[90], while the peaks at q = 14.0 nm^{-1}, and q = 29.2 nm^{-1} contain contributions from both PS and PEO. As shown in the inset of Figure 4.5, the addition of LiTFSI leads to the growth of a new amorphous halo centered around q = 9.6 nm^{-1}. To our knowledge, the formation of this scattering halo, which corresponds to correlations of ~0.65 nm, with increasing salt concentration has never been reported. For concentrations larger than r = ~0.225, we see another shift in the amorphous WAXS scattering (inset Figure 4.6). In this case, the peak centered at q = 14.0 nm^{-1} begins to shift to lower values q, and the intensity between that peak and the salt-induced peak at q = 9.6 nm^{-1} increases, essentially merging them into one very broad amorphous halo. In this concentration range (r = 0.225-0.550), the halo centered at q = 29.2 nm^{-1} in the neat polymer also noticeably shifts to lower q-vales. While determining the nature of these correlations is beyond the scope of this study, it is clear that the short-range interactions within the amorphous PEO/LiTFSI microphases of SEO(52-55)/LiTFSI electrolytes change significantly with salt concentration. It may be possible that these short-range correlations observed in WAXS represent the driving force for the self-assembly of high salt concentration SEO(52-55)/LiTFSI electrolytes (Figure 4.4c-d).

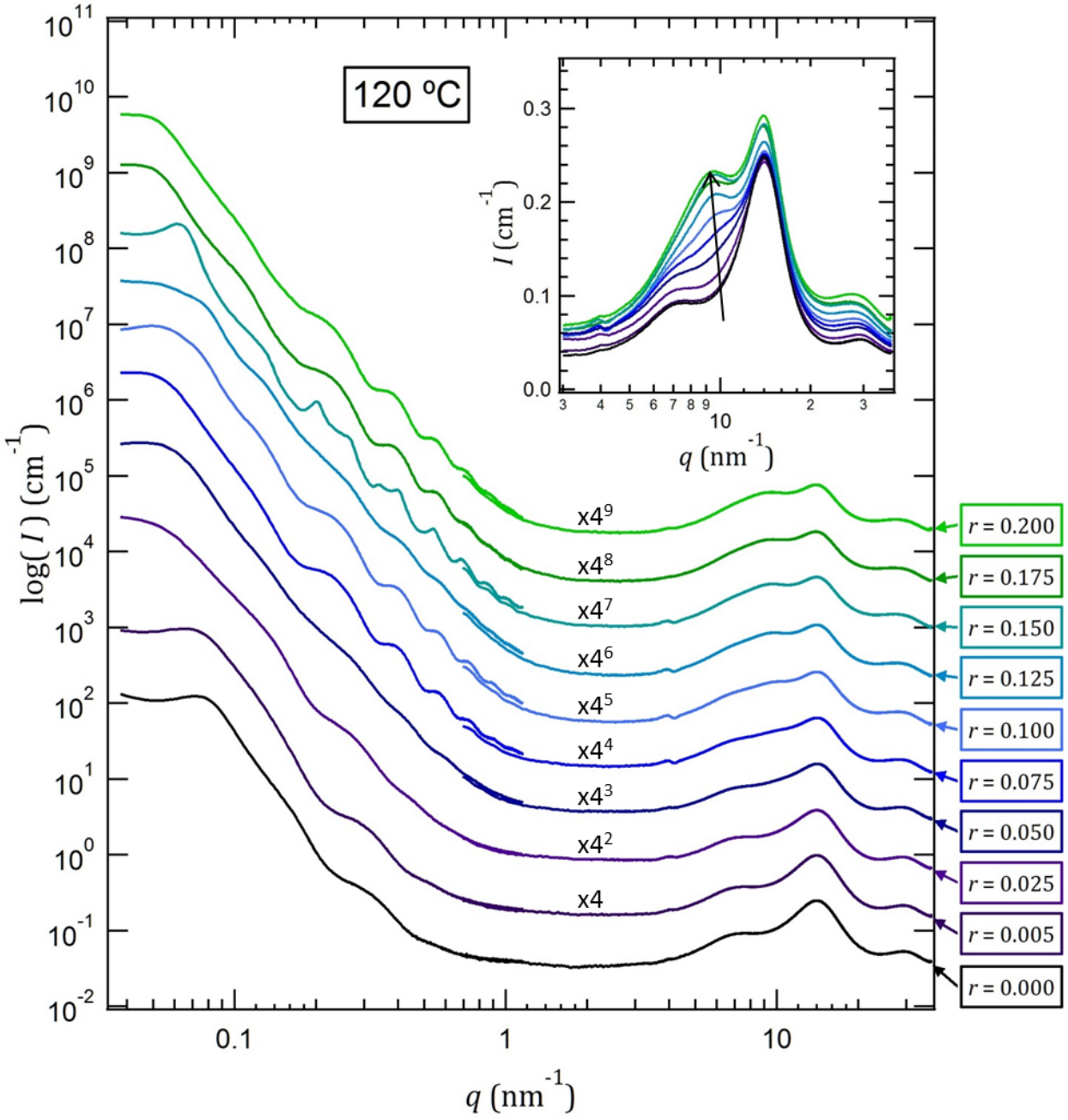

Figure 4.5: Combined SAXS/WAXS profiles for SEO(52-55)/LiTFSI with r = 0 – 0.200 at 120 °C. Each salt concentration is indicated by a data tag. Intensities are absolute, but offset by the factors indicated on the plot for clarity. The inset provides the WAXS data on an absolute linear scale, with the black arrow highlighting the appearance of a new correlation with increasing salt concentration.

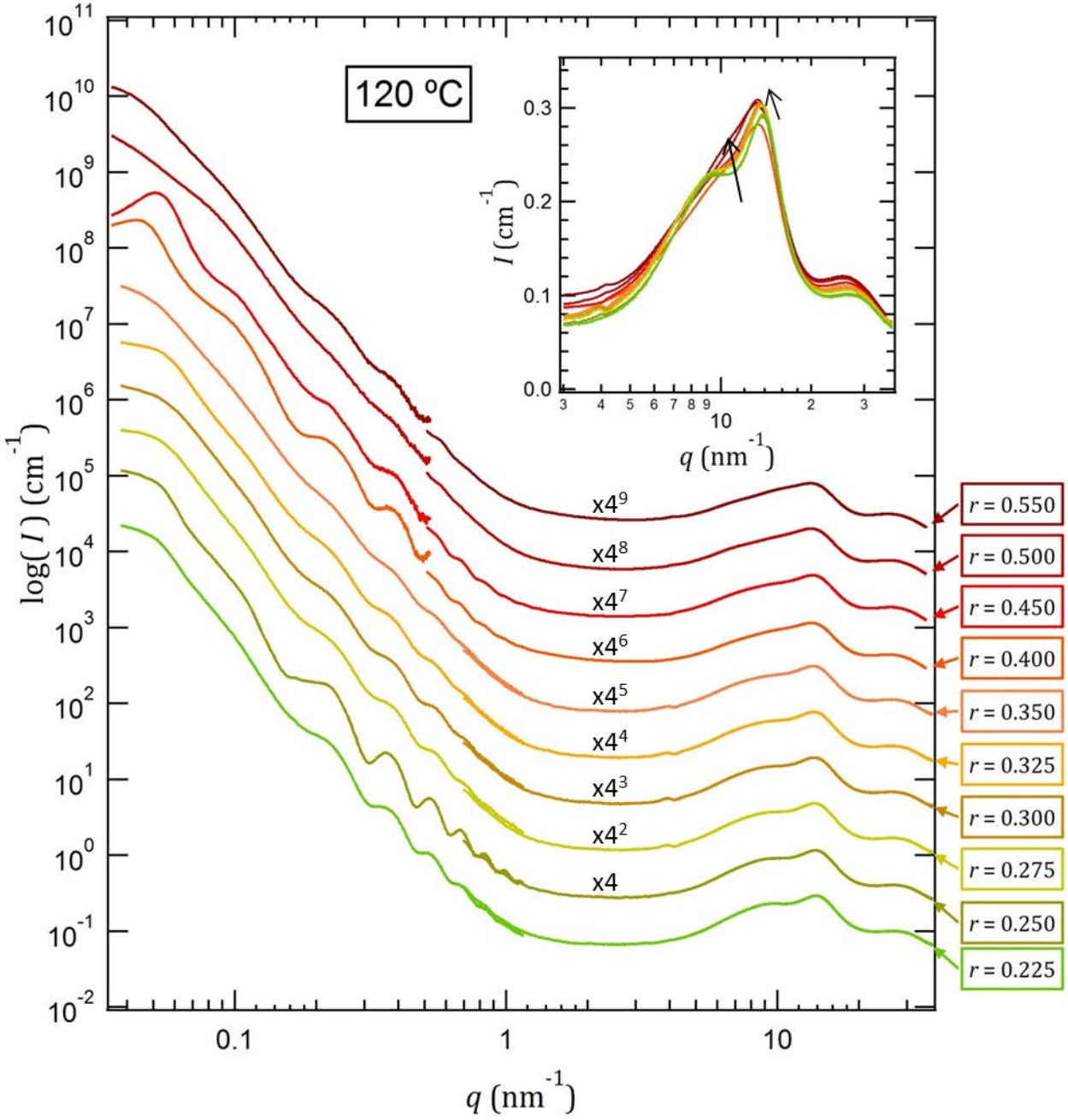

Figure 4.6: Combined SAXS/WAXS profiles for SEO(52-55)/LiTFSI with r = 0.225 – 0.550 at 120 °C. Each salt concentration is indicated by a data tag. Intensities are absolute, but offset by the factors indicated on the plot for clarity. The inset provides the WAXS data on an absolute linear scale, with the black arrow indicating the general change observed with increasing salt concentration.

Regardless of the origin of the structures observed in SEO(52-55)/LiTFSI at high salt concentration, the fact that they remain stable at elevated temperatures has important implications for the nature of the conducting PEO/LiTFSI phase. We have shown that the nanostructure of an electrolyte can influence the solvation environment for LiTFSI, leading to the thermodynamic partitioning of salt between structurally different phases.[27] In the present study, the coexisting nanostructures seen at high salt concentrations are likely only kinetically

stable; however, if one of the nanostructures has a more favorable solvation environment, the salt should still partition between the structural phases in order to adopt the lowest possible energy state. In Figure 4.7 we plot the glass transition temperature of the PEO/LiTFSI phase, measured by DSC, as a function of salt concentration. An increase in the T_g of PEO upon salt addition is a well-known phenonmenon.[12] The relationship between T_g and salt concentration for homopolymer PEO[84] and lower molecular weight SEO[28] electrolytes have been observed to be monotonic up to LiTFSI concentrations of r = ~0.40. In Figure 4.7 we observed a departure from this behavior, wherein multiple "steps" are seen in the T_g values with increasing salt concentration. As in Figure 4.3, we provide vertical dashed lines in Figure 4.7 that indicate the stoichiometric salt concentrations for each PEO/LiTFSI crystal complex. Furthermore, samples that portrayed WAXS crystallinity at room temperature are indicated by filled symbols. It is clear from Figure 4.7 that, just like the coexisting nanostructures observed through SAXS and STEM, there is a correlation between each "step" in T_g and the formation of each PEO/LiTFSI complex; T_g generally increases between, and plateaus at, PEO/LiTFSI complex-forming concentrations. We posit that unusual T_g behavior observed for SEO(52-55)/LiTFSI electrolytes stems from salt partitioning between microphase structures, wherein the partitioning facilitates a constant concentration within the amorphous PEO/LiTFSI domains that provide the signal for a glass transition in DSC. We note that the SEO(52-55)/LiTFSI(r = 0.500) and SEO(52-55)/LiTFSI(r = 0.550) samples are expected to precipitate pure LiTFSI[91], which may account for their lower T_g's (i.e., not all of the salt is solvated).

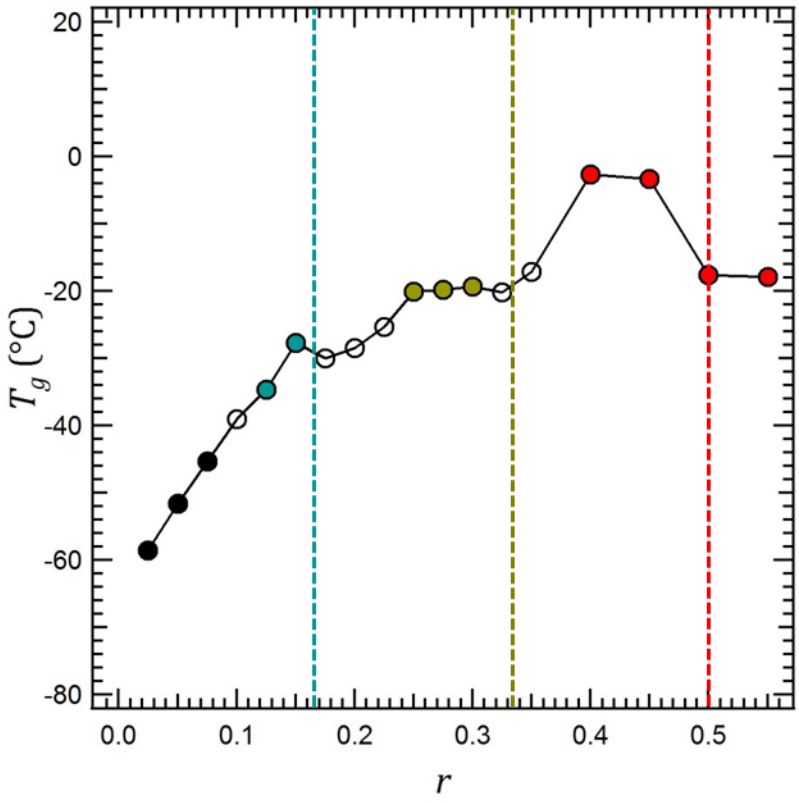

Figure 4.7: The glass transition temperature of the PEO/LiTFSI phase measured by DSC as a function of salt concentration. Filled circles indicate concentrations where crystallinity of: PEO (black fill); the C_6 complex (turquoise fill); the C_3 complex (earth-green fill); and the C_2 complex (red fill) were observed with WAXS at 30 °C. The vertical dashed lines indicate the stoichiometric concentrations for each PEO/LiTFSI complex. Note: the T_g

values for the r = 0.000 – 0.005 samples were omitted due to the strong crystallization of PEO upon quenching to -80 °C.

Coexisting nanostructures, with concomitant salt partitioning between structural domains, can be expected to have a noticeable impact on ion conduction. In Figure 4.8, we plot the ionic conductivity of the SEO(52-55)/LiTFSI electrolytes versus salt concentration at 90 °C. For reference, we also plot the conductivity of homopolymer PEO/LiTFSI electrolytes made from a 5 kg mol^{-1} sample (PEO(5)), as reported previously[28]. Each conductivity value represents the average of 3 different conductivity samples, with error bars indicating the standard deviation from the mean. Qualitatively, the conductivity trends between SEO(52-55)/LiTFSI and PEO(5)/LiTFSI electrolytes are very different: the PEO(5)/LiTFSI system shows a single conductivity maximum at r = 0.11, while SEO(52-55)/LiTFSI has many local maxima, and a global maximum at r = 0.275. Interestingly, although the SEO(52-55)/LiTFSI electrolytes contain a significant volume of non-conductive PS, a number of salt concentrations provide conductivity values within error of PEO(5)/LiTFSI, which consists solely of conducting material. Our working hypothesis to explain the erratic conductivity trends in SEO(52-55)/LiTFSI, as well as the conductivity values approaching PEO(5)/LiTFSI, is that salt partitioning between the coexisting nanostructures in SEO(52-55)/LiTFSI leads to domains with the conductive properties equivalent to PEO/LiTFSI samples of a lower/higher salt concentration. Thus, although the total amount of salt within each electrolyte is increasing, the effective concentration for ion conduction might not, i.e., the measured conductivity data would be shifted to the left or right for some samples in Figure 4.8. This explanation is consistent with the T_g measurements provided in Figure 4.7; however, we note that ion conduction encompasses a wide range of physical phenomena and other effects might provide reasonable alternative explanations. What is clear is that for a nominal salt concentration near r = 0.275, the ionic conductivity of an SEO(52-55)/LiTFSI electrolyte can compete with that of homopolymer PEO/LiTFSI.

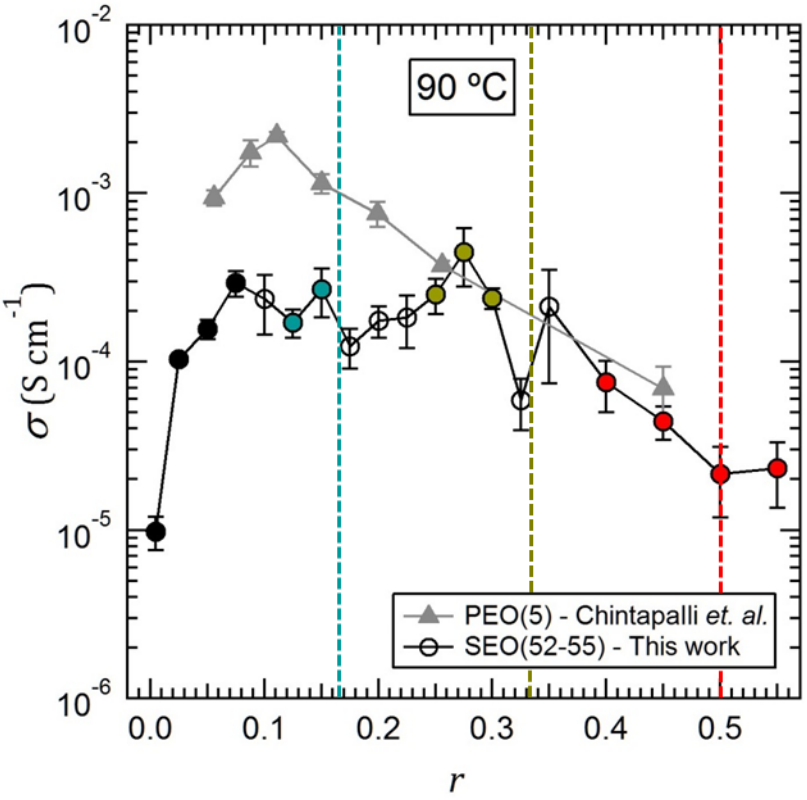

Figure 4.8: Ionic conductivity of the SEO(52-55)/LiTFSI samples (black circles) at 90 °C, with the conductivities reported for PEO(5)/LiTFSI in ref [28] (grey triangles) for reference. Filled circles indicate concentrations where crystallinity of: PEO (black fill); the C_6 complex (turquoise fill); the C_3 complex (earth-green fill); and the C_2 complex (red fill) were observed with WAXS at 30 °C. The vertical dashed lines indicate the stoichiometric concentrations for each PEO/LiTFSI complex. Error bars represent the standard deviation from the average of 3 replicate samples. The data markers are connected by lines for clarity.

4.4 Conclusions

The development of a mechanically rigid solid-state electrolyte with high ionic conductivity represents a promising route to enabling the use of high energy density metal anodes in next generation batteries.[18,20–23] Block copolymer electrolytes (BCEs) composed of polystyrene-*b*-poly(ethylene oxide) (SEO) mixed with lithium bis(trifluoromethanesulfonyl)imide (LiTFSI) salt have been extensively studied as a model system. It is known that ionic conductivity is influenced by SEO molecular weight[29,30], BCE nanostructure[31–33], and salt concentration[29,28]; however, these parameters appear to be inherently coupled due to the thermodynamics of self-assembly[24–28]. Fortunately, it has been shown that BCEs lacking well-defined long-range order actually provide the highest ionic conductivity.[28,33]

In this work, we have extended our analysis of the model SEO/LiTFSI system to encompass strongly segregated (high molecular weight) SEO block copolymers in the high salt concentration limit. Structural analysis (SAXS/WAXS/STEM) of the neat SEO(52-55) polymer used in this study revealed the presence of disordered ellipsoidal nanostructures even after extensive annealing. These nanostructures likely derive from the solvated structure of the

polymer; the electrolytes were lyophilized in this study, however this result indicates the importance of casting conditions when making electrolyte films from high molecular weight block copolymers.

For SEO(52-55)/LiTFSI electrolytes within the concentration range of r = 0.000-0.100, the addition of salt leads to a disruption of PEO crystallinity and the predominant nanostructural motif becomes disordered ellipsoids, indicating that the addition of salt hinders self-assembly. However, in the SEO(52-55)/LiTFSI(r = 0.150) sample, both SAXS and STEM revealed the coexistence of well-ordered lamellar domains and disordered ellipsoids. This unprecedented result reveals the possibility of salt-partitioning between coexisting nanostructures within the electrolyte, which has only been observed in weakly segregated systems during the order-to-disorder transition[27]. The scaling behavior of the T_g for PEO in electrolytes with r > 0.150 supports the occurrence of salt-partitioning. Furthermore, the ionic conductivities of SEO(52-55)/LiTFSI electrolytes in the high salt concentration regime (i.e. r > 0.100) display many maxima with increasing salt concentration, which could be explained by a heterogeneous salt distribution within the samples.

The origin of the coexisting nanostructures in SEO(52-55)/LiTFSI(r = 0.150) appear to be related to the formation of the C_6 PEO/LiTFSI crystal complex[84–87]; however, the presence of glassy PS domains at the crystallization temperature precludes the formation of crystal-induced nanostructures[88,89]. Rather, the appearance of a new correlation peak in the WAXS profile of molten SEO(52-55)/LiTFSI(r = 0.150) suggests that a salt-induced change in PEO chain conformation or inter-chain interactions might drive the self-assembly in this sample. The observation of further changes in the molten WAXS profiles with increasing salt concentration suggest that this mechanism might play a role in the self-assembly of SEO(52-55)/LiTFSI electrolytes at even higher salt concentrations, leading to the nanostructures seen in SEO(52-55)/LiTFSI(r = 0.450).

The competition between self-assembly and kinetic barriers in BCEs formed from a strongly segregated block copolymer has revealed a unique situation wherein coexisting poorly-ordered and well-defined nanostructures allow for stable salt partitioning within the sample. The implications for battery behavior remain unclear; however, attaining ionic conductivities in a BCE that are on par with the conductivity of homopolymer PEO, as we have demonstrated in this work, hold great promise for improved performance.

4.5 Acknowledgements

This work was supported by the Joint Center for Energy Storage Research, an Energy Innovation Hub funded by the U.S. Department of Energy (DOE), Office of Science, Basic Energy Sciences (BES). Thermal analysis was performed at the Molecular Foundry at Lawrence Berkeley National Laboratory. X-ray scattering experiments were performed at Lawrence Berkeley National Laboratory's Advance Light Source, Beamline 7.3.3. The Molecular Foundry and Beamline 7.3.3 of the Advanced Light Source are supported by the Director of the Office of Science, Office of Basic Energy Sciences, of the U.S. Department of Energy under Contract No. DE-AC02-05CH11231. We thank Polite Stewart, Chenhui Zhu, and Eric Schaible for their assistance with the setup and operation of Beamline 7.3.3. I thank Andrew Wang for his

assistance with the conductivity measurements, and Xi (Chelsea) Chen and Xi Jiang for obtaining the STEM micrographs.

4.6 Nomenclature

4.6.1 Abbreviations

BCE	Block copolymer electrolyte
DSC	Differential scanning calorimetry
C_2	2:1 (PEO:LiTFSI) crystal complex
C_3	3:1 (PEO:LiTFSI) crystal complex
C_6	6:1 (PEO:LiTFSI) crystal complex
EO	Ethylene oxide
FEP	Fluorinated ethylene propylene
LiTFSI	Lithium bis(trifluoromethanesulfonyl)imide
PDI	Polydispersity index
PEIS	Potentiostatic electrochemical impedance spectroscopy
PEO	Poly(ethylene oxide)
PS	Polystyrene
SAXS	Small angle X-ray scattering
SEO	Polystyrene-*b*-poly(ethylene oxide) diblock copolymer
STEM	Scanning transmission electron microscopy
THF	Tetrahydrofuran
WAXS	Wide angle X-ray scattering

4.6.2 Symbols

A	Electrode area in conductivity cell, cm^2
I	Absolute scattering intensity, cm^{-1}
L	Electrode thickness in conductivity cell, cm
$M_{n,PEO}$	Number average molecular weight of the PEO block, kg mol^{-1}
$M_{n,PS}$	Number average molecular weight of the PS block, kg mol^{-1}
q	Magnitude of the scattering vector, nm^{-1}
r	Salt concentration $[Li^+][EO]^{-1}$, --
R	dc resistance of the electrolyte, Ω
T_g	Glass transition temperature, °C
T_m	Melting temperature, °C

4.6.3 Greek

χ	Flory-Huggins interaction parameter, --
χ_{eff}	Effective Flory-Huggins interaction parameter, --
λ	Scattering wavelength, nm
θ	Scattering angle, rad
σ	Ionic conductivity, Scm^{-1}

4.7 Supporting Information

4.7.1 SEO(52-55) Characterization (and Purification)

An aliquot of the reaction was collected after the growth of the polystyrene chains; the aliquot was precipitated in hexanes and the solid polystyrene was dried and then characterized with Gel permeation chromatography (GPC) using tetrahydrofuran (THF) as the carrier solvent. The PS block length was determined to be $M_{n,PS}$ = 52 kgmol^{-1} (PDI = 1.02) using polystyrene calibration standards. GPC analysis using dimethylformamide (DMF) as the carrier solvent was performed on the SEO sample after three rounds of precipitation from benzene into hexanes, as well as the on the PS block. As demonstrated in Figure 4.S1a, the as-precipitated SEO sample has residual homopolymer PS impurities. We successfully removed these impurities (see Figure 4.S1b) by casting a film of the as-precipitated SEO sample from a 4:1 ethyl acetate-cyclohexanone blend, followed by a washing step in cyclohexane at ~40 °C. The dispersity of the washed SEO sample was determined to be PDI = 1.1 from the GPC trace in Figure 4.S1b using PEO calibration standards. The slight bump at lower retention volume (V_{ret} = 14 mL) in both SEO samples is likely due to a small fraction of coupled SEO chains; the final PDI calculation includes this contribution.

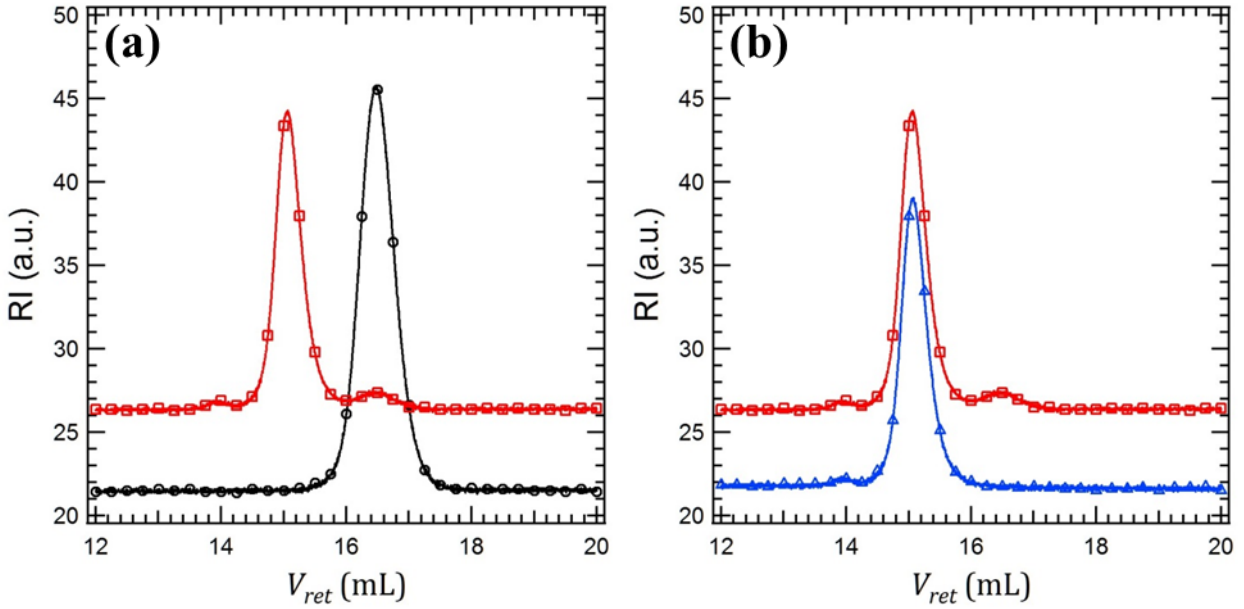

Figure 4.S1: (a) DMF GPC traces for the as-precipitated SEO block copolymer (red squares/curve) and the PS aliquot (black circles/curve). (b) DMF GPC traces for the as-precipitated SEO block copolymer (red squares/curve) and the purified SEO sample (blue triangles/curve). Data makers are only plotted every 75th data point for clarity.

Proton nuclear magnetic resonance spectroscopy (^{1}H NMR) was performed on both the as-precipitated and cyclohexane-washed samples of SEO. As expected, the concentration of styrenic protons (determined from integrating the intensity between 7.27 to 6.24 ppm) relative to PEO backbone protons (determined from integrating the intensity between 4.01 to 3.37 ppm) decreased upon removal of the homopolymer PS impurities. Furthermore, as shown in Figure 4.S2, the amount of residual initiator (P4 *t*-butyl phosphazene base), indicated by the doublet at 2.71 ppm, was significantly decreased during the washing step. The molecular weight of the PEO block, as calculated from the ratio of styrenic and PEO protons (see integrations in Figure

4.S3), was found to be $M_{n,PEO}$ = 55 kgmol^{-1}. Thus, through GPC and NMR characterization, the washed SEO sample is named SEO(52-55), with $M_{n,PS}$ = 52 kgmol^{-1}, $M_{n,PEO}$ = 55 kgmol^{-1}, and PDI = 1.1. As a final purification step, the polymer was dissolved in cyclohexanone/toluene (2.5:1), passed through a 0.45 μm syringe filter, and re-precipitated in hexanes before being dried under vaccum and brought into the argon glovebox for electrolyte preparation.

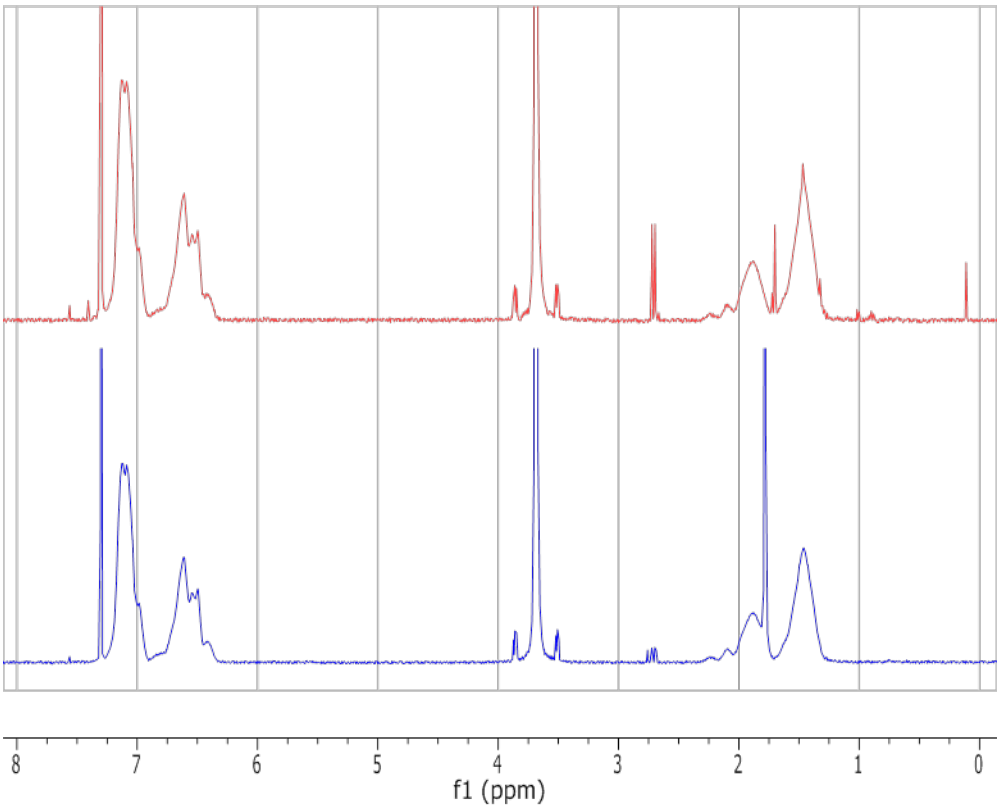

Figure 4.S2: ^{1}H NMR spectra for the as-precipitated (upper red trace) and cyclohexane-washed (lower blue trace) measured in $CDCl_3$.

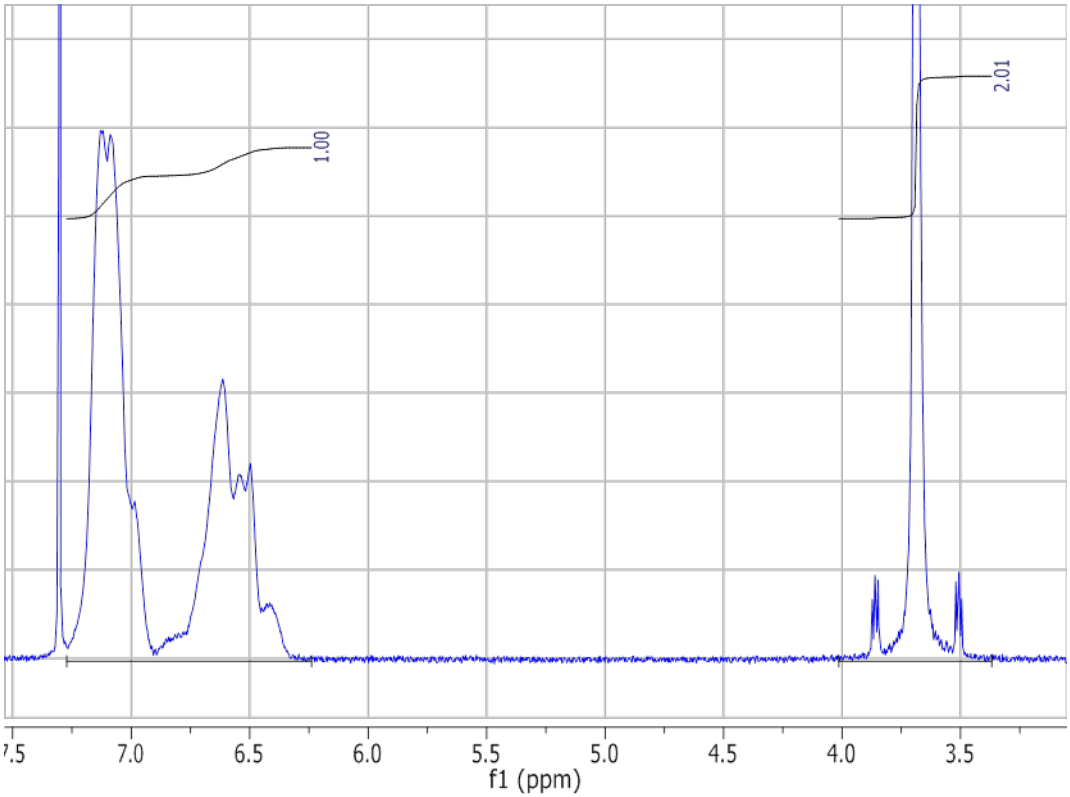

Figure 4.S3: Integration analysis of the styrenic and PEO backbone protons from the cyclohexane-washed SEO sample.

Chapter 5 -Relationship between Ion Dissociation, Melt Morphology, and Electrochemical Performance of Lithium and Magnesium Single-Ion Conducting Block Copolymers[†]

Abstract

Single-ion conducting block copolymers, such as poly(ethylene oxide)-*b*-poly[(styrene-4-sulfonyltrifluoromethylsulfonyl)imide lithium] (PEO-P[(STFSI)Li]), represent an exciting new class of materials capable of improving the performance of solid-state batteries with metal anodes. In this work, we report on the synthesis and characterization of a matched set of lithiated (PEO-P[(STFSI)Li]) and magnesiated (PEO-P[$(STFSI)_2Mg$]) single-ion conducting diblock copolymers. We measure the temperature dependence of ionic conductivity, and through analysis using the Vogel-Tamman-Fulcher (VTF) relation, demonstrate that ion dissociation is significantly lower for all PEO-P[$(STFSI)_2Mg$] samples when compared to their PEO-P[(STFSI)Li] counterparts. The VTF parameter characterizing the activation barrier to ion hopping was similar for both cations, but the VTF prefactor that reflects effective charge carrier concentration was higher in the lithiated samples by an order of magnitude. We study the melt morphology of the single-ion conducting block copolymers using temperature-dependent X-ray scattering, and use the mean-field theory of Leibler to extract the effective Flory-Huggins interaction parameter (χ) for PEO/P[(STFSI)Li] and PEO/P[$(STFSI)_2Mg$] from the X-ray scattering data. We demonstrate a linear relationship between the charge-concentration-related VTF parameter and the parameter quantifying the enthalpic contribution to χ. It is evident that ion dissociation and block copolymer thermodynamics are intimately coupled; ion dissociation in these systems suppresses microphase separation.

5.1 Introduction

The development of high energy-density electrical storage represents an essential task necessary for the efficient implementation of renewable energy sources toward portable technologies, transportation, and improvements to the electrical grid.[1–3] High energy-density batteries represent one solution to portable technologies or grid storage; however, to achieve the energy capacities required for demanding applications such as electric vehicles, next generation batteries will almost certainly require the use of a metal foil anode.[16,92] The use of metal foils, such as lithium, as anodes in rechargeable battery cells introduces many complications, including chemical instability with liquid electrolytes and uneven metal deposition that can lead to a short circuit.[93] One successful approach to mitigating these effects and producing a safe lithium foil battery is to utilize a solid polymer electrolyte.[94]

Most research into the development of solid polymer electrolytes has centered around systems utilizing salt-doped poly(ethylene oxide) (PEO), which is known to readily solvate and conduct ions.[12] Recently a new class of polymer electrolytes has been developed wherein a block

[†] This chapter was reported in *Macromolecules* **2016**, DOI: 10.1021/acs.macromol.6b01886.

copolymer has an ion-containing block (i.e. the anion is covalently bonded the polymer backbone) and a neutral block, such as PEO, that can solvate and transport the counter-ions from the ion-containing block.[34] As demonstrated by Bouchet and coworkers[35], triblock copolymers of poly(ethylene oxide) (PEO) and the lithiated ion-containing polymer, poly(styrene-4-sulfonyltrifluoromethylsulfonyl)imide lithium P[(STFSI)Li], behave as efficient single-ion (i.e. Li^+) conductors that can significantly improve the performance of lithium metal batteries.

In addition to the development of lithium metal batteries, there is significant interest in the development of alternative metal foil battery chemistries, such as magnesium metal, which could provide similar energy-density, while decreasing both raw material cost and the hazards associated with pyrophoric nature of lithium[95]. Unfortunately, stable magnesium conducting electrolytes have yet to be developed.[95–99] We demonstrate the development of magnesium-based single-ion conducting block copolymers.

This study is based on a matched-set of lithiated (Li^+) and magnesiated (Mg^{2+}) single-ion conducting PEO-P(STFSI) block copolymers with varying P(STFSI) block length (i.e charge concentration). We first explore the impact of counter-ion (Li^+ vs. Mg^{2+}) on the ionic conductivity using temperature-dependent potentiostatic electrochemical impedance spectroscopy (PEIS). Our analysis reveals that the number of effective charge carriers contributing to the conductivity for the lithiated sample is about an order of magnitude higher than its magnesiated counterpart. To probe the nanoscale morphology of the single-ion conducting block copolymers, we performed temperature-dependent small and wide angle x-ray scattering (SAXS/WAXS) measurements. Our analysis reveals that counter-ion dissociation in single-ion conducting block copolymers of PEO-P(STFSI) induces compatibility between the two blocks, which in the case of PEO-P[(STFSI)Li] leads to negative effective Flory-Huggins interaction parameters (χ). In conventional block copolymers, thermodynamically driven self-assembly through microphase separation is often leveraged to improve bulk mechanical properties of the electrolyte film.[19,21,22,29,100] The results presented in this paper suggest that this approach is not applicable to single-ion conducting block copolymer electrolytes; single-ion systems with efficient ion conduction are unlikely to exhibit microphase separation. In this scenario, a new strategy must be employed to provide the mechanical support necessary to suppress uneven metal deposition in metal foil batteries[18,19,22]; for example, the introduction of a third incompatible rigid block such as polystyrene.

5.2 Experimental

5.2.1 Polymer Synthesis and Characterization

PEO-P(STFSI) polymers with a constant PEO molecular weight and varying P(STFSI) block length were synthesized as described previously.[36,37] The synthesis of block copolymers was confirmed through gel permeation chromatography (see SI in 5.7.1), and the molecular weight of the P(STFSI) blocks were determined through H^1 NMR spectroscopy (see SI in 5.7.2). The polymerization product has potassium counter-ions for the ion-containing block, which were exchanged through dialysis with lithium chloride (LiCl), as described previously[36,37], and magnesium chloride ($MgCl_2$) in de-ionized water to form PEO-P[(STFSI)Li] and PEO-P[$(STFSI)_2$Mg], respectively. The success of the magnesium ion exchange was confirmed

through Instrumental Neutron Activation Analysis (INAA) of Cl, F, Mg, and K on PEO-P[(STFSI)$_2$Mg] samples (Elemental Analysis Inc., see SI in 5.7.3 for details). The chemical structures of each type of the single-ion conducting block copolymer are shown in Figure 5.1. All of the polymers studied in this work are listed in Table 5.1. The PEO-P[(STFSI)Li] and PEO-P[(STFSI)$_2$Mg] samples were subsequently dried under vacuum for a minimum of 1 week at ambient temperature and then dried under vacuum in a heated glove box antechamber at 90 °C for 24 hours before being brought into an argon (Ar) glovebox (MBraun). Inert atmosphere was maintained for all subsequent sample preparation and analysis.

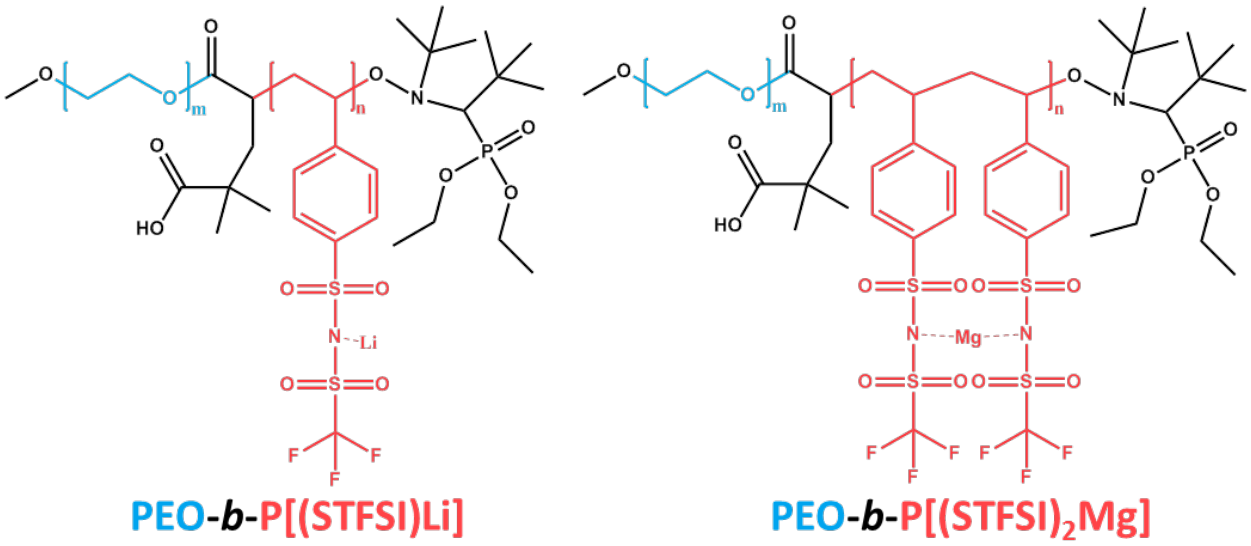

Figure 5.1: Chemical structure for both types of single-ion block copolymers characterized in this study (including endgroups).

Table 5.1: Characteristics of the matched-set of block copolymers. $M_{n,PEO}$ and $M_{n,PSTFSI}$ are the number-average molecular weights of each block, with corresponding number-average degrees of polymerization N_{PEO} and N_{PSTFSI}. ϕ_{PSTFSI} is the volume fraction of the ion-containing block, and r is ratio of cations to ethylene oxide (EO) moieties in each sample.

Sample Name	$M_{n,PEO}$ (kg mol^{-1})	$M_{n,PSTFSI}$ (kg mol^{-1})	N_{PEO}	N_{PSTFSI}	ϕ_{PSTFSI}	r ([cation] [EO]$^{-1}$)
PEO-P[(STFSI)Li](5-3.2)	5.00	3.19	114	9.9	0.32	0.087
PEO-P[(STFSI)Li](5-2.0)	5.00	1.99	114	6.2	0.24	0.054
PEO-P[(STFSI)Li](5-1.1)	5.00	1.05	114	3.3	0.16	0.029
PEO-P[(STFSI)$_2$Mg](5-3.2)	5.00	3.24	114	9.9	0.33	0.043
PEO-P[(STFSI)$_2$Mg](5-2.0)	5.00	2.02	114	6.2	0.24	0.027
PEO-P[(STFSI)$_2$Mg](5-1.1)	5.00	1.08	114	3.3	0.16	0.014
PEO(5)	5.00	-	114	-	-	-

Thermal transitions in PEO, PEO-P[(STFSI)Li], and PEO-P[(STFSI)$_2$Mg] were probed using differential scanning calorimetry (DSC). Samples were prepared in an Ar glovebox by

placing 6-8 mg of polymer into a TZero aluminum pan and sealing with a TZero hermetic lid (T.A. Inc). A reference TZero hermetically sealed pan was also prepared in the Ar glovebox. The actual mass of polymer in the pans was recorded as the difference in mass of the pan and lid before and after polymer addition. In order to ensure the polymers had consistent thermal history, the hermetically sealed DSC samples (and reference pan) were subsequently annealed at 135 °C in a vacuum oven at -10 mmHg for 24 hours, after which the heater was turned off and the samples were allowed to slowly cool. Measurements were performed a minimum of 72 hours after the oven heater was turned off. A heat-quench-heat-cool method was used in order to determine the PEO melting temperature ($T_{m,PEO}$), crystallization temperature ($T_{c,PEO}$), and in cases where observable, glass transition temperature ($T_{g,PEO}$). Details of the DSC method used and analysis performed can be found in the supporting information (Section 5.7.4).

5.2.2 Electrochemical Characterization

The electrochemical response of the ion-containing block copolymers was monitored using Potentiostatic Electrochemical Impedance Spectroscopy (PEIS) on symmetric two-electrode cells. The samples used for PEIS were prepared by melting polymer into a 1/8 inch inner diameter spacer made of 10 mil thick silicone elastomer placed upon a stainless steel shim electrode. After filling the spacer with polymer, a second stainless steel shim was placed on top to seal the polymer within the spacer and serve as the counter electrode. Aluminum tabs were used to contact the stainless steel electrodes, and the entire assembly was vacuum sealed in an air-free pouch material (Showa Denko). The samples were subsequently removed from the Ar glovebox and mounted to a custom built heating stage for variable temperature electrochemical analysis. Triplicate samples of each ion-containing block copolymer were prepared.

PEIS measurements were performed using a Biologic VMP3 multi-channel potentiostat utilizing a 50 mV excitation voltage over a frequency range of 1 MHz to 0.5 Hz. The measurements were performed during a cooling temperature scan, where the samples were first heated to 130 °C and held at temperature for 3 hours before cooling in 10 °C intervals down to 30 °C. The samples were equilibrated for 1 hour at each temperature before performing PEIS measurements.

Resistance due to ion motion was interpreted as the real impedance of the low frequency minimum on a Nyquist plot. In cases of extremely resistive semicrystalline samples, the real impedance at 60 Hz was used to approximate the resistance due to ion motion. The ionic conductivity (σ) was calculated from the real impedance measurements and the sample geometry by $\sigma = \frac{L}{A_S Z_{Re}}$, where L is the sample thickness, A_s is the area defined by the silicone spacer, and Z_{Re} is the real contribution to the impedance measured through PEIS. The reported conductivity values represent the average of the three replicate samples, with error bars that represent their standard deviation from the mean.

5.2.3 Small and Wide Angle X-Ray Scattering (SAXS/WAXS)

X-ray scattering samples were prepared by melt-forming the polymer samples into a 1/8 inch diameter spacer made of 1/32 inch thick Aflas® rubber. The polymer/spacer assembly was subsequently covered with 1 mil Kapton® film windows and enclosed in a custom-built hermetically sealing aluminum sample holder. The hermetically sealed samples, as well as an

empty reference sample were then removed from the Ar glovebox and annealed in a vacuum oven following the same thermal treatment as the DSC samples. SAXS/WAXS experiments were performed at Lawrence Berkeley National Laboratory's Advanced Light Source, Beamline 7.3.3[60] using a transmission setup and a custom-built heating stage. Temperature scans were replicated using both SAXS and WAXS. For each experiment, the samples were initially equilibrated at near ambient conditions (either 30 or 35 °C) where the scattering of semicrystalline samples was recorded. The samples were then heated directly to 130 °C and held at that temperature for at least 1 hour. The stage was subsequently cooled in 20 °C steps down to 90 °C or 70°C. Measurements were performed at each temperature upon waiting at least 30 minutes after the stage reached the set point temperature. Finally, in cases when beamtime was available, the samples were quenched directly to 35 °C and allowed to isothermally crystallize for at least 90 minutes (note, the stage took ~45 minutes to reach 35 °C), with scattering patterns being measured every 10-15 minutes. The sample temperature at each step was determined by the reading of a dummy sample with an inserted thermocouple (details in Section 5.7.5). On average, the sample temperature was found to be a factor of 0.94 times the stage setpoint temperature. For simplicity, we refer to the stage setpoint temperature throughout the text, however, all analysis accounts for the temperature offset.

The scatting data were reduced using the Nika macro developed by Jan Ilavsky[61] in Igor Pro as described in Chapter 2. Isotropic 2D scattering patterns were azimuthally averaged, whereas anisotropic 2D images were reduced using sector averaging. The 1D data sets of intensity (I) versus the magnitude of the scattering vector (q) were further corrected for sample transmission, parasitic scattering from the sample holder (Equations 2.12 and 2.31), and then calibrated to absolute units (cm^{-1}) using a glassy carbon intensity standard provided by Jan Ilavsky (Sample M13)[62], as demonstrated in Chapter 2.6.6. Independent calibration of the SAXS and WAXS intensities allows for the I versus q scattering profiles to be combined without arbitrary scaling, providing structural information over a wide range of length scales i.e. $0.04 < q < 35$ nm^{-1}, which in real space probes length-scales from ~150 nm down to ~0.2 nm. For the purposes of this work, we limit our analysis to molten samples and structural correlations on the order of the polymer chain dimensions (i.e., $0.04 < q < 4$ nm^{-1}). Chapter 6 will focus on the semicrystalline samples and provide a detailed analysis of the WAXS data. The 2D scattering images from all of the samples in the semicrystalline state, as well as the 1D calibrated intensity profiles for all samples at all temperatures are provided in Appendix A2.

5.3 Results and Discussion

The results of the DSC analysis for all of the samples are summarized in Table 5.2 below. All samples exhibited PEO melting peaks after the thermal pretreatment described in the experimental section; however, crystallization during the cooling scan was significantly depressed for PEO-P[$(STFSI)_2Mg$](5-3.2) and was not observed in the PEO-P[(STFSI)Li](5-3.2) sample. The inhibited crystallization in these samples facilitated the observation of the glass transition of PEO (T_g), whereas the strong crystallization of PEO in the other samples precluded the observation of a T_g.

Table 5.2: Sample details and results from DSC analysis. A value of "--" indicates that the transition was not observed.

Sample Name	Sample Mass (mg)	$T_{m,PEO}$ (°C)	$T_{c,PEO}$ (°C)	$T_{g,PEO}$ (°C)
PEO-P[(STFSI)Li](5-3.2)	8.0	55.7	--	-34
PEO-P[(STFSI)Li](5-2.0)	7.1	57.9	35.7	--
PEO-P[(STFSI)Li](5-1.1)	7.0	58.1	35.3	--
PEO-P[$(STFSI)_2$Mg](5-3.2)	8.1	57.2	-28.5	-39
PEO-P[$(STFSI)_2$Mg](5-2.0)	6.4	57.2	17.2	--
PEO-P[$(STFSI)_2$Mg](5-1.1)	7.2	57.9	23.9	--
PEO(5)	6.5	59.8	42.2	--

The results of the variable-temperature PEIS analysis of the PEO-P[(STFSI)Li] and PEO-P[$(STFSI)_2$Mg] single-ion conducting block copolymers are shown in Figure 5.2a, where ionic conductivity is plotted in Arrhenius fashion versus reciprocal temperature. Qualitatively, at temperatures above the melting point of PEO, all of the samples exhibit the modified Arrhenius (i.e. Vogel-Tamman-Fulcher, VTF) behavior typical of polymer electrolytes, wherein ion motion is linked to the dynamics of the solvating polymer chains[12]. At temperatures below the melting point of PEO, the crystallization of the PEO chains freezes the dynamics of most samples and causes a precipitous drop in ionic conductivity down to the limits of instrumental noise for the potentiostat. For clarity we omit the conductivity values from samples that have crystallized; however, the data from all temperatures can be found in Figure 5.S7 in the supporting information.

The first major takeaway from the conductivity data is that for all molecular weights, the lithiated samples exhibit ionic conductivities about an order of magnitude higher than their magnesiated counterparts. In principle, the differences in conductivity could be due to either a difference in the energetic barrier to ion motion (e.g. activation energy) or in the amount of effective charge carriers within the sample. To differentiate between these two potential causes, we fit the temperature-dependent data to the well-known VTF equation[12]:

$$\sigma(\mathrm{T}) = \frac{A}{\sqrt{\mathrm{T}}} e^{\left(-B/R[\mathrm{T}-(T_g-50)]\right)} \tag{5.1}$$

where A and B are fitting parameters relating the effective charge carrier concentration and pseudo-activation energy, respectively, and T_g is the glass transition temperature of the conducting polymer phase. As noted above, only PEO-P[(STFSI)Li](5-3.2) and PEO-P[$(STFSI)_2$Mg](5-3.2) exhibited T_g's in DSC. Therefore, the conductivity of the PEO-P[(STFSI)Li](5-3.2) and PEO-P[$(STFSI)_2$Mg](5-3.2) samples were fit with the VTF equation using A and B as adjustable parameters and the measured $T_{g,PEO}$ from DSC analysis (Table 5.2). To limit the number of adjustable parameters in our fits, B was held constant for the rest of the lithiated and magnesiated series (B_{Li} = 9.6 +/- 0.1 (kJ/mol) and B_{Mg} = 10.5 +/- 0.2 (kJ/mol)). By using a constant value for B, we assume that the activation barrier to ion hopping does not

change significantly with ion concentration in our samples, but rather the apparent activation barrier for ion conduction is only attenuated by differences in polymer dynamics (i.e. the T_g of the conducting phase). All fit parameters with their respective uncertainties are listed in Table 5.S3. We note that value of *B* determined for the lithiated and magnesiated versions of PEO-P(STFSI)(5-3.2) are similar, within 10%, and within the range typically observed for PEO-based polymer electrolytes with added salt[28,101]. The major cause of the difference in conductivity values observed for the PEO-P[(STFSI)Li] and PEO-P[$(STFSI)_2$Mg] is highlighted in Figure 5.2b, where *A* from VTF analysis is plotted versus the volume fraction of ion-containing block, ϕ_{PSTFSI}. In the case of the lithiated polymers, A_{Li} directly correlates with the total concentration of charge, as demonstrated by the linear fit through the origin in Figure 5.2b. The magnesiated polymers, however, have a more complex relationship between A_{Mg} and ϕ_{PSTFSI}, which we found to be best described by the quadratic fit through the origin shown in Figure 5.2b. Perhaps more importantly, comparing of the absolute values of A_{Li} and A_{Mg} reveals that in all cases, A_{Mg} is more than an order of magnitude lower than A_{Li}. Since it is generally believed that the VTF parameter *A* reflects the concentration of effective charge carriers[12], we conclude that the concentration of free magnesium ions in the PEO-P[$(STFSI)_2$Mg] samples is approximately an order of magnitude smaller than that of free lithium in the PEO-P[(STFSI)Li] samples. This behavior is consistent with the nature of the charged species; one expects less dissociation in systems with divalent cations such as Mg^{2+} when compared to monovalent cations such as Li^{+}. We note that further work is needed to establish the efficacy of Mg^{2+} transport in our polymers. For example, in addition to less dissociation, one may also expect a decrease is mobility of divalent cations due to their ability to bind two different polymer chains, thereby creating physical crosslinks. Furthermore, it is important to measure steady-state currents in symmetric Mg-polymer-Mg cells to ascertain that our electrolyte is a single-ion conductor. We note that such experiments are much more difficult than the analogous experiments on lithiated polymers[35–37] due to difficulties in reversible stripping and plating of magnesium[97,102,103].

While there is considerable data on conductivity of lithium single-ion conductors[35–37,104], to our knowledge, there are no studies reporting conductivity values for magnesium single-ion conductors. Most work in the development of Mg^{2+} electrolytes has focused on liquid systems[97,103,105], and many of the studies on polymer electrolytes have used divalent salts that do not solvate as readily as those composed of the bis(trifluoromethanesulfonyl)imide (TFSI) anion (e.g. $Mg(TFSI)_2$)[106–108]. The work of Lee and Allcock[109], wherein they directly compare the conductivities of electrolytes prepared from LiTFSI and $Mg(TFSI)_2$ with the same polymer, poly[bis(2-(2-methoxyethoxy)ethoxy)phosphazene] (MEEP) seems most relevant to this work. They observed similar conductivities between MEEP/LiTFSI and MEEP/$Mg(TFSI)_2$ samples, thus electrolytes composed of divalent cations do not have intrinsically lower conductivities than those composed of monovalent cations. Lee and Allcock hypothesized that the measured conductivities were due predominantly to anion motion, although they did not attempt to measure steady-state currents to prove that conjecture. In our case, anion motion is precluded, thus we attribute our observed conductivity values to the motion of Li^{+} and Mg^{2+}. We have not found any evidence that the motion of Mg^{2+} is intrinsically limited in this new class of single-ion conducting block copolymers.

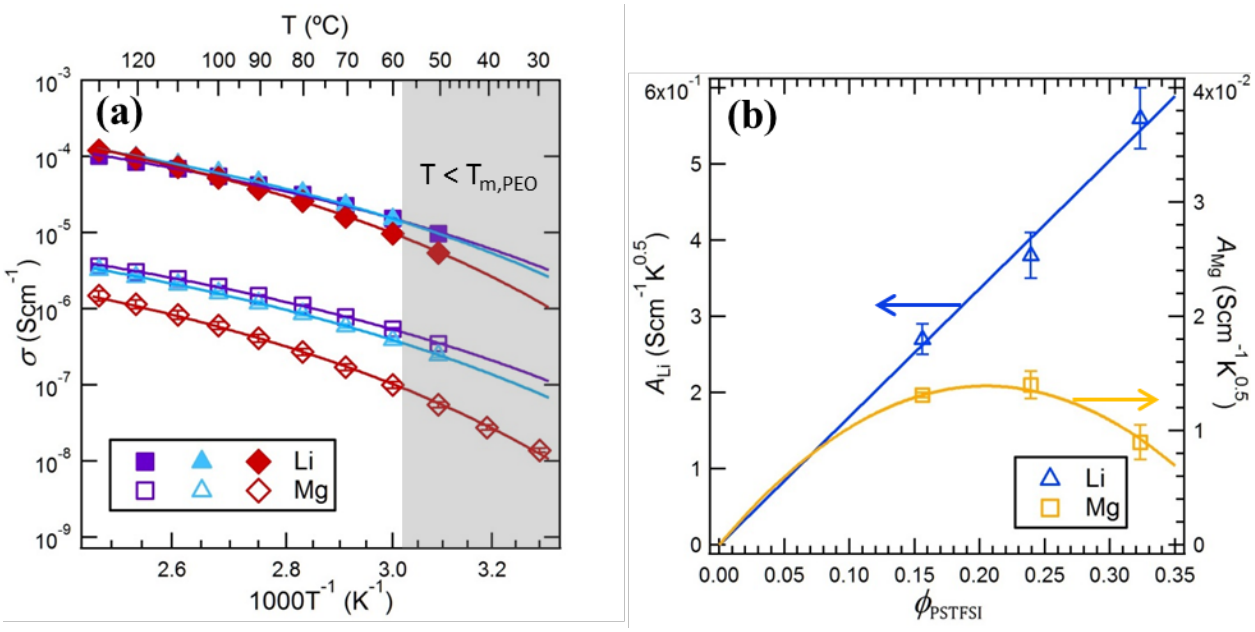

Figure 5.2: (a) Measured temperature-dependent ionic conductivity for all ion-containing block copolymer samples. Closed symbols correspond to Li^+ and open symbols correspond to Mg^{2+} with purple squares = PEO-P(STFSI)(5-1.1); cyan triangles = PEO-P(STFSI)(5-2.0); and red diamonds = PEO-P(STFSI)(5-3.2). Solid curves represent the non-linear least squares fits to Equation 5.1. The shaded region denotes temperatures below the melting point of PEO where crystallization is expected to occur. (b) The VTF fit coefficient *A*, reflecting the number of effective charge carriers per volume, plotted as a function of the volume fraction of ion-containing block for both the lithiated and magnesiated polymers. Error bars represent the uncertainty in the value for *A* from the least squares regression of the VTF fitting, and solid line/curve represent the least squares best fits to the data: $A_{Li} = 1.68\phi_{PSTFSI}$ and $A_{Mg} = 0.136\phi_{PSTFSI} - 0.33\phi_{PSTFSI}^2$.

Figure 5.3 shows the x-ray scattering profiles of both sets of polymers in absolute units, with the absolute scattering intensity of PEO(5) for reference at 90 °C (in the melt state). These profiles were obtained by combining the SAXS and WAXS data as described in the experimental section. The lack of scattering peaks in the SAXS profiles for PEO-P[(STFSI)Li] in Figure 5.3a is consistent with previous observations[36,37]. The SAXS profile of PEO-P[(STFSI)Li](5-3.2) contains a weak shoulder in the vicinity of q = 2.5 nm^{-1}. This may be due to the so-called ionomer peak[110], reflecting the presence of ionic domains with an average inter-domain spacing of ~2.5 nm. Determining the nature of these domains is beyond the scope of the present study. The SAXS profiles for PEO-P[$(STFSI)_2$Mg], on the other hand, contain a broad primary scattering peak. The lack of higher order peaks suggests that the primary scattering peak reflects disordered concentration fluctuations[65]. The position of the primary peak shifts to lower q-values as the P[$(STFSI)_2$Mg] block length increases, consistent with the theory of Leibler[65].

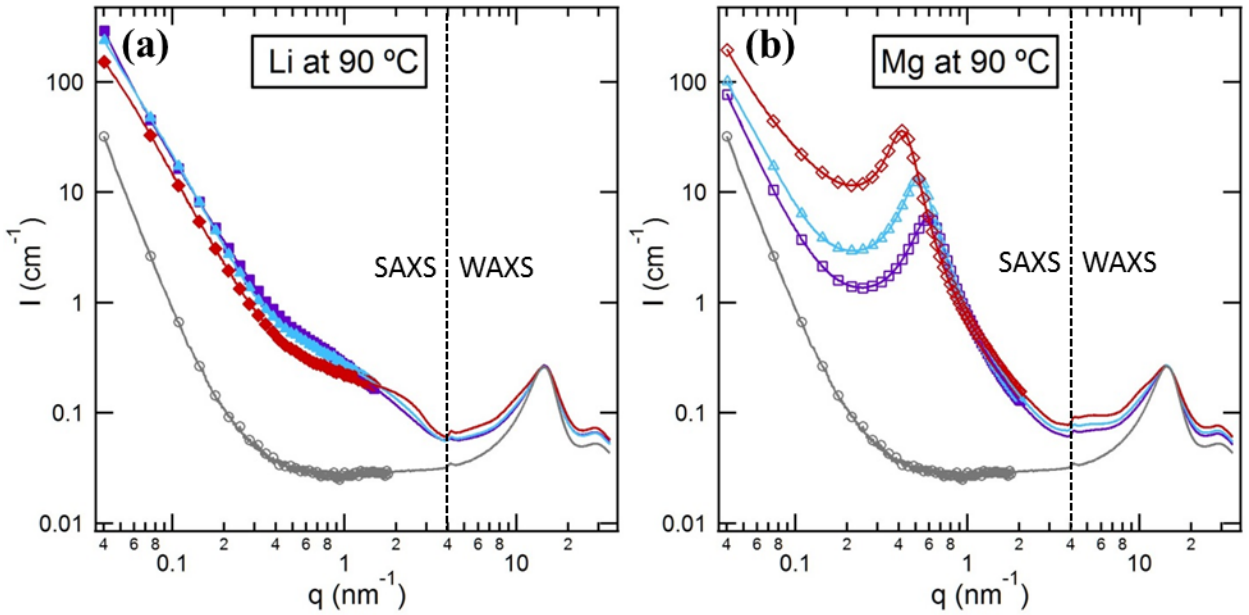

Figure 5.3: Combined SAXS/WAXS profiles for (a) PEO-P[(STFSI)Li] (closed symbols) and (b) PEO-P[(STFSI)$_2$Mg] (open symbols) samples after cooling from 130 °C down to 90 °C, scattering intensity, I, is plotted versus the magnitude of the scattering vector, q. Purple squares/curves = PEO-P(STFSI)(5-1.1); cyan triangles/curves = PEO-P(STFSI)(5-2.0); and red diamonds/curves = PEO-P(STFSI)(5-3.2). For clarity, SAXS data markers are only plotted for every 15th data point and WAXS data are represented by lines only. Scattering from PEO(5) is shown for reference (open grey circles/curves) on both plots. All intensities are presented on an absolute scale. The dashed vertical lines indicate our demarcation between the SAXS and WAXS scattering regimes, which we chose based on the intensity upturn from the first amorphous WAXS halo. The feature in the scattering data near q = 4 nm^{-1} is due to imperfect subtraction of the scattering from the kapton sample holder windows.

Theoretical predictions for scattering profiles from ion-containing block copolymers have not yet been proposed. Lacking a better alternative, we use the mean field theory of uncharged block copolymers proposed by Leibler[65] to analyze our scattering profiles. In Figure 5.4 we show least-squares fits of the well-known Leibler structure factor[65,111] modified to account for polymer chain length dispersity[69] for the magnesiated block copolymers. The fitted parameters for the magnesiated samples are the overall polymer radius of gyration (R_g), which is determined by the position of the scattering peak, and the Flory-Huggins interaction parameter (χ) between PEO and P(STFSI). Detailed information regarding the fitting procedure is provided in the supporting information (Section 5.7.7). As demonstrated in Figure 5.4, the Leibler structure factor provides a reasonable fit to the PEO-P[(STFSI)$_2$Mg] scattering . The excess scattering intensity for low q-values seen in the magnsiated block copolymer data in Figure 5.4 is similar to that observed in other ion-containing block copolymers[26,28,34]. Encouraged by the results from PEO-P[(STFSI)$_2$Mg], we also attempted to model the scattering from the PEO-P[(STFSI)Li]. The radius of gyration of the lithiated samples could not be determined from x-ray scattering due to the lack of a scattering peak. Lacking a better alternative, we used the radius of gyration (R_g) values determined from the matched PEO-P[(STFSI)$_2$Mg] sample for each lithiated sample. Thus the only adjustable parameter for the Leibler structure factor of the PEO-P[(STFSI)Li] samples was the Flory-Huggins interaction parameter (χ). The χ parameters reported here are based on a reference volume of 0.1 nm^3. All parameters obtained from the fits described here are given in Table 5.S4-Table 5.S6 in the supporting information.

The dependence of the Flory-Huggins interaction parameter on ϕ_{PSTFSI} for both lithiated and magnesiated block copolymers at 90 °C is shown in Figure 5.4d. In the case of magnesiated copolymers, χ is positive and decreases with increasing ϕ_{PSTFSI}. In contrast, χ values obtained from PEO-P[(STFSI)Li](5-2.0) and PEO-P[(STFSI)Li](5-3.2) are negative, i.e. no positive value of χ could suitably model the scattering from the PEO-P[(STFSI)Li](5-2.0) and PEO-P[(STFSI)Li](5-3.2) samples. The black dashed curves in Figure 5.4a-c indicate the predicted scattering for $\chi = 0$. The only lithiated sample with a positive χ is PEO-P[(STFSI)Li](5-1.1).

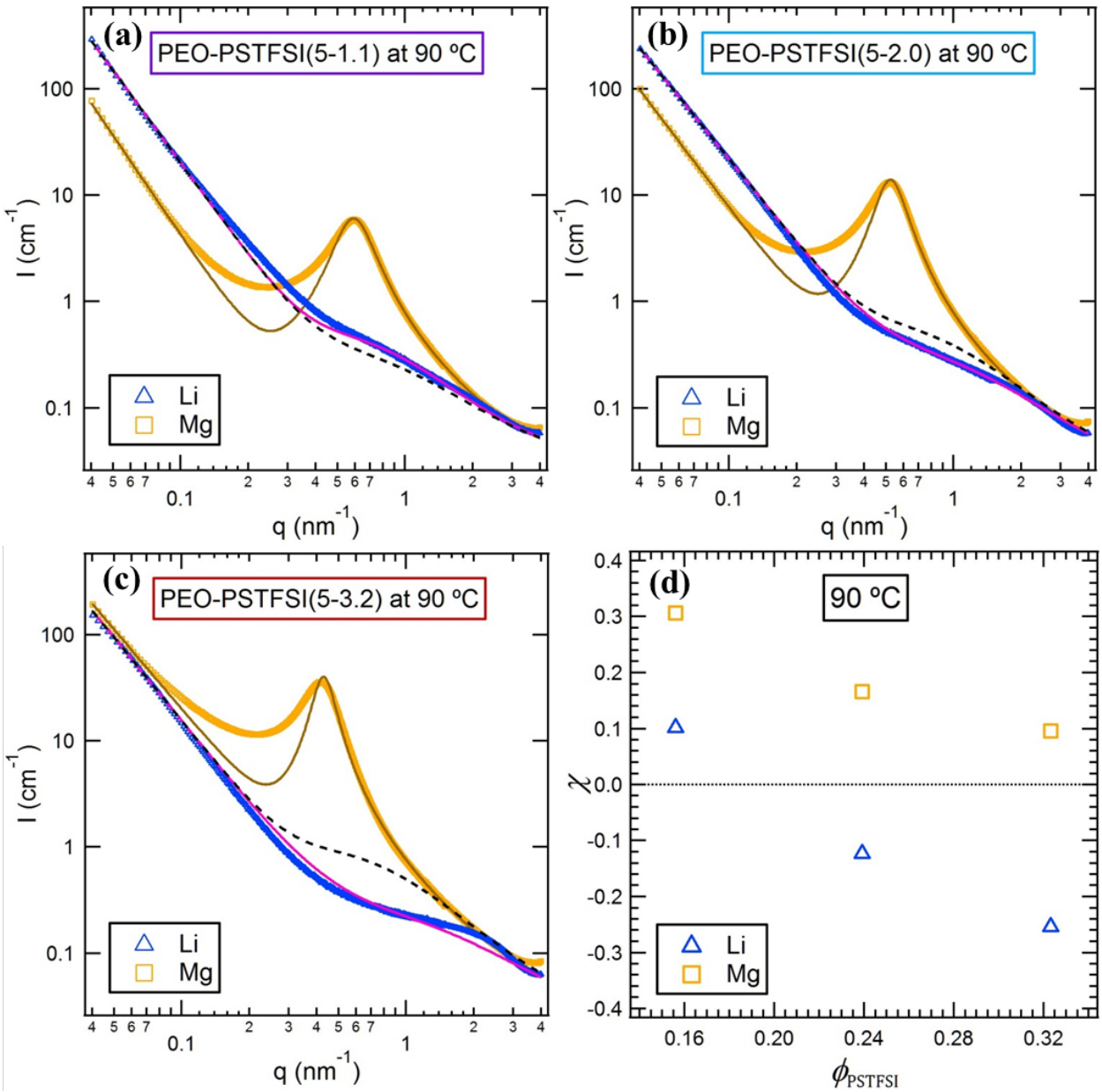

Figure 5.4: (a-c) Scattering intensity, *I*, versus magnitude of the scattering vector, q, of lithiated and magnesiated pairs at 90 °C. Experimental data were fit to Leibler's mean field theory to estimate the Flory-Huggins interaction parameter, χ. Experimental data: lithiated samples = blue triangles; magnesiated samples = gold squares (symbols overlap due to high resolution). Theoretical fits: lithiated samples = solid magenta curves; magnesiated sample = solid dark gold curves. The dashed black curves indicate the model prediction for $\chi = 0$. (d) The fitted χ-parameter

values used to model the data in (a-c) versus the volume fraction of ion-containing polymer block, ϕ_{PSTFSI}. Values for PEO-P[(STFSI)Li] samples (χ_{Li}) are indicated by blue triangles and those for PEO-P[$(STFSI)_2$Mg] (χ_{Mg}) are denoted by gold squares. The $\chi = 0$ axis value is denoted by a dashed line for reference.

The fitting procedure described above was applied to data obtained at 110 and 130 °C to determine the temperature dependence of χ_{Li} and χ_{Mg}. Figure 5.5a shows the result of this analysis in a plot of χ versus inverse temperature. The solid lines through each data set represent the linear least-squares fit to Equation 5.2 below

$$\chi(\mathrm{T}) = \alpha + \frac{\beta}{\mathrm{T}} \tag{5.2}$$

where α and β are the fit parameters. In Figure 5.5b, we plot α versus ϕ_{PSTFSI} for both PEO-P[(STFSI)Li] (α_{Li}) and PEO-P[$(STFSI)_2$Mg] (α_{Mg}) samples. α_{Li} and α_{Mg} have qualitatively opposite trends: α_{Li} increases with increasing ϕ_{PSTFSI} while α_{Mg} decreases with increasing ϕ_{PSTFSI}. In Figure 5.5c, we plot β versus ϕ_{PSTFSI} for both sets of PEO-P[(STFSI)Li] (β_{Li}) and PEO-P[$(STFSI)_2$Mg] (β_{Mg}) samples. β_{Li} is negative and decreases with increasing ϕ_{PSTFSI}. In contrast, the β_{Mg} values are negligibly small and essentially independent of ϕ_{PSTFSI}.

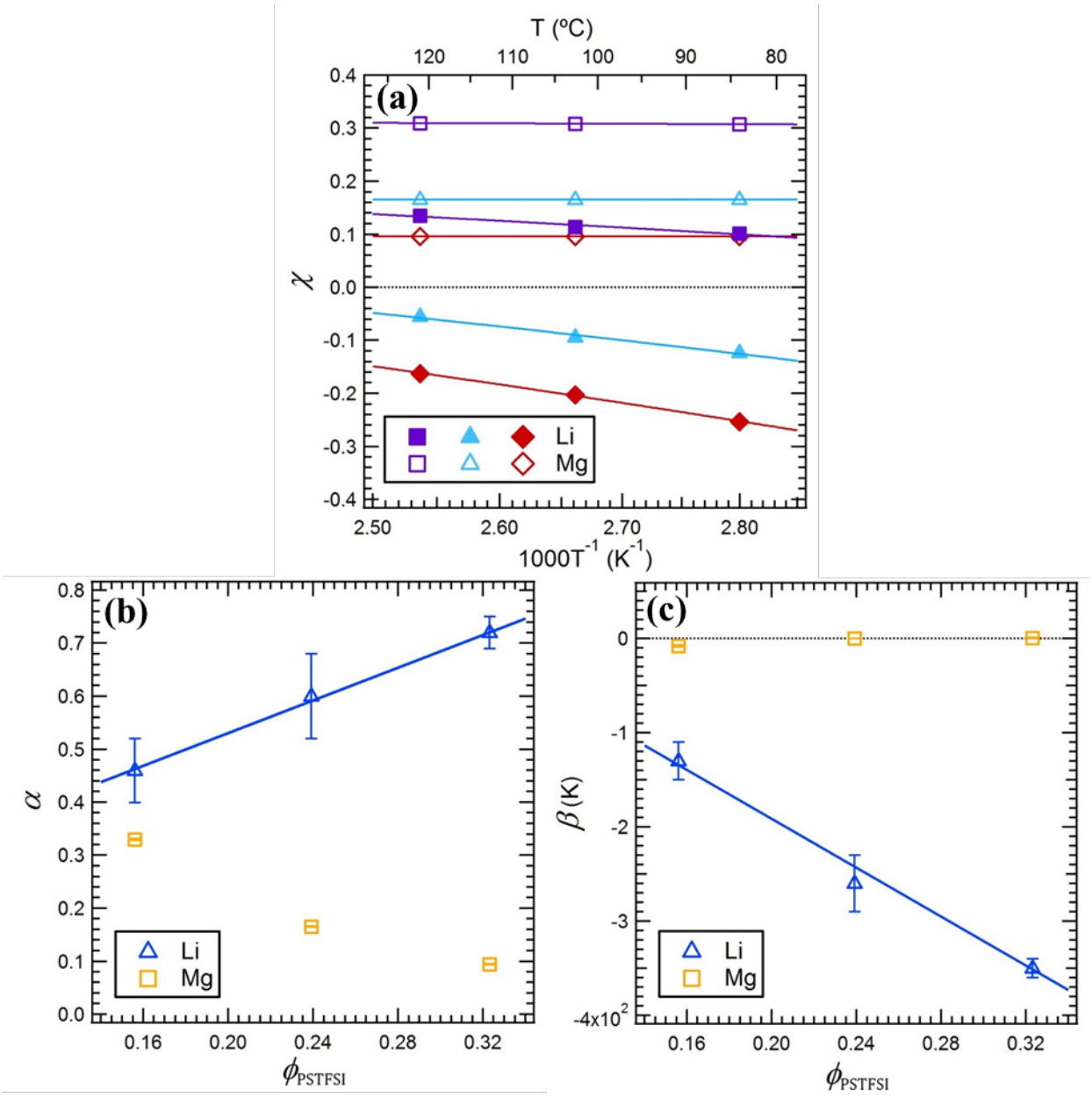

Figure 5.5: (a) Flory-Huggins interaction parameter, χ, determined by fitting SAXS data versus reciprocal temperature. Closed symbols correspond to Li samples and open symbols correspond to Mg samples, with purple squares = PEO-P(STFSI)(5-1.1); cyan triangles = PEO-P(STFSI)(5-2.0); and red diamonds = PEO-P(STFSI)(5-3.2). Solid lines indicate the linear least squares fits to Equation 5.2. Dotted line indicates $\chi = 0$. (b) The fitting constant (α) from Equation 5.2 determined from the linear fits in (a) plotted versus volume fraction of the ion-containing block, ϕ_{PSTFSI}. Values for PEO-P[(STFSI)Li] samples (α_{Li}) are indicated by blue triangles and those for PEO-P[(STFSI)$_2$Mg] (α_{Mg}) are denoted by gold squares. (c) The fitting constant (β) from Equation 5.2 determined from the linear fits in (a) plotted versus ϕ_{PSTFSI}. Values for PEO-P[(STFSI)Li] samples (β_{Li}) are indicated by blue triangles and those for PEO-P[(STFSI)$_2$Mg] (β_{Mg}) are denoted by gold squares. Error bars in (b-c) represent the fitting error in the parameters and solid lines through the α_{Li} and β_{Li} data indicate the linear least square fits: $\alpha_{Li} = 0.2 + 1.5\phi_{PSTFSI}$ and $\beta_{Li} = 70 - 1.3 \times 10^3 \phi_{PSTFSI}$. The dotted line in (c) indicates $\beta = 0$.

In Figure 5.6, we plot β obtained from analysis of the SAXS data versus A obtained from analysis of the PEIS data. It is evident that β and A are correlated, suggesting a relationship

between ion dissociation and self-assembly. In the case of PEO-P[(STFSI)$_2$Mg] samples where little ion-dissociation occurs, the polymer morphology resembles that of a typical disordered diblock copolymer, with concentration fluctuations on length-scales on the order of the radius of gyration of the polymer chains. In the case of PEO-P[(STFSI)Li], on the other hand, dissociation of the lithium ions suppresses concentration fluctuations. Figure 5.6 provides evidence for the fact that dissociated lithium ions induce mixing of PEO and P(STFSI)Li blocks due to favorable interactions between the ions and PEO.

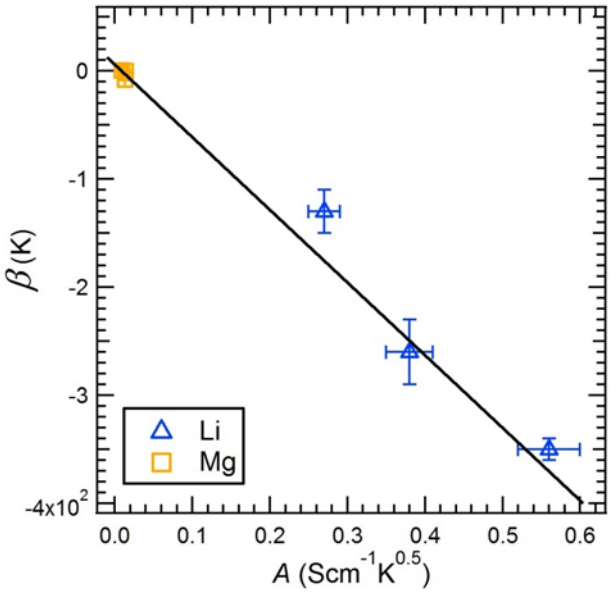

Figure 5.6: Parameter β, which quantifies the temperature-dependence χ ($\chi(T) = \alpha + \frac{\beta}{T}$), plotted as a function of the VTF parameter related to the effective charge carrier concentration (A) for all samples. Error bars represent the fitting uncertainty for each parameter and the solid line is the best fit to the data accounting for the errors in both axes: $\beta = -670A + 5.9$.

5.4 Conclusion

In the pursuit of developing high energy-density batteries with metallic anodes, single-ion conducting block copolymers represent an exciting class of materials that has demonstrated improvements in battery performance.[35] In this work, we report on the synthesis of a matched set of lithiated and magnesiated single-ion conducting block copolymers, PEO-P[(STFSI)Li] and PEO-P[(STFSI)$_2$Mg]. The melt morphology of the block copolymers was studied by X-ray scattering, and temperature dependence of ionic conductivity was determined by PEIS experiments. The effective Flory-Huggins interaction parameter (χ) for PEO/P[(STFSI)Li] and PEO/P[(STFSI)$_2$Mg] was estimated by analyzing the X-ray scattering data using the mean-field theory of Leibler. The VTF equation was used to analyze the conductivity data. We demonstrate a linear relationship between the parameter β that characterizes the temperature dependence of χ and the VTF parameter A, which reflects the concentration of effective charge carriers. We thus demonstrate that block copolymer polymer self-assembly is coupled to ion dissociation.

There is great interest in using microphase separated block copolymers as electrolytes due to their ability to decouple electrical and mechanical properties.[19,22] In these systems, the microphase separation is driven by thermodynamic incompatibility between the polymer blocks, quantified by the product χN. For example, in the case of symmetric block copolymers, microphase separation will occur if χN exceeds 10.5.[65] For the copolymers used in this study, microphase separation is predicted to occur if χN exceeds values ranging from 11 to 30, depending on ϕ_{PSTFSI}. While the χ-values determined for the magnesiated samples suggest that microphase separation might occur at larger chain lengths (i.e. larger *N*) than those used in this study, the values of χ determined for lithiated samples are negative in most cases. We thus predict that PEO-P[(STFSI)Li] will be homogeneous (i.e. not microphase separated), regardless of chain length. (Crystallization of the PEO block can lead to microphase separation in these systems[36,37], but this phenomenon is not of interest in this study because crystalline PEO is essentially non-conducting). We have shown that microphase separation only occurs in the absence of ion dissociation. Thus, while we may be able to obtain microphase separated PEO-P[$(STFSI)_2Mg$] samples, the ionic conductivity of these samples is likely to be very low. To obtain mechanically rigid single-ion conducting block copolymers, it will be necessary to synthesize ABC triblock polymers with an additional incompatible C-block to provide mechanical support (e.g. PEO-P[(STFSI)Li]-PS).

5.5 Acknowledgements

This work was supported by the Joint Center for Energy Storage Research, an Energy Innovation Hub funded by the U.S. Department of Energy (DOE), Office of Science, Basic Energy Sciences (BES). Thermal analysis was performed at the Molecular Foundry at Lawrence Berkeley National Laboratory. X-ray scattering experiments were performed at Lawrence Berkeley National Laboratory's Advance Light Source, Beamline 7.3.3. The Molecular Foundry and Beamline 7.3.3 of the Advanced Light Source are supported by the Director of the Office of Science, Office of Basic Energy Sciences, of the U.S. Department of Energy under Contract No. DE-AC02-05CH11231. We thank Polite Stewart, Chenhui Zhu, and Eric Schaible for their assistance with the setup and operation of Beamline 7.3.3, as well as Hilda Buss for her assistance with the NMR analysis of the single-ion conducting block copolymers.

5.6 Nomenclature

5.6.1 Abbreviations

AgB	Silver Behenate
DSC	Differential Scanning Calorimetry
EO	Ethylene Oxide
^{1}H NMR	Proton Nuclear Magnetic Resonance
INAA	Instrumental Neutron Activation Analysis
MEEP	poly[bis(2-(2-methoxyethoxy)ethoxy)phosphazene]
PEIS	Potentiostatic Electrochemical Impedance Spectroscopy
PEO	Poly(ethylene oxide)
PEO-P[(STFSI)Li]	Poly(ethylene oxide)-*b*-poly[(styrene-4-sulfonyltrifluoromethylsulfonyl)imide lithium]

PEO-P[(STFSI)$_2$Mg]	Poly(ethylene oxide)-*b*-poly[(styrene-4-sulfonyltrifluoromethylsulfonyl)imide magnesium]
P(STFSI)	poly[(styrene-4-sulfonyltrifluoromethylsulfonyl)imide] – unspecified ion
PS	Polystyrene
S-D	Sample to Detector Distance
SAXS	Small Angle X-ray Scattering
TFSI	bis(trifluoromethanesulfonyl)imide
VTF	Vogel-Tamman-Fulcher
WAXS	Wide Angle X-Ray Scattering

5.6.2 Symbols

A	Effective charge carrier concentration (from VTF fit), Scm^{-1}K$^{0.5}$
A_s	Conductivity sample electrode area, cm^2
B	Effective activation barrier (from VTF fit), kJmol^{-1}
I	Scattering intensity, cm^{-1}
L	Conductivity sample thickness, cm
$M_{n,PEO}$	Number average molecular weight of PEO block, kg mol^{-1}
$M_{n,PSTFSI}$	Number average molecular weight of P(STFSI) block, kg mol^{-1}
N_{PEO}	Number average degree of polymerization of PEO block, -
N_{PSTFSI}	Number average degree of polymerization of P(STFSI) block, -
q	Magnitude of the scattering vector, nm^{-1}
R	Gas constant, kJmol^{-1}K^{-1}
R_g	Radius of gyration, nm
T	Temperature, K
T_g	Glass transition temperature, K
$T_{m,PEO}$	Melting temperature of PEO, K
Z_{Re}	Real component of conductivity sample impedance, Ω

5.6.3 Greek

α	Temperature-independent contribution to the interaction parameter, -
β	Temperature-dependent contribution to the interaction parameter, K
χ	Monomer-monomer interaction parameter, -
ϕ_{PSTFSI}	Volume fraction of the P(STFSI) block, -
λ	Scattering wavelength, nm
ρ_{PSTFSI}	Density of poly[(styrene-4-sulfonyltrifluoromethylsulfonyl)imide], gcm^{-3}
θ	Scattering angle, rad
σ	Ionic conductivity, Scm^{-1}

5.7 Supporting Information

5.7.1 Gel Permeation Chromatography

Gel permeation chromatography (GPC) was performed on the ion-containing block copolymers as well as the PEO macro-initiator. The GPC configuration used was the same as described previously[36] with the solvent being a mixture of acetonitrile and water. Figure 5.S1 demonstrates the shift in the PEO(5)-Blocbuiler MA macro-initiator peak upon polymerization

of the ion-containing block to form the single-ion conducting diblock copolymer. The peak located at 19 mL is due to PEO(5) homopolymer that was not functionalized with the Blocbuilder MA initiator; upon functionalization with Blocbuilder MA, PEO(5) elutes at the lower volume of 17.5 mL. We attribute this shift to specific interactions between the Blocbuilder molecules and the GPC column. The weak peak at 19mL indicates that a small amount of PEO(5) homopolymer impurity remains in all samples.

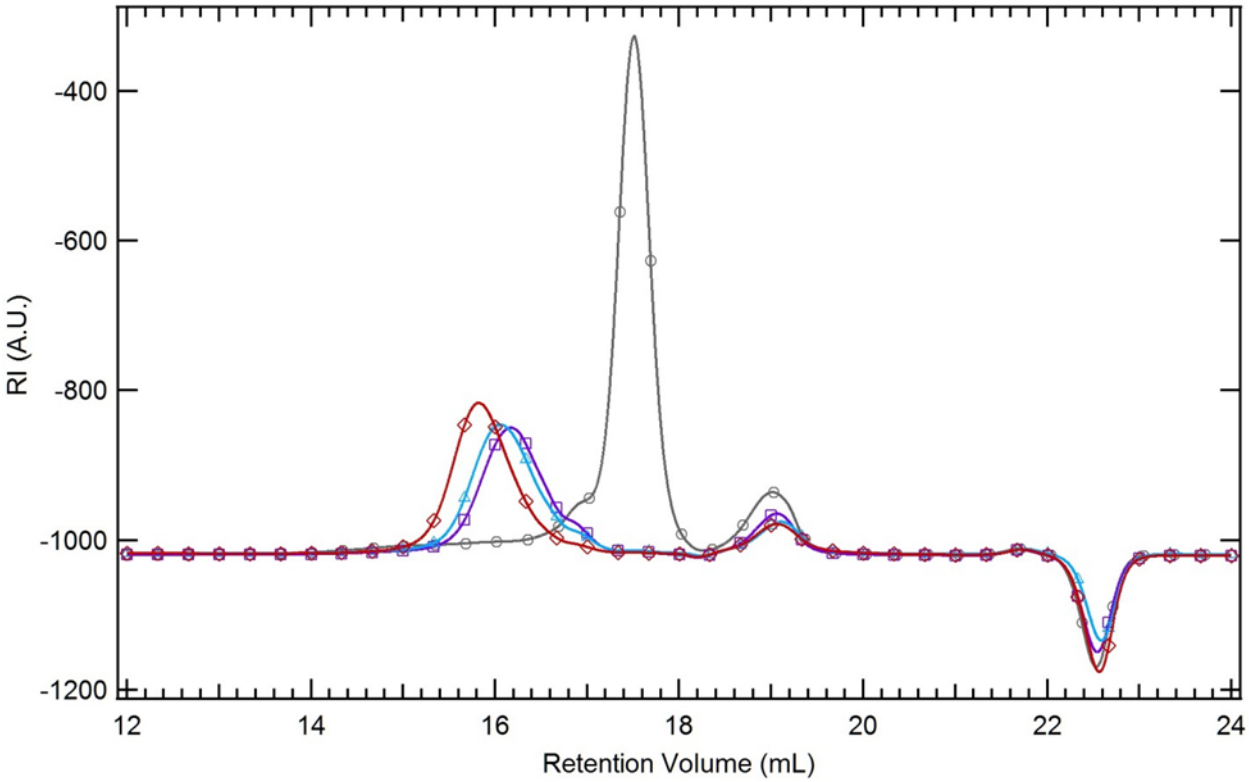

Figure 5.S1: Chromatograms of PEO(5)-Blocbuiler MA macro-initiator (grey circles/lines), PEO-P(STFSI)(5-1.1) (purple squares/lines), PEO-P(STFSI)(5-2.0) (cyan triangles/lines), and PEO-P(STFSI)(5-3.2) (red diamonds/lines). Data markers are plotted every 200 data points.

5.7.2 Nuclear Magnetic Resonance Spectroscopy

^{1}H nuclear magnetic resonance (NMR) was performed on the ion-containing diblock copolymers to determine the number average degree of polymerization of the ion-containing block. The spectra contribution from the phenyl protons on the ion-containing block was determined by integrating the broad peaks between 6-9 ppm ($^1H_{ph}$). The contributions from the ethylene oxide protons, as well as the methoxy endgroup of the PEO chains were determined by peak fitting the entire spectra between 1-4.6ppm, and selecting the peaks at 3.53 ($^1H_{EO}$) and 3.26 ($^1H_{MeO}$). Finally, the contribution from the carboxylic acid of the blocboulder MA endgroup was determined by integrating the peak near 12ppm between 11-13ppm ($^1H_{COOH}$). The spectra of all three block copolymer molecular weights are superimposed in Figure 5.S2, with insets highlighting each region of interest. The peak areas from integration and fitting are provided in Table 5.S1 along with the calculations of the degree of polymerization of the PEO macro-initiator determined through end group analysis ($N_{EO/MeO}$). The degree of polymerization of P(STFSI) determined through endgroup analysis from the methoxy ($N_{PSTFSI/MeO}$) and carboxylic

acid endgroups ($N_{PSTFSI/COOH}$), as well as through the ratio PEO backbone protons ($N_{PSTFSI/EO}$). The degree of polymerization of P(STFSI) determined through endgroup analysis from the methoxy endgroups ($N_{PSTFSI/MeO}$) is reported in the main text and is used for subsequent analysis.

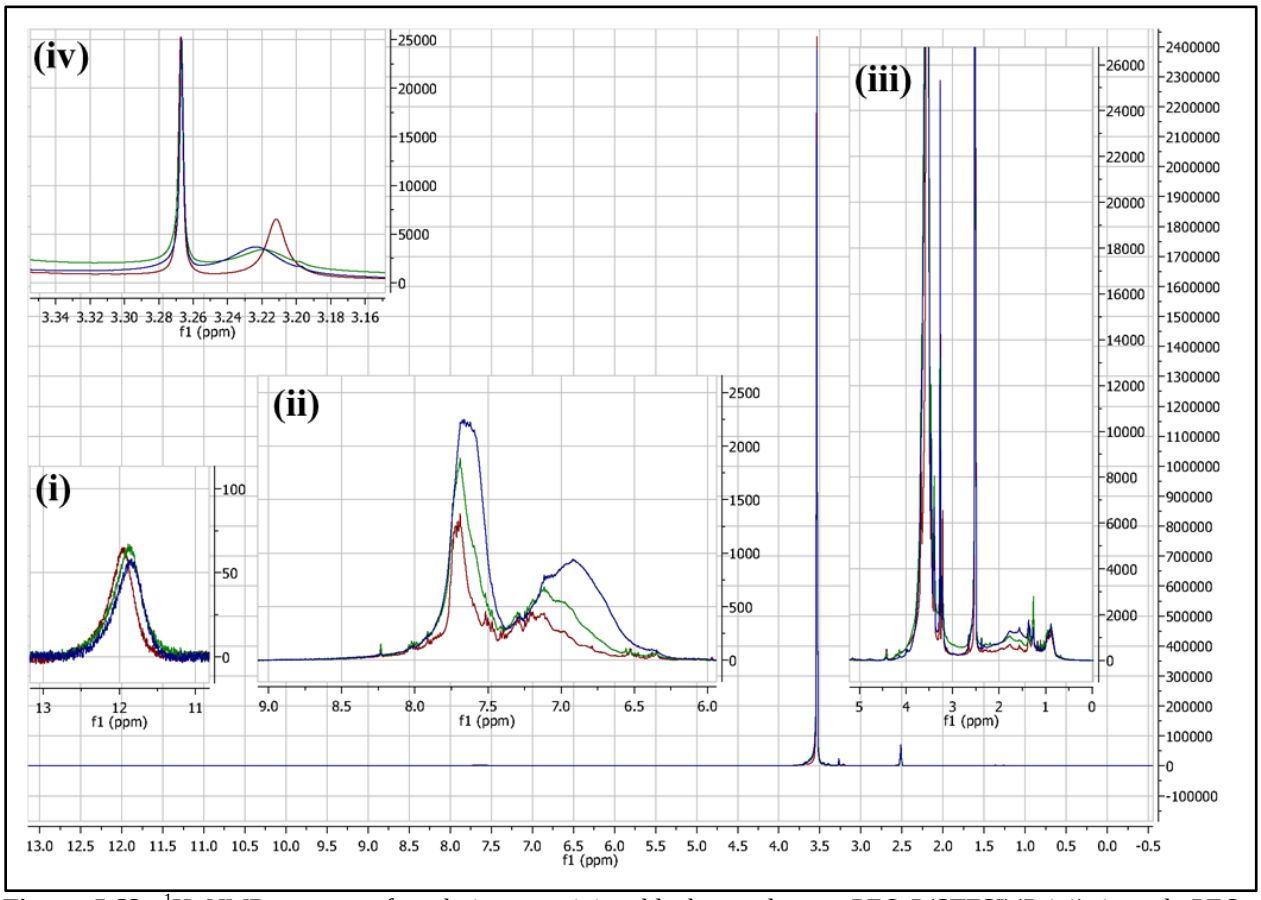

Figure 5.S2: ^{1}H NMR spectra of each ion-containing block copolymer: PEO-P(STFSI)(5-1.1) in red, PEO-P(STFSI)(5-2.0) in green, and PEO-P(STFSI)(5-3.2) in blue. (i) inset magnifying the carboxylic acid endgroup peak. (ii) inset magnifying the styrenic proton peaks. (iii) inset showing the region which was fit to extract the EO proton and methoxy endgroup proton peaks. (iv) Inset magnifying the methoxy endgroup peak.

Table 5.S1: Results from NMR analysis of the ion-containing block copolymers.

Sample Name	$^{1}H_{Ph}$ ($x10^{-6}$)	$^{1}H_{EO}$ ($x10^{-7}$)	$^{1}H_{MeO}$ ($x10^{-5}$)	$^{1}H_{COOH}$ ($x10^{-5}$)	$N_{EO/MeO}$	$N_{PSTFSI/EO}$	$N_{PSTFSI/MeO}$	$N_{PSTFSI/COOH}$
PEO-P(STFSI)(5-3.2)	5.238	6.186	3.953	1.146	117.4	9.6	9.9	11.4
PEO-P(STFSI)(5-2.0)	3.438	6.847	4.159	1.433	123.5	5.7	6.2	6.0
PEO-P(STFSI)(5-1.1)	2.153	7.859	4.943	1.190	119.2	3.1	3.3	4.5

5.7.3 Elemental Analysis

Instrumental Neutron Activation Analysis from performed by Elemental Analysis Inc. on the magnesiated ion-containing block copolymers. The fluorine (F), magnesium (Mg), chlorine (Cl), and potassium (K) nuclei were probed. Based on the chemical structure of the PTFSI polymer backbone, we anticipate 6 F nuclei for every 1 Mg nucleus in order to maintain charge electroneutrality; however, in all cases we observe an excess of Mg. Cl could in principle supply

the additional negative charges to balance the excess of Mg, however, the INAA analysis indicates that there is not a sufficient amount present within the samples. To gain more clarity, we calculate the apparent net charge within the samples, and then normalize the net charge by the total expected charge of the polymer backbone from the F nuclei (net charge per chain). We find that on average there is an excess of 2^+ charge per chain, or one additional Mg nuclei per chain (Table 5.S2). Although we have not completely confirmed the cause of this discrepancy, we suggest that the carboxylic acid proton from the blocbuilder MA endgroup could be ion-exchanged with magnesium to account for one of the excess charges. It remains unclear what balances the second charge.

Table 5.S2: Results from the INAA of the magnesiated ion-containing block copolymers.

Sample Name	F (ppm)	Mg (ppm)	Cl (ppm)	K (ppm)	Net Charge (ppm)	Net Charge (Chain^{-1})	Excess Mg (Atom Chain^{-1})
PEO-P[(STFSI)$_2$Mg](5-3.2)	2389	471	3	< 20	163	2.03	1.01
PEO-P[(STFSI)$_2$Mg](5-2.0)	1579	335	1	< 14	157	1.85	0.92
PEO-P[(STFSI)$_2$Mg](5-1.1)	1079	284	2	< 14	221	2.01	1.00

5.7.4 Thermal Analysis

The differential scanning calorimetry (DSC) measurements were performed as follows. The samples were loaded into the DSC and equilibrated at 30 °C, then a heat scan of 5 °C/min was used to reach 130 °C. PEO melting temperature ($T_{m,PEO}$) was extracted from this scan. Samples were then held isothermally for 20 minutes in order to let them equilibrate. Next, the samples were equilibrated directly to -80 °C and heated at 10 °C/min back up to 130 °C. If observed, the T_g of PEO ($T_{g,PEO}$) was determined from this scan using the inflection point of the change in slope with "Glass/Step Transition" function in the TA Universal Analysis software package. Finally, a controlled cooling scan of 5 °C/min from 130 °C down to 0, -20, or -80 °C was used to determine the crystallization point of PEO ($T_{c,PEO}$). The data from each scan are shown in Figure 5.S3-Figure 5.S5 below.

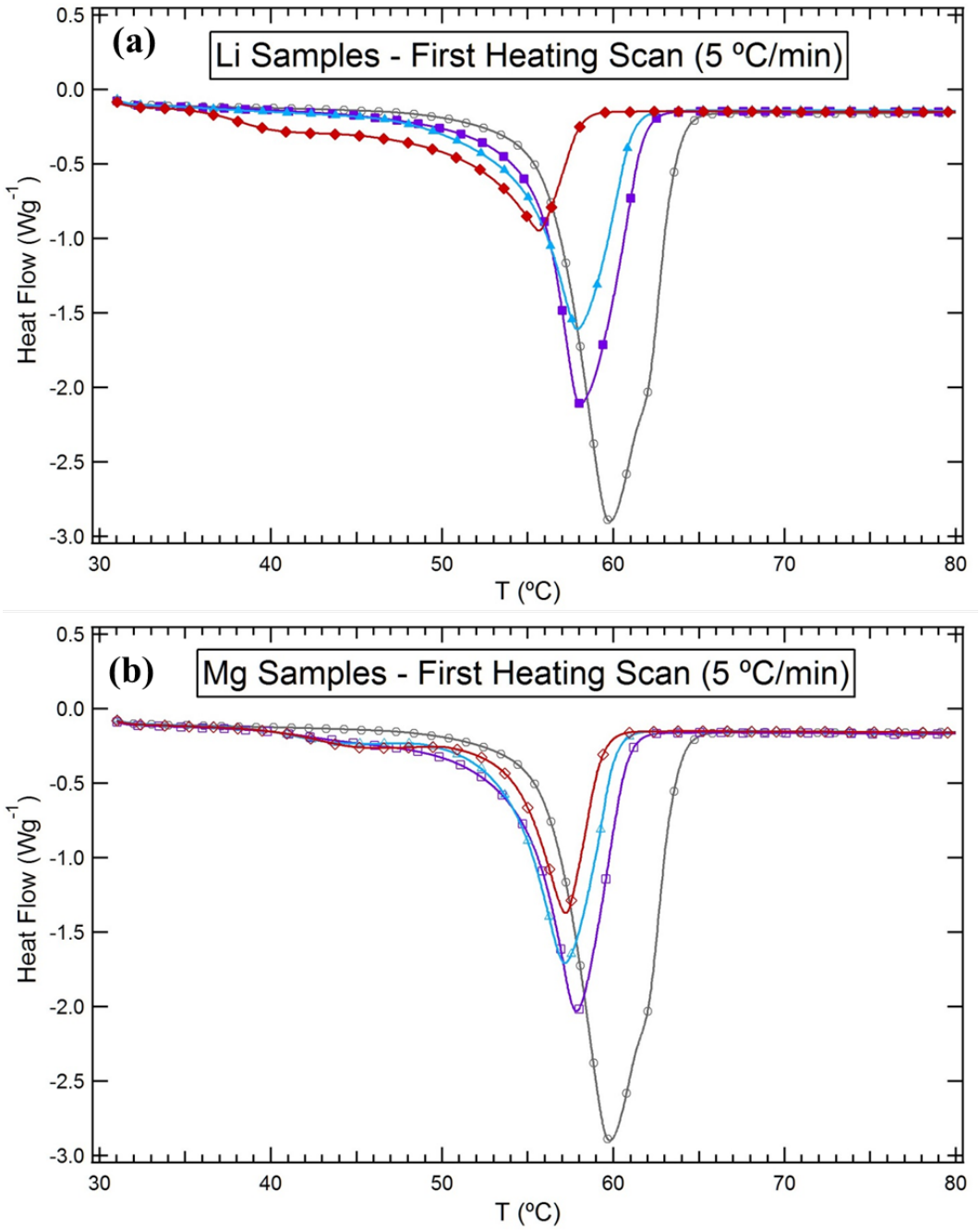

Figure 5.S3: First heating thermograms of the samples after controlled thermal pretreatment. (a) Lithiated samples: PEO-P[(STFSI)Li](5-1.1) filled purple squares, PEO-P[(STFSI)Li](5-2.0) filled cyan triangles, PEO-P[(STFSI)Li](5-3.2) filled red diamonds, and PEO(5) open grey circles. (b) Magnesiated samples: PEO-P[$(STFSI)_2$Mg](5-1.1) open purple squares, PEO-P[$(STFSI)_2$Mg](5-2.0) open cyan triangles, PEO-P[$(STFSI)_2$Mg](5-3.2) open red diamonds, and PEO(5) open grey circles. Exotherms are up and data markers are plotted every 50^{th} data point.

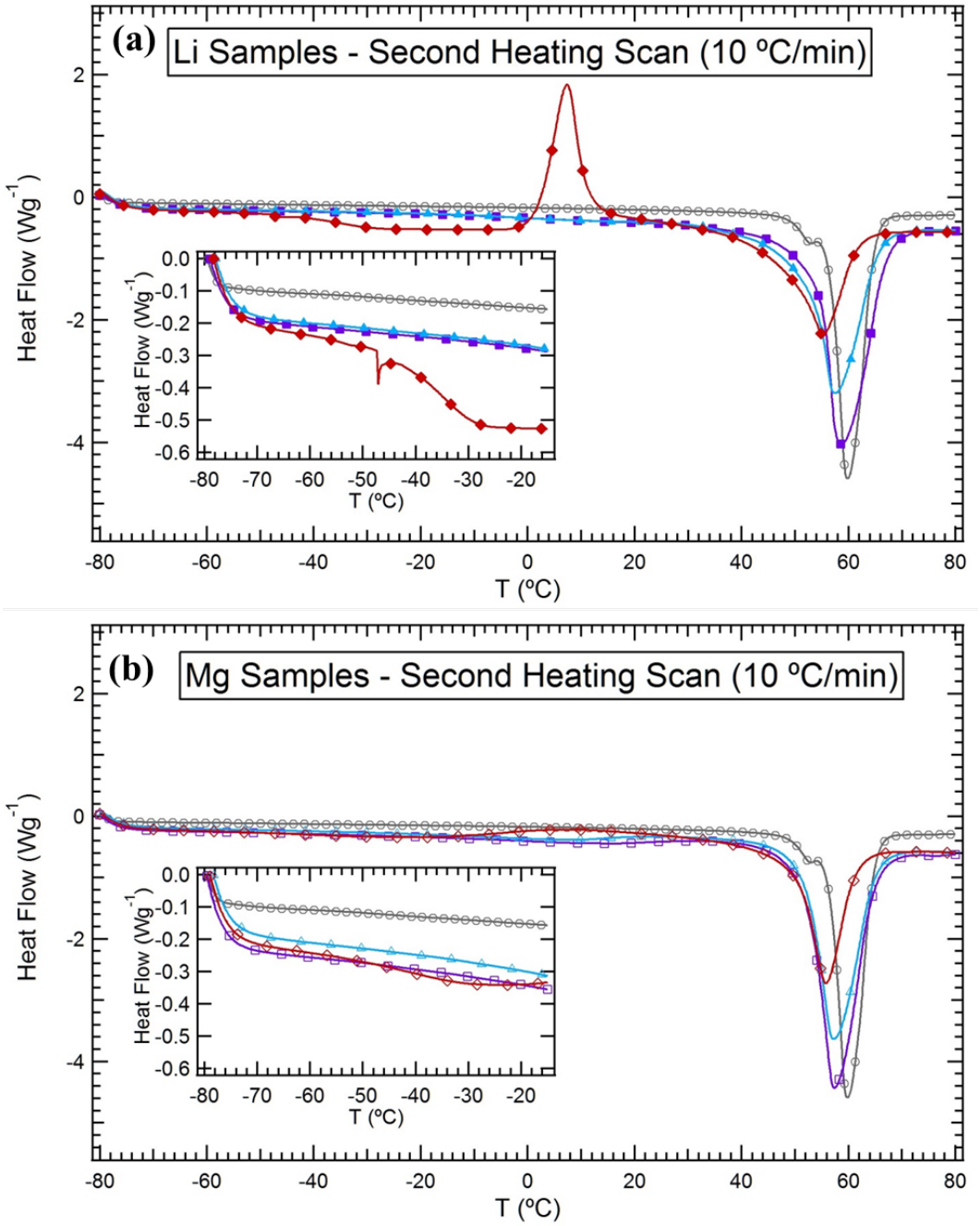

Figure 5.S4: Second heating thermograms of the samples after quenching to -80 °C. (a) Lithiated samples: PEO-P[(STFSI)Li](5-1.1) filled purple squares, PEO-P[(STFSI)Li](5-2.0) filled cyan triangles, PEO-P[(STFSI)Li](5-3.2) filled red diamonds, and PEO(5) open grey circles. (b) Magnesiated samples: PEO-P[$(STFSI)_2$Mg](5-1.1) open purple squares, PEO-P[$(STFSI)_2$Mg](5-2.0) open cyan triangles, PEO-P[$(STFSI)_2$Mg](5-3.2) open red diamonds, and PEO(5) open grey circles. Exotherms are up and data markers are plotted every 50th data point.

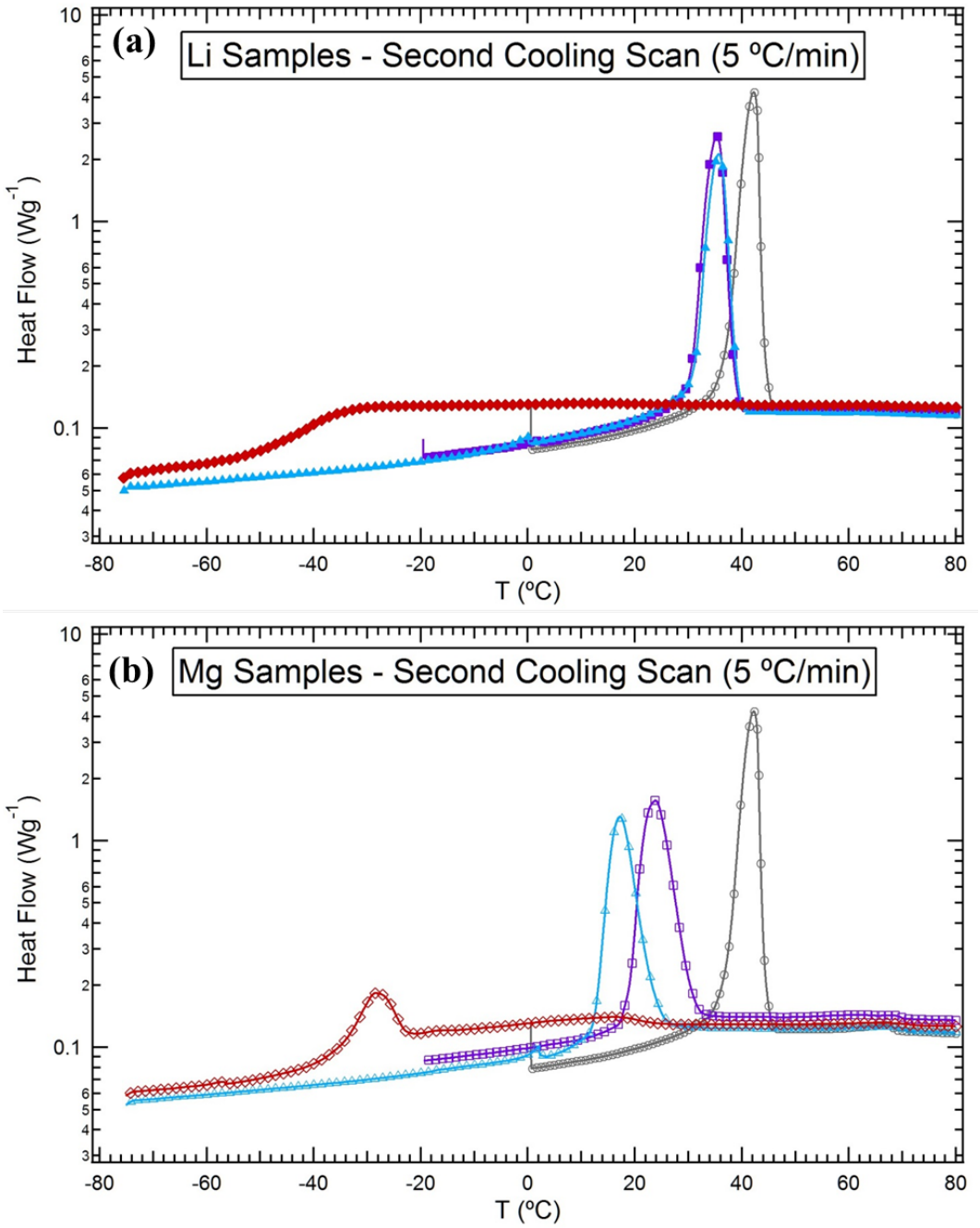

Figure 5.S5: Controlled second cooling scan. (a) Lithiated samples: PEO-P[(STFSI)Li](5-1.1) filled purple squares, PEO-P[(STFSI)Li](5-2.0) filled cyan triangles, PEO-P[(STFSI)Li](5-3.2) filled red diamonds, and PEO(5) open grey circles. (b) Magnesiated samples: PEO-P[$(STFSI)_2$Mg](5-1.1) open purple squares, PEO-P[$(STFSI)_2$Mg](5-2.0) open cyan triangles, PEO-P[$(STFSI)_2$Mg](5-3.2) open red diamonds, and PEO(5) open grey circles. Exotherms are up and data markers are plotted every 50^{th} data point.

5.7.5 SAXS/WAXS Temperature Stage Calibration

A temperature calibration dummy SAXS/WAXS sample was prepared in a manner identical to the samples described in the main text; however, a small thermocouple was imbedded in the polymer before the holder was sealed up. No scattering data was recorded from this sample. The polymer temperature within the dummy sample at a number of different stage setpoint temperatures along with a linear regression analysis are provided in Figure 5.S6 below. This regression was used to determine the actual sample temperatures from the X-ray scattering experiments.

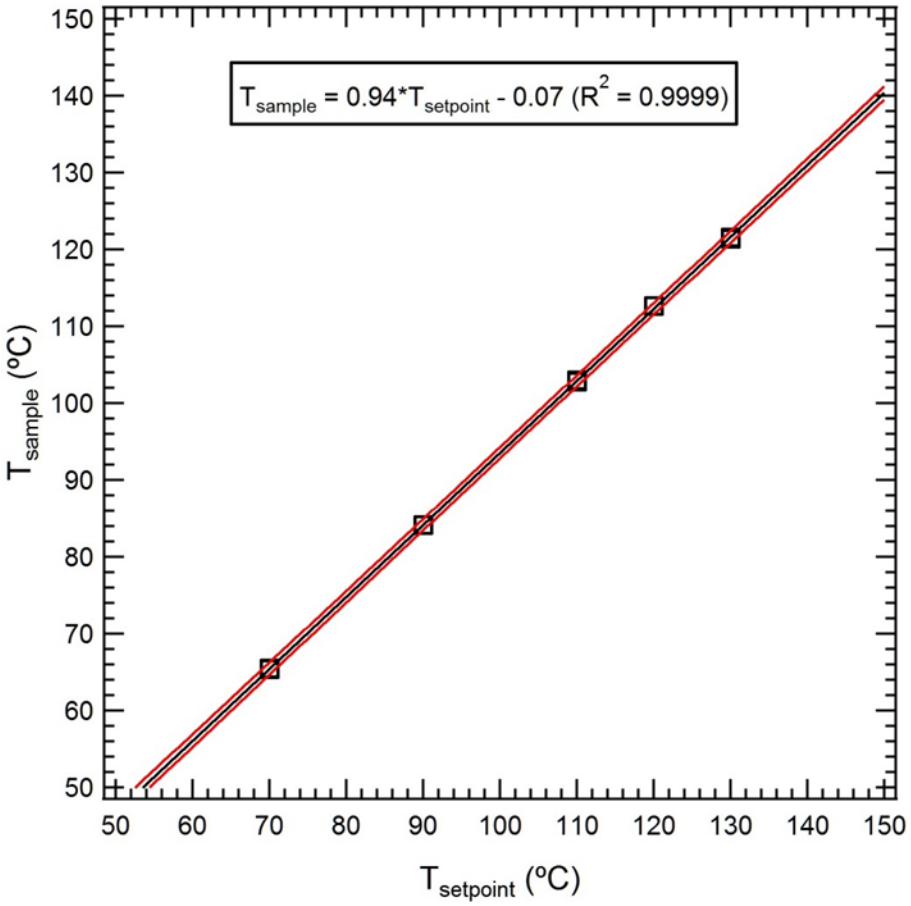

Figure 5.S6: Results from the temperature calibration dummy sample. Data are plotted as open squares, the black line indicates the linear best fit to the data (equation provided on plot), and the red lines indicate the 99% prediction interval based upon the regression analysis. We note that the data shown are from both heating and cooling; however they superimpose perfectly and cannot be distinguished.

5.7.6 Electrochemical Analysis

The ionic conductivity values for all single-ion conducting polymers are provided in Figure 5.S7 below. As described in the main text, the ionic conductivity versus temperature data was fit with the VTF equation to decouple the charge carrier concentration and energetic activation barrier contributions. The fitted parameters are listed in Table 5.S3 below.

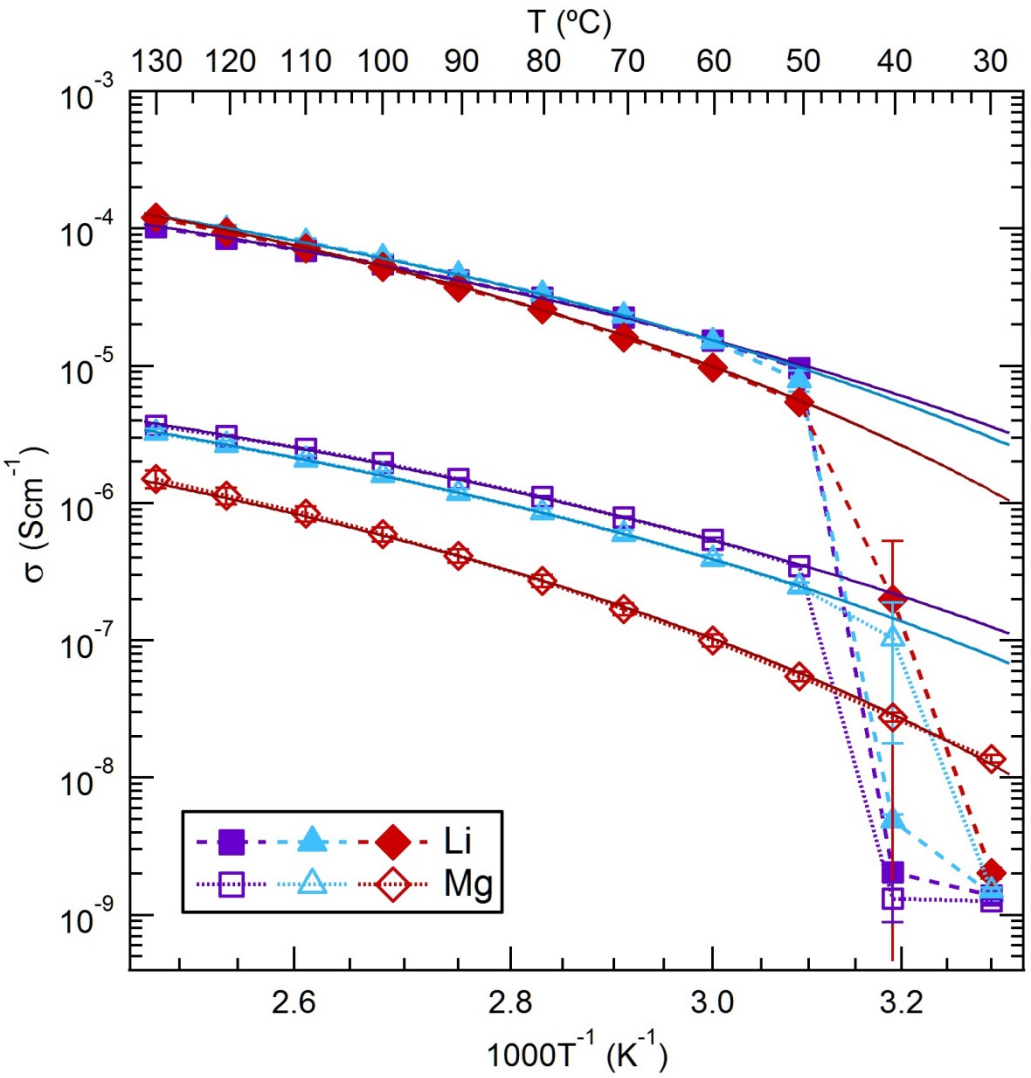

Figure 5.S7: Measured temperature-dependent ionic conductivity for all ion-containing block copolymer samples. Closed symbols correspond to Li^+ and open symbols correspond to Mg^{2+} with purple squares = PEO-P(STFSI)(5-1.1); cyan triangles = PEO-P(STFSI)(5-2.0); and red diamonds = PEO-P(STFSI)(5-3.2). Solid lines represent the non-linear least squares best fit to the VTF equation. In most cases, error bars, which represent the standard deviation from 3 replicate samples, are smaller than the data markers.

Table 5.S3: VTF parameters determined through the nonlinear least squares fitting of temperature-dependent conductivity data. Italic values in square brackets were held constant during the least squares minimization and the values in parentheses represent the standard deviation of the fitting error for the last significant digit of the fitted parameter.

Sample Name	A ($Scm^{-1}K^{0.5}$)	B ($kJmol^{-1}$)	T_g (°C)
PEO-P[(STFSI)Li](5-3.2)	0.56(4)	9.6(1)	*[-34]*[a]
PEO-P[(STFSI)Li](5-2.0)	0.38(3)	*[9.6]*	-50(2)
PEO-P[(STFSI)Li](5-1.1)	0.27(3)	*[9.6]*	-59(3)
PEO-P[$(STFSI)_2$Mg](5-3.2)	0.009(2)	10.5(2)	*[-39]*[a]
PEO-P[$(STFSI)_2$Mg](5-2.0)	0.014(1)	*[10.5]*	-57(2)
PEO-P[$(STFSI)_2$Mg](5-1.1)	0.0131(2)	*[10.5]*	-65.2(5)

[a] Value determined through DSC analysis

5.7.7 SAXS Data Modeling

The scattering of the ion-containing diblock copolymers above the melting temperature of PEO was modeled by a structure factor based on RPA formulation by Leibler[65]. The absolute scattering intensity was calculated by

$$I_{Leibler}(q)[\mathrm{cm}^{-1}] = (B_A - B_B)^2 v_{ref} S_{AA\_Leibler}(q) \tag{S5.1}$$

Where B_A and B_B are the x-ray scattering length densities of each polymer block, v_{ref} is the volume of lattice site used in the RPA derivation, and $S_{AA\_Leibler}(q)$ is the structure factor. In this work, the scattering length densities were approximated using Equation S5.2

$$B_i(\mathrm{cm}^{-2}) \approx \frac{\mathrm{r}_e(\mathrm{cm\ electron}^{-1}) z_i^{\circ}(\mathrm{electrons\ mon}^{-1})}{v_i(\mathrm{nm}^3\ \mathrm{mon}^{-1}) 1 \times 10^{-21}(\mathrm{cm}^3\ \mathrm{nm}^{-3})} \tag{S5.2}$$

where the subscript *i* refers to species *A* or *B*, $\mathrm{r}_e = 2.81 \times 10^{-13}$ is the cross sectional scattering radius of a free electron, z_i° is the total number of electrons per monomer unit, and v_i is the monomer volume. For the purposes of this study, the monomer volumes were calculated from the monomer molecular mass (M_i°) and polymer mass density (ρ_i) through

$$v_i(\mathrm{nm}^3\ \mathrm{mon}^{-1}) = \frac{M_i^{\circ}(\mathrm{g\ mol}^{-1}) 1 \times 10^{21}(\mathrm{nm}^3\ \mathrm{cm}^{-3})}{\rho_i(\mathrm{g\ cm}^{-3}) \mathrm{N}_{AV}(\mathrm{mon\ mol}^{-1})} \tag{S5.3}$$

where $\mathrm{N}_{AV} = 6.023 \times 10^{23}$ is Avogadro's number. The reference volume used throughout this work is

$$v_{ref}(\mathrm{vol\ site}^{-1}) = 0.1\ \mathrm{nm}^3\ \mathrm{site}^{-1} = 1 \times 10^{-22} \mathrm{cm}^3\ \mathrm{site}^{-1} \tag{S5.4}$$

and the Leibler structure factor can be broken down into the ideal structure factors (S_{AA}°, S_{BB}°, and S_{AB}°) of each block and the entire chain by Equation S5.5.

$$S_{AA\_Leibler}(q) = \left[\frac{S^{\circ}_{AA}(q) + S^{\circ}_{BB}(q) + 2S^{\circ}_{AB}(q)}{S^{\circ}_{AA}(q)S^{\circ}_{BB}(q) - \left(S^{\circ}_{AB}(q)\right)^2} - 2\chi_{AB}\right]^{-1} \quad \text{(S5.5)}$$

where χ_{AB} is the monomer-monomer interaction parameter for the two chemically different blocks. The ideal structure factor for self-interactions of a polymer chain is

$$S^{\circ}_{ii}(q) = N^{ref}P(\phi_i) \quad \text{(S5.6)}$$

where ϕ_i is the volume fraction occupied by species *i*, N^{ref} is the number of lattice sites occupied per chain, and $P_i(q)$ is the form factor of an isolated chain. In the case of a diblock copolymer melt, all sites are occupied by either monomers of *A* or *B*, thus the total number of lattice sites per chain is

$$N^{ref} = N_i^{ref} + N_j^{ref} \quad \text{(S5.7)}$$

and the volume fraction of either species can be defined as

$$\phi_i \equiv \frac{N_i^{ref}}{N_i^{ref} + N_j^{ref}} \quad \text{(S5.8)}$$

where subscript *j* refers to the second polymer block. The number of sites occupied per chain was calculated from its degree of polymerization (N_i), monomer volume (v_i), and the lattice site volume (v_{ref}) through

$$N_i^{ref}(\text{sites chain}^{-1}) \equiv \frac{N_i(\text{mon chain}^{-1})v_i(\text{nm}^3\ \text{mon}^{-1})}{v_{ref}(\text{nm}^3\ \text{site}^{-1})} \quad \text{(S5.9)}$$

where the degree of polymerization was calculated from the number average molecular weight ($M_{n,i}$) by

$$N_i(\text{mon chain}^{-1}) = \frac{M_{n,i}[\text{g mol(chain)}^{-1}]}{M_i^{\circ}[\text{g mol(mon)}^{-1}]} \quad \text{(S5.10)}$$

For simplicity, the isolated chain form factor ($P_i(\phi_i)$) for each polymer block was assumed to be a Gaussian coil, which is given by the Debye relation modified for chain length dispersity[25,69]

$$P(\phi_i) = \frac{2}{u^2}\left[\phi_i u - 1 + \left(\frac{k}{k + \phi_i k}\right)^k\right];\ u \equiv q^2R_g^2 \quad \text{(S5.11)}$$

Where k is the dispersity index, q is the magnitude of the scattering vector, R_g is the radius of gyration of the entire polymer. The radius of gyration can be approximated by

$$R_g = \sqrt{R_{g,i}^2 + R_{g,j}^2} \tag{S5.12}$$

Where the subscripts i and j refer to each polymer block, whose radius of gyration can be approximated by

$$R_{g,i}^2 = \frac{N_i^{ref}\left(l_i^{ref}\right)^2}{6} \tag{S5.13}$$

Where l_i^{ref} is the statistical segment length based on the same reference volume used to calculate N_i^{ref}[112].

The ideal structure factor of the corresponding diblock copolymer consisting of two polydisperse Gaussian coils is given by Equation S5.14

$$S_{ij}^{\circ}(q) = \frac{N^{ref}}{2}\left[P(1) - P(\phi_i) - P\left(\phi_j\right)\right] \tag{S5.14}$$

The modeled scattering profiles shown in the main text were calculated using Equation S5.1 along with an additional function ($I_{bkg}(q)$) to account for scattering due to other phenomena not related to the nanoscale morphology of the polymer. In this case, the intensity due to random density fluctuations within the material (I_{fl}) was modeled as a constant value over all angles, and the high intensity upturn at low scattering angles (approaching the beamstop) was modeled with a power law ($I_{Pwr}(q)$) as shown in Equation S5.15. The physical origins of the power law scattering at low q, which is commonly observed in SAXS, are unclear; however, they are well-fit to the power law expression and thus can be neglected when interpreting the scattering due to polymer microstructure that appears at higher q values.

$$I_{bkg}(q) = I_{fl} + I_{Pwr}(q) = y_0 + y_1 q^{-y_2} \tag{S5.15}$$

The modeled intensities shown in Figure 5.5a-c of the main text were generated by Equation S5.16

$$I_{model}(q) = I_{Leibler}(q) + I_{bkg}(q) \tag{S5.16}$$

With the exception of k, ρ_{PSTFSI}, R_g, and χ_{AB}, all parameters required to model $I_{Leibler}(q)$ were determined experimentally or from literature estimates. The molecular weights of PEO and the P(STFSI) blocks were determined, as described earlier by GPC and NMR, respectively. The temperature-dependent density of amorphous PEO was approximated by $\rho_{PEO}(\mathrm{T}) = 1.139 - 7.31 \times 10^{-4}\mathrm{T}(^{\circ}\mathrm{C})$ according to the polymer handbook[113] and $l_{PEO}^{ref} = 0.72$

was used from ref [112]. We used a value of $\rho_{PSTFSI} = 1.57$ (gcm^{-1}) in all cases, based on the van Krevelen group addition analysis performed previously[37]. We do not account for changes in ρ_{PSTFSI} due to the different counter ions between the Li and Mg versions of the polymer, nor do we adjust ρ_{PSTFSI} for changes in temperature. The remaining three parameters (k, l_{PSTFSI}^{ref}, and χ_{AB}) were allowed to be adjusted along with the background function parameters to achieve the fits to the experimental data.

In practice, the parameters were adjusted in the following manner:

1) $I_{Pwr}(q)$ was determined for each sample by fitting the scattering data between $0.05 < q < 0.10$ nm^{-1}. PEO-P[$(STFSI)_2Mg$](5-3.2) represents one exception where the data between $0.04 < q < 0.065$ nm^{-1} was used to determine $I_{Pwr}(q)$.

2) The data from each magnesiated block copolymer at 130 °C was used to determine the dispersity index, k, for each polymer backbone by using the parameters found in step (1) in Equation S5.16 and simultaneously adjusting k, R_g, χ_{AB}, and the constant fluctuating background intensity (y_0). In order to approximate R_g, we use Equations S5.12 and S5.13 while setting $l_{PEO}^{ref} = l_{PSTFSI}^{ref}$ and using an arbitrary scaling factor (%Stretch) to scale the radius of gyration for each block, as shown in Equation S5.17 below. We determined the dispersity indices for PEO-P[$(STFSI)_2Mg$](5-1.1), PEO-P[$(STFSI)_2Mg$](5-2.0), and PEO-P[$(STFSI)_2Mg$](5-3.2) to be 3.84, 7.40, and 3.86, respectively. These values correspond to dispersities (PDIs) between 1.13-1.26[25].

3) The data from all magnesiated samples at 90 and 110 °C were fit by adjusting only %Stretch, χ_{AB}, and y_0

4) The data from all lithiated samples at 90, 110, and 130 °C were fit by adjusting only χ_{AB} and y_0. For the lithiated samples that exhibited negative interaction parameters (e.g. PEO-P[(STFSI)Li](5-2.0) and PEO-P[(STFSI)Li](5-3.2)), chain stretching is expected to be minimal and thus %Stretch was set to 0. Lacking a better alternative, the %Stretch for PEO-P[(STFSI)Li](5-1.1) was held at the value determined for PEO-P[$(STFSI)_2Mg$](5-1.1).

$$R_{g,i}^2 = \frac{N_i^{ref}\left(\%\text{Stretch} * l_{PEO}^{ref}\right)^2}{6} \tag{S5.17}$$

We note that all scattering intensity values were weighted by a 10% error during least-squares minimization to ensure the fits represented the entire q-range analyzed. The q-range analyzed for each polymer backbone are as follows: PEO-P(STFSI)(5-1.1) = $0.5 < q < 3$ nm^{-1}; PEO-P(STFSI)(5-2.0) = $0.46 < q < 3$ nm^{-1}; and PEO-P(STFSI)(5-3.2) = $0.4 < q < 3$ nm^{-1}. These ranges were chosen in order to capture the scattering peak from the magnesiated samples without skewing the fits by including a significant amount of the low-q data below the peak maximum. Representative fits to a lithiated and magnesiated sample are shown in Figure 5.S8 below, and the adjusted parameters used to fit all of the samples at each temperature are provided in Table 5.S4-Table 5.S6.

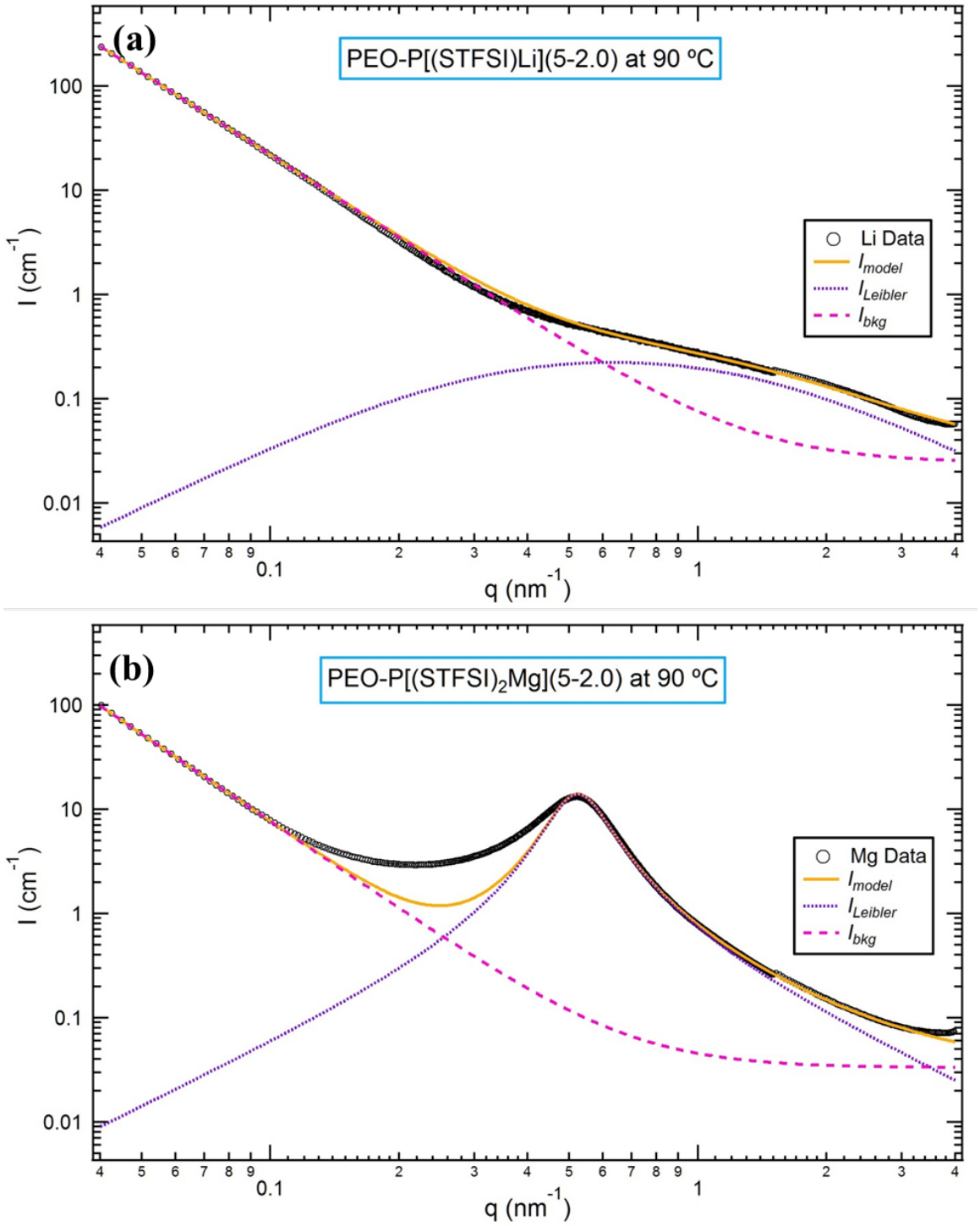

Figure 5.S8: Examples showing the fitting contributions for (a) PEO-P[(STFSI)Li](5-2.0) and (b) PEO-P[(STFSI)$_2$Mg](5-2.0) at 90 °C

Table 5.S4: Adjusted model parameters for the scattering measured at 90 °C

Sample at 90 °C	% Stretch	χ	y_0 (cm^{-1})	y_1 (cm^{-1})	y_2
PEO-P[(STFSI)Li](5-3.2)	*0.0*	-0.253	0.024	0.038	2.61
PEO-P[(STFSI)Li](5-2.0)	*0.0*	-0.123	0.024	0.052	2.63
PEO-P[(STFSI)Li](5-1.1)	*11.8*	0.102	0.032	0.026	2.89
PEO-P[$(STFSI)_2$Mg](5-3.2)	23.9	0.0963	0.033	0.063	2.50
PEO-P[$(STFSI)_2$Mg](5-2.0)	21.0	0.1656	0.033	0.012	2.79
PEO-P[$(STFSI)_2$Mg](5-1.1)	11.8	0.3074	0.029	0.0032	3.12

Table 5.S5: Adjusted model parameters for the scattering measured at 110 °C

Sample at 110 °C	% Stretch	χ	y_0 (cm^{-1})	y_1 (cm^{-1})	y_2
PEO-P[(STFSI)Li](5-3.2)	*0.0*	-0.202	0.029	0.039	2.61
PEO-P[(STFSI)Li](5-2.0)	*0.0*	-0.095	0.029	0.056	2.62
PEO-P[(STFSI)Li](5-1.1)	*10.4*	0.114	0.039	0.026	2.89
PEO-P[$(STFSI)_2$Mg](5-3.2)	21.3	0.0962	0.032	0.072	2.46
PEO-P[$(STFSI)_2$Mg](5-2.0)	19.1	0.1656	0.035	0.014	2.78
PEO-P[$(STFSI)_2$Mg](5-1.1)	10.4	0.3088	0.031	0.0038	3.04

Table 5.S6 :Adjusted model parameters for the scattering measured at 130 °C

Sample at 130 °C	% Stretch	χ	y_0 (cm^{-1})	y_1 (cm^{-1})	y_2
PEO-P[(STFSI)Li](5-3.2)	*0.0*	-0.162	0.029	0.042	2.59
PEO-P[(STFSI)Li](5-2.0)	*0.0*	-0.055	0.019	0.058	2.62
PEO-P[(STFSI)Li](5-1.1)	*9.5*	0.135	0.035	0.026	2.90
PEO-P[$(STFSI)_2$Mg](5-3.2)	19.2	0.0961	0.030	0.079	2.43
PEO-P[$(STFSI)_2$Mg](5-2.0)	17.8	0.1656	0.037	0.014	2.84
PEO-P[$(STFSI)_2$Mg](5-1.1)	9.5	0.3096	0.033	0.0049	2.92

Chapter 6 - Relationship between Microphase Separation and Poly(ethylene oxide) Crystallization in Lithium and Magnesium Single-Ion Conducting Block Copolymers[‡]

Abstract

The crystallization of polymers within nanostructured materials, such as self-assembled block copolymers, has been the subject of considerable investigation because it provides the opportunity to study complex competition between the thermodynamic driving force for crystallization and crystallization kinetics. A fundamental question regarding the behavior of single-ion conducting block copolymers derived from poly(ethylene oxide)-*b*-poly[(styrene-4-sulfonyltrifluoromethylsulfonyl)imide (PEO-P[(STFSI)]) is how the presence of the ion-containing block influences PEO crystallization. In this study, we report on the crystallization behavior PEO in a matched-set library of lithiated (PEO-P[(STFSI)Li]) and magnesiated (PEO-P[$(STFSI)_2$Mg]) single-ion conducting block copolymers. Analysis of semi crystalline samples prepared with careful thermal pretreatment reveals that the PEO crystallinity is independent of cation identity, and that crystallization induces the formation of lamellar nanostructures. The cation, however, does appear to influence the perfection of PEO crystallites and concomitant nanostructures; magnesiated samples show consistently more disorder. Through *in situ* analysis of crystallization kinetics with small and wide angle X-ray scattering, we show that crystallization is hindered by the presence of concentration fluctuations within the magnesiated samples prior to crystallization, thus leading to the increased disorder of those samples. Therefore, by influencing the melt structure, cation identity in single-ion conducting block copolymer can also influence crystallization behavior.

6.1 Introduction

Single-ion conducting block copolymers have recently garnered considerable interest for their potential application in high energy lithium metal batteries.[34–37] A promising class of single-ion conducting block copolymers comprise the ion-containing polymer, poly(styrene-4-sulfonyltrifluoromethylsulfonyl)imide lithium (P[(STFSI)Li]), and the ion-conducting polymer, poly(ethylene oxide) (PEO).[35] Recently we reported on ion transport in a library of single-ion conducting diblock copolymers of PEO-*b*-P[STFSI], with both lithium and magnesium counter-ions.[114] That work was restricted to temperatures above the melting point of PEO. The purpose of the present paper is to extend our analysis of the same polymer library to include temperatures below the melting point of PEO.

Crystallization in block copolymers has been well-studied and is known to both induce and be influenced by nanostructuring.[89,115–120] In the case of microphase separated block copolymers, polymer crystallization can either be confined within the nanoscale microphase domains or the crystallites may "break out" from the microphase domains and destroy the self-assembled nanostructure of the polymer.[89,115,118–120] For block copolymers that are disordered in the melt, polymer crystallization can effectively induce periodic nanostructural order.[115–117] Our

[‡] This chapter has been submitted for publication.

objective is to study the interplay between microphase separation and crystallization in single-ion conducting block copolymers from the melt, which to our knowledge has never been explored.

The block copolymers of interest are shown in Figure 6.1. The lithiated and magnesiated versions of each sample were prepared from the same precursor; we refer to samples derived from the same precursors as matched pairs. The main difference between our system and all previous studies on block copolymer crystallization (e.g. refs [89,115–120] from above paragraph) is the presence of ionic moieties in the non-crystalline block. In PEO/salt mixtures, the addition of moderate amounts of salt reduces PEO crystallinity and decreases crystallization temperature.[28,84,121,122] This is due to interactions between the cation and ether oxygens along the PEO backbone. There is no added salt in our system: interactions between cations and ether oxygens can only occur if the cations dissociate away from the P[STFSI] backbone. Whether or not confined crystallization occurs in our single-ion conducting block copolymers, as well as the kinetics of crystallization, are thus intrinsically coupled to ion dissociation. We use small and wide angle X-ray scattering (SAXS/WAXS) in conjunction with scanning transmission electron microscopy (STEM) and differential scanning calorimetry (DSC) to study this coupling.

6.2 Experimental

6.2.1 Materials

The synthesis and characterization of the single-ion conducting block copolymer library was described previously[114] (Chapter 5). The after synthesis, PEO-P[(STFSI)Li] and PEO-P[(STFSI)$_2$Mg] samples were dried under vacuum for a minimum of 1 week at ambient temperature and then dried under vacuum in a heated glove box antechamber at 90 °C for 24 hours before being brought into an argon (Ar) glovebox (MBraun). Inert atmosphere was maintained for all subsequent sample preparation and analysis. We provide the chemical structures of the lithiated and magnesiated versions of the single-ion conducting block copolymer in Figure 6.1, as well as the chain characteristics of each sample in Table 6.1.

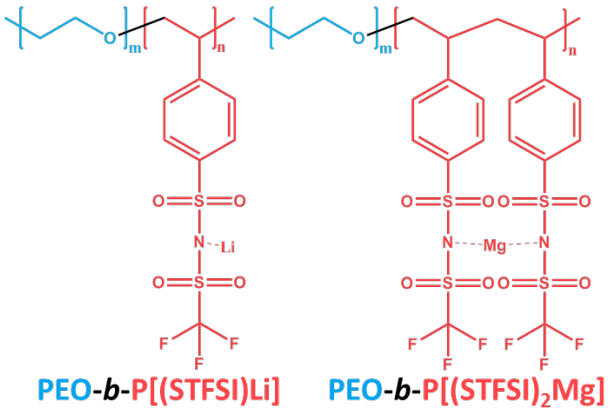

Figure 6.1: Chemical structure for both types of single-ion block copolymers characterized in this study.

Table 6.1: Characteristics of the matched-set of block copolymers

Sample Name	$M_{n,PEO}$ [kg mol^{-1}]	$M_{n,P(STFSI)}$ [kg mol^{-1}]	N_{PEO}	N_{PSTFSI}	ϕ_{PEO}
PEO-P[(STFSI)Li](5-3.2)	5.00	3.19	114	9.9	0.68
PEO-P[(STFSI)Li](5-2.0)	5.00	1.99	114	6.2	0.76
PEO-P[(STFSI)Li](5-1.1)	5.00	1.05	114	3.3	0.84
PEO-P[$(STFSI)_2$Mg](5-3.2)	5.00	3.24	114	9.9	0.67
PEO-P[$(STFSI)_2$Mg](5-2.0)	5.00	2.02	114	6.2	0.76
PEO-P[$(STFSI)_2$Mg](5-1.1)	5.00	1.08	114	3.3	0.84
PEO(5)	5.00	-	114	-	1

6.2.2 Thermal Analysis

In Chapter 5 reported on the thermal characterization of PEO(5), PEO-P[(STFSI)Li], and PEO-P[$(STFSI)_2$Mg] samples as measured with differential scanning calorimetry (DSC)[114]. In this work, we expand upon our analysis of that data in order to explore the crystallization behavior of PEO. For convenience, we summarize the methodology used here, and provide the analysis details in the supporting information (Section 6.7.1). The DSC samples were prepared in an Ar glovebox by placing 6-8 mg of polymer into a TZero aluminum pan and sealing with a TZero hermetic lid (T.A. Inc). A reference TZero hermetically sealed pan was also prepared in the Ar glovebox. In order to ensure the polymers had consistent thermal history, the hermetically sealed DSC samples (and reference pan) were subsequently annealed at 135 °C in a vacuum oven at -10 mmHg for 24 hours, after which the heater was turned off and the samples were allowed to slowly cool. Measurements were performed a minimum of 72 hours after the oven heater was turned off. A heat-quench-heat-cool method was used in order to determine the melting temperature (T_m) and fractional crystallinity (x_{cr}^{DSC}), crystallization temperature (T_c), and in cases where observable, glass transition temperature (T_g) of PEO.[114]

6.2.3 Small and Wide Angle X-Ray Scattering (SAXS/WAXS)

The details involving scattering sample preparation and data collection were described in Chapter 5.[114] In brief, all SAXS/WAXS samples, including an empty reference cell, were prepared inside of an Ar glovebox. The polymer samples were made by melt-forming into a custom-built hermetically sealed sample holder with 1 mil Kapton® film windows. The samples were subsequently removed from the glovebox and thermally pretreated using the sample protocol described above for the DSC samples.

As noted in Section 5.2.3, The SAXS/WAXS experiments were performed at Lawrence Berkeley National Laboratory's Advanced Light Source, Beamline 7.3.3[60] using a transmission setup and a custom-built heating stage. Temperature scans were replicated using both SAXS and WAXS. For each experiment, the samples were initially equilibrated at near ambient conditions (either 30 or 35 °C) where the scattering of semicrystalline samples was recorded. The samples were then heated directly to 130 °C and held at that temperature for at least 1 hour. The stage was subsequently cooled in 20 °C steps down to 90 °C or 70°C. Measurements were performed at each temperature upon waiting at least 30 minutes after the stage reached the setpoint temperature. Finally, in cases when beamtime was available, the samples were quenched directly

to 35 °C and allowed to isothermally crystallize for at least 90 minutes (note, the stage took ~45 minutes to reach 35 °C), with scattering patterns being measured every 10-15 minutes. Details of the data reduction are provided in Section 5.2.3, and all of the absolute scattering profiles can be found in Appendix A2.

6.2.4 Scanning Transmission Electron Microscopy (STEM)

STEM measurements were performed on two of the semicrystalline ion-containing block copolymers, PEO-P[(STFSI)Li](5-2.0) and PEO-P[$(STFSI)_2$Mg](5-2.0). These samples underwent the same thermal treatment as the DSC and SAXS/WAXS samples. The thermally pretreated samples were cryo-microtomed at −90 °C in a Leica FC6. Sections with thickness approximately 100nm were obtained using a diamond knife and picked up onto lacey carbon-coated copper grids (Electron Microscopy Sciences). STEM Samples were stained in ruthenium tetroxide vapor for 30 min prior to experiments. STEM experiments were performed on an FEI Titan microscope operated at 200kV at the National Center for Electron Microscopy of the Molecular Foundry, Lawrence Berkeley National Lab. The microscope is equipped with a high angle annular dark field detector (HAADF).

6.3 Results and Discussion

The results of the thermal analysis of the single-ion conducting block copolymers are provided in Table 6.2 below. The DSC data used to obtain these results are shown in Figure 5.S1-Figure 5.S3 in the previous chapter. In addition to the single-ion conducting block copolymers, we show data obtained from homopolymer PEO(5), which we use as a "baseline" for interpreting our results. In all cases, a melting temperature (T_m) between 55 and 60 °C is observed. In PEO homopolymers, single crystals with once- or twice-folded PEO chains exhibit melting temperatures between 57 and 60°C.[123,124] The slightly depressed melting temperature of PEO-P[(STFSI)Li](5-3.2) suggests the presence of some kinetically trapped thrice-folded chain crystals[123], or it may demonstrate melting point depression due to the presence of dissociated ionic species[28,84,121,122]. The crystallinity of PEO (x_{cr}^{DSC}), defined as the mass fraction of crystalline PEO relative to the total mass of PEO within the sample, was calculated using Equation 6.1

$$x_{cr}^{DSC} = \frac{\Delta H_m}{w_{PEO}\Delta H_m^o} \tag{6.1}$$

where ΔH_m is the experimental melting enthalpy and w_{PEO} is the weight fraction of PEO within the block copolymer. We assume that the ideal melting enthalpy of fully crystalline PEO, $\Delta H_m^o = 206$ (Jg^{-1})[113]. Literature values of ΔH_m^o range from 198 to 216.[113,125,126] Interestingly, ΔH_m values of matched pairs are identical (Table 6.2). Crystallinity is thus only affected by w_{PEO} and is independent of cation type. In contrast, the crystallization temperatures (T_c) of matched pairs, measured at the same cooling rate that was used in the melting experiments (5 °C/min), are very different. As expected, T_c values of the block copolymers are lower than the value obtained from PEO(5), indicating that presence of the ion-containing amorphous block impedes crystallization. In the magnesiated samples, T_c decreases monotonically as the molecular weight of the ion-containing block increases. More complex

behavior is seen in the lithiated samples. PEO-P[(STFSI)Li](5-1.1) and PEO-P[(STFSI)Li](5-2.0) display similar T_c's that are higher than their magnesiated matched pair. However, PEO-P[(STFSI)Li](5-3.2) exhibited no crystallization peak, while T_c of its magnesiated matched pair was measured at -28.5 °C. It is evident that crystallization of the PEO block in our systems is not a simple function of the volume fraction of the amorphous block.

Table 6.2: Results from the DSC analysis of the melting and recrystallization of PEO in the matched-set block copolymer library.

Sample Name	T_m [°C]	ΔH_m [Jg^{-1}]	w_{PEO}	x_{cr}^{DSC}	T_c [°C]
PEO-P[(STFSI)Li](5-3.2)	55.7	72.5	0.58	0.60	--
PEO-P[(STFSI)Li](5-2.0)	57.9	101	0.68	0.73	35.7
PEO-P[(STFSI)Li](5-1.1)	58.1	121	0.78	0.76	35.3
PEO-P[(STFSI)$_2$Mg](5-3.2)	57.2	71.9	0.58	0.60	-28.5
PEO-P[(STFSI)$_2$Mg](5-2.0)	57.2	100	0.68	0.72	17.2
PEO-P[(STFSI)$_2$Mg](5-1.1)	57.9	119	0.78	0.75	23.9
PEO(5)	59.8	175	1	0.85	42.2

In Figure 6.2 we provide the combined SAXS/WAXS profiles for all of the lithiated and magnesiated single-ion conducting block copolymers, as well as PEO(5), at ambient temperature after consistent thermal pre-treatment, as described in the experimental section. In all cases, the WAXS scattering indicates the presence of crystalline PEO domains. Furthermore, integer-spaced peaks in all SAXS profiles suggest the presence of a lamellar nanostructure. We confirm the lamellar ordering in PEO-P[(STFSI)Li](5-2.0) and PEO-P[(STFSI)$_2$Mg](5-2.0) with STEM in Figure 6.2c-d. We note here that the higher degree of long-range order (i.e. grain size) observed in P[(STFSI)Li](5-2.0) is consistent with the anisotropic 2D SAXS/WAXS profiles observed in all of the lithiated samples (Appendix A2); the 2D SAXS/WAXS profiles for the magnesiated samples were isotropic in all cases, consistent with the poor long-range ordering observed for PEO-P[(STFSI)$_2$Mg](5-2.0) in Figure 6.2d. The locations of the primary scattering peak for each sample, denoted by the solid black triangles in Figure 6.2a-b, were determined by fitting the data in the vicinity of the peak with a Gaussian curve on a sloping background (SI in 6.7.3).

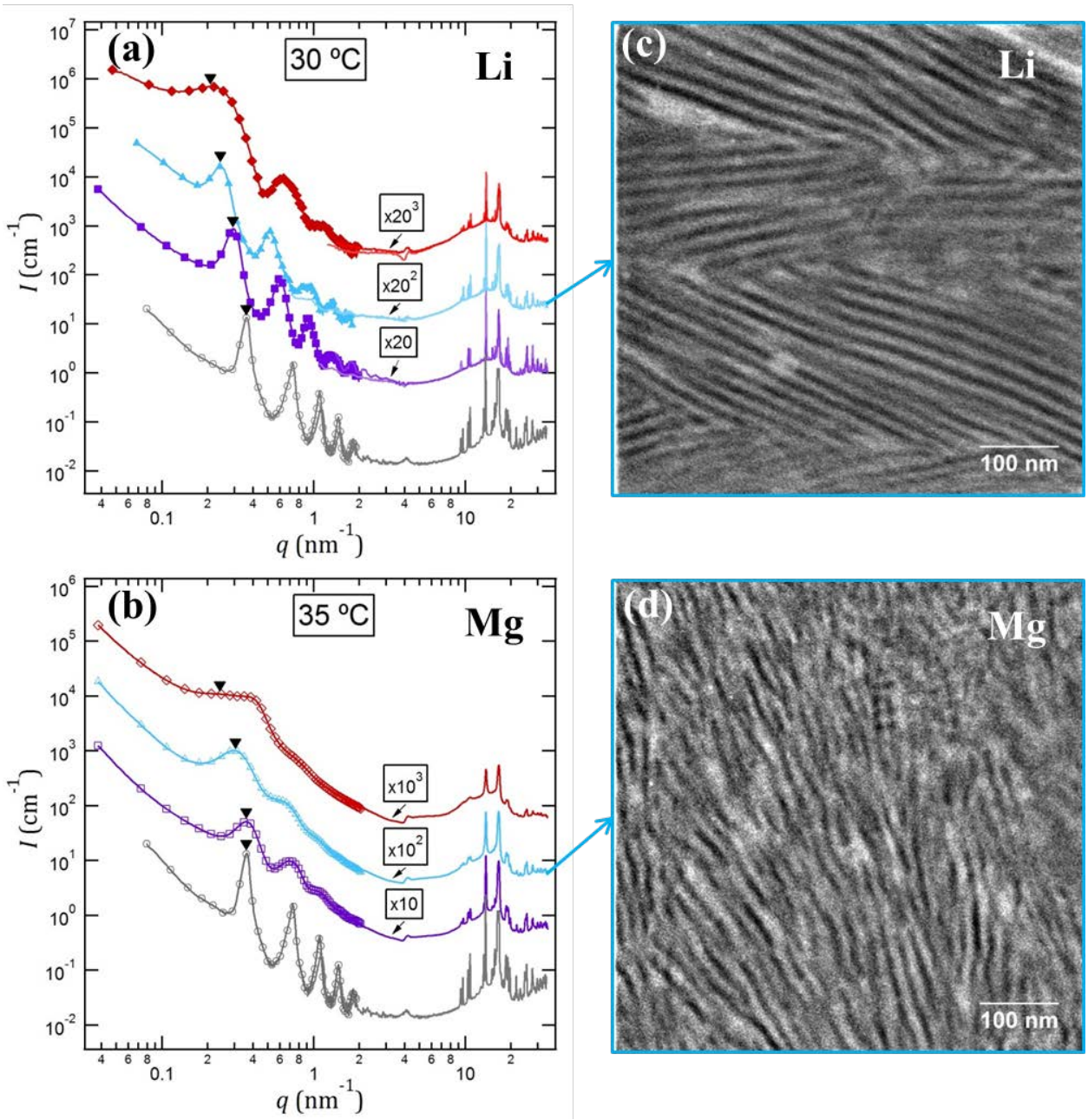

Figure 6.2: (a-b) Combined SAXS/WAXS profiles where scattering intensity, *I*, is plotted versus the magnitude of the scattering vector, *q* for (a) the lithiated (PEO-P[(STFSI)Li]) (closed symbols) and (b) magnesiated (PEO-P[$(STFSI)_2$Mg]) (open symbols) samples at ambient conditions after thermal pretreatment. Red diamonds/curves = PEO-P(STFSI) (5-3.2); cyan triangles/curves = PEO-P(STFSI)(5-2.0); purple squares/curves = PEO-P(STFSI)(5-1.1); and for reference, that scattering from PEO(5) is provided in open grey circles/curves. For clarity, SAXS data markers are only plotted for every 15th data point, WAXS data are represented by lines between data points, and the absolute intensity profiles are offset by the factors indicated on the plot. The locations of the primary scattering peaks are marked with black upside down triangles. The feature in the scattering data near q = 4 nm^{-1} is due to imperfect subtraction of the scattering from the kapton sample holder windows. (c-d) STEM micrographs from thermally pretreated, cryo-microtomed, and stained samples of (c) PEO-P[(STFSI)Li](5-2.0) and (d) PEO-P[$(STFSI)_2$Mg](5-2.0). The bright phase indicates PEO-rich regions.

In order to explore the relationship between PEO crystallization and the lamellar nanostructure of the single-ion conducting block copolymers, we have developed a framework to extract the absolute volumetric crystallinity of PEO from the calibrated WAXS data shown in Figure 6.2a-b. A detailed derivation is provided in the supporting information (Section 6.7.2.2); however, in brief, we have extended the approximation that was proposed by Goppel[56], and recently employed by Balko and coworkers[127], to allow for the analysis of block copolymers with one crystallizable block. The Goppel approximation is based on the measurement of the scattering intensity due to the amorphous fraction of a crystallizable polymer in both the semicrystalline (I_{scr}) and fully molten (I_{molten}) state. Through a molar balance, it can be shown that the amorphous volume fraction (ϕ_{am}^{scr}), and hence crystalline volume fraction (ϕ_{cr}^{WAXS}), of the semicrystalline sample is given by

$$\phi_{am}^{scr} \approx \frac{I_{scr}(q_0)}{I_{molten}(q_0)} = 1 - \phi_{cr}^{WAXS} \tag{6.2}$$

where q_0 is the scattering vector chosen to evaluate I_{scr} and I_{molten}. For Equation 6.2 to provide an accurate measure of ϕ_{cr}^{WAXS}, the intensity contributions from incoherent scattering and diffuse scattering from crystalline disorder must be negligible compared to the contribution from amorphous polymer at q_0[56,127]; however, we note that errors induced by incoherent and diffuse scattering will lead to lower values of ϕ_{cr}^{WAXS}, thus the Goppel approximation can be considered a lower bound of the crystalline fraction. In the case of a simple semicrystalline homopolymer, I_{scr} and I_{molten} can be left in arbitrary units as long as the measurements were performed on the same sample (i.e. after recording the scattering from the semicrystalline sample, the sample is melted and the scattering is measured again to determine I_{molten}). However, in a diblock copolymer with one crystallizable block, the amorphous scattering intensity arises from both the amorphous polymer block (e.g. P(STFSI)) as well as the amorphous fraction of the crystallizable block. In the supporting information (Section 6.7.2.2) we show that by making an additional WAXS measurement of the fully molten homopolymer of the crystallizable block, the calibrated intensity values can be used with a re-casting of Goppel's approximation to compute the absolute crystalline volume fraction of PEO within the single-ion conducting block copolymers. Due to the complication of amorphous scattering from the non-crystallizable block, we have not yet utilized more detailed analytical techniques to probe PEO crystallinity in our system[128,129].

Table 6.3: Quantitative analysis results from the SAXS/WAXS profiles in Figure 6.2a-b.

Sample Name	ϕ_{cr}^{WAXS}	d_{SAXS} [nm]
PEO-P[(STFSI)Li](5-3.2)	0.59[a] 0.55[b]	30.2
PEO-P[(STFSI)Li](5-2.0)	0.70[a] 0.67[b]	26.0
PEO-P[(STFSI)Li](5-1.1)	0.78[a] 0.75[b]	21.6
PEO-P[$(STFSI)_2$Mg](5-3.2)	0.52	26.2
PEO-P[$(STFSI)_2$Mg](5-2.0)	0.64	20.1
PEO-P[$(STFSI)_2$Mg](5-1.1)	0.65	17.4
PEO(5)	0.79[a] 0.80[b]	17.5

[a] Value from the blue-highlighted sector averages in Figure A2.2, Figure A2.3, Figure A2.5, and Figure A2.7
[b] Value from the pink-highlighted sector averages in Figure A2.2, Figure A2.3, Figure A2.5, and Figure A2.7

Table 6.3 summarizes the quantitative analysis of the SAXS/WAXS data from Figure 6.2, where we provide the absolute crystallinity of PEO and the inter-lamellar domain spacing (d_{SAXS}) determined from the primary SAXS peak position (q^*) by $d_{SAXS} = \frac{2\pi}{q^*}$ (see SI in 6.7.2.1). To compare the crystallinities determined by DSC and WAXS, we calculate the volumetric crystal fraction from DSC (ϕ_{cr}^{DSC}) as

$$\phi_{cr}^{DSC} = \frac{\left(x_{cr}^{DSC} / \rho_{cr}^{PEO} \right)}{\left(x_{cr}^{DSC} / \rho_{cr}^{PEO} \right) + \left((1 - x_{cr}^{DSC}) / \rho_{am}^{PEO} \right)} \tag{6.3}$$

where ρ_{cr}^{PEO} = 1.24 [gcm^{-3}] is the density of crystalline PEO and ρ_{am}^{PEO} = 1.12 [gcm^{-3}] is the density of amorphous PEO near ambient temperature[56]. In Figure 6.3a, we demonstrate the relationship between the values for PEO crystallinity determined through thermal analysis (ϕ_{cr}^{DSC}) and those obtained by the Goppel approximation (ϕ_{cr}^{WAXS}). We see good agreement (within +/- 5%) between ϕ_{cr}^{DSC} and ϕ_{cr}^{WAXS} for PEO(5) and the lithiated samples; however, the values determined for the magnesiated block copolymers are systematically lower by approximately 7%. We believe the cause of this deviation is due to errors from an increased level of diffuse scattering arising from disorder within the PEO crystals[56].

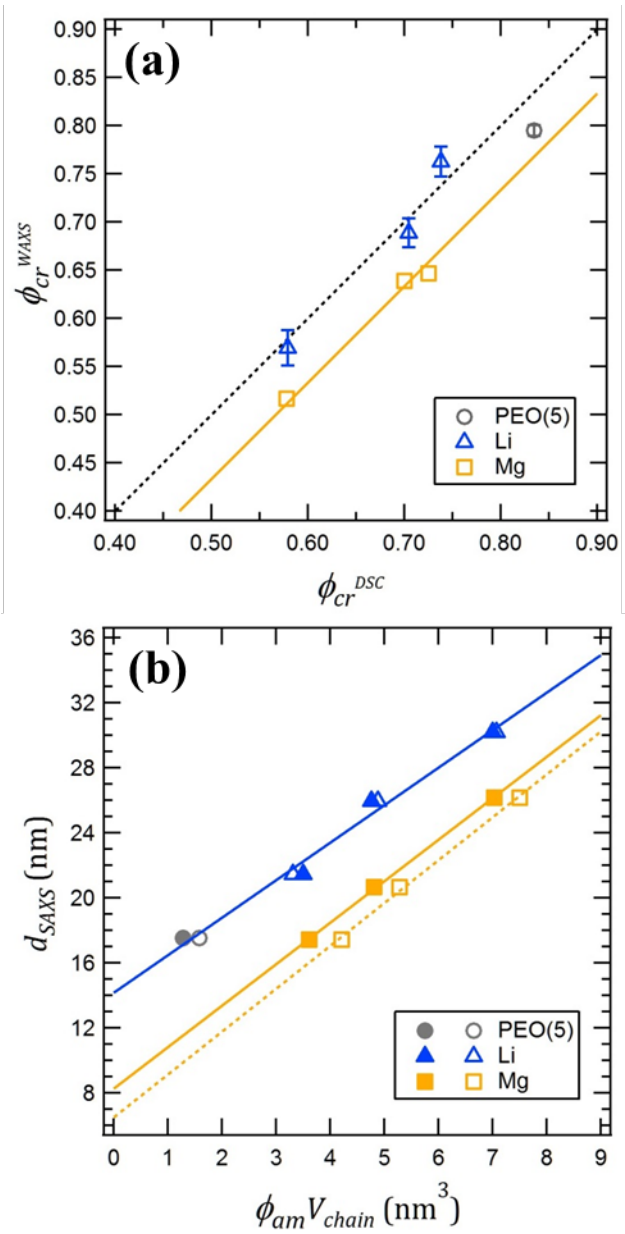

Figure 6.3: (a) Comparison of the fractional crystallinity of PEO determined through structural analysis (WAXS, ϕ_{cr}^{WAXS}) and thermal analysis (DSC, x_{cr}^{DSC}). Blue triangles indicate lithiated samples, gold squares indicate magnesiated samples, and grey circles indicate PEO(5). The error bars for PEO(5) and the lithiated samples indicate the range of values determined from different sector averages of the 2D WAXS data. The dashed black line indicates the prediction for a perfect correlation between ϕ_{cr}^{WAXS} and ϕ_{cr}^{DSC}, whereas the solid gold line represents a perfect correlation with a constant offset, determined by the best fit of a line with slope =1 to the magnesiated data: $\phi_{cr}^{WAXS} = \phi_{cr}^{DSC} - 0.067(6)$. (b) The relationship between nanostructure determined through SAXS and the fractional crystallinity of PEO. The lamellar spacing between PEO crystals (d_{SAXS}) is plotted versus the total amorphous volume contributed per chain ($\phi_{am}V_{chain}$). Blue triangles indicate lithiated samples, gold squares indicate magnesiated samples, and grey circles indicate PEO(5). Closed symbols use ϕ_{cr}^{DSC} to calculate ϕ_{am}, while open symbols use ϕ_{cr}^{WAXS}. The solid blue line represents the linear fit to the data from the lithiated polymers combined with the data from PEO(5): $d_{SAXS} = 2.3(1)\phi_{am}V_{chain} + 14.2(5)$ (R^2 = 0.9887). The solid gold line represents the linear fit to the data from the magnesiated polymers using ϕ_{am} calculated from ϕ_{cr}^{DSC}: $d_{SAXS} = 2.55(6)\phi_{am}V_{chain} + 8.2(3)$ (R^2 = 0.9995), and the dashed gold line is the linear fit to the magnesiated polymers using ϕ_{am} calculated

from ϕ_{cr}^{WAXS}: $d_{SAXS} = 2.6(1)\phi_{am}V_{chain} + 6.5(8)$ (R^2 = 0.9974). The fitting uncertainty in the last digit of each fit parameter is indicated by the value in parentheses.

To characterize the relationship between PEO crystallization and the nanostructures observed in SAXS, in Figure 6.3b we plot the inter-lamellar domain spacing measured with SAXS (d_{SAXS}) versus the total amorphous volume fraction within the sample, $\phi_{am} \equiv \phi_{PSTFSI} + \phi_{PEO}^{am} = \phi_{PSTFSI} + \phi_{PEO}[1 - (\phi_{cr}^{DSC}$ or $\phi_{cr}^{WAXS})]$, multiplied by the single-chain volume, $V_{chain} = N_{PEO}v_{PEO} + N_{PSTFSI}v_{PSTFSI}$, where N_{PEO} and N_{PSTFSI} are the degrees of polymerization for each block, and v_{PEO} and v_{PSTFSI} are their respective monomer volumes. If the PEO crystal thickness (L_{cryst}) remains constant between samples (i.e. each PEO chain is folded the same number of times) and nearly all chains participate in crystallization, then the inter-lamellar domain spacing can be expected to scale as

$$d_{SAXS} = \frac{\phi_{am}V_{chain}}{\alpha} + L_{cryst} \tag{6.4}$$

where α [nm^2] is the areal density of PEO-PSTFSI block junctions on the PEO crystal surface, which is fixed by the number of times the PEO chains fold within the crystal. We find that Equation 6.4 accounts for the scaling behavior observed in all of the single-ion conducting block copolymers. In the case of the lithiated block copolymers, the scaling behavior falls in line with the data for PEO(5), and L_{cryst} = 14.2 ± 0.5 nm, as determined by the intercept of the linear fit shown in Figure 6.3b. For a PEO sample with $M_{n,\,PEO}$ = 5 kg mol^{-1}, the thicknesses of crystalline lamellae comprising once- and twice-folded chains are 15.0 nm and 10.6 nm, respectively.[123] It appears that the PEO crystals in the lithiated polymer primarily comprise once-folded chains. The value of L_{cryst} for the lithiated samples also stands in good agreement with the width of the PEO-rich domains observed in the STEM image from PEO-P[(STFSI)Li](5-2.0) in Figure 6.2c. This indicates that a single once-folded PEO crystal spans the width of microphase separated PEO lamellae. The magnesiated block copolymers fall upon a completely separate trend (Figure 6.3b), with L_{cryst} = 8.2 ± 0.3 nm when using ϕ_{cr}^{DSC} to calculate ϕ_{am} or L_{cryst} = 6.5 ± 0.8 nm when using ϕ_{cr}^{WAXS} to calculate ϕ_{am}. The lower value(s) of L_{cryst} in the magnesiated samples appears to be related to increased disorder. For example, he widths of the PEO-rich domains in the STEM micrograph of PEO-P[$(STFSI)_2$Mg](5-2.0) in Figure 6.2d appear significantly larger than L_{cryst}, indicating that several small crystallites span the width of the microphase separated PEO lamellae.

It is known that the morphology of polymer crystals is kinetically controlled.[115–118] We probed the kinetic of PEO crystallization by quenching the block copolymers from temperatures well above the melting temperature of PEO to 35 °C, and then monitored the morphological development by *in situ* X-ray scattering. Time = 0 is defined as the time at which the sample temperature reached 35 °C (typically 45 minutes after the quench was initiated). In Figure 6.4a we provide the combined SAXS/WAXS profiles for PEO-P[$(STFSI)_2$Mg](5-2.0) during such an experiment. For time ≤ 30 min, the SAXS profile exhibits a single broad peak at q = 0.509 nm^{-1}, which we attribute to periodic concentration fluctuations that are typically found in amorphous block copolymers in the disordered state[27,65]. In this time window, the WAXS profile only contains intensity from the broad amorphous scattering halo[56]. Between time = 45 and 120 min, three changes occur in the scattering profile: the scattering peak from disordered fluctuations diminishes, a new scattering peak emerges at q= 0.325 nm^{-1}, and the WAXS intensity at q=14.6

nm^{-1} decreases. The vertical dashed lines in Figure 6.4a are located at q= 0.325 and 14.6 nm^{-1}. The correlated changes in SAXS and WAXS at these two values of *q* are due to the formation of PEO-rich crystals. The Bragg peaks corresponding to PEO crystals are evident in the WAXS data obtained after time = 45 min. The formation of PEO crystals results in a dramatic increase in the length scale of the periodic structure from 12 to 19 nm. Such large changes in periodic length scale during an disorder-to-order transition are only seen in block copolymers wherein the major component is crystallizing.[117] It may be worth noting that the scattering intensity at q = 0.397 nm^{-1} (between the crystalline and disordered SAXS peaks) in Figure 6.4a is independent with time. The reason for this is not clear.

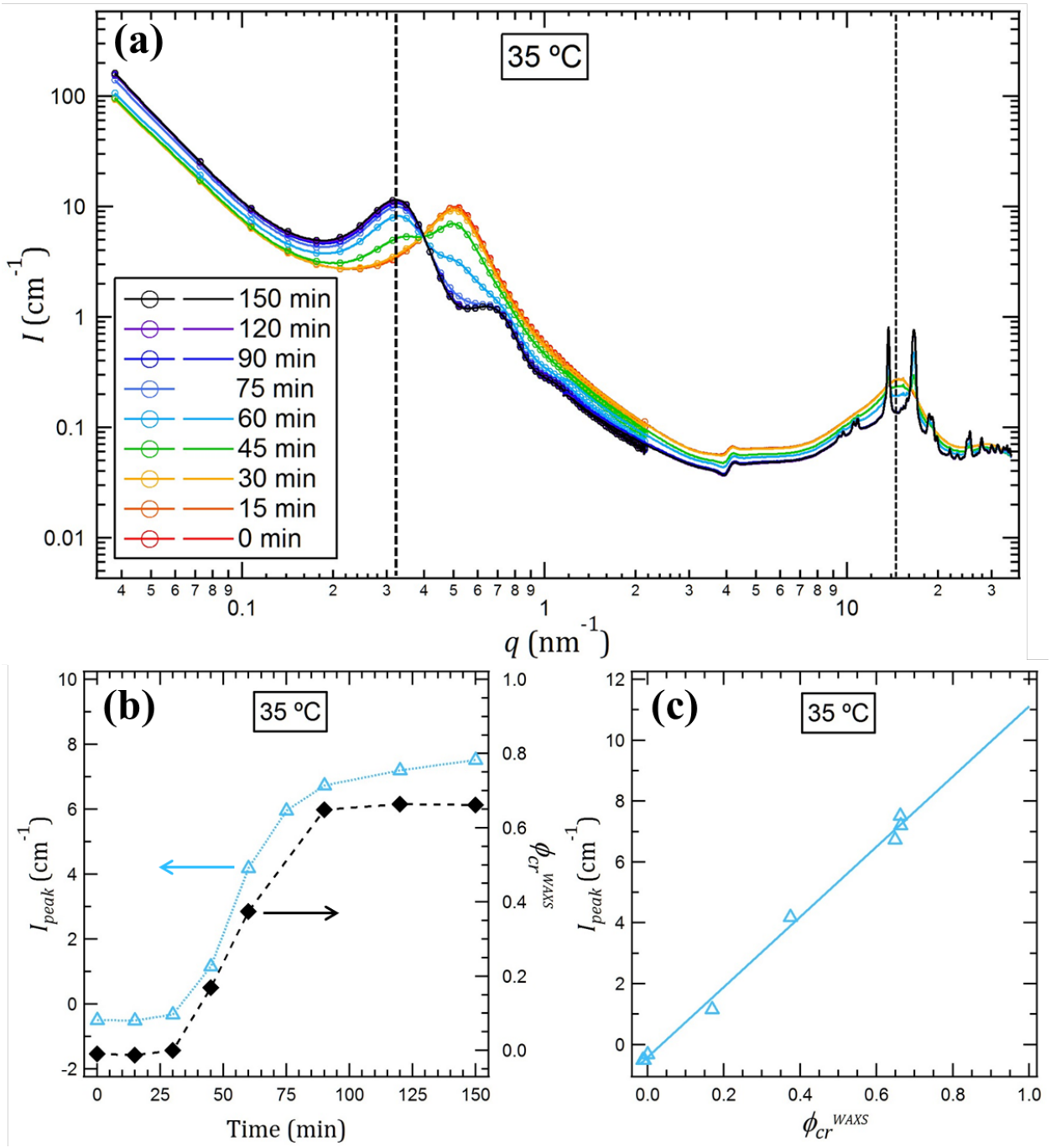

Figure 6.4: (a) Time-dependent combined SAXS/WAXS patterns from PEO-P[(STFSI)$_2$Mg](5-2.0) during isothermal crystallization at 35 °C. The dashed vertical lines indicate the q-values where intensities were extracted to calculate I_{peak} and ϕ_{cr}^{WAXS}. For clarity, the SAXS data markers are only plotted for every 15th data point and WAXS data are represented by lines between data points. (b) I_{peak} (left axis, open cyan triangles) and ϕ_{cr}^{WAXS} (right axis, filled black diamonds) plotted vs. time during isothermal crystallization of PEO-P[(STFSI)$_2$Mg](5-2.0). Dashed curves are meant to guide the eye. (c) I_{peak} vs. ϕ_{cr}^{WAXS} from the data shown in (b). The solid line indicates the linear fit to the data: $I_{peak} = 11.5(3)\phi_{cr}^{WAXS} - 0.4(1)$ ($R^2 = 0.995$).

In Figure 6.4b we quantify our qualitative observations by plotting the normalized intensity (I_{peak}) of the primary SAXS peak (q^* = 0.0325 nm^{-1}), calculated using Equation 6.5, as well as the absolute PEO crystalline fraction (ϕ_{cr}^{WAXS}) versus time.

$$I_{peak} \equiv I_{35°C}(q^*) - I_{90°C}(q^*) \tag{6.5}$$

It is clear that I_{peak} and ϕ_{cr}^{WAXS} are correlated, which we demonstrate conclusively in Figure 6.4c by plotting I_{peak} versus ϕ_{cr}^{WAXS}. We note that I_{peak} reflects SAXS intensity at q = 0.0325 nm^{-1}, while ϕ_{cr}^{WAXS} reflects WAXS intensity at q =14.6 nm^{-1}. The linear relationship shown by the regression analysis in Figure 6.4c indicates that I_{peak} is a measure of relative crystallinity.

In Figure 6.5 we show time-dependent SAXS profiles for PEO-P[(STFSI)Li](5-3.2) after quenching from 70°C to 35 °C. We see the development of crystalline lamellae, indicated by the growth of a peak at q = 0.215 nm^{-1}. The main difference between the lithiated sample in Figure 6.5 and magnesiated sample in Figure 6.4 is the absence of the broad scattering peak due to concentration fluctuations in the fully amorphous state (compare time = 0 data in Figure 6.4a and Figure 6.5).

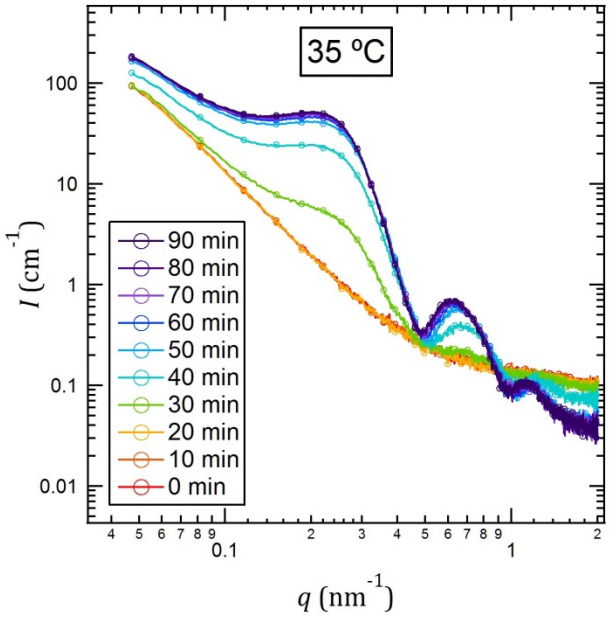

Figure 6.5: Time-dependent *in situ* SAXS profiles from PEO-P[(STFSI)Li](5-3.2) during isothermal crystallization at 35 °C.

The *in situ* SAXS experiments described above were performed on all of the single-ion conducting block copolymers. (The *in situ* SAXS profiles from samples not shown in Figure 6.4 and Figure 6.5 are provided in Appendix A2). In Figure 6.6, we plot I_{peak} extracted from all of the samples versus time. In Figure 6.6a, we show that PEO-P[(STFSI)Li](5-1.1) and PEO-P[(STFSI)Li](5-2.0) are essentially fully crystallized by the time the *in situ* SAXS heating stage reached 35 °C. This result is consistent with DSC observations. Interestingly, PEO-P[(STFSI)Li](5-3.2), which did not portray a detectable crystallization temperature during the DSC cooling scan, began to rapidly crystallize 20 minutes after the stage reached the 35 °C

setpoint. The crystallization time for PEO-P[(STFSI)Li](5-3.2), approximated using the linear fits in Figure 6.6a, was 53 minutes. We posit that the cooling rate employed in the DSC experiments precluded crystallization in this sample. It is evident in Figure 6.6a that the rate of crystallization decreases as the molecular weight of the PSTFSI block is increased from 1.1 to 3.2 kg mol^{-1}. In Figure 6.5b we show the time dependence of I_{peak} of the magnesiated block copolymers. In this set, the rate of crystallization also decreases with increasing molecular weight of the PSTFSI block. Crystallization of PEO-P[$(STFSI)_2Mg$](5-1.1) is essentially complete at time = 0. With a crystallization time of 71minutes, the crystallization of PEO-P[$(STFSI)_2Mg$](5-2.0) is qualitatively similar to PEO-P[(STFSI)Li](5-3.2). The crystallization of PEO-P[$(STFSI)_2Mg$](5-3.2) is very slow and was not observed over the course of the experiment; note that I_{peak} only increases by 2 cm^{-1} during the experiment (Figure 6.6b) (negative values of I_{peak} can be obtained because of our definition (Equation 6.5)). WAXS data obtained at time = 150 min for PEO-P[$(STFSI)_2Mg$](5-3.2) showed no evidence of PEO Bragg peaks (Appendix A2). The rate of crystallization in the magnesiated samples as measured by SAXS is reflective of their crystallization temperatures observed by DSC. Table 6.4 summarizes the approximate crystallization times for each set of matched-pairs.

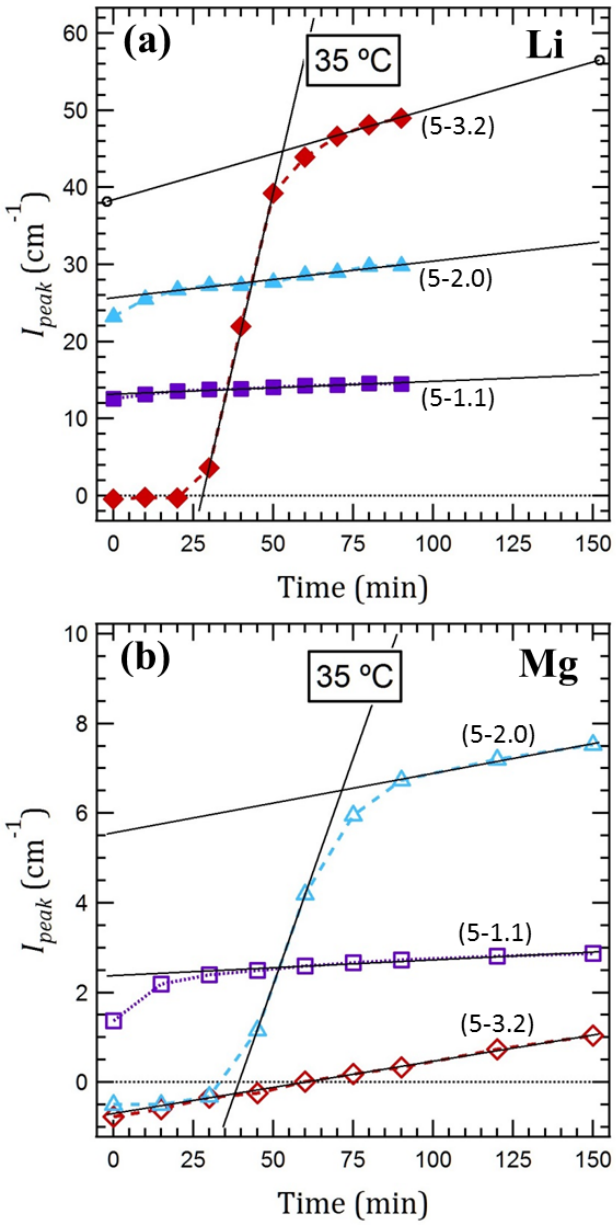

Figure 6.6: Evolution of the semicrystalline SAXS peak intensity (I_{peak}) with time during isothermal crystallization at 35 °C for (a) the lithiated samples (closed symbols) and (b) the magnesiated samples (open symbols). Red diamonds = PEO-P(STFSI)(5-3.2); cyan triangles = PEO-P(STFSI)(5-2.0); purple squares = PEO-P(STFSI)(5-1.1). The dashed curves are meant to guide the eye. The black lines were used to approximate the crystallization times for each sample.

Table 6.4: Approximate crystallization times from the data in Figure 6.6.

Matched Pair	Li	Mg
PEO-P(STFSI)(5-3.2)	~53 min	> 150 min
PEO-P(STFSI)(5-2.0)	< 10 min	~71 min
PEO-P(STFSI)(5-1.1)	< 0 min	< 15 min

We posit that the differences in crystallization kinetics observed between matched pairs of lithiated and magnesiated single-ion conducting block copolymers stems from differences in their melt nanostructures. Before crystallization, the SAXS profile from PEO-P[(STFSI)$_2$Mg](5-2.0) indicates the presence of periodic concentration fluctuations, whereas the SAXS profile from PEO-P[(STFSI)Li](5-3.2) is essentially featureless and does not indicate a periodic structure. The SAXS invariant (Q) provides a measure of the magnitude of electron density fluctuations within a sample, which is related to the magnitude of concentration fluctuations through the difference in scattering length densities of the two polymer blocks.[55] The invariant is defined as

$$Q = \frac{1}{2\pi^2}\int_{q_{min}}^{q_{max}} I(q)q^2 \mathrm{d}q \; [=]\mathrm{cm}^{-1}\mathrm{nm}^{-3} \tag{6.6}$$

In principle, the integration limits should be $q_{min} = 0$ and $q_{max} = \infty$; however, in practice, the extrapolation of $I(q)$ and $q = 0$ and $q = \infty$ leads to significant errors in the calculation of Q.[55,56] We set the integration bounds based on the experimentally measured SAXS q-range ($q_{min} =$ 0.04 nm^{-1} and $q_{max} = 2.0$ nm^{-1}) and used the NCNR Analysis Macro[130] package for Igor Pro to calculate the invariant. In Figure 6.7, we plot Q versus time during the isothermal crystallization of PEO-P[(STFSI)Li](5-3.2) and PEO-P[(STFSI)$_2$Mg](5-2.0), the two samples wherein crystallization kinetics occurred on accessible timescales. The trends observed in these two samples are qualitatively different, with Q increasing for PEO-P[(STFSI)Li](5-3.2) and Q decreasing for PEO-P[(STFSI)$_2$Mg](5-2.0) as the PEO chains crystallize. Furthermore, the absolute values of Q in the fully molten state (i.e. at time = 0) for PEO-P[(STFSI)$_2$Mg](5-2.0) is nearly 4 times greater than that of PEO-P[(STFSI)Li](5-3.2). We first analyze the discrepancy in values of Q in the molten state, and then propose a mechanism that can explain the opposing trends in Q during crystallization.

In an ideal two-phase system with sharp interfaces, the invariant (Q_{ideal}) is determined by the volume fraction of each phase and their scattering contrast:

$$Q_{ideal} = 1 \times 10^{-21}(B_A - B_B)^2\phi_A\phi_B[=]\mathrm{cm}^{-1}\mathrm{nm}^{-3} \tag{6.7}$$

where B_A and B_B are the scattering length densities and ϕ_A and ϕ_B are the volume fractions of phases A and B. The factor of 1×10^{-21} is necessary to convert the $(B_A - B_B)^2[=]\mathrm{cm}^{-4}$ term into the appropriate units. The phases of interest here are PEO and the PSTFSI. In Table 6.5 we provide the values of $1 \times 10^{-21}(B_A - B_B)^2$ and $\phi_A\phi_B$, which are calculated as described previously[114], for PEO-P[(STFSI)$_2$Mg](5-2.0) and PEO-P[(STFSI)Li](5-3.2) at 35 °C. We provide these calculations under two conditions: First assuming fully amorphous PEO (ρ_{am}^{PEO} = 1.112 gcm^{-3})[113], and second assuming 100% crystalline PEO (ρ_{cr}^{PEO} = 1.24 gcm^{-3})[56]. In both cases we use a density for the P(STFSI) block of ρ_{PSTFSI} = 1.57 gcm^{-3}.[37] The changes in Q_{ideal} during crystallization can be estimated using the data in Table 6.5. In both cases Q_{ideal} is predicted to decrease by a factor of about 2. The qualitative differences in the time dependence of Q seen in Figure 6.7 thus cannot be explained by the factors that affect Q_{ideal} (Table 6.5). Rather, we posit that the observed difference in Q stems from the nature of the interface between PEO-rich and PSTFSI-rich domains within the samples.

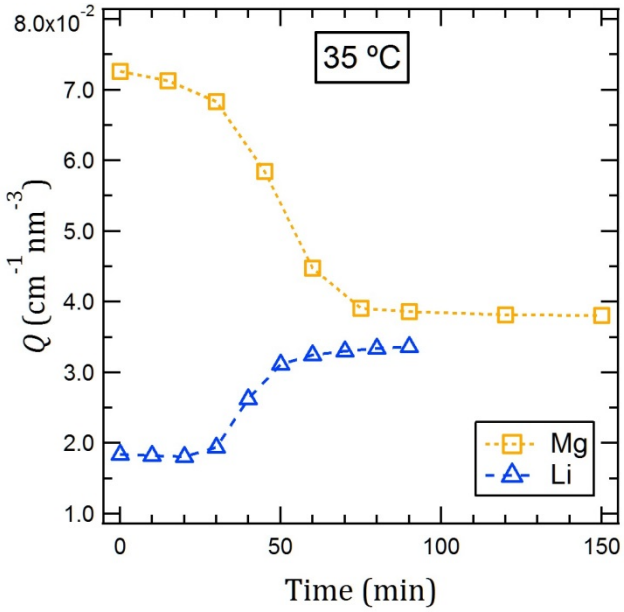

Figure 6.7: Evolution of the scattering invariant (Q) during the isothermal crystallization of PEO-P[(STFSI)Li](5-3.2) (blue triangles) and PEO-P[$(STFSI)_2$Mg](5-2.0) (gold squares) at 35 °C. Dashed curves are meant to guide the eye.

Table 6.5: Calculated values relating Q_{ideal} assuming fully amorphous PEO and 100% crystalline PEO in the PEO-P[(STFSI)Li](5-3.2) and PEO-P[$(STFSI)_2$Mg](5-2.0) samples.

Sample	Amorphous PEO		100% Crystalline PEO	
	$1 \times 10^{-21}(B_A - B_B)^2$ [cm^{-1}][nm^{-3}]	$\phi_A\phi_B$	$1 \times 10^{-21}(B_A - B_B)^2$ [cm^{-1}][nm^{-3}]	$\phi_A\phi_B$
PEO-P[$(STFSI)_2$Mg](5-2.0)	1.11	0.19	0.46	0.20
PEO-P[(STFSI)Li](5-3.2)	1.06	0.22	0.43	0.23

For a two-phase system with diffuse interface boundaries, the relation for the ideal invariant (Q_{ideal}) in Equation 6.7 must be modified. By using a three-dimensional Gaussian smoothing function, the invariant for a two-phase system with diffuse interfaces (Q_{diff}) can be written as

$$Q_{diff} = 1 \times 10^{-21}(B_A - B_B)^2\phi_A\phi_B\left(1 - \frac{t}{l_p}\right) \tag{6.8}$$

where t is the thickness of the interface region and l_p is Porod's length of inhomogeneity, which describes the average "domain size" within the sample[55]. In Table 6.6, we provide the measured invariants (Q) for PEO-P[$(STFSI)_2$Mg](5-2.0) and PEO-P[(STFSI)Li](5-3.2) before and after PEO crystallization, along with the corresponding calculated values of Q_{ideal} for those samples in the fully amorphous and 100% crystalline state, respectively. In the final column of Table 6.6,

we provide the value of t/l_p necessary to yield the experimentally measured invariant values assuming a diffuse interface, which we calculate using Q and Q_{ideal} in Equation 6.9:

$$\frac{t}{l_p} = 1 - \frac{Q}{Q_{ideal}} \tag{6.9}$$

It is clear from Table 6.6 that in the melt, the thickness (t) of the diffuse interface layer in PEO-P[(STFSI)Li](5-3.2) relative to the "domain size" (l_p) is much larger than in the PEO-P[(STFSI)$_2$Mg](5-2.0) sample. In fact, the value of $t/l_p = 0.92$ indicates that "domains" in PEO-P[(STFSI)Li](5-3.2) are essentially all interface i.e. the PEO and P[(STFSI)Li] are well mixed. This is consistent with our observation of a negative Flory-Huggins interaction parameter (χ) between PEO and P[(STFSI)Li] in PEO-P[(STFSI)Li](5-3.2).[114] In contrast, the value of $t/l_p = 0.65$ calculated for PEO-P[(STFSI)$_2$Mg](5-2.0) in the melt shows that although the interfaces are quite diffuse, reasonably well-defined P[(STFSI)$_2$Mg]-rich "domains" exist within the sample. Thus we attribute the ~4x difference in Q between PEO-P[(STFSI)$_2$Mg](5-2.0) and PEO-P[(STFSI)Li](5-3.2) at time = 0 to the presence/absence of defined PTFSI-rich domains in the melt. We note that the values for t/l_p provided in Table 6.6 represent an upper bound for (t), since the measured invariant (Q) used in Equation 6.9 is determined from a limited region of q-space.

Table 6.6: Experimental (Q) and ideal (Q_{ideal}) invariant values for PEO-P[(STFSI)Li](5-3.2) and PEO-P[(STFSI)$_2$Mg](5-2.0) at the beginning and end of the *in situ* SAXS experiments. t/l_p values are the results from Equation 6.9.

Sample	Q [cm^{-1}][nm^{-3}]	Q_{ideal} [cm^{-1}][nm^{-3}]	$\frac{t}{l_p}$
PEO-P[(STFSI)$_2$Mg](5-2.0) at Time = 0	0.073	0.21	0.65
PEO-P[(STFSI)Li](5-3.2) at Time = 0	0.018	0.24	0.92
PEO-P[(STFSI)$_2$Mg](5-2.0) at Time = 150	0.038	0.09	0.58
PEO-P[(STFSI)Li](5-3.2) at Time = 90	0.033	0.10	0.66

As PEO crystallizes in the single-ion conducting polymers, domains of pure crystalline PEO form, which have a higher mass density than amorphous PEO. The more dense PEO domains provide a lower contrast with P(STFSI), as demonstrated by the values for $1 \times 10^{-21}(B_A - B_B)^2$ in Table 6.5. Thus as PEO crystallizes in PEO-P[(STFSI)$_2$Mg](5-2.0), where P[(STFSI)$_2$Mg] domains are already present, the total contrast is reduced and the invariant decreases. On the other hand, when PEO crystallizes in PEO-P[(STFSI)Li](5-3.2), the crystalline PEO domains form within an essentially homogeneous phase of mixed PEO and P[(STFSI)Li]. Thus the creation of new domains with sharper interfaces (see t/l_p in Table 6.6) leads to the increase in the invariant upon crystallization observed in Figure 6.7. We note that the treatment of the invariant above is derived for a two-phase system, and strictly speaking, the semi crystalline samples might need to be treated as three-phase systems; however, the qualitative

interpretation of our results should still hold. Extension of our treatment to three-phase systems is outside the scope of this paper.

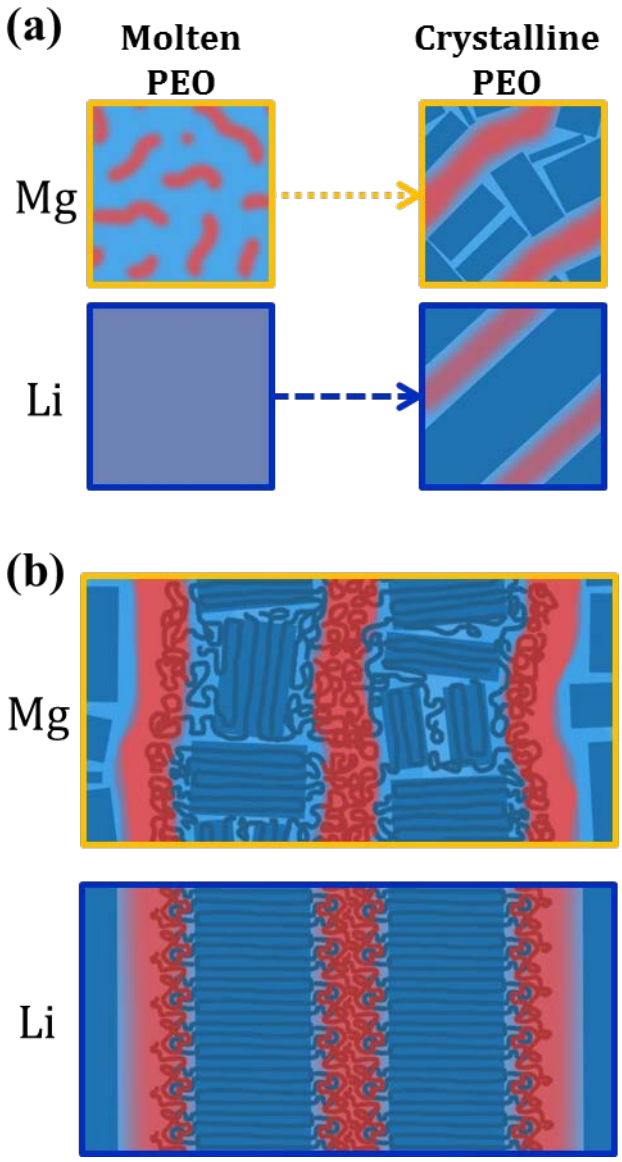

Figure 6.8: (a) Schematics depicting possible composition profiles and (b) chain configurations that could lead to the observed invariants, as well as the scattering profiles in Figure 6.4 and Figure 6.5. The cartoons highlighted in gold represent PEO-P[(STFSI)$_2$Mg], and the cartoons highlighted with blue represent PEO-P[(STFSI)Li]. Red indicates P(STFSI), cyan indicates amorphous PEO, blue parallelograms indicate crystalline PEO, and violet indicates well-mixed PEO and P(STFSI).

In Figure 6.8 we provide schematics of the nanostructures of molten and semicrystalline PEO-P[(STFSI)$_2$Mg] and PEO-P[(STFSI)Li] that are consistent with the structural insights from the static SAXS/WAXS and STEM measurements in Figure 6.2, as well as with the *in situ* scattering data from Figure 6.4 and Figure 6.5. In Figure 6.8a, we demonstrate periodic concentration fluctuations in the PEO-P[(STFSI)$_2$Mg] melt, whereas PEO-P[(STFSI)Li] is homogeneous. Upon crystallization, the periodicity of the fluctuations in PEO-P[(STFSI)$_2$Mg] increases by nearly a factor of two, consistent with the *in situ* SAXS from PEO-

P[(STFSI)$_2$Mg](5-2.0). We believe the timescales associated with thickening of the P[(STFSI)$_2$Mg]-rich domains causes the slower crystallization kinetics and increased disorder observed in the magnesiated samples. In contrast, crystallization in PEO-P[(STFSI)Li] leads to the formation of periodic fluctuations from the homogeneous melt, as revealed by an increase in the scattering invariant upon crystallization. In Figure 6.8b, we demonstrate possible chain configurations that could lead to the semicrystalline structures depicted in Figure 6.8a. In the magnesiated case, the crystallization of PEO can occur within regions of relatively pure PEO, but competes with the phase-separated P[(STFSI)$_2$Mg] domains, and must effectively "break out" to form long-range crystals. Consequently, many small crystallites of varying orientation are formed within the PEO-rich domains, consistent with the irregular lamellae observed by STEM (Figure 6.2d), the isotropic 2D SAXS patterns (Appendix A2), and the increased diffuse WAXS scattering (Figure 6.3a) observed for all magnesiated samples. Since PEO crystal growth in PEO-P[(STFSI)Li] occurs within a homogeneous medium, the crystals can propagate unobstructed over large distances. This leads to the large well-ordered lamellar crystals (Figure 6.2c) that produce anisotropic 2D SAXS patterns (Appendix A2).

6.4 Conclusion

Single-ion conducting block copolymers composed of the ion-containing polymer, poly(styrene-4-sulfonyltrifluoromethylsulfonyl)imide (P(STFSI)), and the ion solvating/conducting polymer, poly(ethylene oxide) (PEO) represent a unique class of materials, wherein single-ion conduction occurs by solvating and transporting the cation with the neutral polymer block (PEO).[35–37] In this study we report on the crystallization behavior of PEO within a matched set library of lithiated (PEO-P[(STFSI)Li]) and magnesiated (PEO-P[(STFSI)$_2$Mg]) single-ion conducting block copolymers. PEO crystallinity, melting temperatures (T_m), and crystallization temperatures (T_c) were probed using DSC on samples prepared with consistent thermal pretreatment. The same thermal pretreatment was applied to samples used to study the nanostructure of the polymers with SAXS/WAXS and STEM. The DSC crystallinity was found to be constant between matched pairs, indicating that the cation identity does not significantly influence the total amount of PEO crystallization after thermal pretreatment. However, the differences in nanostructure and crystal perfection between matched pairs, as observed through SAXS/WAXS and STEM, indicate that crystal formation is influenced by the nature of the cation.

The kinetics of PEO crystallization was probed using *in situ* SAXS/WAXS during isothermal crystallization at 35 °C. In all cases we found that increasing the molecular weight (i.e., volume fraction) of the ionic block slows down crystallization. Interestingly, there was also a marked difference in the crystallization times between matched pairs. Analyzing the invariant of the *in situ* X-ray scattering profiles provides insight into the kinetics of crystallization. During crystallization, the invariant increases with time for the lithiated samples, while it decreases with time for the magnesiated samples. Traditional analysis of the invariant using an ideal two-phase model with sharp interfaces cannot describe this result: acknowledging the diffuse nature of the interface between crystalline and amorphous domains is necessary. In the lithiated sample, the width of the interface decreases substantially during crystallization, due to the formation of well-define PEO crystal domains. In the magnesiated sample there is only a modest decrease in interfacial width, indicating that the magnesiated microphases were relatively well-defined prior

to PEO crystallization. We conclude that the required thickening of these P[(STFSI)$_2$Mg]-rich domains is upon PEO crystallization is responsible for the both the slowed kinetics and defect-prone crystals and crystallization-induced nanostructures observed in the magnesiated samples. Thus the cation identity, which we previously demonstrated to play a large role in melt morphology[114], also influences the crystallization within single-ion conducting block copolymers.

6.5 Acknowledgements

This work was supported by the Joint Center for Energy Storage Research, an Energy Innovation Hub funded by the U.S. Department of Energy (DOE), Office of Science, Basic Energy Sciences (BES). Thermal analysis was performed at the Molecular Foundry at Lawrence Berkeley National Laboratory. X-ray scattering experiments were performed at Lawrence Berkeley National Laboratory's Advance Light Source, Beamline 7.3.3. The Molecular Foundry and Beamline 7.3.3 of the Advanced Light Source are supported by the Director of the Office of Science, Office of Basic Energy Sciences, of the U.S. Department of Energy under Contract No. DE-AC02-05CH11231. We thank Polite Stewart, Chenhui Zhu, and Eric Schaible for their assistance with the setup and operation of Beamline 7.3.3. We thank Xi (Chelsea) Chen for obtaining the STEM micrographs of the semi crystalline samples.

6.6 Nomenclature

6.6.1 Abbreviations

AgB	Silver Behenate
DSC	Differential Scanning Calorimetry
PEO	Poly(ethylene oxide)
PEO-P[(STFSI)Li]	Poly(ethylene oxide)-*b*-poly[(styrene-4-sulfonyltrifluoromethylsulfonyl)imide lithium]
PEO-P[(STFSI)$_2$Mg]	Poly(ethylene oxide)-*b*-poly[(styrene-4-sulfonyltrifluoromethylsulfonyl)imide magnesium]
P(STFSI)	poly[(styrene-4-sulfonyltrifluoromethylsulfonyl)imide] – unspecified ion
PS	Polystyrene
S-D	Sample to Detector Distance
SAXS	Small Angle X-ray Scattering
STEM	Scanning Transmission Electron Microscopy
WAXS	Wide Angle X-Ray Scattering

6.6.2 Symbols

d_{SAXS}	Inter-lamellar domain spacing, nm
ΔH_m	Experimentally measured specific melting enthalpy, Jg^{-1}
ΔH_m^o	Ideal specific melting enthalpy, Jg^{-1}
I	Scattering intensity, cm^{-1}
I_{peak}	Intensity at $q = q^*$, normalized by the molten sample intensity, cm^{-1}
L_{cryst}	Crystal lamellae thickness, nm
$M_{n,PEO}$	Number average molecular weight of PEO block, kg mol^{-1}

$M_{n,PSTFSI}$	Number average molecular weight of P(STFSI) block, kg mol^{-1}
N_{PEO}	Number average degree of polymerization of PEO block, --
N_{PSTFSI}	Number average degree of polymerization of P(STFSI) block, --
q	Magnitude of the scattering vector, nm^{-1}
q^*	Position of the primary SAXS peak, nm^{-1}
q_0	Location where I_{scr} and I_{molten} are evaluated to calculate ϕ_{cr}^{WAXS}, nm^{-1}
Q	Scattering invariant, cm^{-1}
Q_{diff}	Scattering invariant for two-phase system with diffuse interfaces, cm^{-1}
Q_{ideal}	Ideal scattering invariant for two-phase system, cm^{-1}
q_{max}	Maximum attainable scattering angle in SAXS, nm^{-1}
q_{min}	Minimum attainable scattering angle in SAXS, nm^{-1}
T_c	Crystallization temperature, °C
T_g	Glass transition temperature, °C
T_m	Melting temperature, °C
v_{PEO}	Monomer volume for EO, nm^3
v_{PSTFSI}	Monomer volume for STFSI, nm^3
V_{chain}	Volume of a single chain, nm^3
w_{PEO}	Weight fraction of PEO, --
x_{cr}^{DSC}	Mass fractional crystallinity calculated through DSC, --

6.6.3 Greek

α	Areal density of block junctions on the PEO crystal surface, nm^{-2}
χ	Flory-Huggins interaction parameter, --
ϕ_{am}^{scr}	Amorphous volume fraction of a semi crystalline polymer block, --
ϕ_{am}	Total amorphous volume fraction within a semi crystalline polymer, --
ϕ_{cr}^{DSC}	Volume fractional crystallinity calculated through DSC, --
ϕ_{cr}^{WAXS}	Volume fractional crystallinity calculated through WAXS, --
ϕ_{PEO}	Volume fraction of the PEO block, --
ϕ_{PSTFSI}	Volume fraction of the P(STFSI) block, --
λ	Scattering wavelength, nm
ρ_{am}^{PEO}	Density of amorphous poly(ethylene oxide), gcm^{-3}
ρ_{cr}^{PEO}	Density of crystalline poly(ethylene oxide), gcm^{-3}
ρ_{PSTFSI}	Density of poly[(styrene-4-sulfonyltrifluoromethylsulfonyl)imide], gcm^{-3}
θ	Scattering angle, rad

6.7 Supporting Information

6.7.1 Thermal Analysis

The differential scanning calorimetry (DSC) measurements were performed as follows: the samples were loaded into the DSC and equilibrated at 30 °C, then a heat scan of 5 °C/min was used to reach 130 °C. PEO melting temperature was extracted from this scan. Samples were then held isothermally for 20 minutes in order to let them equilibrate. Next, the samples were equilibrated directly to -80 °C and heated at 10 °C/min back up to 130 °C. If observed, the T_g of PEO was determined from this scan using the inflection point of the change in slope with

"Glass/Step Transition" function in the TA Universal Analysis software package. Finally, a controlled cooling scan of 5 °C/min from 130 °C down to 0, -20, or -80 °C was used to determine the crystallization point of PEO. The data from each scan are shown in Figure 5.S1-Figure 5.S3 in the previous chapter.

The PEO crystalline fraction for the thermally pre-treated samples was calculated based on the measured enthalpy of melting (ΔH_m) and the ideal enthalpy of melting for PEO (ΔH_m°). In the case of the block copolymer samples, the measured specific enthalpy of melting must be scaled by the weight fraction of PEO in order to calculate the crystalline fraction. First, the PEO weight fraction (w_{PEO}) is calculated from Equation S6.1

$$w_{PEO} = \frac{M_{n,PEO}(\text{gmol}^{-1})}{M_{n,PSTFSI}(\text{gmol}^{-1}) + M_{n,PEO}(\text{gmol}^{-1}) + M_{BB}^\circ(\text{gmol}^{-1})} \tag{S6.1}$$

where $M_{BB}^\circ = 381(\text{gmol}^{-1})$ is the molecular weight of the Blocbuilder MA group used for the chain growth of P(STFSI). The crystallinity is then calculated as described in the main text.

6.7.2 Scattering Analysis

6.7.2.1 Determination of Primary SAXS Peak Position

The primary SAXS peak position for every sample was determined through non-linear least squares regression of Gaussian peak on a power-law sloping background, as shown in Equation S6.2

$$I_{fit}(q) = I_{pwr}(q) + I_{gauss}(q) = y_1 q^{-y_2} + Ce^{\left[-\left(\frac{q-q^*}{W}\right)^2\right]} \tag{S6.2}$$

where y_1 and y_2 are constants that are manually set before the least squares optimization, C and W are fitted constants relating the peak height and width, respectively, and q^* is the fitted primary peak position. Equation S6.2 provided excellent fits to the primary peak of all semicrystalline samples except for PEO-P[(STFSI)$_2$Mg](5-3.2), which had scattering intensity from the broad disordered scattering peak in the vicinity of the primary peak. In this case, two Gaussian peaks on a power-law background were used to determine q^* (Equation S6.3).

$$I_{fit}(q) = I_{pwr}(q) + I_{gauss}(q) = y_1 q^{-y_2} + Ce^{\left[-\left(\frac{q-q^*}{W}\right)^2\right]} + De^{\left[-\left(\frac{q-q_d^*}{W_d}\right)^2\right]} \tag{S6.3}$$

The position (q_d^*) and width (W_d) of the disordered scattering peak were independently determined and held constant during the least squares optimization used to determine the semi-crystalline peak position, where C, w, q^*, and D were simultaneously optimized to achieve the best fit to the data. The peak fits for each sample are shown in Figure 6.S2 through Figure 6.S8 below, with the corresponding fitting parameters provided in the plot inset.

6.7.2.2 Determination of Absolute Crystallinity from WAXS Data

The PEO crystalline fraction (ϕ_{cr}^{WAXS}) was calculated from the absolute WAXS intensity using a method based on that proposed by Goppel[56] and more recently applied by Balko and coworkers[127]. The general framework of this method is based on measuring the amorphous fraction of polymer in a semi crystalline sample, which then allows one to compute the crystalline fraction through a simple molar balance. The amorphous fraction is determined by selecting a position in q-space (q_0) where there is significant scattering intensity for the fully amorphous material (within the amorphous WAXS halo), but lies between Bragg peaks in the semicrystalline sample. The assumption is that if q_0 is far enough away from any Bragg peak and incoherent scattering intensity is negligible, then the intensity measured at q_0 will only be due to the amorphous scattering volume. Thus if one can measure WAXS for a sample in both the semi crystalline (*scr*) and fully molten (*molten*) states, the amorphous fraction (ϕ_{am}), and hence crystalline fraction (ϕ_{cr}^{WAXS}), can be approximated by

$$\phi_{am} \approx \frac{I_{scr}(q_0)}{I_{molten}(q_0)} = 1 - \phi_{cr}^{WAXS} \tag{S6.4}$$

where $I_{scr}(q_0)$ and $I_{molten}(q_0)$ are simply the measured intensity of the semi crystalline and molten samples at q_0, respectively. We applied this approximation to the PEO(5) sample using the absolute WAXS intensity at q = 14.6 (nm^{-1}) from the semi crystalline (35 °C) and molten (90 °C) states (see Figure 6.S2) and calculated ϕ_c^{WAXS} =0.79-0.80, which is remarkably similar to the value of $\phi_{cr}^{DSC} = 0.83$ obtained through thermal analysis. Encouraged by this result, we have attempted to adapt this simple approximation toward the analysis of the ion-containing block copolymers.

We start with the simple case of a single component (*1comp*, homopolymer) semicrystalline material. In such a sample, WAXS intensity can arise from both coherent (*coh*) and incoherent (*inc*) scattering events. All structural information comes from the coherent scattering events that can be separated into crystalline (*cr*) and amorphous (*am*) contributions. Thus the absolute intensity for a single component semicrystalline material ($I_{scr}^{1comp}(q)$) is

$$I_{scr}^{1comp}(q) = I_{coh}(q) + I_{inc}(q) = \phi_{cr} I_{cr}(q) + \phi_{am} I_{am}(q) + I_{inc}(q) \tag{S6.5}$$

where $I_{coh}(q)$ and $I_{inc}(q)$ are the intensities due to coherent and incoherent scattering, ϕ_{cr} and ϕ_{am} are the crystalline and amorphous volume fractions, $I_{cr}(q)$ and $I_{am}(q)$ are their corresponding absolute scattering functions. By choosing an appropriate value of $q = q_0$ such that $I_{cr}(q_0)$ and $I_{inc}(q_0)$ become negligible, the intensity at q_0 can be defined as

$$I_{scr}^{1comp}(q_0) = \phi_{cr} I_{cr}(q_0) + \phi_{am} I_{am}(q_0) + I_{inc}(q_0) \approx \phi_{am} I_{am}(q_0) \tag{S6.6}$$

If the sample is subsequently melted (and incoherent scattering is still negligible) the intensity of the molten sample can be written as

$$I_{molten}^{1comp}(q_0) = I_{am}(q_0) + I_{inc}(q_0) \approx I_{am}(q_0) \tag{S6.7}$$

And thus taking the results from Equations S6.6 and S6.7, we can write

$$\frac{I_{scr}^{1comp}(q_0)}{I_{molten}^{1comp}(q_0)} \approx \frac{\phi_{am} I_{am}(q_0)}{I_{am}(q_0)} = \phi_{am} \tag{S6.8}$$

which is equivalent to Equation S6.4. It is important to note that equations S6.4 and S6.8 assume that the density and scattering function at q_0 of the amorphous phase have a negligible dependence on temperature.

A similar approach can be taken to determine the amorphous fraction of a semicrystalline material in a two component system, such as the ion-containing block copolymers of PEO and P(STFSI) in this study. In this case, the total semicrystalline WAXS intensity is given by

$$I_{scr}^{PEO-PSTFSI}(q) = \phi_{cr}\phi_{PEO} I_{cr}(q) + \phi_{am}\phi_{PEO} I_{am}^{PEO}(q) + \phi_{PSTFSI} I_{am}^{PSTFSI}(q) + I_{inc}(q) \tag{S6.9}$$

where $I_{scr}^{PEO-PSTFSI}$ is the absolute scattering intensity of the sample, ϕ_{PEO} and ϕ_{PSTFSI} are the total volume fractions of PEO and P(STFSI), and $I_{cr}^{PEO}(q)$, $I_{am}^{PEO}(q)$, and $I_{am}^{PSTFSI}(q)$ are the scattering functions for each phase (ϕ_{cr} and ϕ_{am} are defined as in Equation S6.5). If, once again, we can choose a q_0 such that $I_{cr}^{PEO}(q_0)$ and $I_{inc}(q_0)$ are negligible, then we can approximate the semicrystalline scattering as

$$I_{scr}^{PEO-PSTFSI}(q_0) \approx \phi_{am}\phi_{PEO} I_{am}^{PEO}(q_0) + \phi_{PSTFSI} I_{am}^{PSTFSI}(q_0) \tag{S6.10}$$

Also, as before, the scattering from the fully molten ($I_{molten}^{PEO-PSTFSI}(q_0)$) sample is approximately

$$I_{molten}^{PEO-PSTFSI}(q_0) \approx \phi_{PEO} I_{am}^{PEO}(q_0) + \phi_{PSTFSI} I_{am}^{PSTFSI}(q_0) \tag{S6.11}$$

It is clear that Equations S6.10 and S6.11 alone cannot be used to determine ϕ_{am}; however, if an additional measurement of the scattering from molten homopolymer PEO is performed, we can also define

$$I_{molten}^{PEO}(q_0) \approx I_{am}^{PEO}(q_0) \tag{S6.12}$$

Where $I_{molten}^{PEO}(q_0)$ is the intensity of the fully molten PEO sample evaluated at the same temperature and q_0 as $I_{molten}^{PEO-PSTFSI}(q_0)$. If we scale the value of $I_{molten}^{PEO}(q_0)$ by the volume fraction of PEO in the single-ion conducting block copolymer, we can use Equations S6.11 and S6.12 to determine $I_{am}^{PSTFSI}(q_0)$ by

$$I_{molten}^{PEO-PSTFSI}(q_0) - \phi_{PEO} I_{molten}^{PEO}(q_0) \approx \phi_{PSTFSI} I_{am}^{PSTFSI}(q_0) \tag{S6.13}$$

Equation S6.13 provides $I_{am}^{PSTFSI}(q_0)$, which should be independent of sample and, with knowledge of ϕ_{PSTFSI}, can be used with Equations S6.10 and S6.11 to determine the crystallinity of PEO. In practice, we calculate the LHS of Equation S6.13 for each sample, and plot the result

vs ϕ_{PSTFSI}. We then extract the slope of a linear regression through the origin to determine $I_{am}^{PSTFSI}(q_0)$, as shown in Figure 6.S1 below. With a value for $I_{am}^{PSTFSI}(q_0)$ known, Equation S6.14 below can be used to determine the amorphous PEO fraction (ϕ_{am}) in the ion-containing block copolymers, and hence ϕ_c^{WAXS} through the relation in Equation S6.4.

$$\frac{I_{scr}^{PEO-PSTFSI}(q_0) - \phi_{PSTFSI} I_{am}^{PSTFSI}(q_0)}{I_{molten}^{PEO-PSTFSI}(q_0) - \phi_{PSTFSI} I_{am}^{PSTFSI}(q_0)} \approx \frac{\phi_{am}\phi_{PEO} I_{am}^{PEO}(q_0)}{\phi_{PEO} I_{am}^{PEO}(q_0)} = \phi_{am} \qquad \text{(S6.14)}$$

In addition to the assumptions noted for Equations S6.4 and S6.8, Equation S6.14 requires that the total volume fraction of PEO (ϕ_{PEO}) is independent of temperature and PEO crystallinity, and that $I_{am}^{PSTFSI}(q_0)$ is insensitive to temperature. The variation of ϕ_{PEO} with varying crystalline fraction for the samples in the present study should be less than 4%. In the present study, we used $q_0 = 14.6$ (nm^{-1}) with the absolute scattering data from PEO(5) and lithiated and magnesiated single-ion conducting block copolymers after thermal pretreatment and at 90 °C to determine ϕ_c^{WAXS} (values provided in Table 6.3 of the main text). As shown in Figure 6.S1, we found $I_{am}^{PSTFSI}(q_0) = 0.258 \pm 0.009$ cm^{-1} for the lithiated samples, and $I_{am}^{PSTFSI}(q_0) = 0.269 \pm 0.007$ cm^{-1} for the magnesiated samples. Furthermore, the temperature-dependent WAXS data for the molten block copolymer samples in Figure 6.S3 through Figure 6.S8 below indicate that $I_{am}^{PSTFSI}(14.6\ \text{nm}^{-1})$ is insensitive to temperature. Table 6.S1 bleow provides the absolute intensity values extracted for the semicrystalline samples and the molten samples (90 °C) that were used to calculate ϕ_c^{WAXS}.

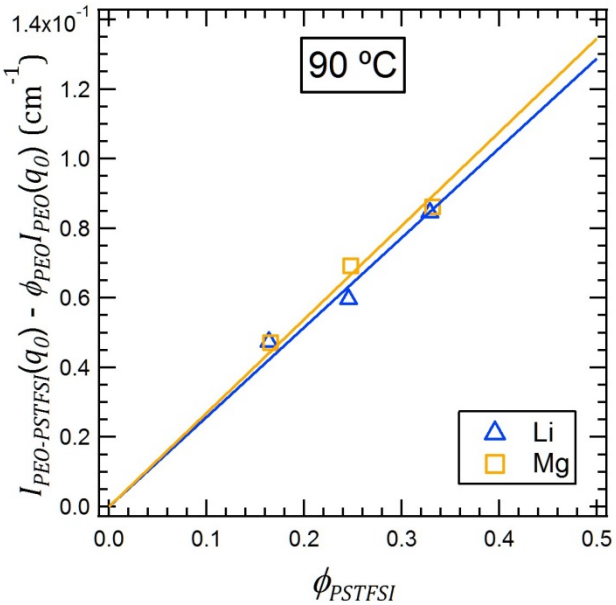

Figure 6.S1: Plot of the LHS of Equation S6.13 versus ϕ_{PSTFSI}. Blue triangles represent PEO-P[(STFSI)Li] samples and gold squares represent PEO-P[(STFSI)$_2$Mg] samples. Solid lines represent linear regressions through the origin, whose slopes (RHS of Equation S6.13) yield: $I_{am}^{PSTFSI}(q_0) = 0.258 \pm 0.009$ cm^{-1} for the lithiated samples and $I_{am}^{PSTFSI}(q_0) = 0.269 \pm 0.007$ cm^{-1} for the magnesiated samples.

6.7.3 Results from Scattering Analysis

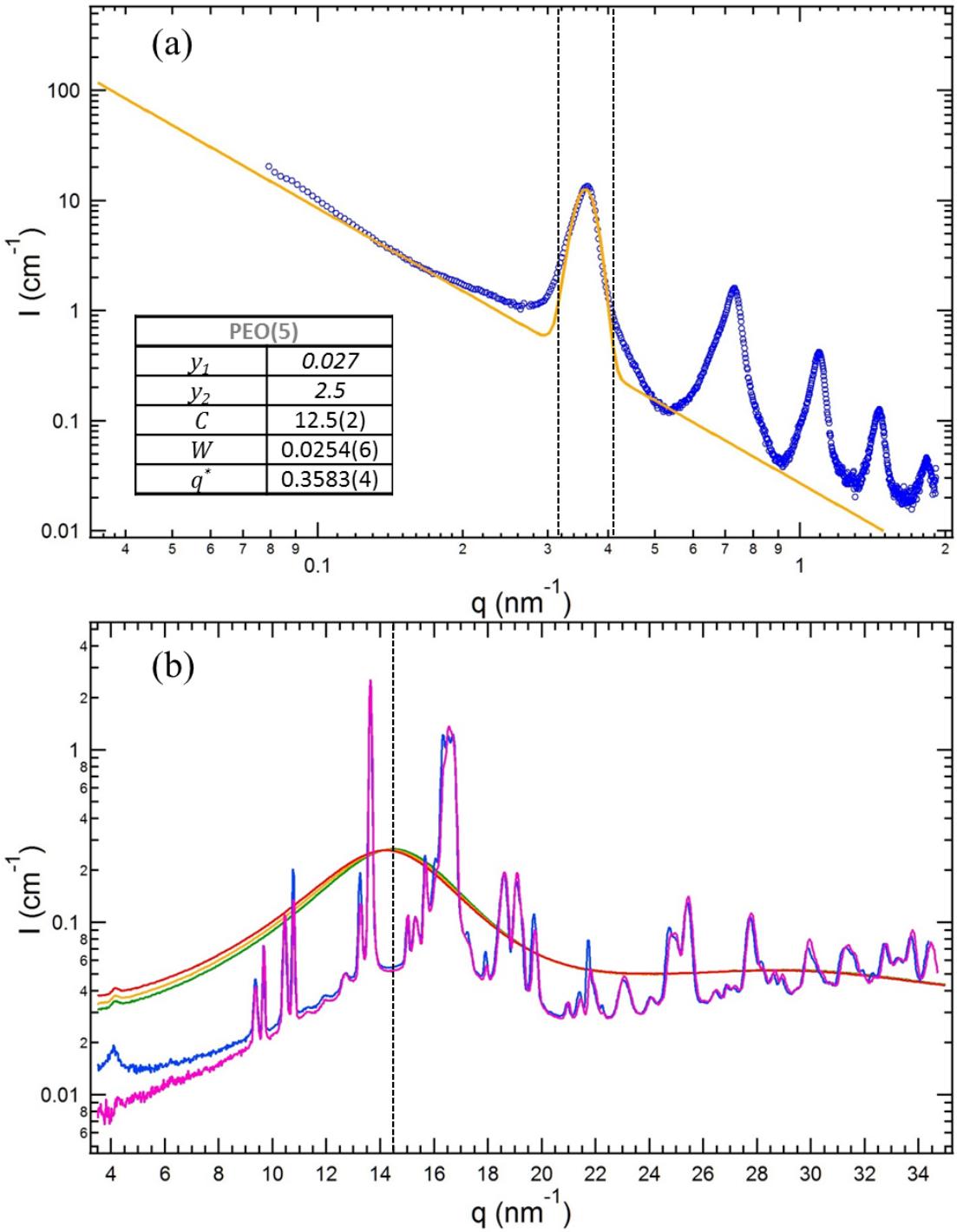

Figure 6.S2: (a) Fitting of the primary SAXS peak from PEO(5) with Equation S6.2. The data are indicated by blue circles, the optimal fit is represented by the gold line, and the interval over which the nonlinear least squares optimization was performed is indicated by the dashed vertical lines. The parameters for the fitting function are provided in the inset, where the number in parentheses represents the uncertainty (one standard deviation) in the last digit. (b) WAXS profiles for PEO(5) at 30 °C (pink and blue), 90 °C (green), 110 °C (gold), and 130 °C (red). The vertical dashed line indicates where the intensity was recorded in order to calculate the crystalline fraction of PEO at 35 °C.

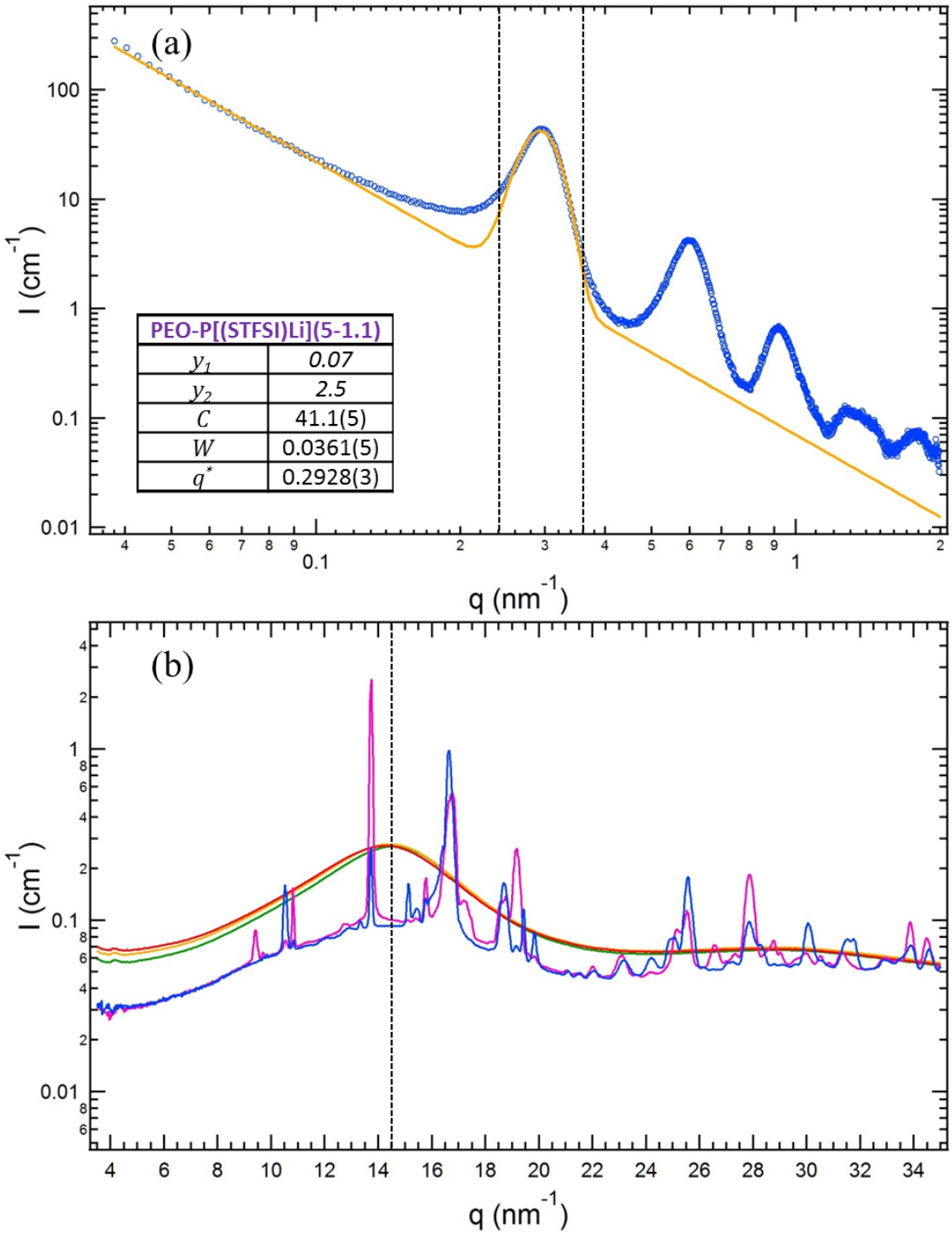

Figure 6.S3: (a) Fitting of the primary SAXS peak from PEO-P[(STFSI)Li](5-1.1) at 30 °C with Equation S6.2. The data are indicated by blue circles, the optimal fit is represented by the gold line, and the interval over which the nonlinear least squares optimization was performed is indicated by the dashed vertical lines. The parameters for the fitting function are provided in the inset, where the number in parentheses represents the uncertainty (one standard deviation) in the last digit. (b) WAXS profiles for PEO-P[(STFSI)Li](5-1.1) at 30 °C (pink and blue), 90 °C (green), 110 °C (gold), and 130 °C (red). The vertical dashed line indicates where the intensity was recorded in order to calculate the crystalline fraction of PEO-P[(STFSI)Li](5-1.1) at 30 °C.

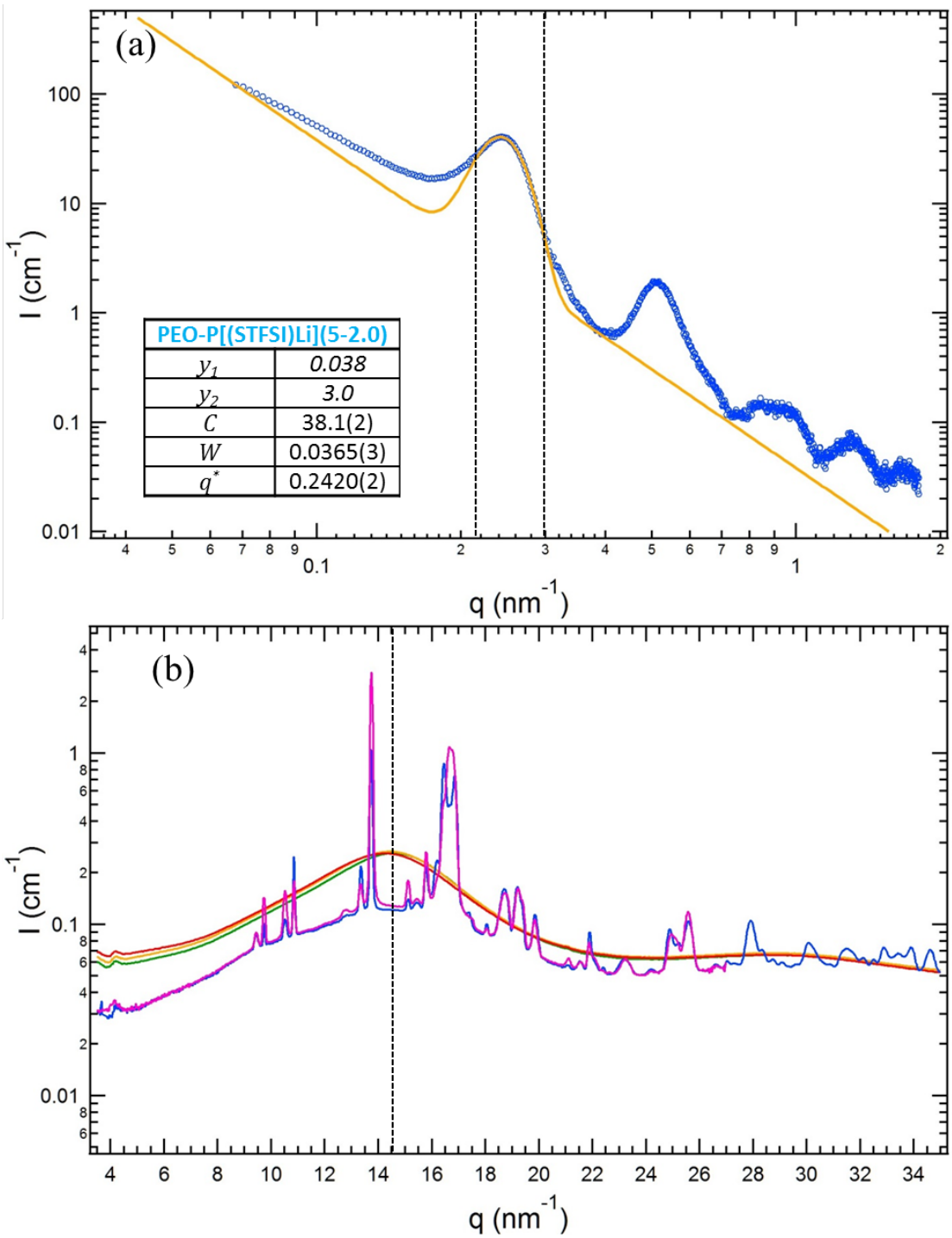

Figure 6.S4: (a) Fitting of the primary SAXS peak from PEO-P[(STFSI)Li](5-2.0) at 30 °C with Equation S6.2. The data are indicated by blue circles, the optimal fit is represented by the gold line, and the interval over which the nonlinear least squares optimization was performed is indicated by the dashed vertical lines. The parameters for the fitting function are provided in the inset, where the number in parentheses represents the uncertainty (one standard deviation) in the last digit. (b) WAXS profiles for PEO-P[(STFSI)Li](5-2.0) at 30 °C (pink and blue), 90 °C (green), 110 °C (gold), and 130 °C (red). The vertical dashed line indicates where the intensity was recorded in order to calculate the crystalline fraction of PEO-P[(STFSI)Li](5-2.0) at 30 °C.

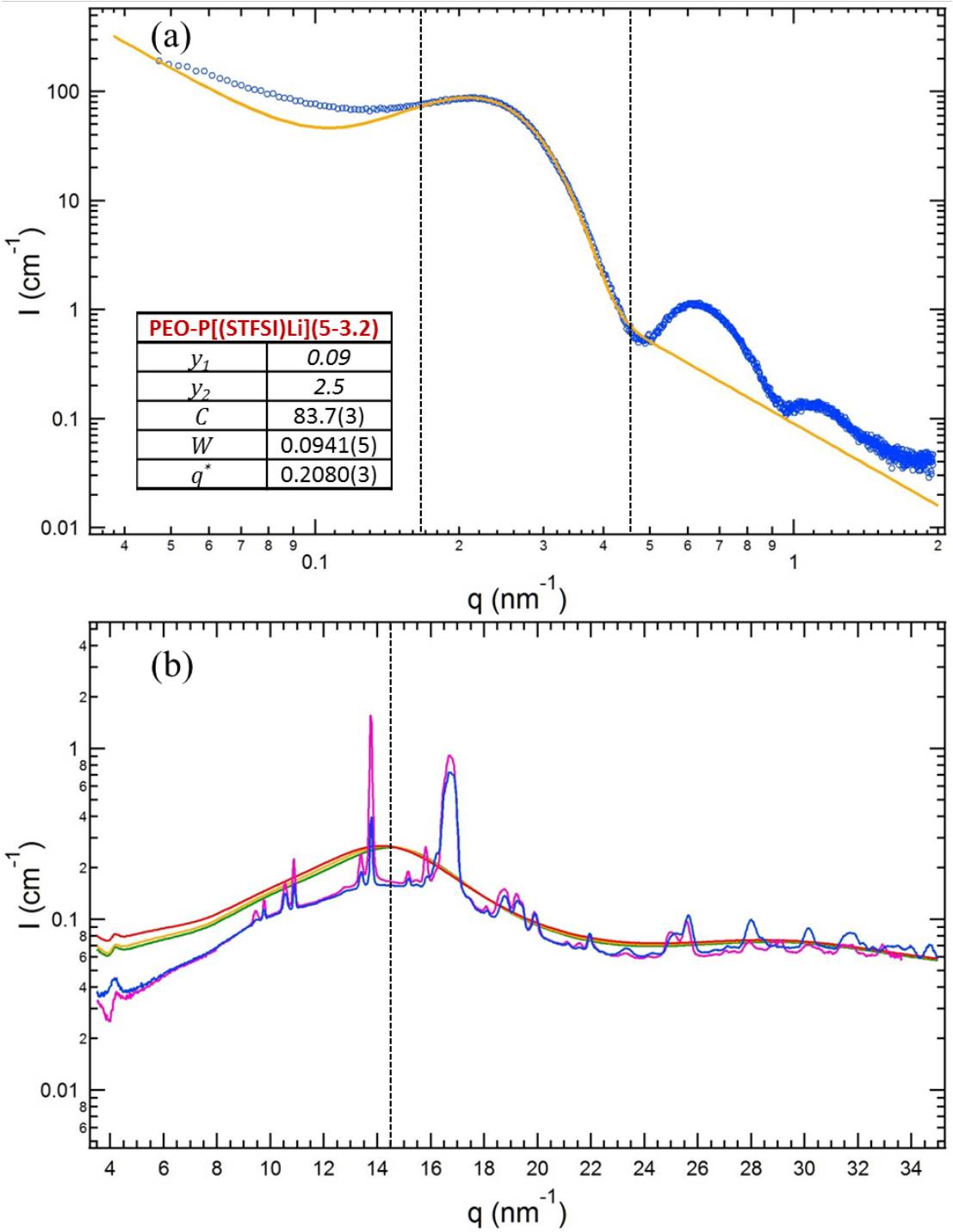

Figure 6.S5: (a) Fitting of the primary SAXS peak from PEO-P[(STFSI)Li](5-3.2) at 30 °C with Equation S6.2. The data are indicated by blue circles, the optimal fit is represented by the gold line, and the interval over which the nonlinear least squares optimization was performed is indicated by the dashed vertical lines. The parameters for the fitting function are provided in the inset, where the number in parentheses represents the uncertainty (one standard deviation) in the last digit. (b) WAXS profiles for PEO-P[(STFSI)Li](5-3.2) at 30 °C (pink and blue), 90 °C (green), 110 °C (gold), and 130 °C (red). The vertical dashed line indicates where the intensity was recorded in order to calculate the crystalline fraction of PEO-P[(STFSI)Li](5-3.2) at 30 °C.

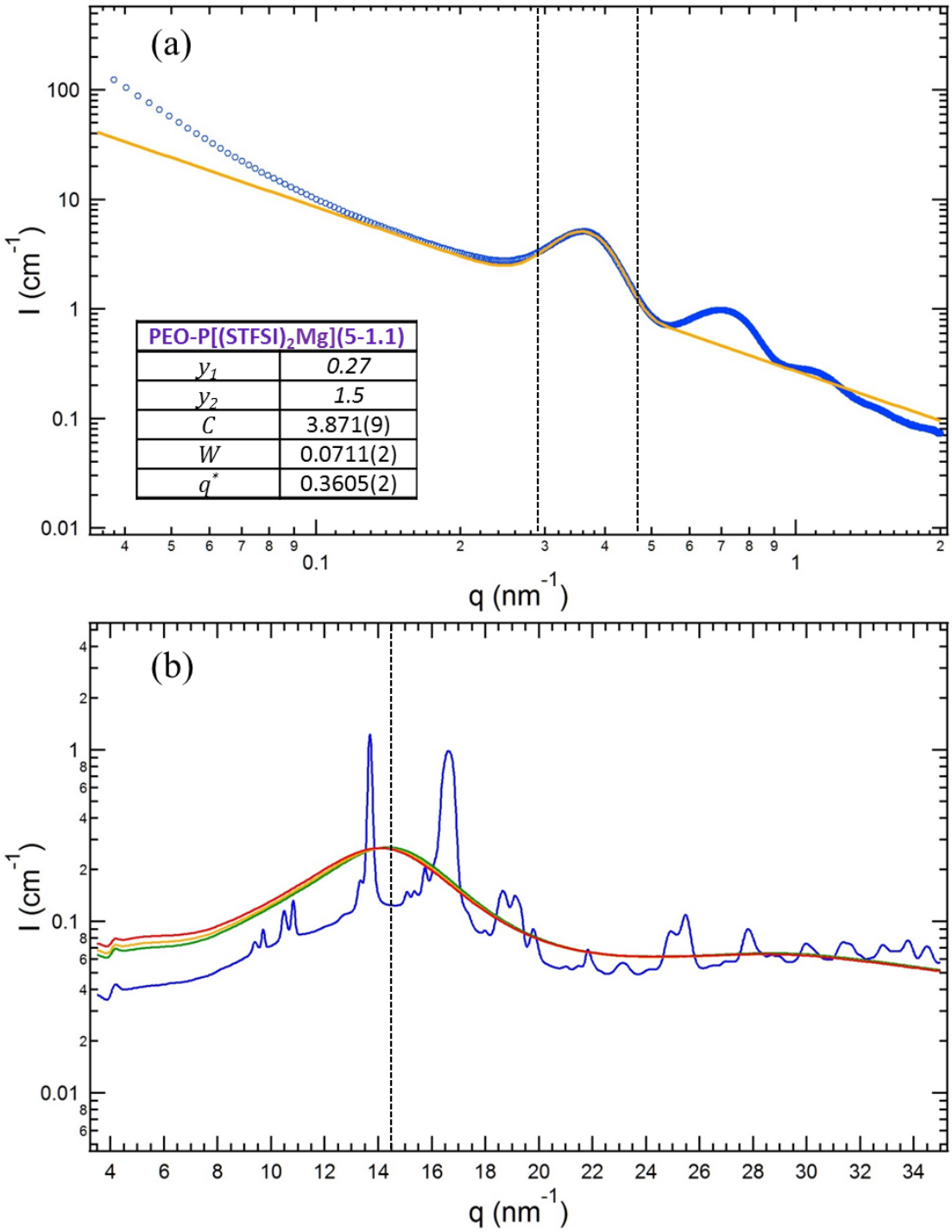

Figure 6.S6: (a) Fitting of the primary SAXS peak from PEO-P[(STFSI)$_2$Mg](5-1.1) at 35 °C with Equation S6.2. The data are indicated by blue circles, the optimal fit is represented by the gold line, and the interval over which the nonlinear least squares optimization was performed is indicated by the dashed vertical lines. The parameters for the fitting function are provided in the inset, where the number in parentheses represents the uncertainty (one standard deviation) in the last digit. (b) WAXS profiles for PEO-P[(STFSI)$_2$Mg](5-1.1) at 30 °C (blue), 90 °C (green), 110 °C (gold), and 130 °C (red). The vertical dashed line indicates where the intensity was recorded in order to calculate the crystalline fraction of PEO-P[(STFSI)$_2$Mg](5-1.1) at 35 °C.

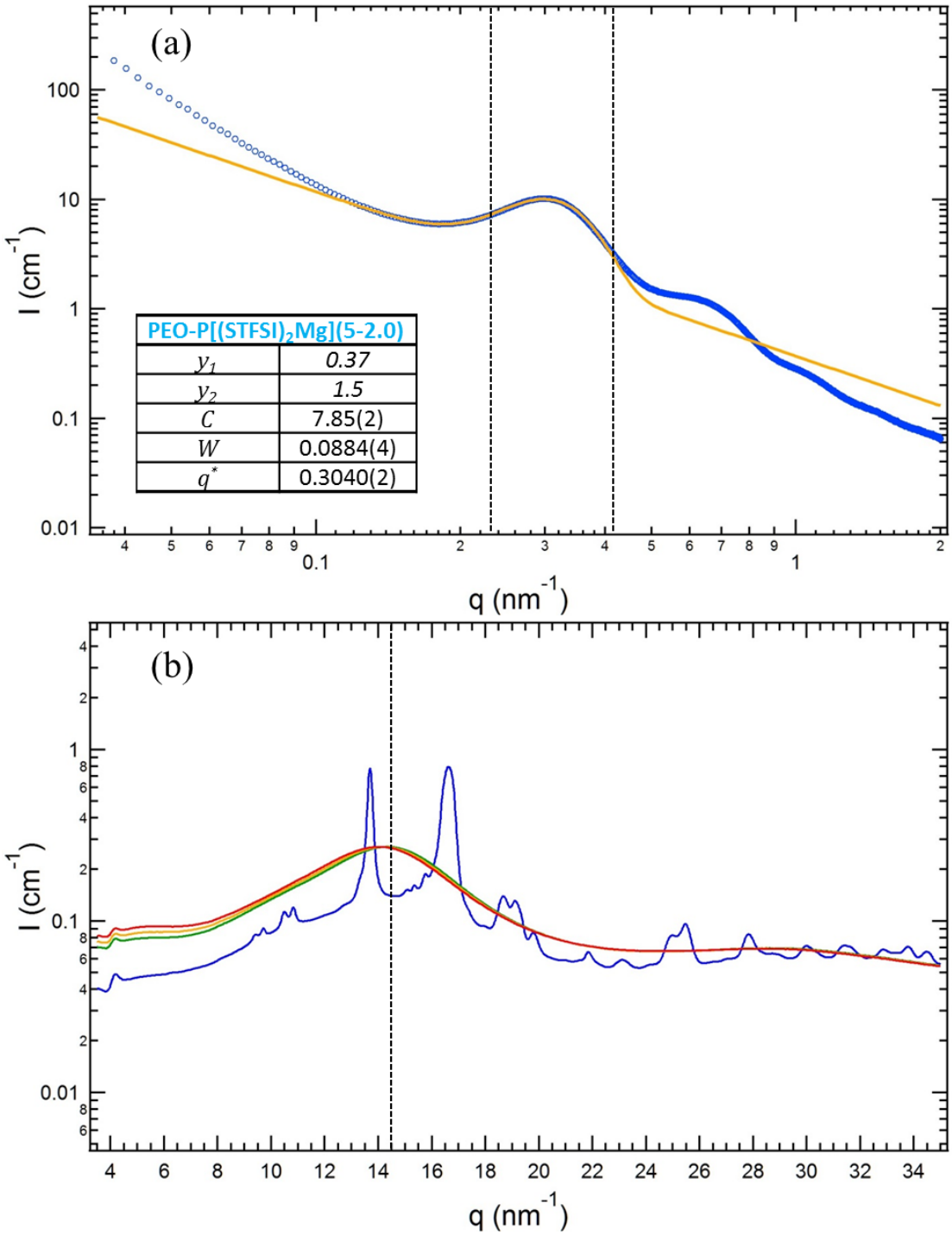

Figure 6.S7: (a) Fitting of the primary SAXS peak from PEO-P[(STFSI)$_2$Mg](5-2.0) at 35 °C with Equation S6.2. The data are indicated by blue circles, the optimal fit is represented by the gold line, and the interval over which the nonlinear least squares optimization was performed is indicated by the dashed vertical lines. The parameters for the fitting function are provided in the inset, where the number in parentheses represents the uncertainty (one standard deviation) in the last digit. (b) WAXS profiles for PEO-P[(STFSI)$_2$Mg](5-2.0) at 30 °C (blue), 90 °C (green), 110 °C (gold), and 130 °C (red). The vertical dashed line indicates where the intensity was recorded in order to calculate the crystalline fraction of PEO-P[(STFSI)$_2$Mg](5-2.0) at 35 °C.

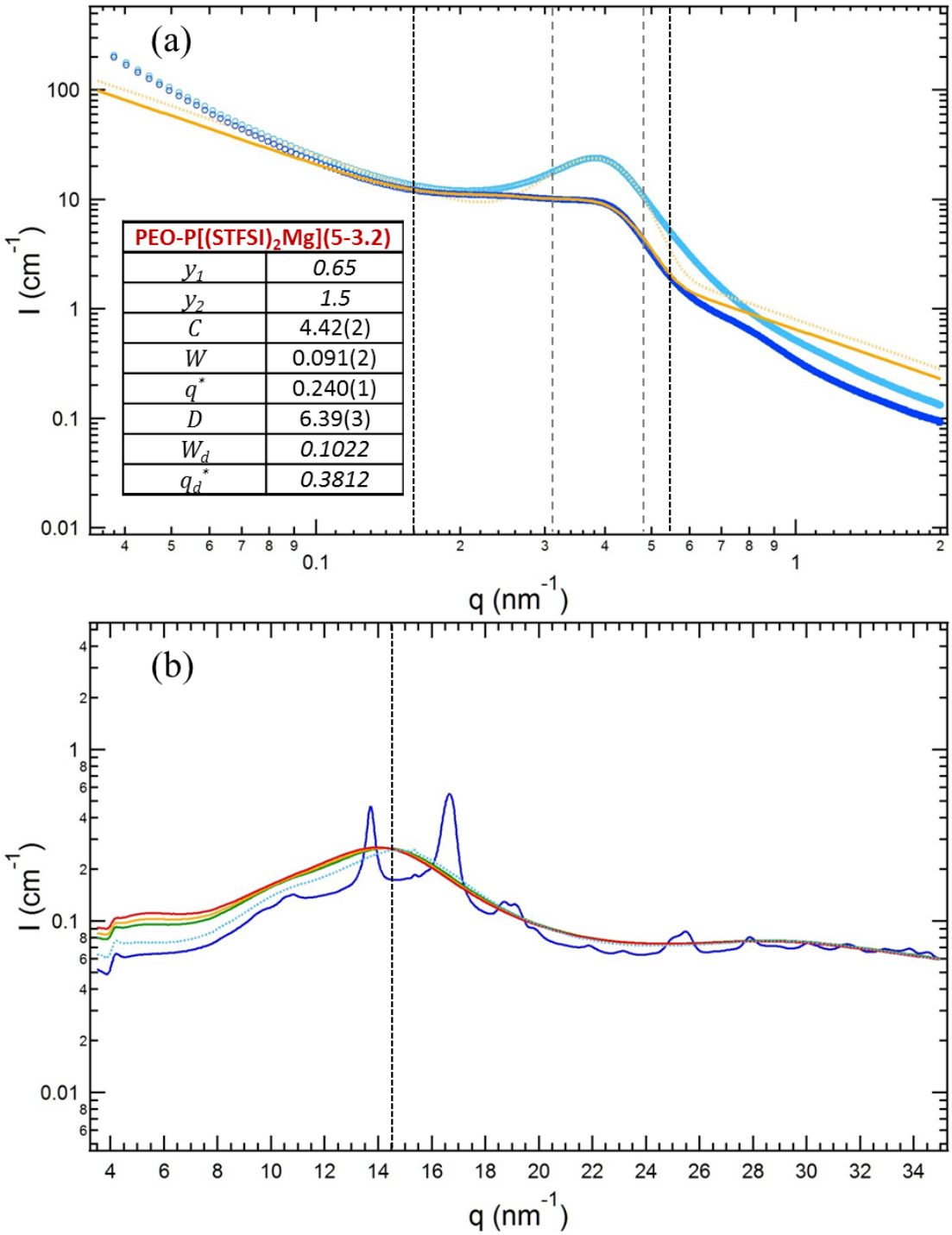

Figure 6.S8: (a) Fitting of the primary SAXS peak from PEO-P[(STFSI)$_2$Mg](5-3.2) at 35 °C with Equation S6.3. Initially the scattering from amorphous PEO-P[(STFSI)$_2$Mg](5-3.2) at 35 °C (cyan circles) was fitted (dashed light gold line) with Equation S6.2 within the region indicated by the vertical gray long-dashed lines. The fitted amorphous peak parameters were then used in Equation S6.3, where the amorphous peak height (*D*) was adjusted simultaneously with the semi-crystalline primary peak parameters to achieve the best fit (gold line) to the data (blue circles) over the interval indicated by the vertical black short-dashed lines. The parameters for the fitting function are provided in the inset, where the number in parentheses represents the uncertainty (one standard deviation) in the last digit. (b) WAXS profiles for PEO-P[(STFSI)$_2$Mg](5-3.2) at 30 °C (blue and cyan), 90 °C (green), 110 °C (gold),

and 130 °C (red). The vertical dashed line indicates where the intensity was recorded in order to calculate the crystalline fraction of PEO-P[(STFSI)$_2$Mg](5-3.2) at 35 °C.

Table 6.S1: Summary of the WAXS amorphous fraction analysis performed on PEO(5) and all of the single-ion conducting block copolymers.

Sample Name	*I(q= 14.6)* (30°C)	*I(q= 14.6)* (35°C)	*I(q= 14.6)* (90 °C)	ϕ_{cr}^{WAXS}
PEO-P[(STFSI)Li](5-3.2)	0.158[a] 0.165[b]	--	0.263	0.55[b]-0.59[a]
PEO-P[(STFSI)Li](5-2.0)	0.122[a] 0.127[b]	--	0.260	0.67[b]-0.70[a]
PEO-P[(STFSI)Li](5-1.1)	0.093[a] 0.100[b]	--	0.269	0.75[b]-0.78[a]
PEO-P[(STFSI)$_2$Mg](5-3.2)	--	0.173	0.263	0.52
PEO-P[(STFSI)$_2$Mg](5-2.0)	--	0.140	0.269	0.64
PEO-P[(STFSI)$_2$Mg](5-1.1)	--	0.124	0.268	0.65
PEO(5)	--	0.053[b] 0.056[a]	0.265	0.79[a]-0.80[b]

[a] Value from the blue-highlighted sector averages in Figure A2.2, Figure A2.3, Figure A2.5, and Figure A2.7
[b] Value from the pink-highlighted sector averages in Figure A2.2, Figure A2.3, Figure A2.5, and Figure A2.7

6.7.4 Nomenclature

6.7.4.1 Abbreviations

LHS	Left Hand Side
RHS	Right Hand Side

6.7.4.2 Subscripts

am	Amorphous
coh	Coherent
cr	Crystalline
inc	Incoherent
molten	Molten
scr	Semicrystalline

6.7.4.3 Superscripts

1comp	Single component
PEO	Poly(ethylene oxide)
PEO-PSTFSI	Poly(ethylene oxide)-*b*-poly[(styrene-4-sulfonyltrifluoromethylsulfonyl)imide]
PSTFSI	poly[(styrene-4-sulfonyltrifluoromethylsulfonyl)imide]

6.7.4.4 Symbols

C	Coefficient in Equations S6.2- S6.3, cm^{-1}
D	Coefficient in Equation S6.3, cm^{-1}
I_{fit}	Fitting function used to determine the location of the primary SAXS peak, cm^{-1}

M_{BB}°	Molecular weight of Blocboulder MA, g mol^{-1}
W	peak-width fitting parameter in Equations S6.2- S6.3, nm,$^{-1}$
W_d	peak-width fitting parameter for disordered peak in Equation S6.3, nm^{-1}
y_1	Coefficient in Equations S6.2- S6.3, cm^{-1}
y_2	Coefficient in Equations S6.2- S6.3, --

6.7.4.5 Greek

ϕ_{am}	Amorphous volume fraction of a semicrystalline polymer block, --
ϕ_{cr}	Crystalline volume fraction of a semicrystalline polymer block, --
ϕ_{cr}^{WAXS}	Volumetric crystallinity calculated through WAXS, --
ϕ_{PEO}	Total volume fraction of PEO block, --
ϕ_{PSTFSI}	Total volume fraction of P(STFSI) block, --

Chapter 7 - Relationship between Mobility and Lattice Strain in Electrochemically Doped Poly(3-hexylthiophene)[§]

Abstract

Conjugated semiconducting polymers, such as poly(3-hexylthiophene) (P3HT), are poised to play an integral role in the development organic electronic devices; however, their performance is governed by factors that are intrinsically coupled: dopant concentration, carrier mobility, crystal structure, and mesoscale morphology. We utilize synchrotron x-ray scattering and electrochemical impedance spectroscopy to probe the crystal structure and electronic properties of P3HT *in situ* during electrochemical doping. We show that doping strains the crystalline domains, coincident with an exponential increase in hole mobility. We believe these observations provide guidance for the development of improved theoretical models for charge transport in semiconducting polymers.

7.1 Introduction

The mechanism of charge transport within conjugated semiconducting polymers has been the subject of extensive study for decades, especially in recent years with the advent of commercial applications such as organic photovoltaics (OPVs), organic field effect transistors (OFETs), and organic light emitting diodes (OLEDs).[131–133] A common feature of all semiconducting polymers is a high degree of structural disorder, which generally requires an inter-molecular hopping mechanism to achieve macroscopic charge transport.[134,135] While models that describe electron transport in completely disordered semiconducting polymers have been developed [136,137], the performance of many materials, such as poly(3-hexylthiophene) (P3HT), are complicated by their semicrystalline nature, which creates discrete regions of higher structural order within a disordered amorphous matrix[138–141]. The electronic performance of these materials has been shown to be significantly influenced by the degree of ordering, which in turn can be affected by polymer molecular weight, purity, and processing conditions.[142–145] In addition to all of these complexities, the method of producing charge carriers (e.g. field effect, chemical doping, or electrochemical doping) and their total concentration can lead to measured carrier mobilities that differ by up to four orders of magnitude.[48,142,146,147] Establishing the underpinnings of experimental observations is non-trivial due to these competing and interrelated effects. The goal of this work is to present clear experimental evidence of how doping influences the microstructure and electronic properties of P3HT while all other parameters that affect electron transport are kept constant.

The key to our experimental approach is the use of the block copolymer a poly(3-hexylthiophene)-b-poly(ethylene oxide) (P3HT-PEO). P3HT-PEO has previously been shown to microphase separate into nanoscale domains of P3HT-rich and PEO-rich phases. Previous studies have shown that the crystalline lattice of P3HT is not perturbed by the presence of the PEO block.[43,45] By adding an ionic species, such as lithium bis(trifluoromethanesulfonyl)imide (LiTFSI), the PEO-rich domains can act as an electrolyte, providing efficient transport of ionic

[§] This chapter was reported in *ACS Macro Lett.* **2015**, *4*, 1386–1391.

species throughout the bulk material.[43,45] The intimate mixing of electrolyte and P3HT (i.e. each P3HT nanodomain is effectively a thin film surrounded by PEO/LiTFSI electrolyte) enables the construction of the all solid-state electrochemical cell shown in Figure 7.1. The all-solid cell prevents any complexities that might arise from solvent swelling of the P3HT, thus any changes to the structure of P3HT during electrochemical doping can be directly attributed to the doping process itself. Furthermore, unlike most electrochemical doping studies, which utilize an electrode coated with a thin film of conjugated polymer soaked in an electrolyte, the P3HT-PEO/LiTFSI layer in our solid-state cell is typically ~350 μm thick. The thick film geometry allows us to effectively measure the bulk electronic properties (through-plane) and the bulk P3HT microstructure (transmission geometry) *in situ* during electrochemical doping. To our knowledge, this is the first time that both the P3HT microstructure and its electronic properties have been simultaneously measured as a function of doping level.

7.2 Experimental

The block copolymer studied in this work was synthesized, purified, and characterized using the techniques described by Javier et al[45]. It has a P3HT molecular weight (M_{P3HT}) of 7 (kg mol^{-1}) and a PEO molecular weight (M_{PEO}) of 2 (kg mol^{-1}) and will be referred to as P3HT-PEO(7-2). Salt-containing P3HT-PEO samples were prepared by mixing solutions of polymer (P3HT-PEO in benzene) and salt (LiTFSI in tetrahydrofuran), followed by freeze drying to yield a solid powder of P3HT-PEO(7-2)/LiTFSI with a salt concentration of r = 0.085, where r denotes the molar ratio of Li^+ ions to ethylene oxide (EO) moieties[43]. The degree of P3HT crystallinity in the freeze-dried samples was determined to be 62% by differential scanning calorimetry using an ideal melting enthalpy of 33 (J g^{-1}) (see Supporting Information (SI) Section S1 for details)[127]. Small angle X-ray scattering (SAXS) was used to probe the nanostructure of P3HT-PEO(7-2)/LiTFSI, which was found to be consistent with the nanofibrillar morphology observed in previous work[42,43,45] (SI Section S2).

In situ electrochemical cells used for X-ray scattering were assembled using similar techniques to Patel et al[42] (detailed description in SI Section S3). In short, the P3HT-PEO(7-2)/LiTFSI is contained within a spacer of defined area and thickness, with one nickel mesh electrode on the surface and another embedded within. A solid polymer electrolyte consisting of polystyrene-b-poly(ethylene oxide) (SEO) mixed with LiTFSI served as a separator and lithium metal was used as the counter electrode. The entire cell was assembled and vacuum-sealed in an airtight pouch within an argon glovebox. A schematic of the sample cell is shown in Figure 7.1 below.

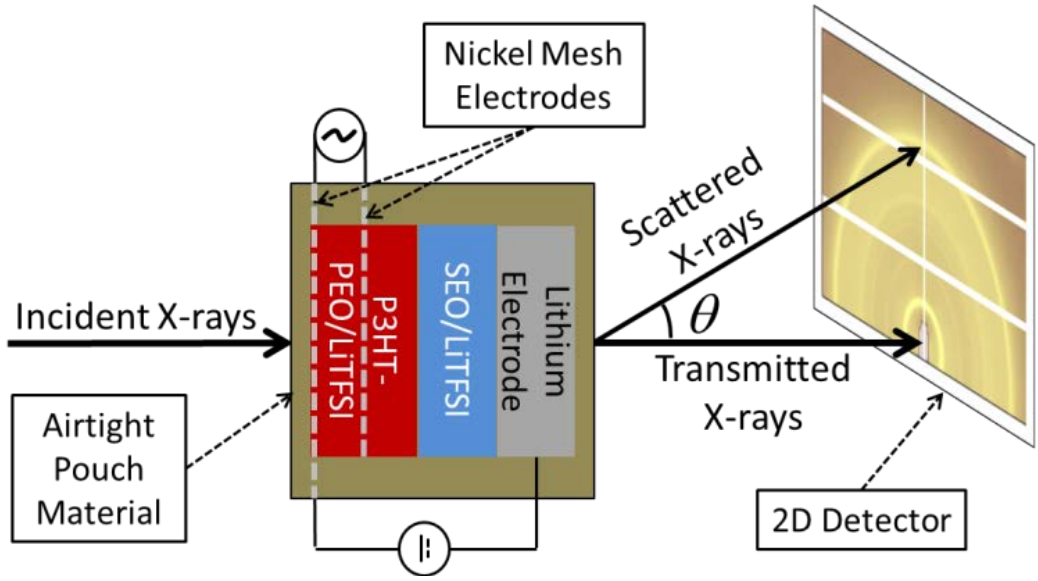

Figure 7.1: A schematic of the *in situ* electrochemical cell and the configuration used for WAXS measurements.

All experiments were performed at 90 ^{o}C to ensure that the PEO phase was amorphous with suitable ionic conductivity[43]. Electrochemical oxidation (doping) was performed galvanostatically between the outer nickel mesh electrode and the lithium electrode (anode) with a current density such that each oxidation step was completed in 30 minutes. Doping was performed in increments of $r_{ox} = 0.005$ or $r_{ox} = 0.01$, where r_{ox} is the ratio of electrons removed to the total number of hexylthiophene (HT) monomers. At the end of each oxidation step, the cell was allowed to relax for 20 minutes and then the negative lead was disconnected from the lithium electrode and connected to the inner (embedded) nickel mesh electrode (see Figure 7.1). The conductive properties of the P3HT were then probed using potentiostatic electrochemical impedance spectroscopy (PEIS) between the two nickel mesh electrodes. The open circuit potential between the two mesh electrodes was zero (within instrumental resolution) prior to commencing the impedance measurements, which implies a uniform charge distribution through the P3HT-PEO electrode. The bulk conductivity of P3HT (σ) was calculated from $\sigma = \delta L/AR$, where δ is a correction factor to account for the mesh electrode geometry, L is the distance between the two nickel mesh electrodes, A is the area defined by the sample spacer, and R is the measured bulk electronic resistance. As noted previously[42], there is hysteresis in the polymer properties between consecutive doping and dedoping experiments; all data shown in this letter are from the second oxidation cycle of both samples. Sections S4-S6 in the SI provide detailed information for the electrochemical oxidation and PEIS measurements, electrode geometry correction factor, and first (break-in) cycle conductivity values, respectively.

Two of such cells described above were taken to a syncrotron wide angle x-ray scattering (WAXS) apparatus on Beamline 7.3.3 at the Advanced Light Source, Lawrence Berkeley National Laboratory[60]. The P3HT crystalline structure was probed *in situ* during electrochemical oxidation by performing WAXS measurements immediately after PEIS measurements, approximately 30 minutes after each oxidation step. The isotropic 2D scattering patterns were azimuthally averaaged using the Nika macro developed by Jan Ilavsky[61] to yield 1D data sets of intensity (I) versus the magnitude of the scattering vector, $q = \frac{4\pi}{\lambda}\sin\left(\frac{\theta}{2}\right)$, where λ is the

radiation wavelength and θ is the scattering angle depicted in Figure 7.1. Scattering intensity from a sample cell containing all of the components except the P3HT-PEO(7-2)/LiTFSI was used for background correction (SI Section S7). Peak positions of interest (q^*) were determined by fitting the corrected WAXS data in the vicinity of the peak with a Lorentzian function of the form, $I(q) = I_o + \frac{C_1}{(q-q^*)^2+C_2}$,where I_o, C_1, C_2, and q^* were varied in Igor Pro's built-in Levenberg-Marquardt nonlinear least-squares algorithm to achieve the best fit.

7.3 Results and Discussion

In Figure 7.2a, we plot P3HT conductivity as a function of doping level from two replicate samples. The data are consistent with those obtained previously for electrochemically doped P3HT-PEO[42], which were corrected by the electrode geometry factor (δ) (see SI Section S5) and are plotted for comparison. The increase in conductivity seen in Figure 7.2a can, in principle, be attributed to changes in both carrier concentration and carrier mobility. We calculate mobility (μ_{ox}) using $\mu_{ox} = \sigma / ne$, where n is the electrochemically generated charge carrier density, and e is the elementary charge.[42] We assume all current transferred between the electrodes of electrochemical cell goes directly toward generating charge carriers. Consequently, n is the upper limit for charge carrier density, which in turn yields the lower bound for the calculated charge carrier mobility. In Figure 7.2b, we plot mobility as function of doping level. It is clear from Figure 7.2b that the level of electrochemical doping in P3HT-PEO(7-2)/LiTFSI strongly influences carrier mobility.

For reference, in Figure 7.2c we plot the hole mobility of P3HT measured by electrochemical doping of P3HT-PEO/LiTFSI with the comprehensive list of homopolymer P3HT field effect mobility values (μ_{FET}) formerly assembled by Noriega and Rivnay *et al*[138]. The abscissa in Figure 7.2c is the average degree of polymerization of P3HT. Agreement is seen between the two approaches for $r_{ox} \geq 0.06$ despite the differences in polymer samples (block copolymer versus homopolymer), doping mechanisms, and direction of measurement (in-plane versus through-plane). Similar observations for P3HT homopolymer soaked in liquid electrolytes have been reported[48], suggesting that the P3HT domains in P3HT-PEO conduct through the same mechanism as homopolymer P3HT.

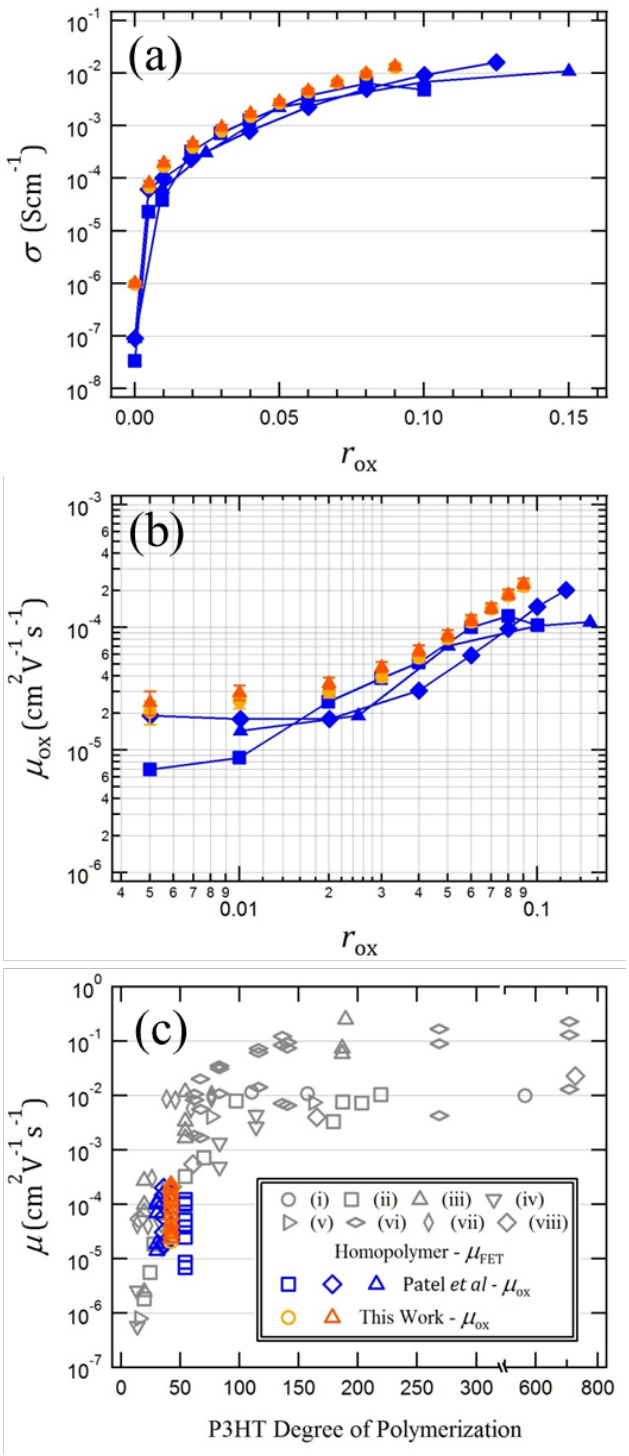

Figure 7.2: (a) Electronic conductivity plotted as a function of doping level for P3HT-PEO. Blue data are taken from ref [42]: squares P3HT-PEO(9-2), diamonds P3HT-PEO(6-2), triangles P3HT-PEO(5-4). The yellow circles and orange triangles were measured for replicate samples of P3HT-PEO(7-2) in this work. (b) The corresponding mobility values from plot (a) as a function of doping level. (c) P3HT mobility plotted as a function of P3HT degree of polymerization for the P3HT-PEO samples [same data labels as (a) and (b)], along with the compilation of field effect mobility values (black symbols) assembled by Noriega and Rivnay *et al*[148]. References to the individual studies are as follows: circles (i)[148], squares (ii)[149], triangles (iii)[150], upside-down triangles (iv)[151], sideways triangles (v)[143], horizontal diamonds (vi)[152], vertical diamonds (vii)[153], and square diamonds (viii)[154].

The impact of electrochemical doping on the P3HT microstructure is revealed through the WAXS profiles shown in Figure 7.3. Scattering peaks corresponding to the (*h*00) direction are observed at 3.62 nm^{-1} (100), 7.23 nm^{-1} (200), and 10.85 nm^{-1} (300) in the undoped polymer (r_{ox} = 0). These peaks correspond to the lamellar stacking of the P3HT backbones and are labelled with black triangles. The peak observed at 16.69 nm^{-1} in the undoped polymer (r_{ox} = 0), labeled by a blue triangle, corresponds to the (020) direction and is related to the π-π stacking distance between adjacent chains.[155–158] A schematic of the P3HT structure is provided in the inset of Figure 7.3a. Any un-labeled peak in Figure 7.3a can be attributed to the parasitic scattering from the empty electrochemical cell (Figure 7.S7 in the SI). All of the WAXS peaks related to the P3HT crystal structure shift upon doping. The lamellar stacking peaks shift to lower *q*-values (Figure 7.3b), while the π-π stacking peak shifts to higher q-values (Figure 7.3c) as P3HT is oxidized. The oxidation of P3HT is balanced by the deposition of lithium on the anode (see Figure 7.1). The $TFSI^-$ anion left behind in the process must migrate into the P3HT microphase to balance the charge from the hole generated by the removal of an electron from P3HT. The expansion of the lamellar stacking seen in Figure 7.3b is attributed to the incorporation of the $TFSI^-$ anions into the lattice. This result is consistent with the results of Kawai and coworkers, where homopolymer P3HT films were electrochemically doped in an electrolyte bath[49,159], as well as the analogous intercalation of small molecules and fullerenes between the side chains of other conjugated polymer systems[160]. Interestingly, electrochemical doping results in a contraction of the π-π stacking distance (Figure 7.3c). Although the exact nature of the stress that induces the π-π stacking contraction is still under investigation, we demonstrate below that the decrease in the distance between polymer chains in the π-π stacking direction is strongly correlated with the observed increase in hole mobility as the doping level is increased. It is important to note that the widths and areas under each peak are unaffected by doping, indicating that crystallinity is not disrupted by the intercalation of the $TFSI^-$ dopant ion. Furthermore, no additional scattering peaks are observed as doping is increased; therefore, we conclude that all of the observed structural changes can simply be viewed as doping induced strains to the existing orthorhombic crystal lattice of undoped P3HT[49,156,159,161].

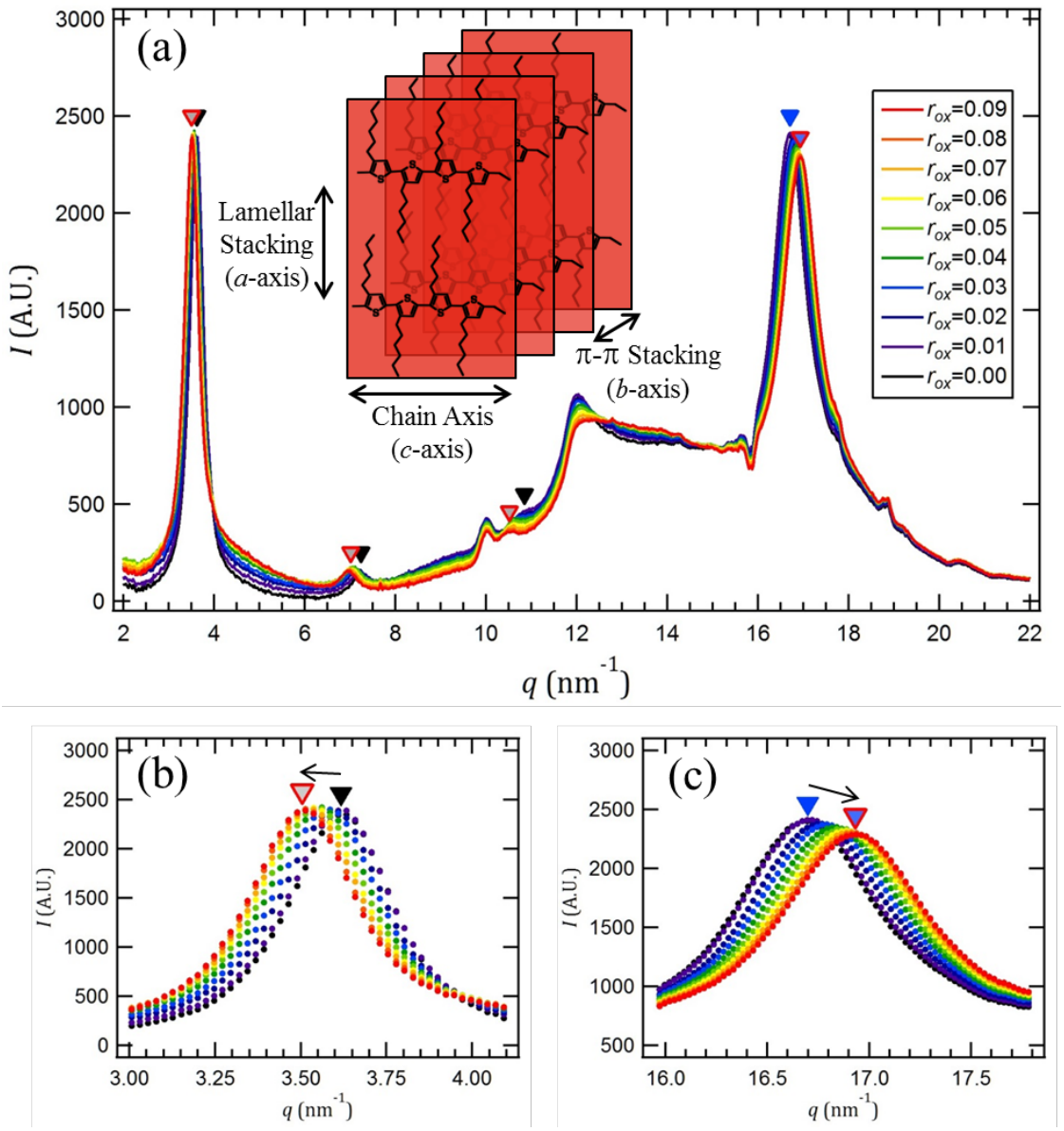

Figure 7.3: (a) Representative 1D WAXS profiles for one of the P3HT-PEO replicates for a range of doping levels. Peaks corresponding to P3HT (100, 200, 300, and 020) are indicated with triangle markers. The solid black and blue markers indicate the peak positions before doping and the red highlighted markers indicate the peak positions at r_{ox} =0.09. The inset provides a schematic for the crystal structure of P3HT. (b) Expanded view of the (100) peaks. (c) Expanded view of the (020) peaks.

We quantify the lattice strain in the P3HT crystal structure by: $\text{Lattice Strain}\ (\%) = \frac{d(r_{ox})-d_o}{d_o} \times 100$, where $d(r_{ox})$ and d_o are the doped and un-doped real-space lattice dimensions, respectively, determined from either the (100) lamellar stacking or the (020) π-π stacking peak positions. Figure 7.4a quantifies the effect of electrochemical oxidation on the P3HT lattice in the lamellar and π-π stacking directions. Comparing Figure 7.2b and Figure 7.4a reveals that both hole mobility and lattice strain scale with the logarithm of doping level for r_{ox} >0.01. It is widely accepted that macroscopic transport in P3HT is limited by the rate of interchain hopping in the π-π stacking direction, where there is the largest degree of interchain coupling[134,162] . In

Figure 7.4b we plot the hole mobility as a function of the π-π stacking lattice strain wherein a clear exponential relationship between the mobility and π-π interchain spacing is observed. Interestingly, hopping-based models predict that mobility is proportional to the square of the interchain charge transfer integral (t^2), which is often modeled as an exponential, $t=t_o e^{(-\gamma a)}$, where (a) is the intersight (π-π interchain) distance, and the prefactor (t_o) and exponential coefficient (γ) govern the extent to which lattice structure influence charge transport.[134,148,163] Although other factors such as changes in the density of states (DOS) will also contribute to the observed changes in mobility with doping level[135,136,164], the clear correlation between lattice strain and mobility demonstrates that structural changes during electrochemical doping are intrinsically linked to the subsequent charge transport characteristics of electrochemically doped conjugated polymers.

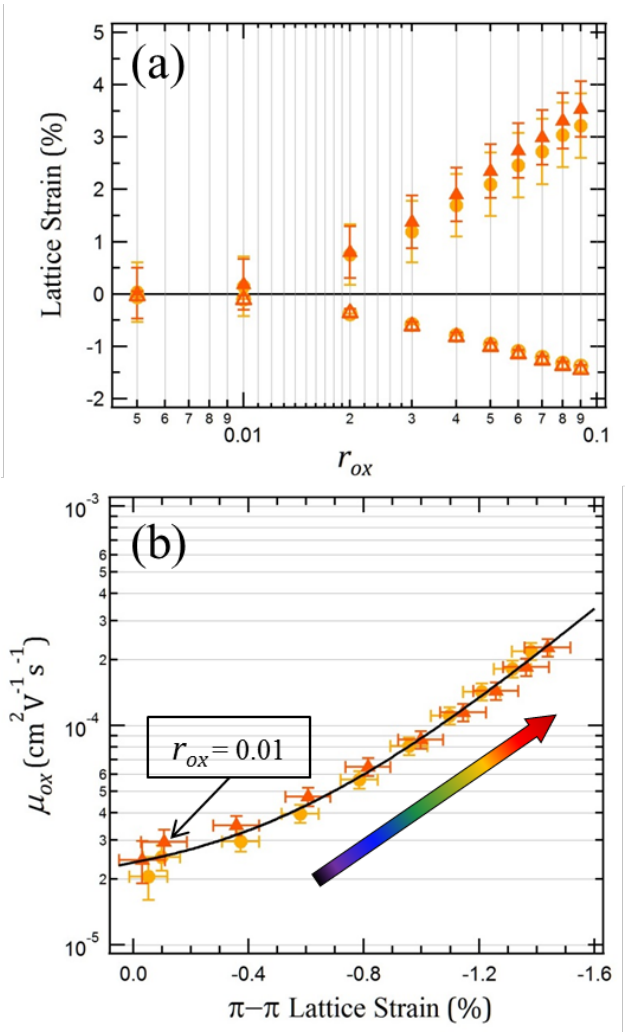

Figure 7.4: (a) Lattice strain of the two replicate samples plotted as a function of doping level. Closed symbols correspond to the lamellar stacking (100) spacing and open symbols represent the π-π stacking (020) spacing. (b) Mobility plotted as a function of the π-π lattice strain for the two replicate samples in this work. The solid line represents the best fit of $\mu_{ox} = y_o + De^{(-\tau\alpha)}$, where α is the π-π lattice strain (%) and y_o, D, and τ are fit parameters found to be y_o = 1.8(3)x10^{-5} (cm^{2}V^{-1}s^{-1}), D = 5(1) x10^{-6} (cm^{2}V^{-1}s^{-1}), and τ = 2.6(2). The colored arrow indicates the direction of increasing doping level.

7.4 Conclusions

In summary, through the use of a custom designed all solid-state electrochemical cell, we have conclusively demonstrated that electrochemical doping of P3HT induces systematic changes to the packing structure of crystalline P3HT domains. The induced strains in the crystalline lattice, positive in the (100) direction and negative in the (020) direction, facilitate the incorporation of anionic ($TFSI^-$) dopants and tighter packing in the π-π stacking direction. *In situ* measurement of the conductive properties of the P3HT, which allowed us to directly compare the mobility of hole charge carriers with the induced strains in the P3HT lattice, revealed an exponential relationship between the π-π stacking distance and the measured mobility. We believe that our results shed new light on the interplay between crystal structure, dopant concentration, and charge transport in semi-crystalline conjugated polymers.

7.5 Acknowledgements

This work was primarily supported by the Joint Center for Energy Storage Research, an Energy Innovation Hub funded by the U.S. Department of Energy (DOE), Office of Science, Basic Energy Sciences (BES). X-ray scattering experiments were performed at Lawrence Berkeley National Laboratory's Advance Light Source, Beamline 7.3.3. Beamline 7.3.3 of the Advanced Light Source is supported by the Director of the Office of Science, Office of Basic Energy Sciences, of the U.S. Department of Energy under Contract No. DE-AC02-05CH11231.

7.6 Nomenclature

7.6.1 Abbreviations

DOS	Density of States
EO	Ethylene oxide
HT	Hexyl Thiophene
LiTFSI	Lithium bis(trifluoromethanesulfonyl)imide
OFET	Organic Field Effect Transistor
OLED	Organic Light Emitting Diode
OPV	Organic Photovoltaic
P3HT	Poly(3-hexylthiophene)
P3HT-PEO	Poly(3-hexylthiophene)-*block*-poly(ethylene oxide) diblock copolymer
PEO	Poly(ethylene oxide)
PEIS	Potentiostatic Electrochemical Impedance Spectroscopy
SAXS	Small Angle X-ray Scattering
SEO	Polystyrene-*block*-poly(ethylene oxide) diblock copolymer
WAXS	Wide Angle X-Ray Scattering

7.6.2 Symbols

a	Inter-sight spacing, nm
A	Electrode area, cm^2
C_1	Constant in Lorentzian fitting expression, a.u.
C_2	Constant in Lorentzian fitting expression, a.u.

d_o	Lattice spacing un-oxidized P3HT, nm
$d(r_{ox})$	Lattice spacing of P3HT as a function of oxidation level, nm
D	Fitting constant in expression for mobility as a function of lattice strain, $cm^2V^{-1}s^{-1}$
e	The elementary charge, C
I	Scattering intensity, a.a.
I_o	Constant in Lorentzian fitting expression,
L	Sample thickness in conductivity formula, cm
M_{P3HT}	Molecular weight of P3HT block, g mol^{-1}
M_{PEO}	Molecular weight of PEO block, g mol^{-1}
n	Charge density of oxidized P3HT, C cm^{-3}
q	Scattering vector, nm^{-1}
q^*	Peak position in Lorentzian fitting expression, nm^{-1}
r	LiTFSI salt concentration, $[Li^+][EO]^{-1}$
r_{ox}	P3HT oxidation level, $[e^-]_{removed}[HT]^{-1}$
R	Electronic resistance, Ω
t	Transfer integral, --
t_o	Prefactor in transfer integral expression, --
y_o	Fitting constant in expression for mobility as a function of lattice strain, $cm^2V^{-1}s^{-1}$

7.6.3 Greek

α	Lattice strain in expression for mobility as a function of lattice strain, --
δ	Correction factor for mesh electrode geometry, --
γ	Exponential coefficient in transfer integral expression, nm^{-1}
λ	Scattering wavelength, nm
μ	Mobility, $cm^2V^{-1}s^{-1}$
μ_{FET}	Mobility measured by the field effect transistor, $cm^2V^{-1}s^{-1}$
μ_{ox}	Mobility measured through electrochemical oxidation, $cm^2V^{-1}s^{-1}$
θ	Scattering angle, rad
σ	Electronic conductivity, Scm^{-1}
τ	Fitting constant in expression for mobility as a function of lattice strain, --

7.7 Supporting Information

7.7.1 Differential Scanning Calorimetry (DSC) Analysis of P3HT-PEO(7-2)/LiTFSI

DSC was performed on a 9mg sample of freeze-dried P3HT-PEO(7-2)/LiTFSI. The sample was heated to 90C at 10K/min, and then annealed for one hour at 90C. The sample was then heated to 250C at 10K/min, and subsequently cooled at 10K/min back to 90C in order to observe the melting and recrystallization of P3HT. The melting and crystallization peaks were integrated, and an ideal melting enthalpy of 33 J/g[127] was used to calculate the P3HT degree of crystallinity. The degree of crystallinity was determined to be 62% for the freeze-dried sample, and 77% for the recrystallized sample. Thus we can conclude that although the free-drying process inhibits the crystallization of P3HT, our samples still contain a significant fraction of crystalline domains. The analyzed data are provided in Figure 7.S1 below.

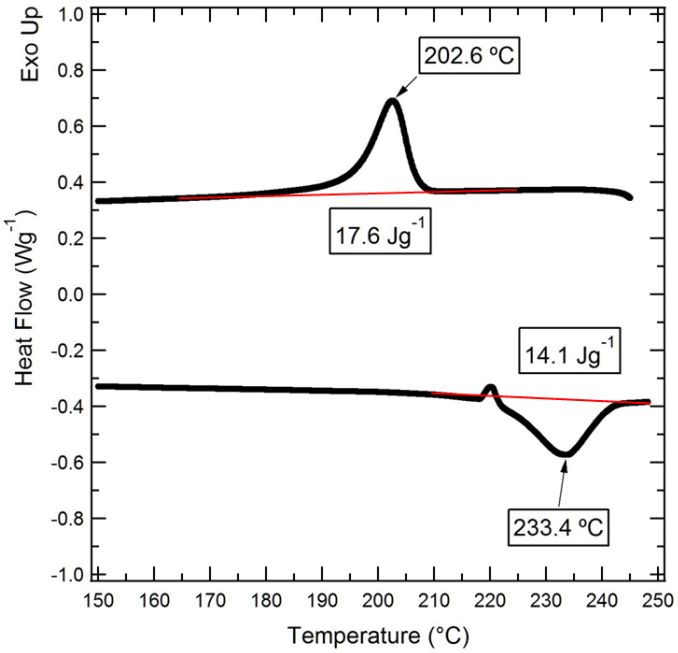

Figure 7.S1: DSC scan demonstrating the melting and recrystallization of P3HT.

7.7.2 Small Angle X-Ray Scattering (SAXS) of Bulk P3HT-PEO(7-2)/LiTFSI

SAXS measurements were made on an undoped sample of P3HT-PEO(7-2)/LiTFSI contained in an airtight sample holder between kapton windows. The two broad peaks shown in Figure 7.S2 are indicative of a self-assembled structure and appear qualitatively consistent with the nanofibrillar morphology observed by Patel and coworkers.[42,43]

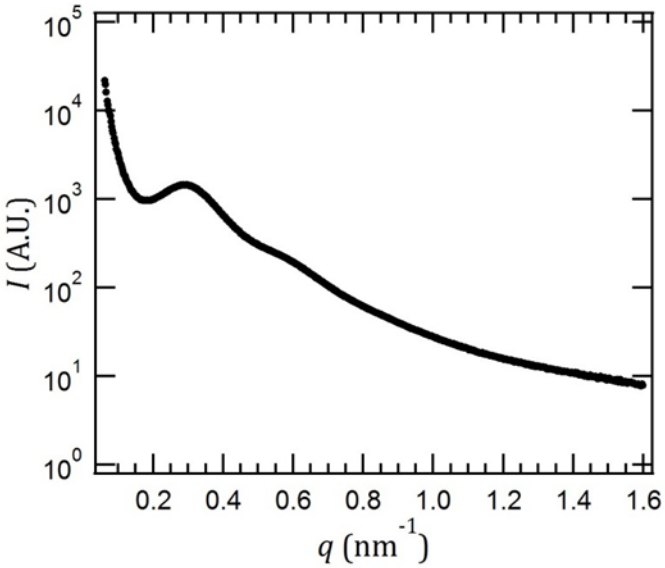

Figure 7.S2: SAXS intensity profile for P3HT-PEO(7-2)/LiTFSI.

7.7.3 In situ Solid-State Sample Preparation

P3HT-PEO/LiTFSI powder was hot pressed (110 °C) into two 150micron thick Garolite G10 spacers with a 5.04 mm diameter. The thickness and mass of the polymer in the spacers were recorded for calculation of electronic conductivity and doping level, respectively. A nickel mesh was sandwiched between the polymer containing spacers, and they were gently hot pressed in order to embed the mesh as an electrode. An additional layer of nickel mesh was hot pressed on one side of the polymer/nickel mesh assembly to serve as a second electrode. A ~25 micron electrolyte layer of SEO(240-269)/LiTFSI was hot pressed onto the other side of the polymer/nickel mesh assembly, and finally a piece of lithium foil was cold pressed onto the SEO/LiTFSI electrolyte layer to serve as an anode for the electrochemical cell. Both nickel mesh electrodes and the lithium metal electrode were contacted with nickel tabs, and the entire assemble was vacuum sealed in an airtight pouch material (Showa Denko) to allow for experiments to be performed outside of the glovebox.

7.7.4 Electrochemical Oxidation and Potentiostatic Electrochemical Impedance Spectroscopy (PEIS) Measurements

First, the samples were equilibrated at 90 ^{o}C on a custom built heating stage for 3 hours. During equilibration, the open circuit voltage (V_{oc}) of the electrochemical cell was monitored between the outer nickel mesh electrode and the lithium electrode: equilibration was considered complete when a steady V_{oc} was achieved, typically between 2.8 and 3.0 V(Li/Li^{+}). During a typical experiment, the first two charging steps were performed at a low current, such that 0.5 mol% of the P3HT were oxidized, or $r_{ox} = 0.005$, where or $r_{ox} = [e^{-}]_{removed}/[HT]$, per step. After achieving $r_{ox} = 0.010$ oxidation, samples were oxidized in $r_{ox} = 0.01$ increments until the voltage required to maintain constant current reached the threshold of 3.8 V(Li/Li^{+}), after which a constant potential of 3.8 V(Li/Li^{+}) was held until that oxidation step was complete.

PEIS measurements utilized an excitation voltage of 50 mV and a frequency range of 1 MHz to 50 mHz. PEIS measurements were performed on the un-oxidized polymer after the initial equilibration step, and approximately 20 minutes after each oxidation step. With the exception of the un-oxidized polymer ($r_{ox} = 0$), the bulk P3HT resistance (R) was interpreted as the impedance at low frequencies, were the phase angle was nearly independent of frequency and approaching a value of 0°. The impedance at such frequencies can be interpreted as a simple direct current (DC) resistance, and this assumption was confirmed by steady state DC polarization experiments. The impedance spectra of the un-oxidized polymer (r_{ox} =0) was complex and the phase angle did not approach a constant value of 0° at low frequencies, thus an order of magnitude approximation of the bulk P3HT resistance for the un-oxidized polymer was assumed from the impedance measured at 50 mHz.

It is important to note that we assume that every electron removed from P3HT during the oxidation step generates a hole, i.e. n is the moles of electrons transferred by the potentiostat during the galvanostatic charging step divided by the volume of P3HT in the thick film. Side reactions with impurities in the cathode may consume some electrons. Thus one may interpret the mobility values obtained by our approach as lower bounds of the true bulk mobility.

7.7.5 Correction Factor Calculations for Mesh Electrode Geometry

In most cases, conductivity is obtained from ac impedance experiments conducted with the material of interest sandwiched between two identical plate electrodes, using Equation S7.1

$$\sigma = \frac{L}{AR} \tag{S7.1}$$

where L is the distance between the two plate electrodes, A is the sample cross-section area which, in this case, is identical to the area of the plates, and R is the measured bulk electronic resistance. However, when we use the three terminal cell of the type shown in Figure 7.1, we are forced to use a mesh electrode. In ref. 3 where we introduced the three terminal cell, the sample was placed between a mesh and a plate electode while in the present study, the sample is placed between two mesh electrodes (Figure 7.S3). Equation S7.1 is not applicable in these cases. We use simple modeling to account for the presence of mesh electrodes.

Charge transport under an applied dc potential through an electrolyte that is assumed to be an Ohmic conductor placed between a plate and a mesh electrode was modeled using the finite-element package COMSOL Multiphysics. The system can be segmented into numerous identical and symmetric units as shown in Figure 7.S3. One of these units was modeled as shown in Figure 7.S4. The electrolyte potential, Φ, was obtained by solving Laplace's equation with an applied potential drop across the plate and mesh electrodes and assuming zero flux at the other boundaries. Typical calculated results are showed in Figure 7.S5 where the modeled potential (color gradient) and current lines emanating from the mesh wires to the plate electrode are shown. The electric current is proportional to the derivative of potential and the electrolyte conductivity ($I = -\sigma\nabla\Phi$).

We assume that the conductivity of the electrolyte in our experiments is given by $\sigma = \delta L/AR$, where δ is a correction factor to account for the mesh electrode geometry (A is the sample cross-section area). The simulation results are used to obtain δ, which is the ratio of the current obtained in the mesh-mesh or mesh-plate cases to that of the plate-plate case. The δ value for the mesh-pate geometry used in ref. 3 was $\delta = 1.45$ (L=180 μm). (Conductivities reported in ref. 3 were not corrected for the electrode geometry.)

Calculations similar to those reported above were used to model mesh-mesh electrodes. (The same mesh was used in both ref. 3 and the present study.) In the model, we assumed that the mesh junctions were either perfectly aligned or having maximal offset. We used the average of the aligned and offset cased to obtain the value of δ = 1.89 (L=180 μm) used for the mesh-mesh electrodes in this work.

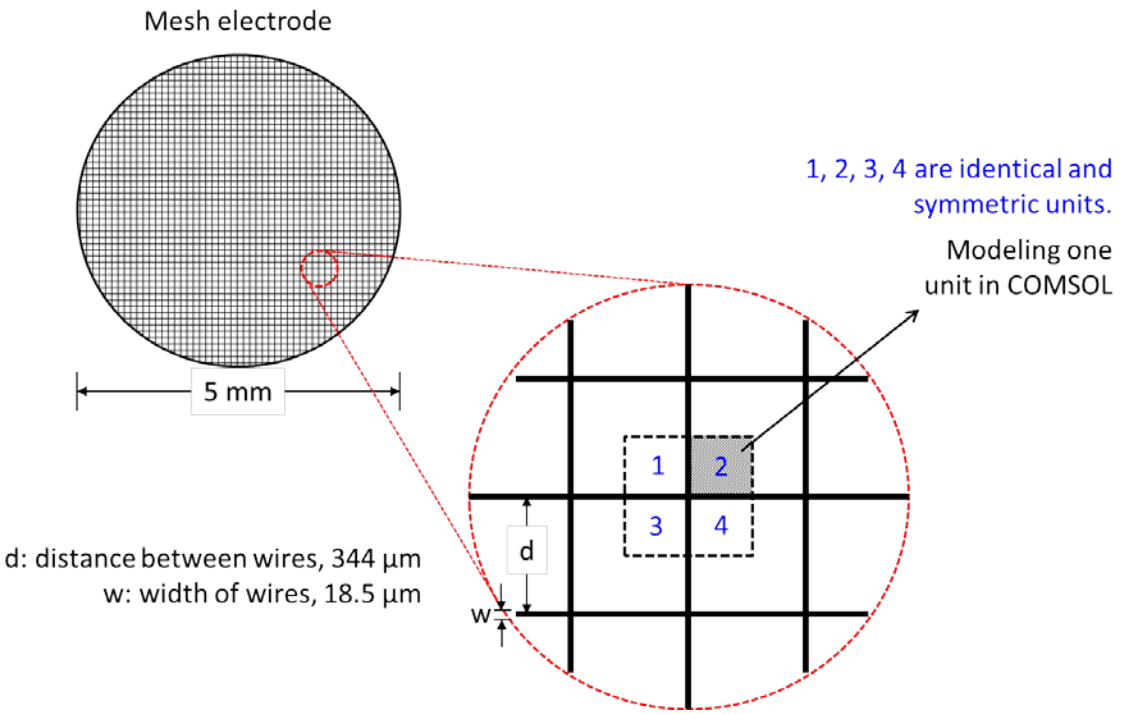

Figure 7.S3: The mesh electrode can be segmented into numerous identical and symmetric units.

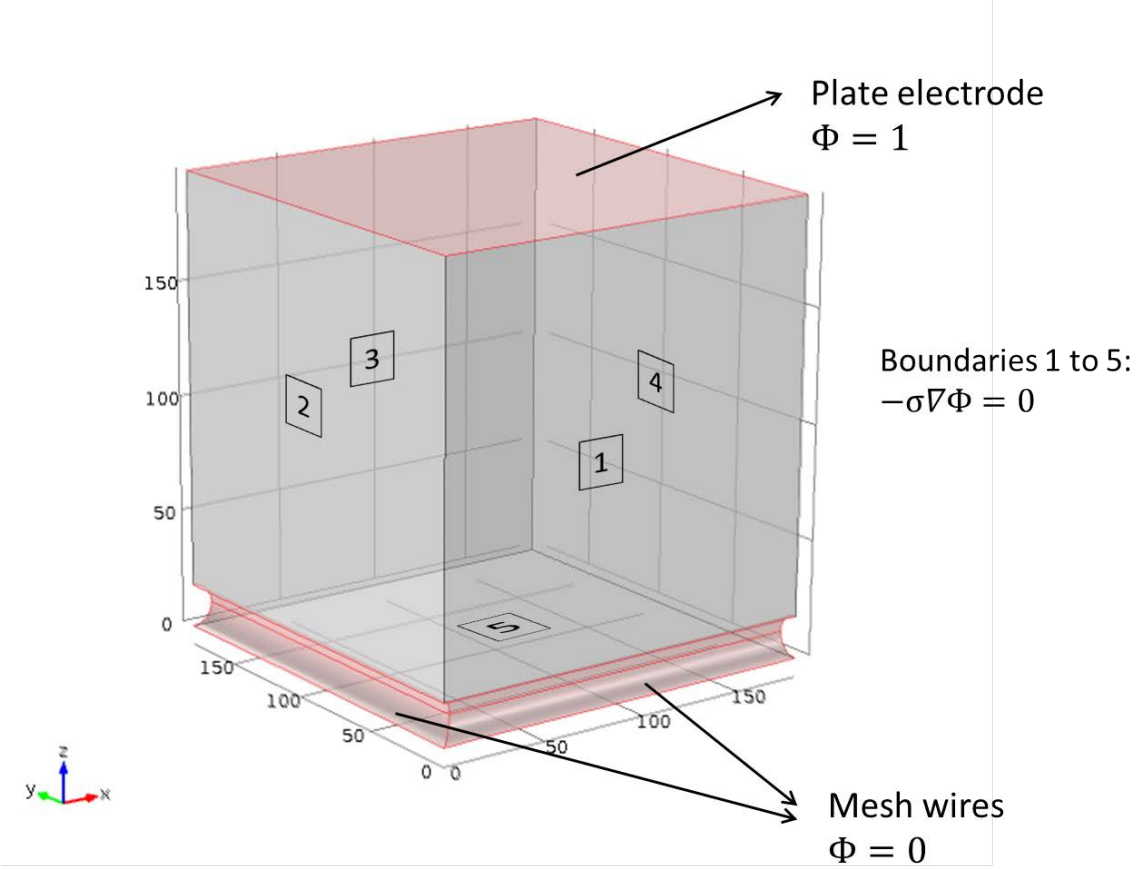

Figure 7.S4: An example of one of the electrode geometries (plate-mesh) for which Laplace's equation was solved in COMSOL.

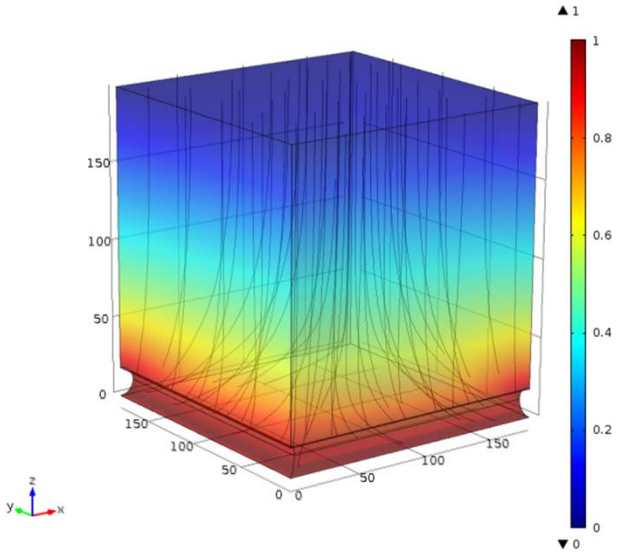

Figure 7.S5: The calculated potential (color gradient) and current lines emanating from the mesh wires to the plate electrode.

7.7.6 1st Oxidation (Break-in) Cycle Data

Initial oxidation of the P3HT-PEO(7-2)/LiTFSI samples demonstrated a non-monatomic trend in electronic conductivity with increasing oxidation level. These results are inconsistent with the trends observed in subsequent cycles, as well as those found in the literature. Furthermore, the total charge passed corresponds to a total doping level of r_{ox} = 0.19, which is significantly higher than the maximum attained for this polymer during subsequent cycles (r_{ox} = 0.09). We interpret this extra charge passed to side reactions within the cell, likely occurring at the lithium electrode surface (solid electrolyte interphase formation). We also note that samples 3 and 4 became damaged during their first experiment (the cells are mechanically fragile) and are thus not reported in the main text. The electronic conductivity as a function of doping level is given in Figure 7.S6 below.

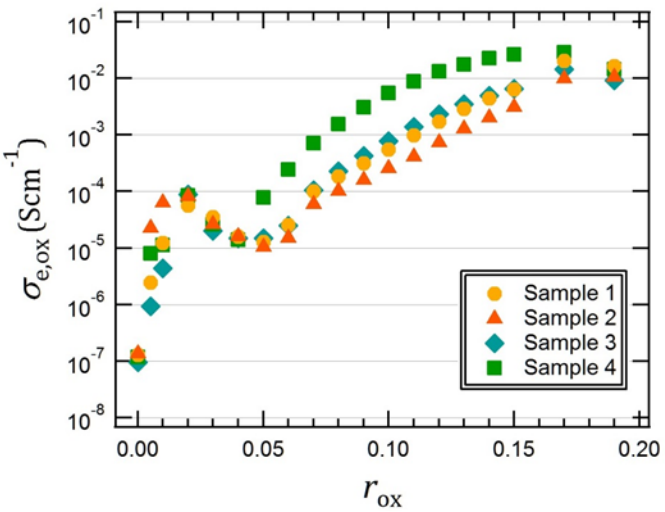

Figure 7.S6: Electronic conductivity of four replicate samples of P3HT-PEO(7-2)/LiTFSI during their first (break-in) oxidation cycle.

7.7.7 WAXS Background Correction

The electrochemical cell used to perform the *in situ* WAXS experiments contributed a significant amount of scattering intensity. In order to correct for this, the scattering intensity of an empty cell was subtracted from the sample data shown in the main text. Due to the configuration of the beamline during the *in situ* WAXS experiments, the transmitted intensity of the samples and the empty cell could not be measured. Thus we multiplied the empty cell scattering intensity by a constant factor of 0.76 before performing the subtraction. The scaling factor was chosen to provide the largest reduction in peaks known to originate from the empty cell without causing any points of negative intensity in the scattering patterns of any of the samples. Figure 7.S7 provides the uncorrected scattering of one sample (before oxidation) and of the empty cell used for the background correction.

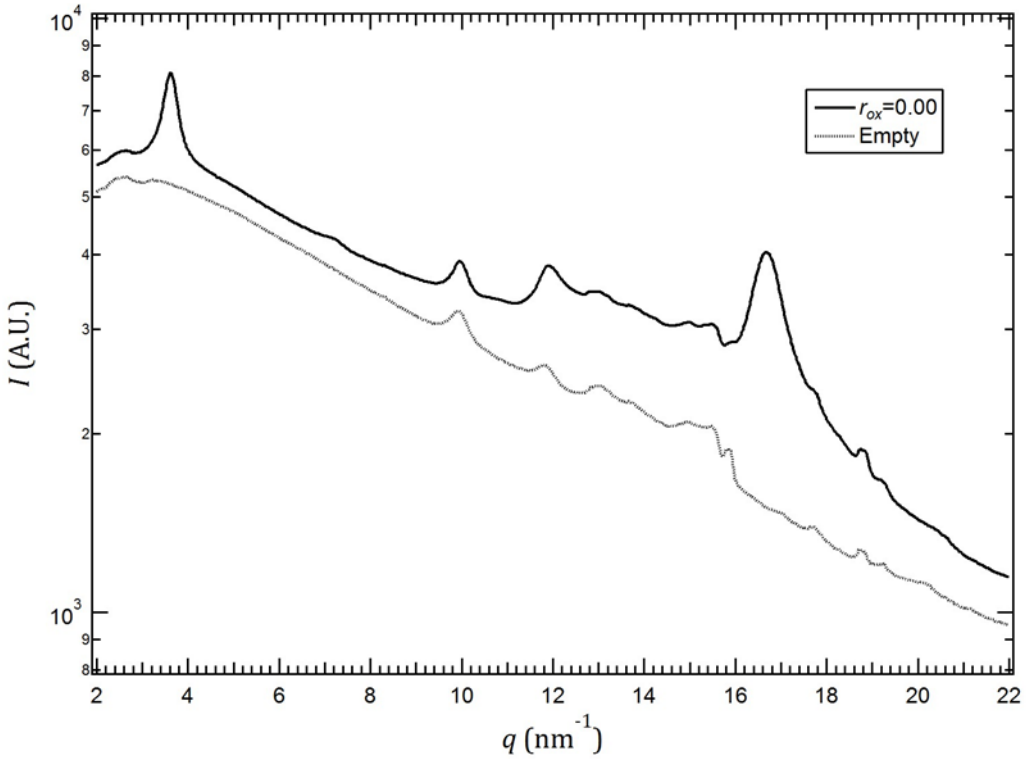

Figure 7.S7: Uncorrected WAXS intensity profiles for an undoped P3HT-PEO(7-2)/LiTFSI sample and the empty cell containing all of the components of the electrochemical cell except P3HT-PEO(7-2)/LiTFSI.

Chapter 8 – Summary

The purpose of this work was to develop better understanding of the influence of ion-polymer interactions on the phase behavior, self-assembly, and electrochemical performance of solid-state block copolymer electrolytes (BCEs). X-ray scattering was chosen as a primary characterization technique because it facilitates the study BCE microstructure over a wide range of length-scales; experiments can be performed under conditions relevant to thermodynamic processes or the conditions within a solid-state battery; and it is amenable to the incorporation of additional *in situ* characterization techniques. The experimental methodology developed for quantitative X-ray scattering, including a detailed derivation of data corrections not readily found in literature, was presented first, providing future experimentalists a solid foundation to follow the results of this work. A discussion on scattering data analysis and interpretation is also provided in Appendix A1.

The first two experimental studies highlighted the influence of adding salt to a neutral block copolymer when forming binary (e.g., polymer + salt) block copolymer electrolytes. In both cases, the BCEs were composed of the block copolymer, polystyrene-*b*-poly(ethylene oxide) (SEO), and lithium bis(trifluoromethanesulfonyl)imide (LiTFSI) salt. The first study utilized a model low molecular weight SEO/LiTFSI system to directly probe the thermodynamic impact of salt-polymer interactions on self-assembly within BCEs. It was revealed that salt-polymer interactions facilitated a thermodynamically stable coexistence between self-assembled lamellae and disordered nanostructures during the order-to-disorder phase transition (ODT). Such a coexistence, which is predicted by the Gibbs phase rule, indicates that salt can partition between "phases" that have different nanostructure. The second study was performed on a high molecular weight SEO, a system far from the ODT phase boundary. In this case, the nanostructures observed for anneals BCE samples indicated kinetic limitations significantly hindered self-assembly. However, at high salt concentrations, some of the BCE samples exhibited the coexistence of self-assembled lamellae and what appears to be a kinetically-trapped nanostructure. In light of the results from the model system, these coexisting nanostructures suggest the possibility of a heterogeneous salt distribution in some high molecular weight BCE samples, which would have interesting implications for their performance within a solid-state battery. These high salt concentration BCEs showed remarkable ionic conductivity values, indicating a possible path for the development of BCEs with improved performance.

The next series of studies focused on a new class of BCEs, wherein the anion of the electrolyte salt is covalently bonded to one of the polymer backbones. Due to the inherent immobilization of the anion, these materials behave as so-called single-ion conductors. Since ion conduction in these systems requires cation dissociation from one of the polymer backbones, thereby creating a charged polymer chain, one could expect a coupling between ion dissociation, polymer nanostructure, and the concomitant electrochemical performance. We studied this coupling by analyzing a library of single-ion conducting polymers composed of poly(ethylene oxide)-*b*-poly[(styrene-4-sulfonyltrifluoromethylsulfonyl)imide] (PEO-P(STFSI)) backbones with both lithium and magnesium counterions. In the melt, we found that ion dissociation leads to a strong mixing of the PEO and P(STFSI) polymer blocks. Since ion conduction requires mobile (i.e., dissociated) cations, single-ion conducting block copolymers that exhibit good

conductive properties will necessarily be mixed i.e., microphase separation will likely not occur. This is expected to have a strong impact on the design of BCEs with improved mechanical properties. In addition to ionic conductivity, ion dissociation was also found to influence PEO crystallization in the single-ion conducting block copolymers. In this case, the homogeneous nature of the samples that showed significant ion dissociation facilitated the growth of large lamellar PEO crystallites, leading to well-ordered lamellar nanostructures. In contrast, concentration fluctuations in the melt for samples with little ion dissociation were found to impede crystal growth, leading to longer crystallization times and poorly-ordered semi crystalline nanostructures. It is clear that cation dissociation, polymer nanostructure, and electrochemical performance are intimately coupled single-ion conductors with a simple diblock chain architecture.

The final study in this work highlighted the power of using *in situ* characterization techniques in conjunction with X-ray scattering. In this work, we sought to explore the structural impact the electrochemical doping of poly(3-hexylthiophene) (P3HT) within the simultaneous ion/electron conductor poly(3-hexylthiophene)-b-poly(ethylene oxide) (P3HT-PEO) mixed with LiTFSI salt. Through a novel sample design and *in situ* experimental setup, we demonstrated a clear correlation between structural changes in the P3HT crystal lattice (measured by WAXS) and the electrochemically measured charge mobility for the first time. Since the doping process requires the presence of a balancing negative charge to maintain electroneutrality, it is likely that the structural changes to the P3HT crystal lattice were at least partially induced by the intercalation of the $TFSI^-$ anion into the crystal structure. Thus, tuning the doping process by designing around the anion-P3HT interactions may represent one route to improving electron conduction in these materials.

References

(1) Denholm, P.; Ela, E.; Kirby, B.; Milligan, M. *Role of Energy Storage with Renewable Electricity Generation*; Golden, CO (United States), 2010.

(2) Denholm, P.; Hand, M. Grid Flexibility and Storage Required to Achieve Very High Penetration of Variable Renewable Electricity. *Energy Policy* **2011**, *39*, 1817–1830.

(3) Jacobson, M. Z.; Delucchi, M. A. Providing All Global Energy with Wind , Water , and Solar Power , Part I : Technologies , Energy Resources , Quantities and Areas of Infrastructure , and Materials. *Energy Policy* **2011**, *39*, 1154–1169.

(4) U.S. Department of Energy. *Grid Energy Storage*; 2013.

(5) U.S. Department of Energy. *Vehicle Technologies Multi-Year Program Plan 2011-2015*; 2010.

(6) Balakrishnan, P. G.; Ramesh, R.; Prem Kumar, T. Safety Mechanisms in Lithium-Ion Batteries. *J. Power Sources* **2006**, *155*, 401–414.

(7) Arbizzani, C.; Gabrielli, G.; Mastragostino, M. Thermal Stability and Flammability of Electrolytes for Lithium-Ion Batteries. *J. Power Sources* **2011**, *196*, 4801–4805.

(8) Goodenough, J. B.; Kim, Y. Challenges for Rechargeable Li Batteries †. *Chem. Mater.* **2010**, *22*, 587–603.

(9) Fenton, D. E.; Parker, J. M.; Wright, P. V. Complexes of Alkali Metal Ions with Poly(ethylene Oxide). *Polymer (Guildf).* **1973**, *14*, 589.

(10) Wright, P. V. Electrical Conductivity in Ionic Complexes of Poly(ethylene Oxide). *Br. Polym. J.* **1975**, *7*, 319–327.

(11) Vashishta, P.; Mundy, J. N.; Shenoy, G. K. Fast Ion Transport in Solids: Electrodes and Electrolytes. **1979**.

(12) Vincent, C. A.; MacCallum, J. R. *Polymer Electrolyte Reviews*; Elsevier Applied Science, 1987.

(13) Armand, M.; Gorecki, W.; Andreani, R. Second International Symposium on Polymer Electrolytes. In *Second International Symposium on Polymer Electrolytes*; Scrosati, B., Ed.; Elsevier Applied Science: New York, NY, 1990; p. 91.

(14) Maranas, J. K. Solid Polymer Electrolytes. In *Dynamics of Soft Matter*; Sakai, V. G.; Alba-Simionesco, C.; Chen, S.-H., Eds.; Springer US, 2012; pp. 123–143.

(15) Thomas, K. E.; Sloop, S. E.; Kerr, J. B.; Newman, J. Comparison of Lithium-Polymer Cell Performance with Unity and Nonunity Transference Numbers. *J. Power Sources* **2000**, *89*, 132–138.

(16) Tarascon, J. M.; Armand, M. Issues and Challenges Facing Rechargeable Lithium Batteries. *Nature* **2001**, *414*, 359–367.

(17) Dollé, M.; Sannier, L.; Beaudoin, B.; Trentin, M.; Tarascon, J.-M. Live Scanning Electron Microscope Observations of Dendritic Growth in Lithium/Polymer Cells. *Electrochem. Solid-State Lett.* **2002**, *5*, A286.

(18) Monroe, C.; Newman, J. The Impact of Elastic Deformation on Deposition Kinetics at Lithium/Polymer Interfaces. *J. Electrochem. Soc.* **2005**, *152*, A396.

(19) Singh, M.; Odusanya, O.; Wilmes, G. M.; Eitouni, H. B.; Gomez, E. D.; Patel, A. J.; Chen, V. L.; Park, M. J.; Fragouli, P.; Iatrou, H.; et al. Effect of Molecular Weight on the Mechanical and Electrical Properties of Block Copolymer Electrolytes. *Macromolecules* **2007**, *40*, 4578–4585.

(20) Harry, K. J.; Higa, K.; Srinivasan, V.; Balsara, N. P. Influence of Electrolyte Modulus on the Local Current Density at a Dendrite Tip on a Lithium Metal Electrode. *J. Electrochem. Soc.* **2016**, *163*, A2216–A2224.

(21) Hallinan, D. T.; Mullin, S. A.; Stone, G. M.; Balsara, N. P. Lithium Metal Stability in Batteries with Block Copolymer Electrolytes. *J. Electrochem. Soc.* **2013**, *160*, A464–A470.

(22) Schauser, N. S.; Harry, K. J.; Parkinson, D. Y.; Watanabe, H.; Balsara, N. P. Lithium Dendrite Growth in Glassy and Rubbery Nanostructured Block Copolymer Electrolytes. *J. Electrochem. Soc.* **2015**, *162*, A398–A405.

(23) Khurana, R.; Schaefer, J. L.; Archer, L. a; Coates, G. W. Suppression of Lithium Dendrite Growth Using Cross-Linked Polyethylene/Poly(ethylene Oxide) Electrolytes: A New Approach for Practical Lithium-Metal Polymer Batteries. *J. Am. Chem. Soc.* **2014**, *136*, 7395–7402.

(24) Young, W.; Epps, T. H. Salt Doping in PEO-Containing Block Copolymers: Counterion and Concentration Effects. *Macromolecules* **2009**, *42*, 2672–2678.

(25) Teran, A. A.; Balsara, N. P. Thermodynamics of Block Copolymers with and without Salt. *J. Phys. Chem. B* **2014**, *118*, 4–17.

(26) Gunkel, I.; Thurn-Albrecht, T. Thermodynamic and Structural Changes in Ion-Containing Symmetric Diblock Copolymers: A Small-Angle X-Ray Scattering Study. *Macromolecules* **2012**, *45*, 283–291.

(27) Thelen, J. L.; Teran, A. A.; Wang, X.; Garetz, B. A.; Nakamura, I.; Wang, Z.-G.; Balsara, N. P. Phase Behavior of a Block Copolymer/Salt Mixture through the Order-to-Disorder Transition. *Macromolecules* **2014**, *47*, 2666–2673.

(28) Chintapalli, M.; Le, T. N. P.; Venkatesan, N. R.; Mackay, N. G.; Rojas, A. A.; Thelen, J. L.; Chen, X. C.; Devaux, D.; Balsara, N. P. Structure and Ionic Conductivity of Polystyrene- *Block* -Poly(ethylene Oxide) Electrolytes in the High Salt Concentration Limit. *Macromolecules* **2016**, *49*, 1770–1780.

(29) Panday, A.; Mullin, S. A.; Gomez, E. D.; Wanakule, N. S.; Chen, V. L.; Hexemer, A.; Pople, J.; Balsara, N. P. Effect of Molecular Weight and Salt Concentration on Conductivity of Block Copolymer Electrolytes. *Macromolecules* **2009**, *42*, 4632–4637.

(30) Yuan, R.; Teran, A. A.; Gurevitch, I.; Mullin, S. A.; Wanakule, N. S.; Balsara, N. P. Ionic Conductivity of Low Molecular Weight Block Copolymer Electrolytes. *Macromolecules* **2013**, *46*, 914–921.

(31) Mullin, S. A.; Teran, A. A.; Yuan, R.; Balsara, N. P. Effect of Thermal History on the Ionic Conductivity of Block Copolymer Electrolytes. *J. Polym. Sci. Part B Polym. Phys.* **2013**, *51*, 927–934.

(32) Teran, A. A.; Mullin, S. A.; Hallinan, D. T.; Balsara, N. P. Discontinuous Changes in Ionic Conductivity of a Block Copolymer Electrolyte through an Order–Disorder Transition. *ACS Macro Lett.* **2012**, *1*, 305–309.

(33) Chintapalli, M.; Chen, X. C.; Thelen, J. L.; Teran, A. A.; Wang, X.; Garetz, B. A.; Balsara, N. P. Effect of Grain Size on the Ionic Conductivity of a Block Copolymer Electrolyte. *Macromolecules* **2014**, *47*, 5424–5431.

(34) Ryu, S.-W.; Trapa, P. E.; Olugebefola, S. C.; Gonzalez-Leon, J. A.; Sadoway, D. R.; Mayes, A. M. Effect of Counter Ion Placement on Conductivity in Single-Ion Conducting Block Copolymer Electrolytes. *J. Electrochem. Soc.* **2005**, *152*, A158.

(35) Bouchet, R.; Maria, S.; Meziane, R.; Aboulaich, A.; Lienafa, L.; Bonnet, J.; Phan, T. N. T.; Bertin, D.; Gigmes, D.; Devaux, D.; et al. Single-Ion BAB Triblock Copolymers as Highly Efficient Electrolytes for Lithium-Metal Batteries. *Nat. Mater.* **2013**, *12*, 452–457.

(36) Inceoglu, S.; Rojas, A. A.; Devaux, D.; Chen, X. C.; Stone, G. M.; Balsara, N. P. Morphology–Conductivity Relationship of Single-Ion-Conducting Block Copolymer Electrolytes for Lithium Batteries. *ACS Macro Lett.* **2014**, 510–514.

(37) Rojas, A. A.; Inceoglu, S.; Mackay, N. G.; Thelen, J. L.; Devaux, D.; Stone, G. M.; Balsara, N. P. Effect of Lithium-Ion Concentration on Morphology and Ion Transport in Single-Ion-Conducting Block Copolymer Electrolytes. *Macromolecules* **2015**, *48*, 6589–6595.

(38) Doyle, M.; Fuller, T. F.; Newman, J. The Importance of the Lithium Ion Transference Number in Lithium/polymer Cells. *Electrochim. Acta* **1994**, *39*, 2073–2081.

(39) Tikekar, M. D.; Archer, L. A.; Koch, D. L. Stability Analysis of Electrodeposition across a Structured Electrolyte with Immobilized Anions. *J. Electrochem. Soc.* **2014**, *161*, 847–855.

(40) Sing, C. E.; Zwanikken, J. W.; Olvera de la Cruz, M. Electrostatic Control of Block Copolymer Morphology. *Nat. Mater.* **2014**, *13*, 694–698.

(41) Radhakrishna, M.; Sing, C. E. Charge Correlations for Precise, Coulombically Driven Self Assembly. *Macromol. Chem. Phys.* **2016**, *217*, 126–136.

(42) Patel, S. N.; Javier, A. E.; Balsara, N. P. Electrochemically Oxidized Electronic and Ionic Conducting Nanostructured Block Copolymers for Lithium Battery Electrodes. *ACS Nano* **2013**, *7*, 6056–6068.

(43) Patel, S. N.; Javier, A. E.; Stone, G. M.; Mullin, S. A.; Balsara, N. P. Simultaneous Conduction of Electronic Charge and Lithium Ions in Block Copolymers. *ACS Nano*

2012, *6*, 1589–1600.

(44) Patel, S. N.; Javier, A. E.; Beers, K. M.; Pople, J. a; Ho, V.; Segalman, R. a; Balsara, N. P. Morphology and Thermodynamic Properties of a Copolymer with an Electronically Conducting Block: poly(3-Ethylhexylthiophene)-Block-Poly(ethylene Oxide). *Nano Lett.* **2012**, *12*, 4901–4906.

(45) Javier, A. E.; Patel, S. N.; Hallinan, D. T.; Srinivasan, V.; Balsara, N. P. Simultaneous Electronic and Ionic Conduction in a Block Copolymer: Application in Lithium Battery Electrodes. *Angew. Chem. Int. Ed. Engl.* **2011**, *50*, 9848–9851.

(46) Bhatt, M. P.; Thelen, J. L.; Balsara, N. P. Effect of Copolymer Composition on Electronic Conductivity of Electrochemically Oxidized Poly(3-Hexylthiophene)- *B* - Poly(ethylene Oxide) Block Copolymers. *Chem. Mater.* **2015**, *27*, 5141–5148.

(47) Wu, S.-L.; Javier, A. E.; Devaux, D.; Balsara, N. P.; Srinivasan, V. Discharge Characteristics of Lithium Battery Electrodes with a Semiconducting Polymer Studied by Continuum Modeling and Experiment. *J. Electrochem. Soc.* **2014**, *161*, A1836–A1843.

(48) Shimotani, H.; Diguet, G.; Iwasa, Y. Direct Comparison of Field-Effect and Electrochemical Doping in Regioregular poly(3-Hexylthiophene). *Appl. Phys. Lett.* **2005**, *86*, 22104.

(49) Kawai, T.; Nakazono, M.; Sugimoto, R.; Yoshino, K. Crystal Structure of Poly(3-Alkylthiophene) and Its Doping Effect. *J. Phys. Soc. Japan* **1992**, *61*, 3400–3406.

(50) Bates, F. S.; Fredrickson, G. H. Block Copolymers—Designer Soft Materials. *Phys. Today* **1999**, *52*, 32.

(51) Fredrickson, G. H.; Bates, F. S. Dynamics of Block Copolymers: Theory and Experiment. *Annu. Rev. Mater. Sci.* **1996**, *26*, 501–550.

(52) Bates, F. S.; Schulz, M. F.; Khandpur, A. K.; Forster, S.; Rosedale, J. H.; Almdal, K.; Mortensen, K. Fluctuations, Conformational Asymmetry and Block Copolymer Phase Behaviour. *Faraday Discuss.* **1994**, *98*, 7–18.

(53) Bates, F. S.; Fredrickson, G. H. Block Copolymer Thermodynamics: Theory and Experiment. *Annu. Rev. Phys. Chem.* **1990**, *41*, 525–557.

(54) Young, W.-S.; Kuan, W.-F.; Epps, T. H. Block Copolymer Electrolytes for Rechargeable Lithium Batteries. *J. Polym. Sci. Part B Polym. Phys.* **2014**, *52*, 1–16.

(55) Roe, R.-J. *Methods of X-Ray and Nuetron Scattering in Polymer Science*; Oxford University Press Inc., 2000.

(56) Alexander, L. E. *X-Ray Diffraction Methods in Polymer Science*; Wiley-Interscience: New York, NY, 1969.

(57) Brûlet, A.; Lairez, D.; Lapp, A.; Cotton, J.-P. Improvement of Data Treatment in Small-Angle Neutron Scattering. *J. Appl. Crystallogr.* **2007**, *40*, 165–177.

(58) Baltá-Calleja, F. J.; Vonk, C. G. *X-Ray Scattering of Synthetic Polymers*; Elsevier: Amsterdam, 1989.

(59) Hubbell, J. H.; Seltzer, S. M. X-Ray Mass Attenuation Coefficients. In *NIST Internal/Interagency Report 5632*; National Institute of Standards and Technology: Gaithersburg, MD, 1996.

(60) Hexemer, A.; Bras, W.; Glossinger, J.; Schaible, E.; Gann, E.; Kirian, R.; MacDowell, A.; Church, M.; Rude, B.; Padmore, H. A SAXS/WAXS/GISAXS Beamline with Multilayer Monochromator. *J. Phys. Conf. Ser.* **2010**, *247*, 12007.

(61) Ilavsky, J. Nika : Software for Two-Dimensional Data Reduction. *J. Appl. Crystallogr.* **2012**, *45*, 324–328.

(62) Zhang, F.; Ilavsky, J.; Long, G. G.; Quintana, J. P. G.; Allen, A. J.; Jemian, P. R. Glassy Carbon as an Absolute Intensity Calibration Standard for Small-Angle Scattering. *Metall. Mater. Trans. A* **2010**, *41*, 1151–1158.

(63) Vaselabadi, S. A.; Shakarisaz, D.; Ruchhoeft, P.; Strzalka, J.; Stein, G. E. Radiation Damage in Polymer Films from Grazing-Incidence X-Ray Scattering Measurements. *J. Polym. Sci. Part B Polym. Phys.* **2016**, *54*, 1074–1086.

(64) Agrawal, R. C.; Pandey, G. P. Solid Polymer Electrolytes: Materials Designing and All-Solid-State Battery Applications: An Overview. *J. Phys. D. Appl. Phys.* **2008**, *41*, 223001.

(65) Leibler, L. Theory of Microphase Separation in Block Copolymers. *Macromolecules* **1980**, *13*, 1602–1617.

(66) Mai, S.; Fairclough, J. P. A.; Hamley, I. W.; Matsen, M. W.; Denny, R. C.; Liao, B.; Booth, C.; Ryan, A. J. Order−Disorder Transition in Poly(oxyethylene)−Poly(oxybutylene) Diblock Copolymers. *Macromolecules* **1996**, *29*, 6212–6221.

(67) Koga, T.; Koga, T.; Hashimoto, T. Ultra-Small-Angle X-Ray Scattering Studies on Order-Disorder Transition in Diblock Copolymers. *J. Chem. Phys.* **1999**, *110*, 11076–11086.

(68) Sakamoto, N.; Hashimoto, T. Order-Disorder Transition of Low Molecular Weight Polystyrene-Block-Polyisoprene. 1. SAXS Analysis of Two Characteristic Temperatures. *Macromolecules* **1995**, *28*, 6825–6834.

(69) Mori, K.; Okawara, A.; Takeji, H. Order-Disorder Transition of Polystyrene-Block-Polyisoprene. I. Thermal Concentration Fluctuations in Single-Phase Melts and Solutions and Determination of χ as a Function of Molecular Weight and Composition. *J. Chem. Phys.* **1996**, *104*, 7765.

(70) Lee, S.; Gillard, T. M.; Bates, F. S. Fluctuations , Order , and Disorder in Short Diblock Copolymers. *AIChE* **2013**, *59*, 3502–3513.

(71) Floudas, G.; Pakula, T.; Fischer, E. W.; Hadjichristidis, N.; Pispas, S. Ordering Kinetics in a Symmetric Diblock Copolymer. *Acta Polym.* **1994**, *45*, 176–181.

(72) Hammond, M. R.; Cochran, E.; Fredrickson, G. H.; Kramer, E. J. Temperature Dependence of Order, Disorder, and Defects in Laterally Confined Diblock Copolymer Cylinder Monolayers. *Macromolecules* **2005**, *38*, 6575–6585.

(73) Fredrickson, G. H.; Helfand, E. Fluctuation Effects in the Theory of Microphase Separation in Block Copolymers. *J. Chem. Phys.* **1987**, *87*, 697.

(74) Wanakule, N. S.; Virgili, J. M.; Teran, A. A.; Wang, Z.-G.; Balsara, N. P. Thermodynamic Properties of Block Copolymer Electrolytes Containing Imidazolium and Lithium Salts. *Macromolecules* **2010**, *43*, 8282–8289.

(75) Nakamura, I.; Balsara, N. P.; Wang, Z.-G. Thermodynamics of Ion-Containing Polymer Blends and Block Copolymers. *Phys. Rev. Lett.* **2011**, *107*, 198301.

(76) Nakamura, I.; Wang, Z.-G. Salt-Doped Block Copolymers: Ion Distribution, Domain Spacing and Effective χ Parameter. *Soft Matter* **2012**, *8*, 9356–9367.

(77) Majewski, P. W.; Gopinadhan, M.; Jang, W.; Lutkenhaus, J. L.; Osuji, C. O. Anisotropic Ionic Conductivity in Block Copolymer Membranes by Magnetic Field Alignment. *J. Am. Chem. Soc.* **2010**, *132*, 17516–17522.

(78) Nakamura, I.; Balsara, N. P.; Wang, Z. First-Order Disordered-to-Lamellar Phase Transition in Lithium Salt-Doped Block Copolymers. *ACS Macro Lett.* **2013**, *2*, 478–481.

(79) Quirk, R. P.; Kim, J.; Kausch, C.; Chun, M. Butyllithium-Initiated Anionic Synthesis of Well-Defined Poly(styrene-Block-Ethylene Oxide) Block Copolymers with Potassium Salt Additives. *Polym. Int.* **1996**, *39*, 3–10.

(80) Hadjichristidis, N.; Iatrou, H.; Pispas, S.; Pitsikalis, M. Anionic Polymerization: High Vacuum Techniques. *J. Polym. Sci. Part A Polym. Chem.* **2000**, *38*, 3211–3234.

(81) de Gennes, P. G. Theory of X-Ray Scattering by Liquid Macromolecules with Heavy Atom Labels. *J. Phys.* **1970**, *31*, 235–238.

(82) Gillard, T. M.; Medapuram, P.; Morse, D. C.; Bates, F. S. Fluctuations, Phase Transitions, and Latent Heat in Short Diblock Copolymers: Comparison of Experiment, Simulation, and Theory. *Macromolecules* **2015**, 150414101051008.

(83) Metwalli, E.; Rasool, M.; Brunner, S.; Müller-Buschbaum, P. Lithium-Salt-Containing High-Molecular-Weight Polystyrene- *Block* -Polyethylene Oxide Block Copolymer Films. *ChemPhysChem* **2015**, n/a-n/a.

(84) Lascaud, S.; Perrier, M.; Vallee, A.; Besner, S.; Prud'homme, J.; Armand, M. Phase Diagrams and Conductivity Behavior of Poly(ethylene Oxide)-Molten Salt Rubbery Electrolytes. *Macromolecules* **1994**, *27*, 7469–7477.

(85) Marzantowicz, M.; Dygas, J. R.; Krok, F.; Nowiński, J. L.; Tomaszewska, a.; Florjańczyk, Z.; Zygadło-Monikowska, E. Crystalline Phases, Morphology and Conductivity of PEO:LiTFSI Electrolytes in the Eutectic Region. *J. Power Sources* **2006**, *159*, 420–430.

(86) Marzantowicz, M.; Krok, F.; Dygas, J. R.; Florjańczyk, Z.; Zygadło-Monikowska, E. The Influence of Phase Segregation on Properties of Semicrystalline PEO:LiTFSI Electrolytes. *Solid State Ionics* **2008**, *179*, 1670–1678.

(87) Marzantowicz, M.; Dygas, J. R.; Krok, F.; Florjańczyk, Z.; Zygadło-Monikowska, E.

Influence of Crystalline Complexes on Electrical Properties of PEO:LiTFSI Electrolyte. *Electrochim. Acta* **2007**, *53*, 1518–1526.

(88) Zhu, L.; Mimnaugh, B. R.; Ge, Q.; Quirk, R. P.; Cheng, S. Z. .; Thomas, E. L.; Lotz, B.; Hsiao, B. S.; Yeh, F.; Liu, L. Hard and Soft Confinement Effects on Polymer Crystallization in Microphase Separated Cylinder-Forming PEO-B-PS/PS Blends. *Polymer (Guildf).* **2001**, *42*, 9121–9131.

(89) Huang, P.; Guo, Y.; Quirk, R. P.; Ruan, J.; Lotz, B.; Thomas, E. L.; Hsiao, B. S.; Avila-Orta, C. a.; Sics, I.; Cheng, S. Z. D. Comparison of Poly(ethylene Oxide) Crystal Orientations and Crystallization Behaviors in Nano-Confined Cylinders Constructed by a Poly(ethylene Oxide)-B-Polystyrene Diblock Copolymer and a Blend of Poly(ethylene Oxide)-B-Polystyrene and Polystyrene. *Polymer (Guildf).* **2006**, *47*, 5457–5466.

(90) Vancso, G.; Snétivy, D.; Tomka, I. Structural Changes during Polystyrene Orientation: A Study of Optical Birefringence and Wide Angle X-Ray Scattering. *J. Appl. Polym. Sci.* **1991**, *42*, 1351–1359.

(91) Marzantowicz, M.; Krok, F.; Dygas, J. R.; Florjańczyk, Z.; Zygadło-Monikowska, E. The Influence of Phase Segregation on Properties of Semicrystalline PEO:LiTFSI Electrolytes. *Solid State Ionics* **2008**, *179*, 1670–1678.

(92) Article, R. Li – O 2 and Li – S Batteries with High Energy Storage. **2012**, *11*, 19–30.

(93) Aurbach, D. A Short Review of Failure Mechanisms of Lithium Metal and Lithiated Graphite Anodes in Liquid Electrolyte Solutions. *Solid State Ionics* **2002**, *148*, 405–416.

(94) Schaefer, J. L.; Lu, Y.; Moganty, S. S.; Agarwal, P.; Jayaprakash, N.; Archer, L. a. Electrolytes for High-Energy Lithium Batteries. *Appl. Nanosci.* **2012**, *2*, 91–109.

(95) Saha, P.; Datta, M. K.; Velikokhatnyi, O. I.; Manivannan, A.; Alman, D.; Kumta, P. N. Rechargeable Magnesium Battery: Current Status and Key Challenges for the Future. *Prog. Mater. Sci.* **2014**, *66*, 1–86.

(96) Muldoon, J.; Bucur, C. B.; Oliver, A. G.; Zajicek, J.; Allred, G. D.; Boggess, W. C. Corrosion of Magnesium Electrolytes: Chlorides – the Culprit. *Energy Environ. Sci.* **2013**, *6*, 482.

(97) Mohtadi, R.; Mizuno, F. Magnesium Batteries: Current State of the Art, Issues and Future Perspectives. *Beilstein J. Nanotechnol.* **2014**, *5*, 1291–1311.

(98) Shterenberg, I.; Salama, M.; Gofer, Y.; Levi, E.; Aurbach, D. The Challenge of Developing Rechargeable Magnesium Batteries. *MRS Bull.* **2014**, *39*, 453–460.

(99) Muldoon, J.; Bucur, C. B.; Oliver, A. G.; Sugimoto, T.; Matsui, M.; Kim, H. S.; Allred, G. D.; Zajicek, J.; Kotani, Y. Electrolyte Roadblocks to a Magnesium Rechargeable Battery. *Energy Environ. Sci.* **2012**, *5*, 5941.

(100) Young, N. P.; Devaux, D.; Khurana, R.; Coates, G. W.; Balsara, N. P. Investigating Polypropylene-Poly(ethylene Oxide)-Polypropylene Triblock Copolymers as Solid Polymer Electrolytes for Lithium Batteries. *Solid State Ionics* **2014**, *263*, 87–94.

(101) Stolwijk, N. A.; Wiencierz, M.; Heddier, C.; Kösters, J. What Can We Learn from Ionic Conductivity Measurements in Polymer Electrolytes? A Case Study on Poly(ethylene Oxide) (PEO)-NaI and PEO-LiTFSI. *J. Phys. Chem. B* **2012**, *116*, 3065–3074.

(102) Vincent, C. A. Ion Transport in Polymer Electrolytes. *Electrochim. Acta* **1995**, *40*, 2035–2040.

(103) Shterenberg, I.; Salama, M.; Yoo, H. D.; Gofer, Y.; Park, J.-B.; Sun, Y.-K.; Aurbach, D. JES FOCUS ISSUE ON ELECTROCHEMICAL INTERFACES IN ENERGY STORAGE SYSTEMS Evaluation of (CF 3 SO 2) 2 N − (TFSI) Based Electrolyte Solutions for Mg Batteries. *J. Electrochem. Soc.* **2015**, *162*, 7118–7128.

(104) Dou, S.; Zhang, S.; Klein, R. J.; Runt, J.; Colby, R. H. Synthesis and Characterization of Poly(ethylene Glycol)-Based Single-Ion Conductors. *Chem. Mater.* **2006**, *18*, 4288–4295.

(105) Ha, S.-Y.; Lee, Y.-W.; Woo, S. W.; Koo, B.; Kim, J.-S.; Cho, J.; Lee, K. T.; Choi, N.-S. Magnesium(II) Bis(trifluoromethane Sulfonyl) Imide-Based Electrolytes with Wide Electrochemical Windows for Rechargeable Magnesium Batteries. *ACS Appl. Mater. Interfaces* **2014**, *6*, 4063–4073.

(106) Huq, R.; Farrington, G. Ion Transport in Divalent Cation Complexes of Poly (Ethylene Oxide). *Solid State Ionics* **1988**, *28–30*, 990–993.

(107) Yang, L. L.; McGhie, A. R.; Farrington, G. C. Ionic Conductivity in Complexes of Poly(ethylene Oxide) and MgCl2. *J. Electrochem. Soc.* **1986**, *133*, 1380.

(108) Liebenow, C. A Novel Type of Magnesium Ion Conducting Polymer Electrolyte. *Electrochim. Acta* **1998**, *43*, 1253–1256.

(109) Lee, D. K.; Allcock, H. R. The Effects of Cations and Anions on the Ionic Conductivity of poly[bis(2-(2-Methoxyethoxy)ethoxy)phosphazene] Doped with Lithium and Magnesium Salts of Trifluoromethanesulfonate and Bis(trifluoromethanesulfonyl)imidate. *Solid State Ionics* **2010**, *181*, 1721–1726.

(110) Wang, W.; Liu, W.; Tudryn, G. J.; Colby, R. H.; Winey, K. I. Multi-Length Scale Morphology of Poly(ethylene Oxide)-Based Sulfonate Ionomers with Alkali Cations at Room Temperature. *Macromolecules* **2010**, *43*, 4223–4229.

(111) Mori, K.; Tanaka, H.; Hashimoto, T. Scattering Functions for Disordered Two-Component Polymer Systems Including Block Polymers. *Macromolecules* **1987**, *20*, 381–393.

(112) Eitouni, H. B.; Balsara, N. P. CHAPTER 19 Thermodynamics of Polymer Blends. In *PHysical Properties of Polymer Handbook 2e*; Mark, J. E., Ed.; 2006; pp. 339–356.

(113) *Physical Properties of Polymers Handbook*; Mark, J. E., Ed.; Springer New York: New York, NY, 2007.

(114) Thelen, J. L.; Inceoglu, S.; Venkatesan, N. R.; Mackay, N. G.; Balsara, N. P. Relationship between Ion Dissociation, Melt Morphology, and Electrochemical Performance of Lithium and Magnesium Single-Ion Conducting Block Copolymers. *Macromolecules* **2016**, DOI: 10.1021/acs.macromol.6b01886.

(115) He, W. N.; Xu, J. T. Crystallization Assisted Self-Assembly of Semicrystalline Block Copolymers. *Prog. Polym. Sci.* **2012**, *37*, 1350–1400.

(116) Quiram, D. J.; Register, R. A.; Marchand, G. R.; Ryan, A. J. Dynamics of Structure Formation and Crystallization in Asymmetric Diblock Copolymers. *Macromolecules* **1997**, *30*, 8338–8343.

(117) Zhu, L.; Chen, Y.; Zhang, A.; Calhoun, B.; Chun, M.; Quirk, R.; Cheng, S.; Hsiao, B.; Yeh, F.; Hashimoto, T. Phase Structures and Morphologies Determined by Competitions among Self-Organization, Crystallization, and Vitrification in a Disordered Poly(ethylene Oxide)-B-Polystyrene Diblock Copolymer. *Phys. Rev. B* **1999**, *60*, 10022–10031.

(118) Ryan, A. J.; Hamley, I. W.; Bras, W.; Bates, F. S. Structure Development in Semicrystalline Diblock Copolymers Crystallizing from the Ordered Melt. *Macromolecules* **1995**, *28*, 3860–3868.

(119) Huang, P.; Zhu, L.; Guo, Y.; Ge, Q.; Jing, A. J.; Chen, W. Y.; Quirk, R. P.; Cheng, S. Z. D.; Thomas, E. L.; Lotz, B.; et al. Confinement Size Effect on Crystal Orientation Changes of Poly(ethylene Oxide) Blocks in Poly(ethylene Oxide)- B -Polystyrene Diblock Copolymers. *Macromolecules* **2004**, *37*, 3689–3698.

(120) Zhu, L.; Cheng, S. Z. D.; Calhoun, B. H.; Ge, Q.; Quirk, R. P.; Thomas, E. L.; Hsiao, B. S.; Yeh, F.; Lotz, B. Phase Structures and Morphologies Determined by Self-Organization, Vitrification, and Crystallization: Confined Crystallization in an Ordered Lamellar Phase of PEO-B-PS Diblock Copolymer. *Polymer (Guildf).* **2001**, *42*, 5829–5839.

(121) Moulin, J.-F.; Damman, P.; Dosière, M. Poly(ethylene Oxide)/lithium Triflate Phase Diagram. *Polymer (Guildf).* **1999**, *40*, 5843–5850.

(122) Vallée, A.; Besner, S.; Prud'Homme, J. Comparative Study of Poly(ethylene Oxide) Electrolytes Made with LiN(CF3SO2)2, LiCF3SO3 and LiClO4: Thermal Properties and Conductivity Behaviour. *Electrochim. Acta* **1992**, *37*, 1579–1583.

(123) Kovacs, A. J.; Straupe, C.; Gonthier, A. Isothermal Growth, Thickening, and Melting of Polyethylene Oxide) Single Crystals in the Bulk. II. *J. Polym. Sci. Polym. Symp.* **2007**, *59*, 31–54.

(124) Kovacs, A. J.; Gonthier, A.; Straupe, C. Isothermal Growth, Thickening, and Melting of Poly(ethylene Oxide) Single Crystals in the Bulk. *J. Polym. Sci. Polym. Symp.* **2007**, *50*, 283–325.

(125) Beaumont, R. H.; Clegg, B.; Gee, G.; Herbert, J. B. M.; Marks, D. J.; Roberts, R. C.; Sims, D. Heat Capacities of Propylene Oxide and of Some Polymers of Ethylene and Propylene Oxides. *Polymer (Guildf).* **1966**, *7*, 401–417.

(126) Afifi-Effat, A. M.; Hay, J. N. Enthalpy and Entropy of Fusion and the Equilibrium Melting Point of Polyethylene Oxide. *J. Chem. Soc. Faraday Trans. 2* **1972**, *68*, 656.

(127) Balko, J.; Lohwasser, R. H.; Sommer, M.; Thelakkat, M.; Thurn-Albrecht, T. Determination of the Crystallinity of Semicrystalline Poly(3-Hexylthiophene) by Means of Wide-Angle X-Ray Scattering. *Macromolecules* **2013**, *46*, 9642–9651.

(128) Ruland, W. X-Ray Determination of Crystallinity and Diffuse Disorder Scattering. *Acta Cryst.* **1961**, *14*, 1180–1185.

(129) Polizzi, S.; Fagherazzi, G.; Benedetti, A.; Battagliarin, M.; Asano, T. A Fitting Method for the Determination of Crystallinity by Means of X-Ray Diffraction. *J. Appl. Crystallogr.* **1990**, *23*, 359–365.

(130) Kline, S. R. Reduction and Analysis of SANS and USANS Data Using IGOR Pro. *J. Appl. Crystallogr.* **2006**, *39*, 895–900.

(131) Malliaras, G.; Friend, R. An Organic Electronics Primer. *Phys. Today* **2005**, *58*, 53–58.

(132) Berggren, M.; Nilsson, D.; Robinson, N. D. Organic Materials for Printed Electronics. *Nat. Mater.* **2007**, *6*, 3–5.

(133) Facchetti, A. π-Conjugated Polymers for Organic Electronics and Photovoltaic Cell Applications †. *Chem. Mater.* **2011**, *23*, 733–758.

(134) Coropceanu, V.; Cornil, J.; da Silva Filho, D. A.; Olivier, Y.; Silbey, R.; Brédas, J.-L. Charge Transport in Organic Semiconductors. *Chem. Rev.* **2007**, *107*, 926–952.

(135) Laquai, F.; Wegner, G.; Bässler, H. What Determines the Mobility of Charge Carriers in Conjugated Polymers? *Philos. Trans. A. Math. Phys. Eng. Sci.* **2007**, *365*, 1473–1487.

(136) Coehoorn, R.; Pasveer, W. F.; Bobbert, P. A.; Michels, M. A. J. Charge-Carrier Concentration Dependence of the Hopping Mobility in Organic Materials with Gaussian Disorder. *Phys. Rev. B* **2005**, *72*, 155206.

(137) Noriega, R.; Salleo, A.; Spakowitz, A. J. Chain Conformations Dictate Multiscale Charge Transport Phenomena in Disordered Semiconducting Polymers. *Proc. Natl. Acad. Sci. U. S. A.* **2013**, *110*, 16315–16320.

(138) Noriega, R.; Rivnay, J.; Vandewal, K.; Koch, F. P. V; Stingelin, N.; Smith, P.; Toney, M. F.; Salleo, A. A General Relationship between Disorder, Aggregation and Charge Transport in Conjugated Polymers. *Nat. Mater.* **2013**, *12*, 1038–1044.

(139) Mollinger, S. a.; Krajina, B. a.; Noriega, R.; Salleo, A.; Spakowitz, A. J. Percolation, Tie-Molecules, and the Microstructural Determinants of Charge Transport in Semicrystalline Conjugated Polymers. *ACS Macro Lett.* **2015**, 708–712.

(140) Gao, J.; Niles, E. T.; Grey, J. K. Aggregates Promote Efficient Charge Transfer Doping of Poly(3-Hexylthiophene). *J. Phys. Chem. Lett.* **2013**, *4*, 2953–2957.

(141) Poelking, C.; Andrienko, D. Effect of Polymorphism, Regioregularity and Paracrystallinity on Charge Transport in Poly(3-Hexylthiophene) [P3HT] Nanofibers. *Macromolecules* **2013**.

(142) Jiang, X.; Harima, Y.; Yamashita, K.; Tada, Y.; Ohshita, J.; Kunai, A. Doping-Induced Change of Carrier Mobilities in poly(3-Hexylthiophene) Films with Different Stacking Structures. *Chem. Phys. Lett.* **2002**, *364*, 616–620.

(143) Zen, A.; Saphiannikova, M.; Neher, D.; Grenzer, J.; Grigorian, S.; Pietsch, U.; Asawapirom, U.; Janietz, S.; Scherf, U.; Lieberwirth, I.; et al. Effect of Molecular Weight

on the Structure and Crystallinity of Poly(3-Hexylthiophene). *Macromolecules* **2006**, *39*, 2162–2171.

(144) Brinkmann, M. Structure and Morphology Control in Thin Films of Regioregular poly(3-Hexylthiophene). *J. Polym. Sci. Part B Polym. Phys.* **2011**, *49*, 1218–1233.

(145) Duong, D. T.; Wang, C.; Antono, E.; Toney, M. F.; Salleo, A. The Chemical and Structural Origin of Efficient P-Type Doping in P3HT. *Org. Electron.* **2013**, *14*, 1330–1336.

(146) Harima, Y.; Eguchi, T.; Yamashita, K. Enhancement of Carrier Mobilities in Poly (3-Methylthiophene) by an Electrochemical Doping. *Synth. Met.* **1998**, *95*, 69–74.

(147) Harima, Y.; Kunugi, Y.; Yamashita, K.; Shiotani, M. Determination of Mobilities of Charge Carriers in Electrochemically Anion-Doped Polythiophene Film. *Chem. Phys. Lett.* **2000**, *317*, 310–314.

(148) Noriega, R.; Rivnay, J.; Vandewal, K.; Koch, F. P. V; Stingelin, N.; Smith, P.; Toney, M. F.; Salleo, A. A General Relationship between Disorder, Aggregation and Charge Transport in Conjugated Polymers. *Nat. Mater.* **2013**, *12*, 1038–1044.

(149) Kline, R. J.; McGehee, M. D.; Kadnikova, E. N.; Liu, J.; Fréchet, J. M. J. Controlling the Field-Effect Mobility of Regioregular Polythiophene by Changing the Molecular Weight. *Adv. Mater.* **2003**, *15*, 1519–1522.

(150) Kline, R. J.; McGehee, M. D.; Kadnikova, E. N.; Liu, J.; Fréchet, J. M. J.; Toney, M. F. Dependence of Regioregular Poly(3-Hexylthiophene) Film Morphology and Field-Effect Mobility on Molecular Weight. *Macromolecules* **2005**, *38*, 3312–3319.

(151) Zen, a.; Pflaum, J.; Hirschmann, S.; Zhuang, W.; Jaiser, F.; Asawapirom, U.; Rabe, J. P.; Scherf, U.; Neher, D. Effect of Molecular Weight and Annealing of Poly(3-Hexylthiophene)s on the Performance of Organic Field-Effect Transistors. *Adv. Funct. Mater.* **2004**, *14*, 757–764.

(152) Chang, J.-F.; Clark, J.; Zhao, N.; Sirringhaus, H.; Breiby, D.; Andreasen, J.; Nielsen, M.; Giles, M.; Heeney, M.; McCulloch, I. Molecular-Weight Dependence of Interchain Polaron Delocalization and Exciton Bandwidth in High-Mobility Conjugated Polymers. *Phys. Rev. B* **2006**, *74*, 115318.

(153) Zhang, R.; Li, B.; Iovu, M. C.; Jeffries-El, M.; Sauvé, G.; Cooper, J.; Jia, S.; Tristram-Nagle, S.; Smilgies, D. M.; Lambeth, D. N.; et al. Nanostructure Dependence of Field-Effect Mobility in Regioregular poly(3-Hexylthiophene) Thin Film Field Effect Transistors. *J. Am. Chem. Soc.* **2006**, *128*, 3480–3481.

(154) Verilhac, J.; Pokrop, R.; LeBlevennec, G.; Kulszewicz-Bajer, I.; Buga, K.; Zagorska, M.; Sadki, S.; Pron, A. Molecular Weight Dependent Charge Carrier Mobility in poly(3,3’ “-Dioctyl-2,2”:5’,2’ ’-Terthiophene). *J. Phys. Chem. B* **2006**, *110*, 13305–13309.

(155) Prosa, T. J.; Winokur, M. J.; Moulton, J.; Smith, P.; Heeger, A. J. X-Ray Diffraction Studies of Iodine-Doped poly(3-Alkylthiophenes). *Synth. Met.* **1993**, *55*, 370–377.

(156) Prosa, T.; Winokur, M.; Moulton, J.; Smith, P.; Heeger, A. X-Ray-Diffraction Studies of

the Three-Dimensional Structure within Iodine-Intercalated poly(3-Octylthiophene). *Phys. Rev. B* **1995**, *51*, 159–168.

(157) Winokur, M. J.; Wamsley, P.; Moulton, J.; Smith, P.; Heeger, A. J. Structural Evolution in Iodine-Doped poly(3-Alkylthiophenes). *Macromolecules* **1991**, *24*, 3812–3815.

(158) Prosa, T. J.; Winokur, M. J.; Moulton, J.; Smith, P.; Heeger, A. J. X-Ray Structural Studies of poly(3-Alkylthiophenes): An Example of an Inverse Comb. *Macromolecules* **1992**, *25*, 4364–4372.

(159) Kawai, T.; Nakazono, M.; Yoshino, K. Effects of Doping on the Crystal Structure of poly(3-Alkylthiophene). *J. Mater. Chem.* **1992**, *2*, 903.

(160) Miller, N. C.; Cho, E.; Gysel, R.; Risko, C.; Coropceanu, V.; Miller, C. E.; Sweetnam, S.; Sellinger, A.; Heeney, M.; McCulloch, I.; et al. Factors Governing Intercalation of Fullerenes and Other Small Molecules between the Side Chains of Semiconducting Polymers Used in Solar Cells. *Adv. Energy Mater.* **2012**, *2*, 1208–1217.

(161) Tashiro, K.; Kobayashi, M.; Kawai, T.; Yoshino, K. Crystal Structural Change in poly(3-Alkyl Thiophene)s Induced by Iodine Doping as Studied by an Organized Combination of X-Ray Diffraction, infrared/Raman Spectroscopy and Computer Simulation Techniques. *Polymer (Guildf).* **1997**, *38*, 2867–2879.

(162) Salleo, A.; Kline, R. J.; DeLongchamp, D. M.; Chabinyc, M. L. Microstructural Characterization and Charge Transport in Thin Films of Conjugated Polymers. *Adv. Mater.* **2010**, *22*, 3812–3838.

(163) Lan, Y.-K.; Huang, C.-I. A Theoretical Study of the Charge Transfer Behavior of the Highly Regioregular Poly-3-Hexylthiophene in the Ordered State. *J. Phys. Chem. B* **2008**, *112*, 14857–14862.

(164) Garcia-Belmonte, G.; Vakarin, E. V.; Bisquert, J.; Badiali, J. P. Doping-Induced Broadening of the Hole Density-of-States in Conducting Polymers. *Electrochim. Acta* **2010**, *55*, 6123–6127.

(165) Su, N. C.; Smith, Z. P.; Freeman, B. D.; Urban, J. J. Size-Dependent Permeability Deviations from Maxwell's Model in Hybrid Cross-Linked Poly(ethylene glycol)/Silica Nanoparticle Membranes. *Chem. Mater.* **2015**, *27*, 2421–2429.

(166) Stöber, W.; Fink, A.; Bohn, E. Controlled Growth of Monodisperse Silica Spheres in the Micron Size Range. *J. Colloid Interface Sci.* **1968**, *26*, 62–69.

(167) Percus, J. K.; Yevick, G. J. Analysis of Classical Statistical Mechanics by Means of Collective Coordinates. *Phys. Rev.* **1958**, *110*, 1–13.

Appendix A1 - Case Studies in X-Ray Scattering Analysis

A1.1 Introduction

After devoting significant effort into attaining quantitative X-ray scattering data, the experimenter is then often left with the question, “What do I do with all of this data?” A cursory search of literature often leads to the answer of “just about anything”. Unfortunately, in many situations, the assumptions required to apply analysis techniques that can be found in most texts do not hold for many experimental systems, especially when studying dense (i.e. non-solution) polymer samples. While it is true that absolute scattering data contains a wealth of structural information, due to the loss of phase information, scattering cannot be used independently; one must always recognize that extracting useful information depends very heavily on their prior knowledge of the system. Therefore, perhaps a better starting point for answering the question of how to analyze one’s scattering data is, “What do I know about my system?”

The aim of this chapter is to provide an example of how to approach X-ray scattering data analysis based on the question above. My approach will be to provide my analysis of two systems that lie at the extremes prior knowledge: in Section A1.2, I will analyze a system where the material has both an unknown composition and an unknown structure, while in Section A1.3, I will highlight what additional information can be learned through quantitative X-ray analysis of a system that has already been well-characterized by other techniques. In each case, I will attempt to emphasize the importance of obtaining information from other characterization techniques, and provide examples of what one could learn if more was known about the given sample.

A1.2 Characterization of an Unknown Sample – Model-Independent Analysis

While it will become clear during this chapter that complementary characterization techniques are essential to fully harness the power of quantitative X-ray scattering, in this section I aim to highlight what information can be gleaned under circumstances where little to nothing is known about the sample prior to X-ray characterization. In this instance, a solid polymeric sample was received through a proprietary source, which did not disclose the material composition. What is known about the material is that it consists of a blend of polymers and/or monomers, wherein at least one component has been chemically cross-linked (thus forming a solid). Furthermore, the sample is known to require a high temperature thermal treatment step in order to improve its physical properties. The source of the material suspected that nano-scale phase separation of the sample components during thermal treatment was responsible for the enhancement of its mechanical properties. Therefore, my goal was to look for indications of nano-scale phase separation in the thermally treated sample, and if present, find out what role thermal treatment plays in the final nanostructure of the material.

A1.2.1 Experimental

In total, three independent X-ray scattering experiments were conducted on two separate samples. In order to address the question of whether or not nano-scale phase separation was occurring within the sample, both SAXS and WAXS measurements were performed on a sample

that had already been thermally treated. The SAXS measurement was made at 30 °C, while WAXS measurements were made at both 30 and 120 °C. Finally, to address the origin of the nanostructure observed in the thermally treated sample, time-dependent SAXS measurements were performed *in situ* during the thermal treatment of a sample at 120 °C. All of these experiments were performed at ALS BL 7.3.3[60] using a custom built heated sample stage.

All of the resulting 2D scattering images were found to be isotropic, and were converted to 1D profiles using the Nika[61] macro, as described in Chapter 2. Furthermore, the 1D SAXS intensity profiles were corrected using Equation 2.12 and the 1D WAXS intensity profiles were corrected using Equation 2.25. Finally, all corrected 1D scattering profiles were calibrated to absolute units following the procedure in Chapter 2.

A1.2.2 Results and Discussion

In Figure A1.1 I plot the results of the SAXS and WAXS experiments at 120 °C, with the corresponding 30 °C profiles provided for reference. As anticipated by the anonymous sample donor, there are periodic correlations on the order of 33 and 11 nm, indicated by shallow maxima in the SAXS profiles, which suggest microphase separated structures. Furthermore, in addition to the typical polymer amorphous halos at large angles, which correspond to correlations of roughly 0.48 and 0.21nm, there is a broad peak in the MAXS regime, which indicates correlations on the order of 1.7 nm. I also note that the positions of each correlation are generally insensitive to temperature; however, the total intensity of the SAXS profile increases with temperature, indicating a change in scattering contrast.

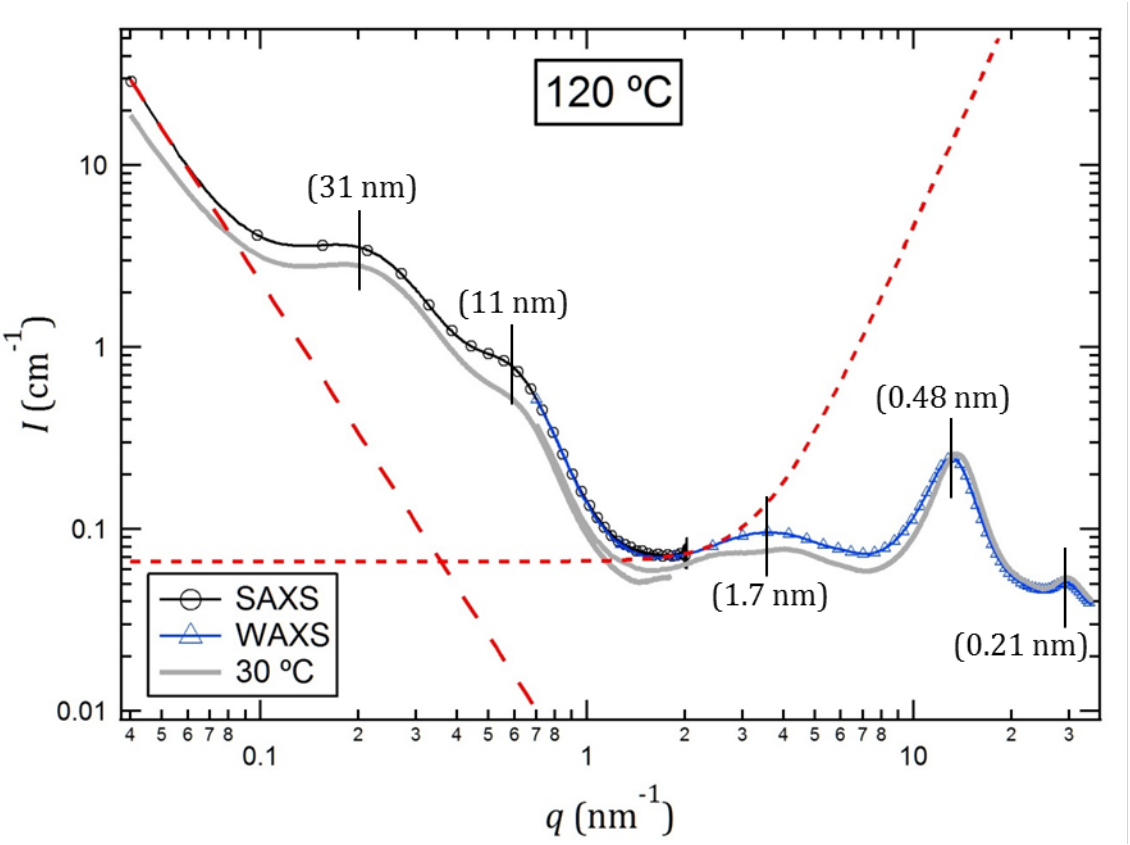

Figure A1.1:Combined absolute SAXS and WAXS profiles for the thermally treated sample at 120 °C. The SAXS profile (black curve/circles) was measured at the end of the *in situ* thermal treatment experiment, while the WAXS profile (blue curve/triangles) was collected from a thermally treated sample that was heated up to 120 °C. The solid grey curves represent the combined SAXS and WAXS profiles for the thermally treated sample at 30 °C, while the dashed red curves demonstrate the power law fits that were used to subtract the background intensity from the SAXS data. The high q fit ($I_{fit}^{Hq}(q)$) is $I_{fit}^{Hq}(q) = 0.067 + 4.5 \times 10^{-4} q^{-4}$, and the low q fit ($I_{fit}^{Lq}(q)$) is $I_{fit}^{Lq}(q) = 3.6 \times 10^{-3} q^{-2.8}$.

In order to better characterize the correlations in the SAXS regime, it is common practice to eliminate scattering intensity due to the other regimes. To eliminate the excess intensity from MAXS/WAXS length-scales, I fit a power law of order 4 ($I_{fit}^{Hq}(q) = B + Cq^{-4}$, where B and C are fit parameters) to the base of the MAXS "peak" and subtract the result from the experimental data[55]. Subtraction of the high q intensity amounts to eliminating "grainy-ness" from the data; the remaining SAXS intensity is due to correlations between domains with homogeneous electron density (Vonk and Roe?). In this work, the fit parameter $C = 4.5 \times 10^{-4}$, determined from the nonlinear least squares regression shown in Figure A1.1, was fixed for all remaining samples; the fit parameter B was adjusted between samples to preclude significant negative intensity values in the high q range of the SAXS data. I also eliminate the strong asymptotic low q scattering in a similar fashion by fitting a free power law ($I_{fit}^{Lq}(q) = Cq^{-D}$, where C and D are fit parameters) to the initial data points at low q (near the beamstop) for each SAXS profile. The resulting function is subtracted from its corresponding SAXS data set. The low q background subtraction is largely based on convenience, and amounts to neglecting any structures or correlations at length-scales larger than those observed in SAXS (i.e. larger than ~150 nm).

Structures at such large length-scales are more amenable to study with other techniques (e.g. scanning electron microscopy, visible light scattering, and optical microscopy), and as such, their contribution to scattering intensity in the SAXS regime are treated as parasitic under most circumstances. The second half of this chapter will highlight a notable exception to this convention.

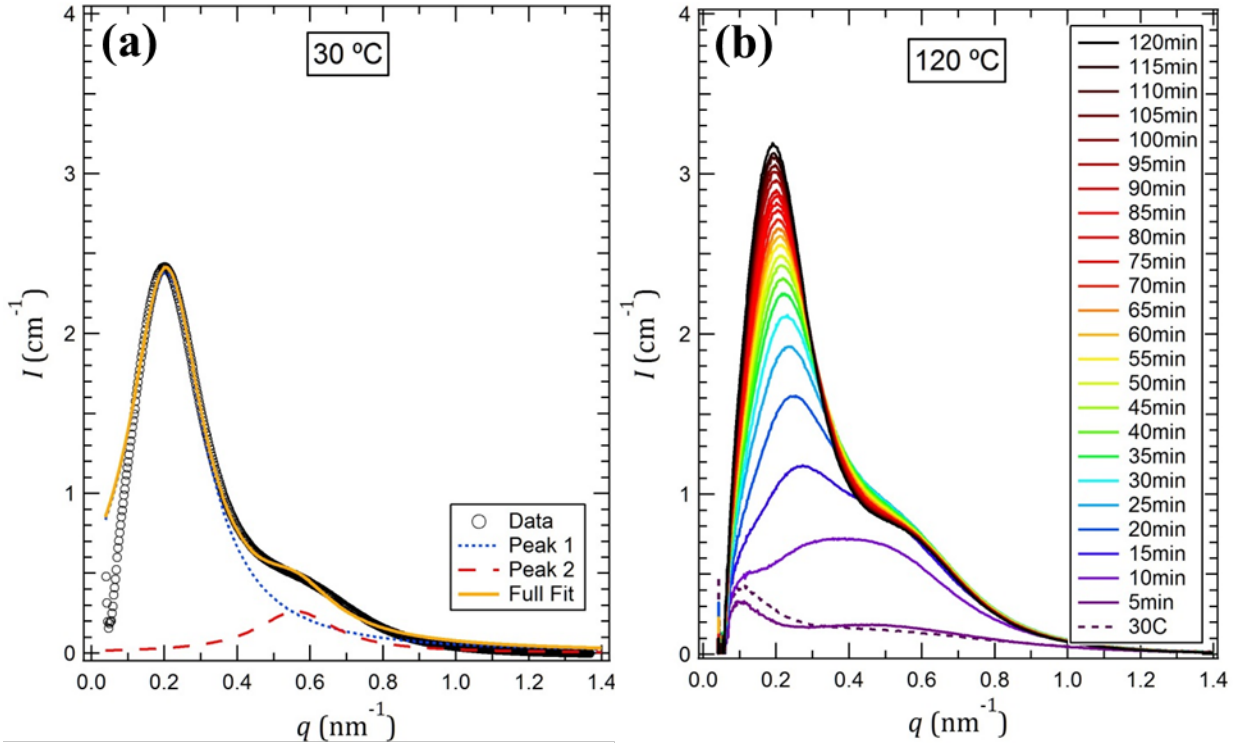

Figure A1.2: (a) Background corrected data from the thermally treated sample at 30 °C. The experimental data is represented by black circles, whereas the solid gold curve represents the best fit from the linear combination of two Lorentzian peak functions. The individual Lorentzian peaks are provided as the dashed curves for reference. (b) Background corrected time-dependent scattering data from a sample *in situ* during thermal treatment at 120 °C. The time for each scattering measurement is related by its color.

The corrected scattering profile for the thermally treated sample at 30 °C is shown in Figure A1.2a. Also demonstrated in Figure A1.2a is a multi-peak fitting analysis performed using the "Multi-Peak Fit" package in Igor Pro, wherein two Lorentzian peak functions (dashed curves) were simultaneously fit to the data, resulting in a suitable replication of the entire scattering profile (solid curve). It is notable that the low q subtraction appears to truncate the data at the lowest q-values; while this is not ideal, for the purpose of this analysis, it has little impact on the final result. The fitting analysis demonstrated in Figure A1.2a facilitates the de-convolution of the contributions to the SAXS profile, and allows us to assign unbiased values to the peak positions; the result from the fit in Figure A1.2a indicates that the correlation lengths are 30.8 nm and 11.2 nm for Peak 1 and Peak 2, respectively. Without additional information regarding the composition of the sample, or structural analysis using a real-space technique (e.g. transmission electron microscopy), we can only speculate as to what structural motifs are responsible for the scattering intensities at these two length-scales; however, one powerful aspect

of quantitative X-ray scattering using a synchrotron light source is that, in addition to characterizing static structures, we can observe structure formation through *in situ* experiments.

Figure A1.2b provides the background subtracted SAXS profiles as a function of time during thermal treatment. The nanostructure of the sample at 30 °C before thermal treatment (dashed curve in Figure A1.2b) did not exhibit any obvious correlations at the length-scales seen in the thermally treated sample. Time = 0 indicates when the heating stage setpoint was changed to 120 °C. The stage reached the target temperature within 5 minutes; however, the sample temperature likely did not reach 120 °C until a short time later (due to the low thermal conductivity of polymeric materials). The SAXS profiles at short times in Figure A1.2b indicate that the structure at ~11 nm forms rapidly upon reaching 120 °C and remains relatively unchanged at later times. Conversely, the peak corresponding to the correlations of ~31 nm in the fully cured sample, starts forming at early times, but continues to grow and shift to lower q throughout the 120 minute experiment.

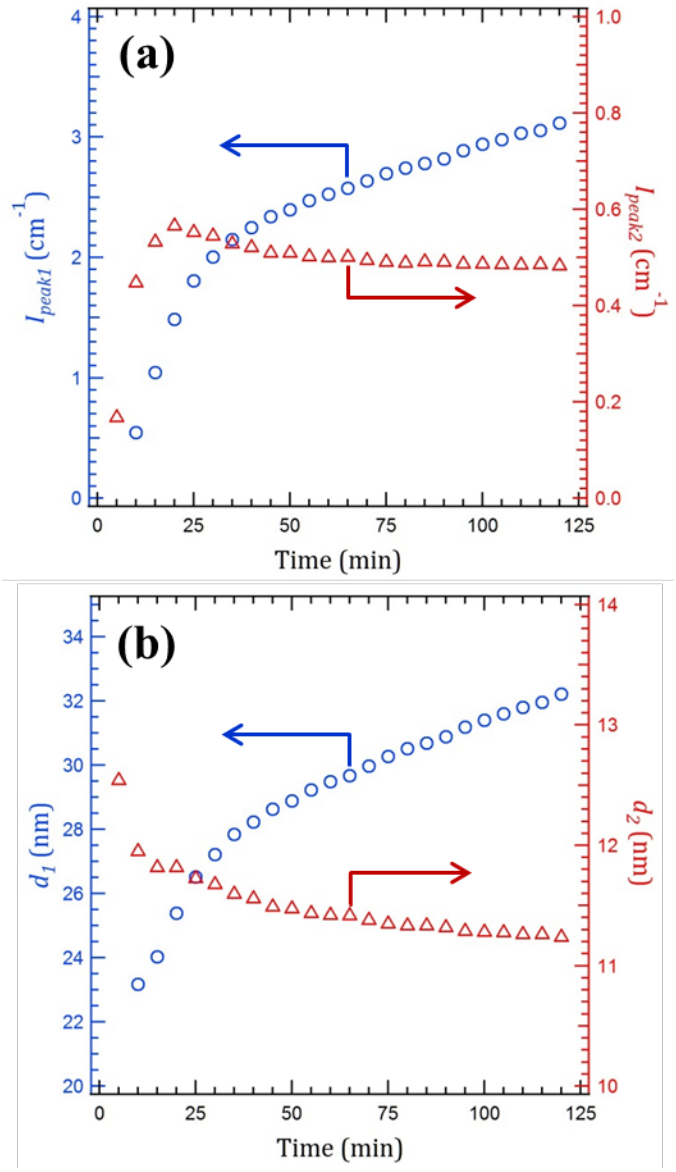

Figure A1.3: (a) The time-dependent peak intensities (I_{peak}) acquired through de-convolution of the data in Figure A1.2b. Data from Peak 1 (I_{peak1}) are provided as blue circles and correspond to the left axis, while data from Peak 2 (I_{peak2}) are given by red triangles and correspond to the right axis. (b) The correlation length (domain spacing) determined from the positions of the de-convoluted peaks. Data from Peak 1 (d_1) are provided as blue circles and correspond to the left axis, while data from Peak 2 (d_2) are given by red triangles and correspond to the right axis.

I used the sample multi-peak fitting analysis demonstrated in Figure A1.2a to de-convolute the time-dependent SAXS profiles in Figure A1.2b. In Figure A1.3a I plot the time-dependence of the peak intensity (I_{peak}) for both peaks. As discussed qualitatively above, the quantitative evaluation of the high q peak (Peak 2) increases rapidly at short times, and then remains relatively constant for Time > 20 min (decreasing slightly between 20 and 50 min). Interestingly, the quantitative evaluation of the low q peak (Peak 1) intensity reveals two distinct trends with time: For Time < ~30 min, the peak intensity increases linearly with a steep slope, which transition to a new linear dependence with a shallower slope for Time > ~40 min. The correlation length (i.e. domain spacing, d) based on the peak position (q^*; $d = \frac{2\pi}{q^*}$) for each peak

are provided in Figure A1.3b. The time-dependence observed for the correlation length derived from Peak 1 appears strongly correlated with its corresponding peak intensity from Figure A1.3b; there are two distinct regimes of linear time-dependence, with the correlation length increasing throughout the experiment. Conversely, the correlation length derived from the time-dependence of Peak 2 decreases monotonically with time.

While peak intensity and correlation length are useful in understanding the time-evolution of the nanostructure within the sample, without real-space evidence or a model to guide our interpretation of what the peaks represent, little can be learned about what is physically happening in the system during thermal treatment. However, the model independent parameter known as the SAXS invariant, Q, might provide some insight. The invariant is defined as[55,56]

$$Q \equiv \frac{1}{2\pi^2}\int_0^\infty I(q)q^2 \mathrm{d}q \,[=]\mathrm{cm}^{-1}\mathrm{nm}^{-3} \tag{A1.1}$$

and physically represents the total scattering power of the system, which is determined by the sample composition and it independent of nanostructure shape and size. For illustrative purposes, the invariant for an ideal two-phase (Q_{ideal}) system with sharp phase boundaries is simple given by[55,56]

$$Q_{ideal} = 1 \times 10^{-21}(B_A - B_B)^2 \phi_A \phi_B [=]\mathrm{cm}^{-1}\mathrm{nm}^{-3} \tag{A1.2}$$

where the prefactor is simply required for unit consistency, and B_A and B_B are the scattering length densities and ϕ_A and ϕ_B are the volume fractions of phases A and B, respectively. The term $(B_A - B_B)^2$ is known as the scattering contrast. Thus for a given amount of components A and B, any sample will yield the same value for Q_{ideal} based on the relative scattering length densities (i.e. electron density) between the two phases, regardless of the shape or size of the A and B domains. The invariant can thus be thought of as the total magnitude of electron density fluctuation within the sample[55]. Note that the theoretical treatment of the scattering invariant precludes intensity contributions from atomic scattering, thus intensities at high q (MAXS/WAXS) should be subtract from the SAXS data before evaluating Q[55,56].

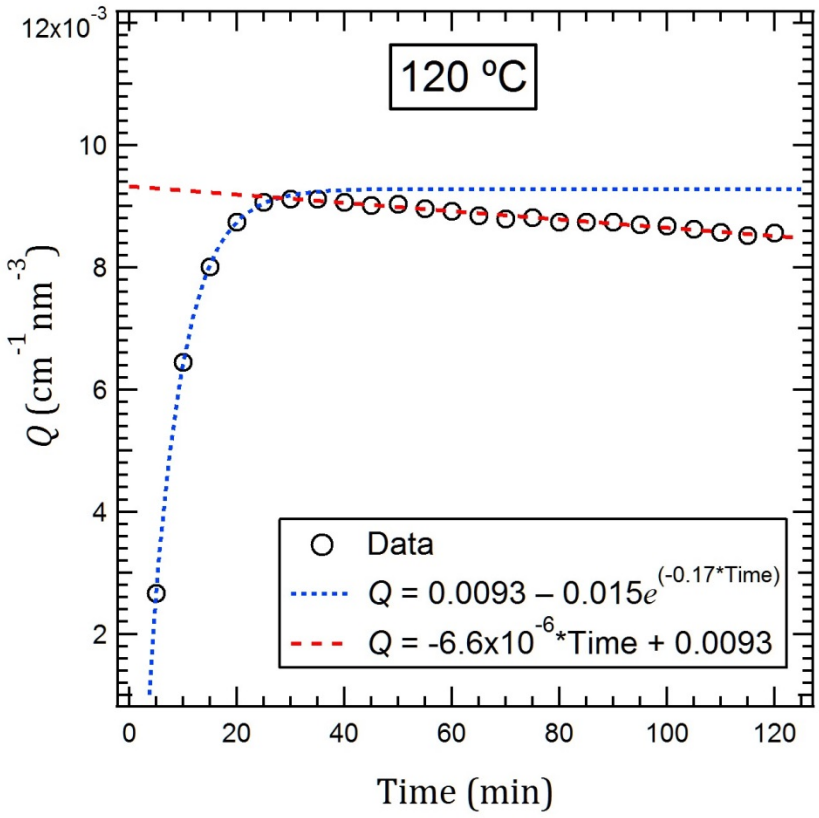

Figure A1.4: Time-dependence of the SAXS invariant. Data are indicated by black circles, while the dashed curves represent best fits from the functions provided in the inset.

In Figure A1.4, I provide the time-dependence of the SAXS invariant (Q) calculated from the background-corrected scattering data provided in Figure A1.2b. The integral in Equation A1.1 was evaluated using the experimental q-range since the background subtraction already precluded intensity contributions from other length-scales. For Time < 30 min, Q increases very rapidly and is well-fit by the exponential function indicated by the dashed blue curve in Figure A1.4. This result is consistent with a rapid onset of phase separation when the temperature is increased to 120 °C. At Time > 30, the invariant decreases linearly, following the dashed red regression line. The transition in time-dependent behavior for the invariant aligns well with the trends in peak intensity (I_{peak}) and domain spacing (d) in Figure A1.3. It is interesting to note that at longer times (Time > 30 min), while the correlation length (d_1) continues to increase for Peak 1, the invariant actually decreases. Multiple scenarios could account for this behavior. One explanation, which assumes a 2-phase system, is that the volume fraction of phase-separated domains reaches 0.50 at ~30 min, and thus as phase separation continues, the $\phi_A\phi_B$ term in Equation A1.2 actually begins to decrease. This scenario could be easily refuted with knowledge of the sample composition (i.e. whether or not a one component represents ~50% of the volume). In a related (2-phase) scenario, the scattering length densities of the mixed and de-mixed phases reach a maximum difference at Time ~30 min, whereupon further de-mixing leads to a decrease in scattering contrast (i.e. the $(B_A - B_B)^2$ term in Equation A1.2). Based on our knowledge of the system -- a partially cross-linked mixture undergoing thermal treatment to improve mechanical properties – a reasonable explanation is that all phase separation occurs at early times (Time < 30 min); and at long times, the phase-separated domains coarsen (d_1 increases), while

the contrast changes (Q decreases) from either (1) the densification of one phase, or (2) the loss of material due to small molecule evaporation. This interpretation is supported by the fact the fit functions used to describe both time-regimes have the same intercept value ($Q(0) = 0.0093$ $cm^{-1}nm^{-1}$), indicating that complete phase separation of the original sample components (i.e. before densification or material loss) would have yielded the same value of Q.

A1.2.3 Conclusion

In this section I have presented the analysis of X-ray scattering data collected from a system with completely unknown composition and structure. The goal of the analysis was to determine if the sample was microphase separated, and if so, gather insight into how thermal treatment affects the nanostructure of the material. Combined absolute SAXS and WAXS measurements on a thermally treated sample demonstrated that the material was indeed microphase separated, and the nanostructure was not significantly influenced by temperature after thermal treatment was complete. I then used *in situ* SAXS measurements during the thermal treatment of an uncured sample to reveal the kinetics of nanostructure formation. Since we were uninterested in structures at length-scales smaller than phase-separated domains, the scattering from WAXS was used to determine a background function that was subsequently used to correct the SAXS data. The corrected SAXS data were found to be well-represented by the linear combination of two Lorentzian functions, indicating periodic correlations at two different length-scales. Although the nature of the correlations remains unknown without further characterization from complementary techniques (e.g. TEM), their time-evolution of the correlation peaks does provide some insight into their origin. Through combined analysis of the time-dependence of the de-convoluted peaks and SAXS invariant, it appears probable that microphase separation occurs rapidly (Time < 30 min) upon heating the sample to 120 °C, whereupon continued thermal treatment facilitates the coarsening of microphase separated domains, and either the densification of one microphase or the loss of small molecule material.

It should be clear that quantitative X-ray scattering is most powerful when combined with complementary characterization techniques and an extensive knowledge of sample composition. However, the ability to rapidly collect data under controlled sample environments at a synchrotron light source expands the experimental utility of X-ray scattering techniques beyond simple structural analysis. Thus, through appropriate interpretation, absolute X-ray scattering data can provide significant physical insight, even in instances where little is known about the nature or composition of the nanostructures within a material.

A1.3 Characterization of a Well-Known Sample – Leveraging Models

In this section, I will analyze the scattering data from a set of samples where the composition has been very well characterized, but the details of the nanostructure are not completely understood. This work was performed in collaboration with Dr. Norman C. Su, and follows from his work in ref 165. In their study, Su and coworkers[165] developed a model nanocomposite membrane system composed of silica (SiO_2) nanoparticles dispersed an a crosslinked poly(ethylene glycol) (PEG) polymer matrix. Three different nanoparticle sizes were used, and for each particle size, three separated membranes with different particle loadings were

made. The goal of this model system was to study the influence of nanoparticle size and loading on gas transport through composite membranes.

In the original study[165], the silica nanoparticles were characterized by transmission electron microscopy (TEM) before preparing the membranes. All of the particles were founds to be roughly spherical and relatively monodisperse. The average size for each particle sample was determined through image analysis of the TEM micrographs. Furthermore, the structure of the composite membranes was analyzed using scanning electron microscopy (SEM) on membrane cross-sections, and it was concluded that the silica nanoparticles were well-dispersed within the composite membranes. Finally, the total particle loading for each membrane sample was determined gravimetrically by the weight change upon thermal decomposition of the membrane. The mass fraction of particles was converted to volume loading using the density of the particles and the crosslinked PEG matrix.[165]

In this work, I will demonstrate how to utilize X-ray scattering data to (1) analyze the particle size, as measured within the membrane, (2) determine the particle loading given the density of each phase, and (3) analyze the inter-particle correlations (dispersion/packing structure) within the membranes. In contrast to Section A1.2, we know a significant amount about the expected structure and composition within these films. Thus, in some cases the results from scattering will represent redundant measurements, which can be used as independent verification, while in others cases the scattering data provides new evidence not attainable from the analysis performed in the original study.

A1.3.1 Experimental

In total, the scattering from 15 membranes will be analyzed in this study: membranes with 5 different volume loadings were prepared for each different particle size. The name for each sample is given by the particle used to form the composite and its loading in vol. %. The smallest particles studied were ~12 nm in diameter and were purchased for the study in ref [165]. Samples using these particles are labeled "Ludox 12nm". The other two particle sizes were synthesized in ref [165] using the Stöber method[166] to produce particles with nominal diameters of 41 nm and 130 nm. Samples using these particles are labeled "Stöber 41nm" and "Stöber 130nm", respectively. In this work, I will analyze all 9 of the original composite membranes evaluated previously[165], as well as two additional membranes from each particle size using nominal loadings of 0.5 vol% and 2.5 vol%. The scattering samples were prepared inside of an argon glovebox after the membranes were thoroughly dried under vacuum. The membranes were hermetically sealed inside custom sample holders with kapton film windows. An empty sample holder was also prepared inside of the glovebox to serve as the "empty cell" scattering reference.

Due to the large differences in size between the various silica particles, the X-ray scattering data had to be collected using a number of different instrument setups. Scattering measurements on the Ludox 12nm membranes were performed at the ALS BL 7.3.3[60] using both SAXS and WAXS geometries, while the Stöber 41nm membranes were measured at the ALS BL 7.3.3 using SAXS only. The Stöber 130nm membranes were measured using a SAXS setup at ALS BL 7.3.3, as well as a SAXS setup at the Stanford Synchrotron Radiation Laboratory (SSRL) BL 1-5. The SAXS and WAXS measurements at ALS BL 7.3.3 utilized detector distances of ~3.8m and ~0.3m, respectively, 10keV X-rays, and a Pilatus 2M (Dectris) detector.

The SAXS measurements at SSRL BL 1-5 utilized a ~3 m detector distance, 7.8 keV X-rays, and a Rayonix 165 CCD Camera. All measurements were made at room temperature.

All of the resulting 2D scattering images were found to be isotropic, and were converted to 1D profiles using the Nika[61] macro, as described in Chapter 2. Furthermore, the 1D SAXS intensity profiles were corrected using Equation 2.12 and the 1D WAXS intensity profiles were corrected using Equation 2.31. Finally, all corrected 1D scattering profiles were calibrated to absolute units following the procedure in Chapter 2.

A1.3.2 Results and Discussion

The scattering function for an isolated spherical object is well-known.[55] The intensity profile ($I(q)$) for the scattering from an ensemble of non-interacting monodisperse spherical particles (e.g., a dilute solution) is related by

$$I(q) = \left(B_p - B_s\right)^2 \phi_p V_p \left\{\frac{3\left[\sin\left(qr_p\right) - \left(qr_p\right)\cos\left(qr_p\right)\right]}{\left(qr_p\right)^3}\right\}^2 \tag{A1.3}$$

where B_p and B_s are the scattering length densities of the particle and the solvent, respectively, ϕ_p is the volume fraction of particles, V_p is the volume of a single particle, and r_p is the particle radius. Inspection of Equation A1.3 reveals that the scattering profile for a dilute solution of particles is completely defined if the scattering length densities of the particle and solvent are known, along with the particle radius and the total volume fraction of particles in solution. Furthermore, as long as the particles are non-interacting, one can use Equation A1.3 with arbitrary scaling to find the particle radius (i.e., if the product $\left(B_p - B_s\right)^2 \phi_p$ is unknown). Figure A1.5 below demonstrates scattering profiles calculated for a 0.1 vol% sample of Stöber silica spheres in a crosslinked PEG "solvent". As demonstrated by the solid black curve in Figure A1.5, the scattering induced by isolated spherical particles leads to an oscillating decay in intensity at length-scales commiserate to and smaller than the particle. The location and periodicity of the oscillations derives from the bracketed term in Equation A1.3 (i.e., the form factor), indicating these oscillations can be used to extract the particle radius from an experimental scattering profile.

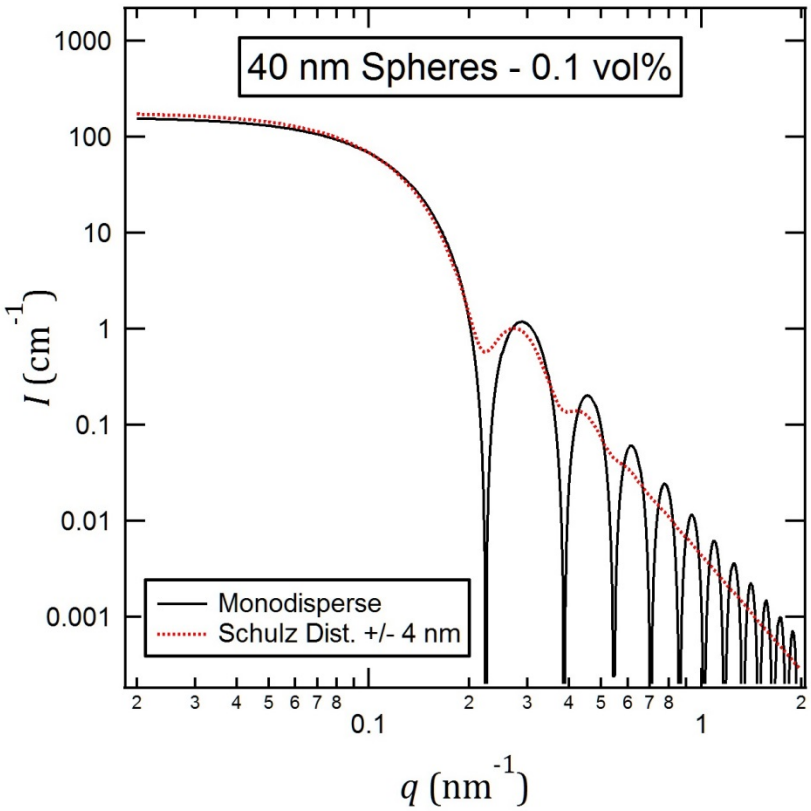

Figure A1.5: Calculated scattering profiles using Equation A1.3 (solid black curve) and a Schulz distribution (dashed red curve, +/- 4 nm) with the scattering length densities for Stöber spheres and crosslinked PEG, a sphere radius of 20nm, and a total loading of 0.1 vol%.

If an ensemble of isolated spherical particles is not perfectly monodisperse, then the solid black profile in Figure A1.5 becomes attenuated. The most striking difference in the scattering profile from a distribution of particle sizes is the damping of the oscillations at high q. The dashed red curve in Figure A1.5 provides the calculated scattering profile for an ensemble of spherical particles with a Schulz distribution of particle sizes, where the mean particle size is 40 nm and the standard deviation is 4 nm. It is clear from Figure A1.5 that most experimental systems, which nearly always have some dispersity, will show a limited number of oscillations in their scattering profiles. Both of the profiles shown in Figure A1.5 were generated using the NCNR Analysis Macro[130] package in Igor Pro. This package, which was developed by Steven Kline at NIST, contains the scattering functions for many structure models, is well-documented, and is overall an excellent resource for analyzing scattering data.

In Figure A1.6 I provide the absolute scattering profiles collected from all of the "dilute" composite films. Each data set also includes the calculated scattering profiles from a best fit of the data to the model of dilute spheres with a Schulz distribution. The best fits were determined using the NCNR Analysis Macro[130] package, with the particle radius (r_p) and standard deviation (σ), as well as the particle volume fraction (ϕ_p) used as fit parameters. The scattering contrast ($(B_p - B_s)^2$) was fixed during the fit, and a constant background intensity (I_{bkg}) was set to $I_{bkg} = 0.03$ cm^{-1} for the Stöber sphere samples and $I_{bkg} = 0.006$ cm^{-1} for the Ludox particle

samples. As demonstrated in Figure A1.6a, the experimental scattering profiles are captured very well by the Schulz spheres model over all q, indicating that the Stöber 130nm particles are approximately spherical and are non-interacting in the composite films at these loadings (i.e., well-dispersed and dilute). In Figure A1.6b-c, the Schulz spheres model could not describe the entire profiles for the Stöber 41nm and the Ludox 12nm particles. For these samples, the Schulz sphere model was fit using a selected portion of the experimental profiles, as indicated by the vertical dashed lines, in order to characterize the particle size. In all cases, a suitable fit of the intensity oscillations was achieved, indicating the particles can be described as approximately spherical. The failure of the model to capture the experimental profiles at low q indicates that the particles are "interacting" i.e., they are spatially correlated (possibly forming aggregate structures), even at these dilute loadings. The fitted particle sizes and standard deviations are provided in Table A1.1. The values are in good agreement with the those determined from TEM in ref [165]; however, the deviation values are consistently larger from X-ray scattering. Since the TEM measurements are taken from a limited number of particles, the distributions determined from the scattering measurements are likely more representative of the true values.

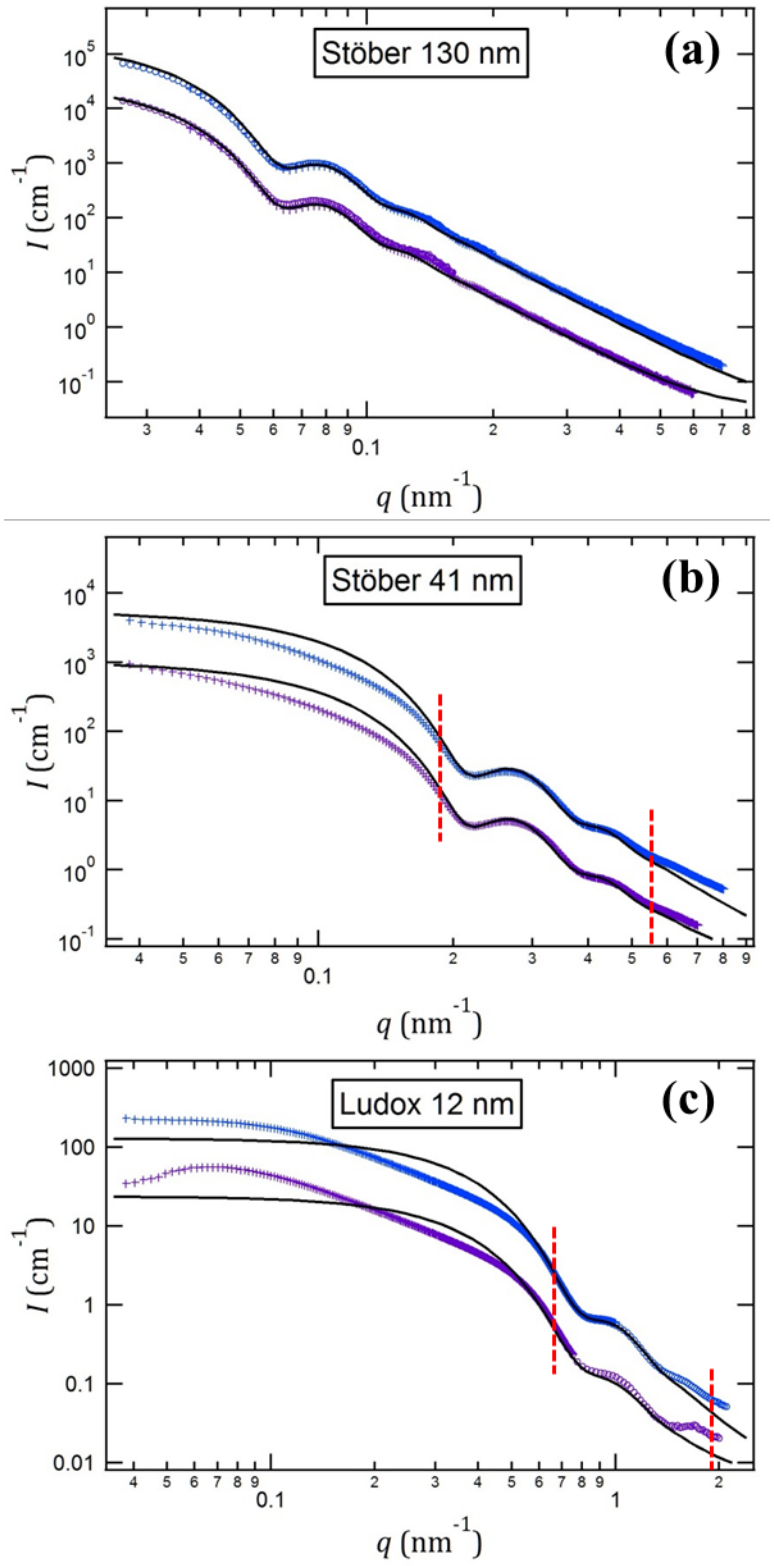

Figure A1.6: (a) Experimental scattering from the Stöber 130 nm particles with $\phi_p = 0.005$ (lower symbols) and $\phi_p = 0.029$ (upper symbols) along with the best fit from a Schulz distribution of spheres (black curves). (b) Experimental scattering from the Stöber 41 nm particles with $\phi_p = 0.004$ (lower symbols) and $\phi_p = 0.024$ (upper symbols) along with the best fit from a Schulz distribution of spheres (black curves). (c) Experimental scattering

from the Ludox 12 nm particles with $\phi_p = 0.004$ (lower symbols) and $\phi_p = 0.020$ (upper symbols) along with the best fit from a Schulz distribution of spheres (black curves). All scattering intensities are absolute. The vertical red dashed lines indicate the region that was fit during the regression analysis in (b) and (c).

Table A1.1: Silica particle diameters, as measured by TEM (D_{TEM}) in ref [165] and SAXS (D_{SAXS}) in this work. The number in parantheses in the heading of each D_{SAXS} collum indicates the nominal particle loading in vol%.

Particle Type	D_{TEM} (nm)	D_{SAXS} (~0.4%) (nm)	D_{SAXS} (~2.5%) (nm)
Ludox 12nm	12 ± 1.2	11 ± 2	11 ± 2
Stöber 41nm	41 ± 3.9	40 ± 5	40 ± 5
Stöber 130nm	130 ± 6.5	140 ± 20	140 ± 20

In addition to characterizing the particle size within the actual composite membranes, we can also use the scattering profiles to determine the total particle loading, independent of any model. To do this, we return to the scattering invariant discussed in the previous section, which is defined by Equation A1.1. In this system, the scattering invariant can have quantitative meaning because we know the chemical make-up of the samples. To compute the invariant, I used the NCNR Analysis Macro[130] package to extrapolate the experimental scattering profiles to $q = 0$ using the Guinier approximation and to $q = \infty$ using a power law of order (-4), followed by numerical integration, also using the NCNR macro. The experimental scattering data for all membranes can be found in Figures A1.8-A1.10 below. Since the composite membranes represent a 2-phase system, the measured invariant from the X-ray scattering profiles should correspond to the values predicted with Equation A1.2. I test this by plotting the experimental scattering invariant versus the particle loading term from Equation A1.2 (values provided by Norman Su, Table A1.2) in Figure A1.7. I note that the scattering length densities from the Ludox silica and Stöber silica are expected to be different due to their different mass densities ($\rho_{\text{Ludox}} = 2.2$ gcm^{-3}; $\rho_{\text{Stöber}} = 2.1$ gcm^{-3})[165]. The predicted invariant values from Equation A1.2 using the two resulting scattering contrasts are provided as dashed lines in Figure A1.7. The scattering length densities for each phase were calculated from Equation 2.3. The values for silica were calculated using the densities above and are $B_{\text{Ludox}} = 1.86 \times 10^{11}$cm^{-2} and $B_{\text{Stöber}} = 1.78 \times 10^{11}$cm^{-2}. The value for the crosslinked PEG matrix was determined assuming a density of $\rho_{\text{PEG}} = 1.18$ gcm^{-3}.[165] It was also assumed that the PEG phase consisted of 700 g mol^{-1} PEG backbones with methacrylate endgroups, yielding $M_{PEG} = 838$ gmol^{-1}; $\eta_{PEG} = 455$ [e$^-$]; and $B_{\text{PEG}} = 1.09 \times 10^{11}$cm^{-2}. In all cases, the predicted and experimental invariant values at dilute loadings are very similar (see inset of Figure A1.7); however, as the particle loadings are increased, the experimental invariant values tend to undershoot the predictions from Equation A1.2. The discrepancies seen between experimental and calculated invariant values could arise for a number of reasons, including: (1) our extrapolation protocol for the scattering profiles does not accurately describe the intensities as $q \to 0$ and $q \to \infty$; (2) our scattering length density values are incorrect; (3) the gravimetrically measured particle loadings are incorrect; or (4) the 2-phase model breaks down due to the presence of diffuse interfaces[55]. For the time being, I will simply assume the 2-phase model holds and use Equation A1.2 with the experimental invariant values to calculate ϕ_{SiO_2} for each of the membranes (Table A1.2).

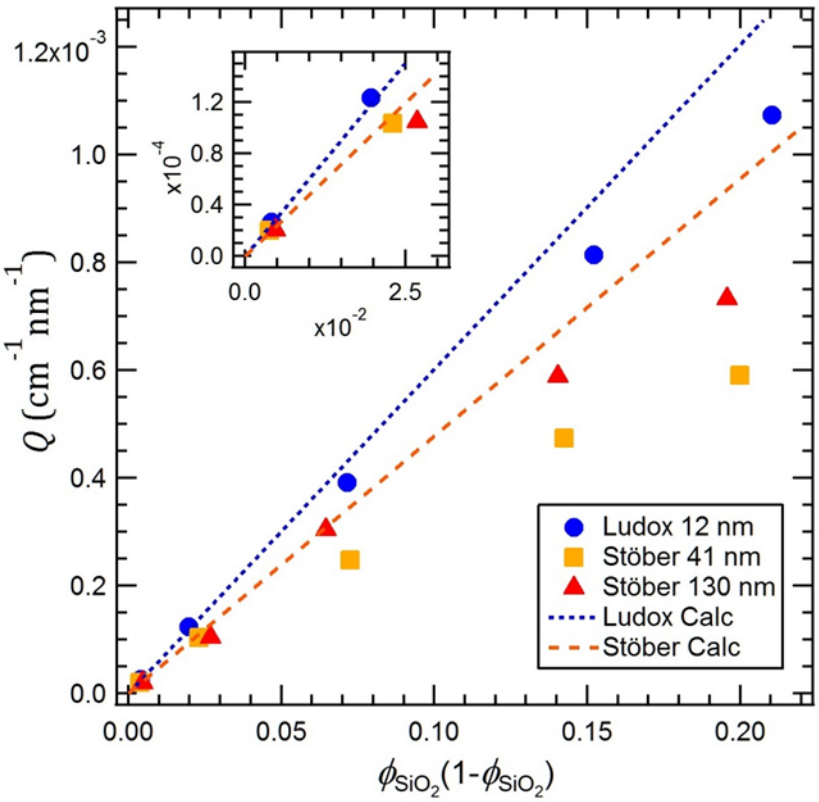

Figure A1.7: A plot of the scattering invariant vs. the particle volume loading determined through gravimetric analysis[165]. The data are shown as symbols, and the dashed lines indicate the predictions from Equation A1.3 using the scattering length density values from Ludox silica (blue short-dash) and Stöber silica (orange long-dash). The inset highlights the results from the composites with dilute loadings.

Thus far we have been able to analyze the particle size and particle loading in the composite membranes from the absolute scattering data alone, with very few assumptions: for the particle size we assumed a Schulz distribution of spheres (absolute intensity not needed), and for the particle loading we had to extrapolate the scattering profiles to $q \to 0$ and $q \to \infty$, assume the scattering length density values for each phase, and assume that the membranes are accurately described as a 2-phase system with sharp phase boundaries. A more refined analysis could be used, such as accounting for diffuse interfaces between the phases; however, that would require additional assumptions. We will now focus our analysis on the "structure" of the membranes, i.e., the arrangement of the silica nanoparticles.

Table A1.2: Particle loadings from each composite membrane determined gravimetrically (ref [165] and Norman Su) and from the scattering invariant through Equation A1.2 in this work.

Membrane	ϕ_{SiO_2} (gravimetric)	ϕ_{SiO_2} (invariant)
Ludox 12nm-0.4%	0.0041	0.0044
Ludox 12nm-2.0%	0.0200	0.0209
Ludox 12nm-7.8%	0.0775	0.0699
Ludox 12nm-19%	0.187	0.161
Ludox 12nm-30%	0.301	0.232
Stöber 41nm-0.4%	0.0038	0.0042
Stöber 41nm-2.4%	0.0236	0.0221
Stöber 41nm-7.9%	0.0788	0.0549
Stöber 41nm-17%	0.172	0.112
Stöber 41nm-28%	0.276	0.144
Stöber 130nm-0.5%	0.0047	0.0043
Stöber 130nm-2.8%	0.0276	0.0225
Stöber 130nm-6.9%	0.0693	0.0685
Stöber 130nm-17%	0.169	0.144
Stöber 130nm-27%	0.267	0.189

Information about the arrangement of particles within a non-periodic (random) dispersion of particles is generally contained in the scattering intensity a q-values such that the product (qr_p) is less than 1, i.e., at length-scales larger than the radius of the particles. In this regime, the scattering intensity from isolated particles is well-understood to follow the Guinier relationship as q approaches 0, which is given by Equation A1.4[55],

$$I(q \to 0) = \left(B_p - B_s\right)^2 \phi_p V_p e^{\left[-\frac{1}{3}(qR_g)^2\right]};\ R_g^2 = \frac{3}{5} r_p^2 \tag{A1.4}$$

where R_g is the radius of gyration for the particle and all other parameters are the same as Equation A1.3. This behavior is portrayed in the low q portion of the fit curves in Figure A1.6. Deviations from this behavior are induced by inter-particle correlations, which can be accounted for in structural models by a so-called "structure factor" ($S(q)$). The structure factor is a function of the total particle loading and interaction potential between particles (attractive vs repulsive, etc).[55] The structure factor in particle systems get incorporated into the scattering function multiplicatively, thus the scattering for a concentrated dispersion of monodisperse spheres could be written as

$$I(q) = \left(B_p - B_s\right)^2 \phi_p V_p \left\{\frac{3\left[\sin\left(qr_p\right) - \left(qr_p\right)\cos\left(qr_p\right)\right]}{\left(qr_p\right)^3}\right\}^2 S(q) \tag{A1.5}$$

where the function is equivalent to Equation A1.3, save for the inclusion of the $S(q)$ term to account for inter-particle correlations (i.e., interferences). The mathematics involved in deriving structure factors is quite complex and well beyond the scope of this case study; however, a number of structure factors have been derived for various inter-particle interaction potentials, many of which are included in the NCNR Analysis Macro package[130]. I will utilize one such structure factor to demonstrate its influence on the scattering intensity for an ensemble of spheres with a Schulz size distribution.

In Figures A1.8-A1.10 below, I provide the measured X-ray scattering profiles from all 15 of the composite membranes (discreet data markers). Also included with each experimental scattering profile is the model prediction from the "Schulz Hard Spheres" model in the NCNR Analysis package[130]. This model represents an ensemble of spheres with a Schulz size distribution and a structure factor based on "hard sphere" interactions, i.e., infinite repulsion at the particle surface and non-interacting at further spacing[130,167]. Each of the modeled profiles in Figures A1.8-A1.10 is calculated with no adjustable parameters: the inputs are the scattering length densities for the particles and the polymer matrix, the particle size distribution, and the particle volume fraction. The volume fractions determined gravimetrically[165] and from the invariant were both used to model the data in plots (a) and (b), respectively, for each of Figures A1.8-A1.10. For consistency, the constant background intensity values (I_{bkg}) that were used when fitting the dilute membrane scattering profiles were also included in the Schulz hard spheres model.

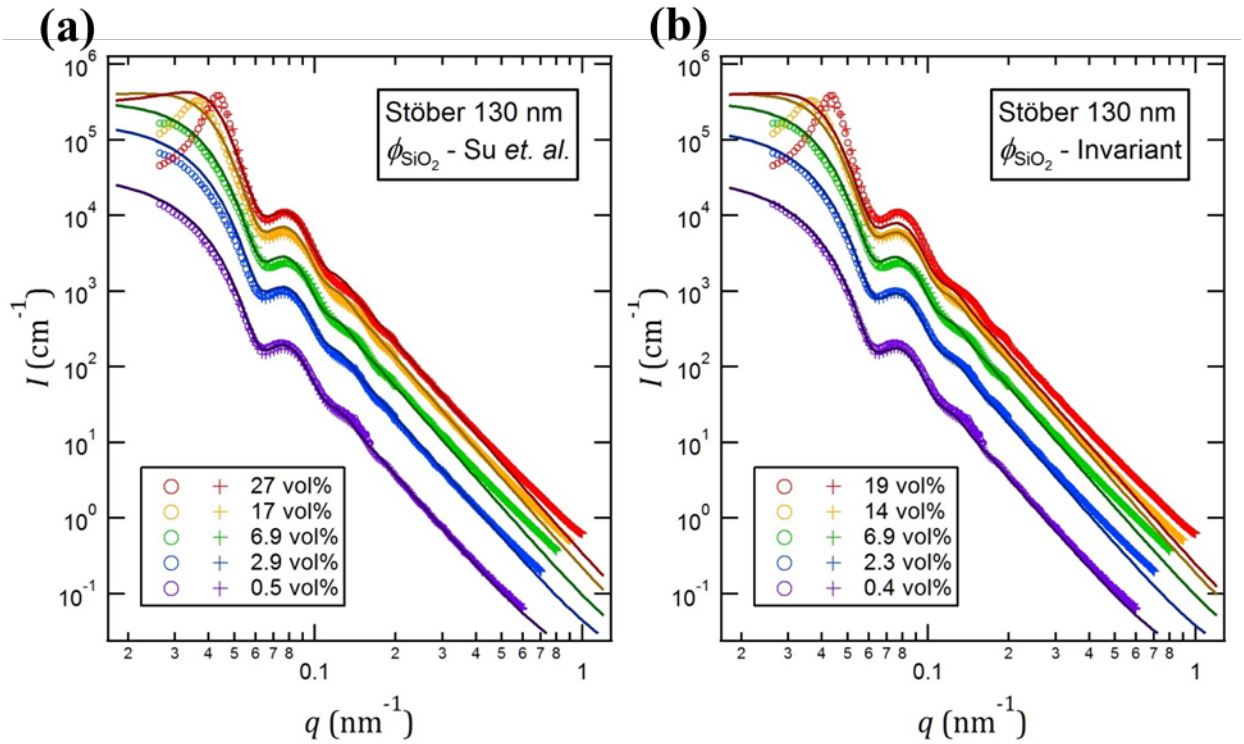

Figure A1.8: SAXS profiles and corresponding model predictions from the "Schulz Hard Spheres" model in the NCNR Analysis Macro package[130]. Experimental data are indicated with discreet markers (circles correspond to the SSRL BL 1-5 SAXS results and crosses correspond to the ALS BL 7.3.3 SAXS results), while the modeled profiles are solid curves. (a) Modeled profiles calculated using the gravimetric particle loadings determined by Norman Su.

(b) Modeled profiles calculated using the particle loadings calculated from the invariant. All models use the particle size distributions determined through the SAXS measurements of the dilute membranes.

In Figure A1.8 I provide the experimental scattering data and "Schulz Hard Spheres" model results for the Stöber 130nm spheres. Within the experimentally measured q-range, the scattering profiles for samples with volume fractions less than 7% are well characterized by the Schulz hard sphere model. At the two highest volume fractions in Figure A1.8a, the form factor scattering due to the individual particles is captured by the model; however, the low q scattering predictions from the hard sphere structure factor completely fail to capture the experimentally observed trends. A similar result is seen in Figure A1.8b, except that even the form factor scattering is not captured adequately in the highest loading sample, indicating that the volume fraction determined by the invariant at this concentration is not accurate. Likely reasons for the failure of the hard sphere structure factor are that the "effective" hard sphere radius (i.e., the radius of closest approach) is larger than the silica particle radius, and/or there is a non-zero interaction potential between particles at distances further from the hard sphere surface. I note that the position of the "peak" at low q in the scattering profiles at high particle loadings indicates the average center-to-center particle distance. For the 27 vol% film in Figure A1.8a, this distance is $d = \frac{2\pi}{q_{peak}} = 150$ nm, which corresponds to an inter-particle spacing of ~10 nm.

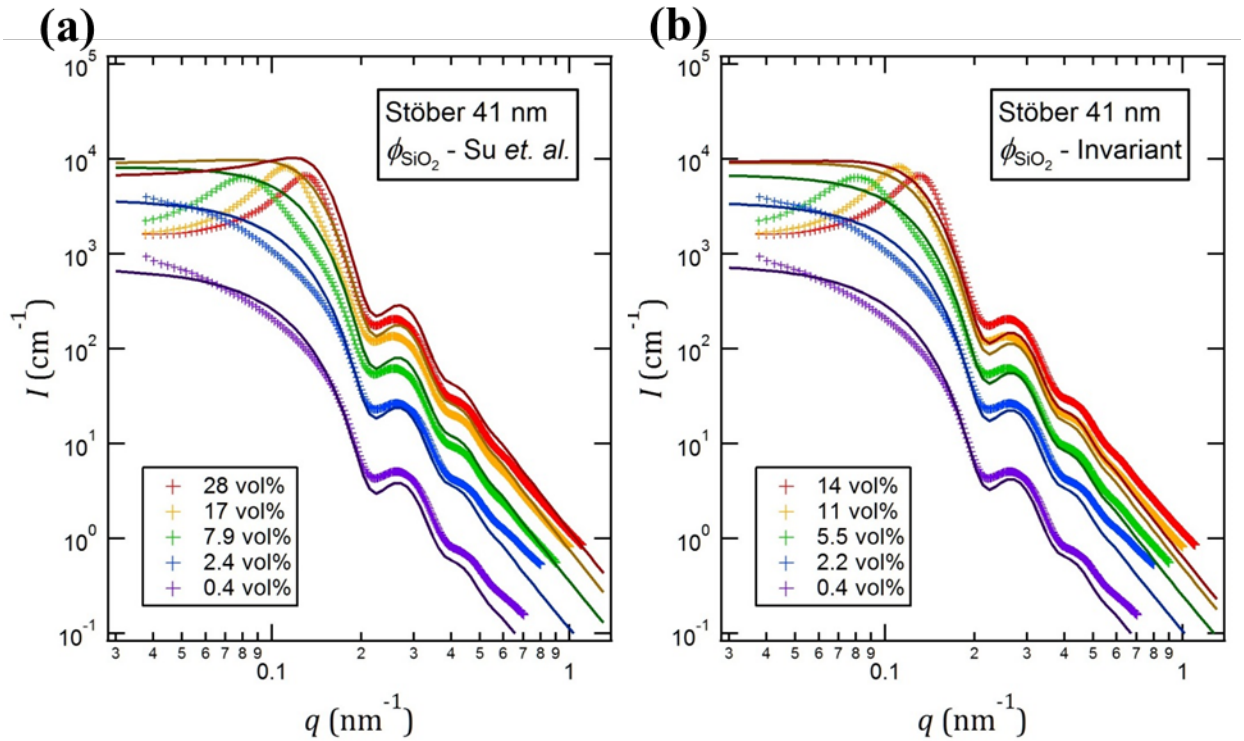

Figure A1.9: SAXS profiles and corresponding model predictions from the "Schulz Hard Spheres" model in the NCNR Analysis Macro package[130]. Experimental data are indicated with discreet markers, while the modeled profiles are solid curves. (a) Modeled profiles calculated using the gravimetric particle loadings determined by Norman Su. (b) Modeled profiles calculated using the particle loadings calculated from the invariant. All models use the particle size distributions determined through the SAXS measurements of the dilute membranes.

In Figure A1.9 I provide the experimental scattering data and "Schulz Hard Spheres" model results for the Stöber 41nm spheres. In this case, the modeled low q scattering intensities

do not capture the observed behavior even in the dilute membranes. The most likely cause for this is that the particles are interacting to form aggregate structures. Furthermore, the overall intensities of the modeled profiles tend to fail to align with the experimental data. This indicates that either the volume fraction or the scattering contrast values are not correct in our model for these samples. The gravimetric volume fractions lead to both under and overestimated model intensities (Figure A1.9a), while the invariant-based volume fractions consistently lead to underestimated model intensities (Figure A1.9b). Interestingly, the inter-particle spacing determined from the low q peak in the 28 vol% sample in Figure A1.9a is ~8.5 nm, which is similar to that of the Stöber 130nm membrane of similar particle loading.

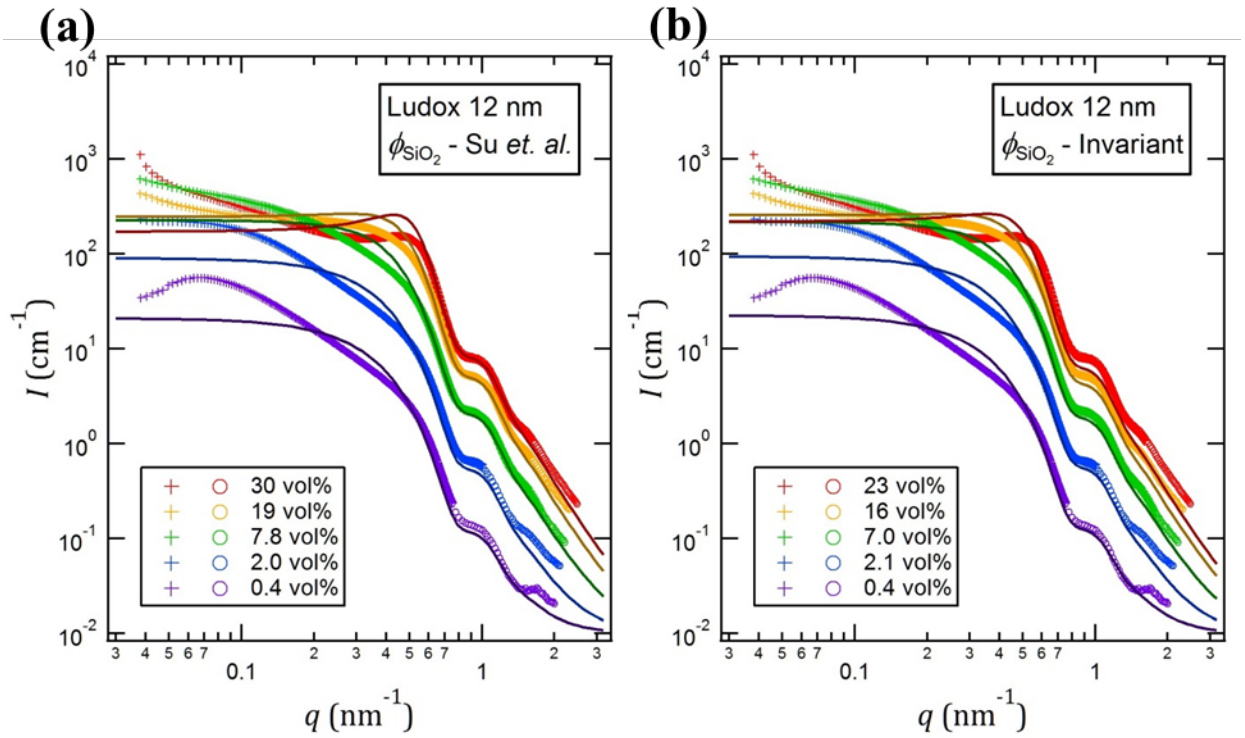

Figure A1.10: SAXS profiles and corresponding model predictions from the "Schulz Hard Spheres" model in the NCNR Analysis Macro package[130]. Experimental data are indicated with discreet markers (crosses correspond to the ALS BL 7.3.3 SAXS results and circles correspond to the ALS BL 7.3.3 WAXS results), while the modeled profiles are solid curves. (a) Modeled profiles calculated using the gravimetric particle loadings determined by Norman Su. (b) Modeled profiles calculated using the particle loadings calculated from the invariant. All models use the particle size distributions determined through the SAXS measurements of the dilute membranes.

In Figure A1.10, I provide the experimental and modeled scattering profiles for the membranes formed from the Ludox 12nm particles. As with the Stöber 41nm spheres, the low q scattering intensities predicted by the model fail to capture experimental observation in all cases. However, for these samples, the overall profile intensities scale with volume fraction in a manner similar to the Stöber 130nm spheres, where the gravimetric volume fractions always provide the appropriate scaling (Figure A1.9a), and the invariant-based volume fractions tend to under-predict the films with the highest loadings (Figure A1.10b). It is clear from the low q scattering of the dilute membrane samples (0.4 and 2.0 vol%) that aggregate structures are formed by the Ludox 12nm particles. This is actually consistent with the TEM analysis of the particles cast from solution, wherein string-like aggregates of ~5-10 particles were a common motif[165]. It

should be possible to develop a model to account for the scattering from these string-like aggregates, but it has not been explored for this system yet. Finally, if we again determine the inter-particle spacing from the low q "peak" in the scattering from the highest loading film (30 vol%, Figure A1.10a), we find a value of ~3nm. This value is much smaller than the inter-particle spacing values observed in the Stöber particle films, which may help explain the anomalous transport properties measured for the Ludox 12nm membranes in ref [165].

A1.3.3 Conclusion

In this case study, I presented the scattering analysis of a series of nanoparticle/polymer composite membranes. The composition (particle size, loading) of the membranes had previously been determined by other techniques.[165] Our goals were to independently verify the previous characterization, as well as begin to explore how the particles were organized within the membrane, i.e., the membrane "structure". The particle sizes were verified by fitting the oscillating "form factor" scattering from membranes with dilute particle loadings. The model used to fit the data was based on a Schulz distribution of spherical particles. In all cases, the particle size distributions determined through X-ray scattering were within error of those determined from TEM image analysis[165] (see Table A1.1). The particle loadings within the membranes were determined using the scattering invariant under the assumption of a 2-phase system with sharp interfaces (Equation A1.2). The values obtained from Equation A1.2 were generally in good agreement with those measure gravimetrically[165], except at the highest particle loadings (see Table A1.2). The cause of the large deviation at high particle loadings is unclear at this time, but might be due to diffuse interfaces between the particles and the polymer matrix. The "structure" of the composite membranes was investigated by comparing the experimental scattering profiles to those generated assuming "hard sphere" inter-particle interactions. For the largest particle size (Stöber 130nm), the model only breaks down at the highest particle loadings, while for the smaller particles, the "hard sphere" assumption does not reflect the scattering profiles at any particle loading. As a whole, there appears to be an attractive potential between the silica nanoparticles. In the Stöber 130nm membranes, the attractive potential is reflected in the sharp low-q peak in scattering profile of membrane with high particle loading, while it manifest in the formation of particle aggregates at all particle loadings for the smaller particle sizes. Finally, the obvious particle aggregation and significantly smaller inter-particle spacing observed in the Ludox 12nm samples appears to be related to its anomalous behavior in ref [165].

In this study, the utility of attaining absolute scattering data should be evident. Knowledge of the components within the sample facilitated a direct connection between membrane composition and the scattering intensity through the scattering contrast ($\left(B_p - B_s\right)^2$). This relationship facilitated the computation of the membrane loading from the scattering invariant, as well as the direct modeling of each scattering profile with no adjustable parameters. Furthermore, it may be pertinent to attempt to fit the scattering from the Ludox 12nm membranes with additional models in order to determine the size/shape of the particle aggregates. In this case, the scattering power can be fixed by the contrast and particle loading, thus limiting the number of adjustable parameters. Overall, it is good practice to attain quantitative scattering data whenever possible. The level of analysis one performs might vary significantly from study to study, but with quality data, all options are on the table.

Appendix A2 – Scattering Data from PEO-P[(STFSI)X] Single-Ion Conductors

A2.1 Schematic of Scattering Geometry

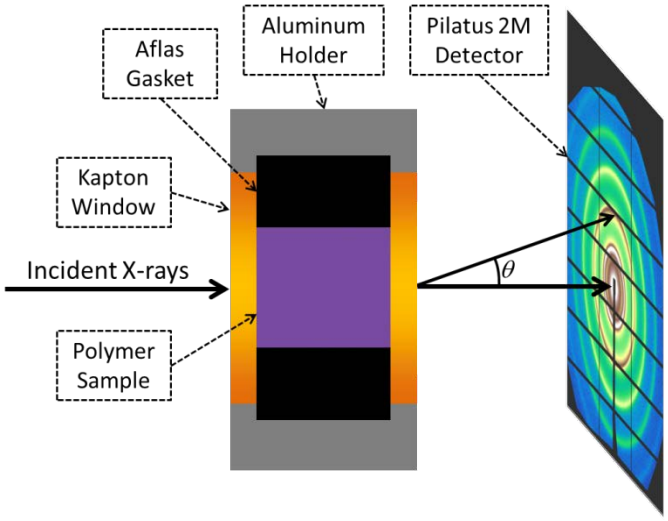

Figure A2.1: Schematic of the SAXS/WAXS transmission sample geometry

Figure A2.1 illustrates the geometry of the transmission SAXS/WAXS experiments performed in Chapter 5.2.3. Beamline 7.3.3 at the Advanced Light Source (ALS) utilizes an multilayer monochromator to provide a high intensity monochromatic 10keV X-ray beam[60]. Scattering profiles were collected on the Pilatus 2M detector, which provides total active area of 254 x 289 mm^2 and has pixel dimensions of 172 x 172 μm^2. The 2D scattering images were processed using the Nika macro developed by Jan Ilavsky[61] in Igor Pro in the following manner. First, an image mask was prepared from an image taken with no sample present, where low intensity pixels were automatically masked. The beamstop and any other geometric artifacts were masked manually. After preparing the mask, the scattering pattern of the silver behenate (AgB) sample was used to calibrate both the beam center and sample-to-detector (SD) distance: the SAXS setup was calibrated using only the primary scattering peak from AgB, whereas the WAXS setup was calibrated using the first five Bragg's peaks from AgB. After the beam center and SD were determined, 2D scattering profiles were converted to 1D profiles of intensity (I) vs. the magnitude of the scattering vector, $q \equiv \frac{4\pi}{\lambda}\sin\frac{\theta}{2}$, where λ is the X-ray wavelength, and θ is the scattering angle. During the conversion, the images were dezingered and masked, corrected for polarization and the variation in solid angle (geometry correction), and then radially averaged using the maximum number of points. In cases where there was obvious radial anisotropy in the 2D scattering images, ±15° sector averages where used (i.e., Figure A2.2, Figure A2.3, Figure A2.5, and Figure A2.7).

A2.2 Scattering Data

This section contains all of the data from the scattering experiments described in Chapter 5.2.3. This data was used for the analysis performed in Chapter 5 and Chapter 6.

A2.2.1 PEO(5)

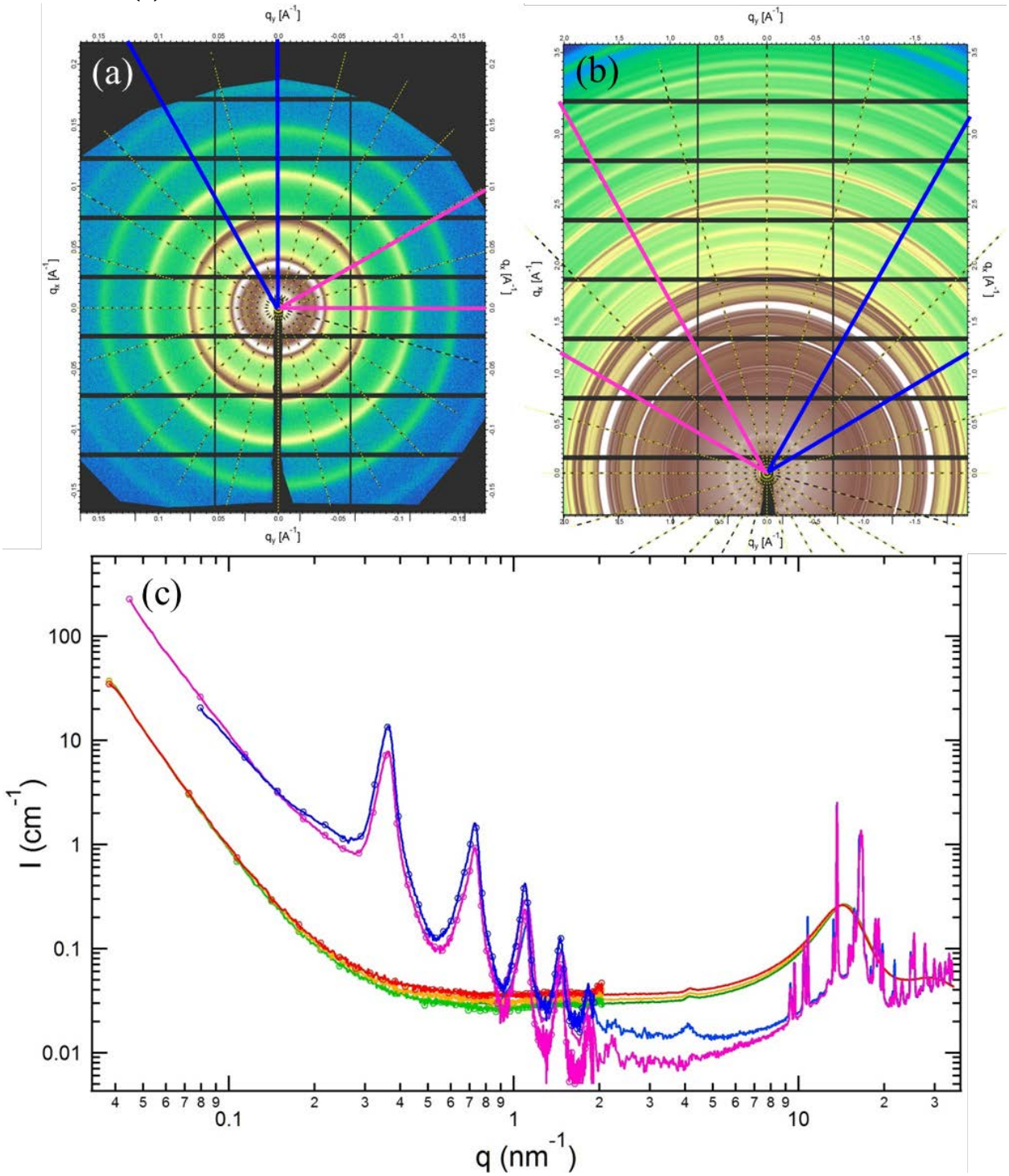

Figure A2.2: 2D (a) SAXS and (b) WAXS scattering images from PEO(5) at 35 °C. The blue and pink lines indicate regions where the sector averages of intensity were computed to yield the corresponding blue and pink 1D

profiles in (c). (c) also provides the amorphous scattering from PEO(5) at 90 °C (green), 110 °C (gold), and 130 °C (red).

A2.2.2 PEO-P[(STFSI)Li](5-1.1)

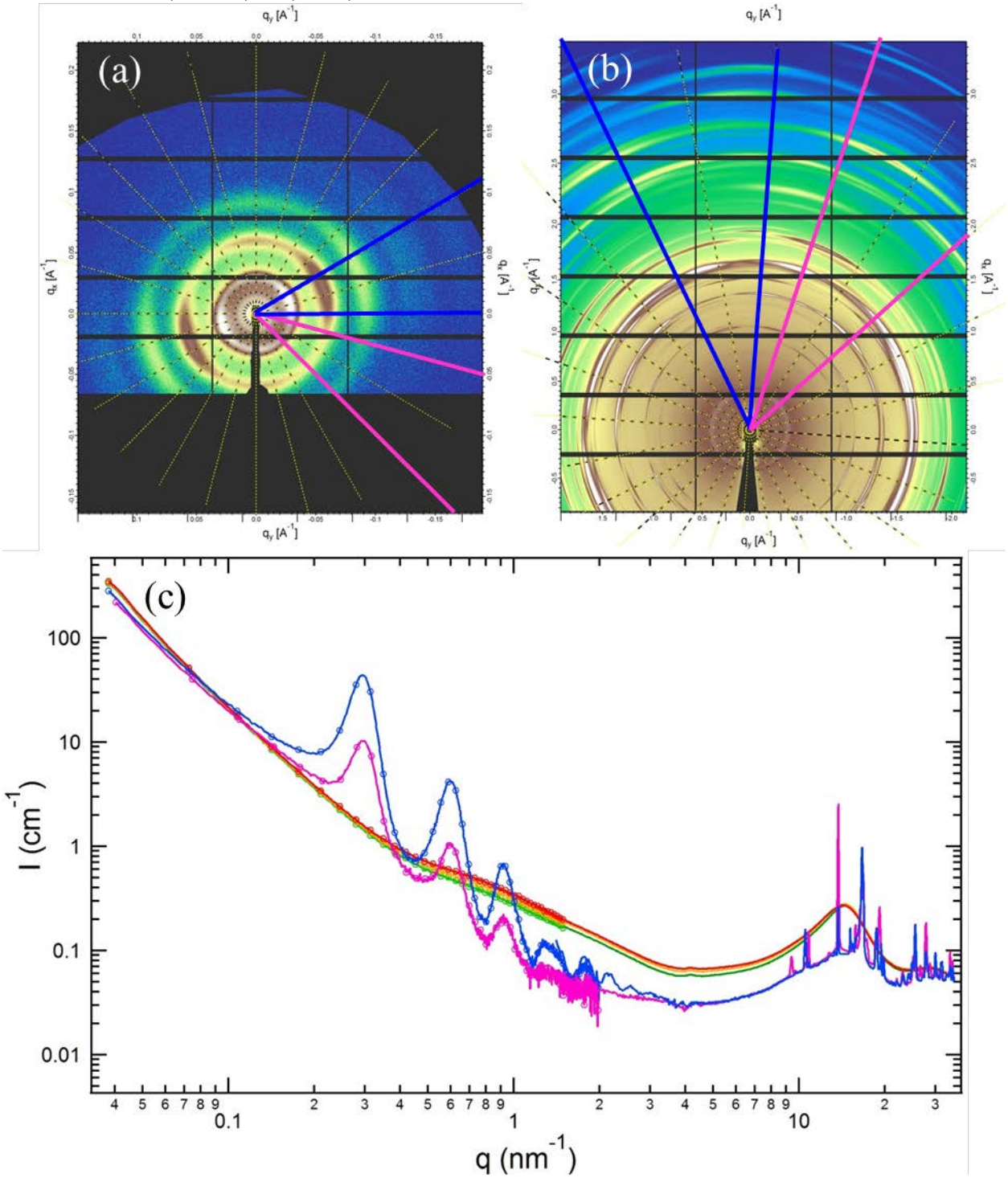

Figure A2.3: 2D (a) SAXS and (b) WAXS scattering images from PEO-P[(STFSI)Li](5-1.1) at 30 °C. The blue and pink lines indicate regions where the sector averages of intensity were computed to yield the corresponding blue and

pink 1D profiles in (c). (c) also provides the amorphous scattering from PEO-P[(STFSI)Li](5-1.1) at 90 °C (green), 110 °C (gold), and 130 °C (red).

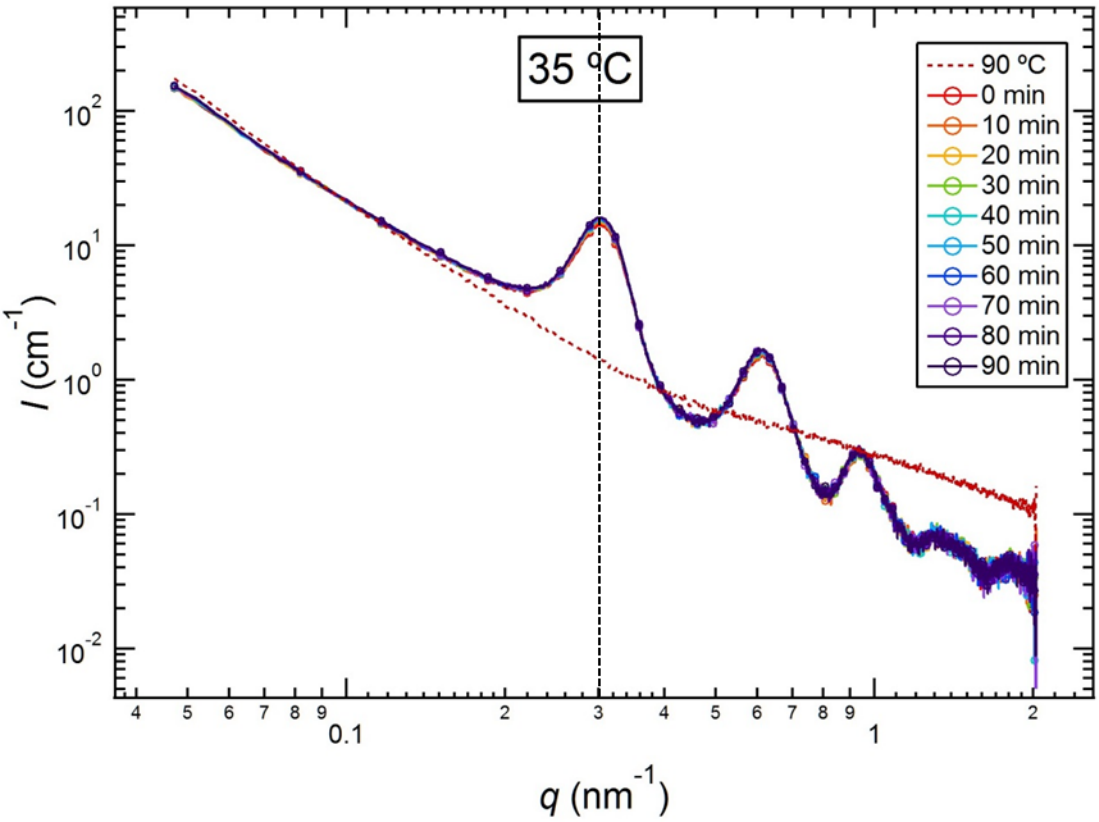

Figure A2.4: *in situ* 1D SAXS profiles for PEO-P[(STFSI)Li](5-1.1) during isothermal crystallization at 35 °C. For reference, the dark red dashed curve represents the scattering from PEO-P[(STFSI)Li](5-1.1) at 90 °C, and the black dashed vertical line indicates where I_{peak} was evaluated.

A2.2.3 PEO-P[(STFSI)Li](5-2.0)

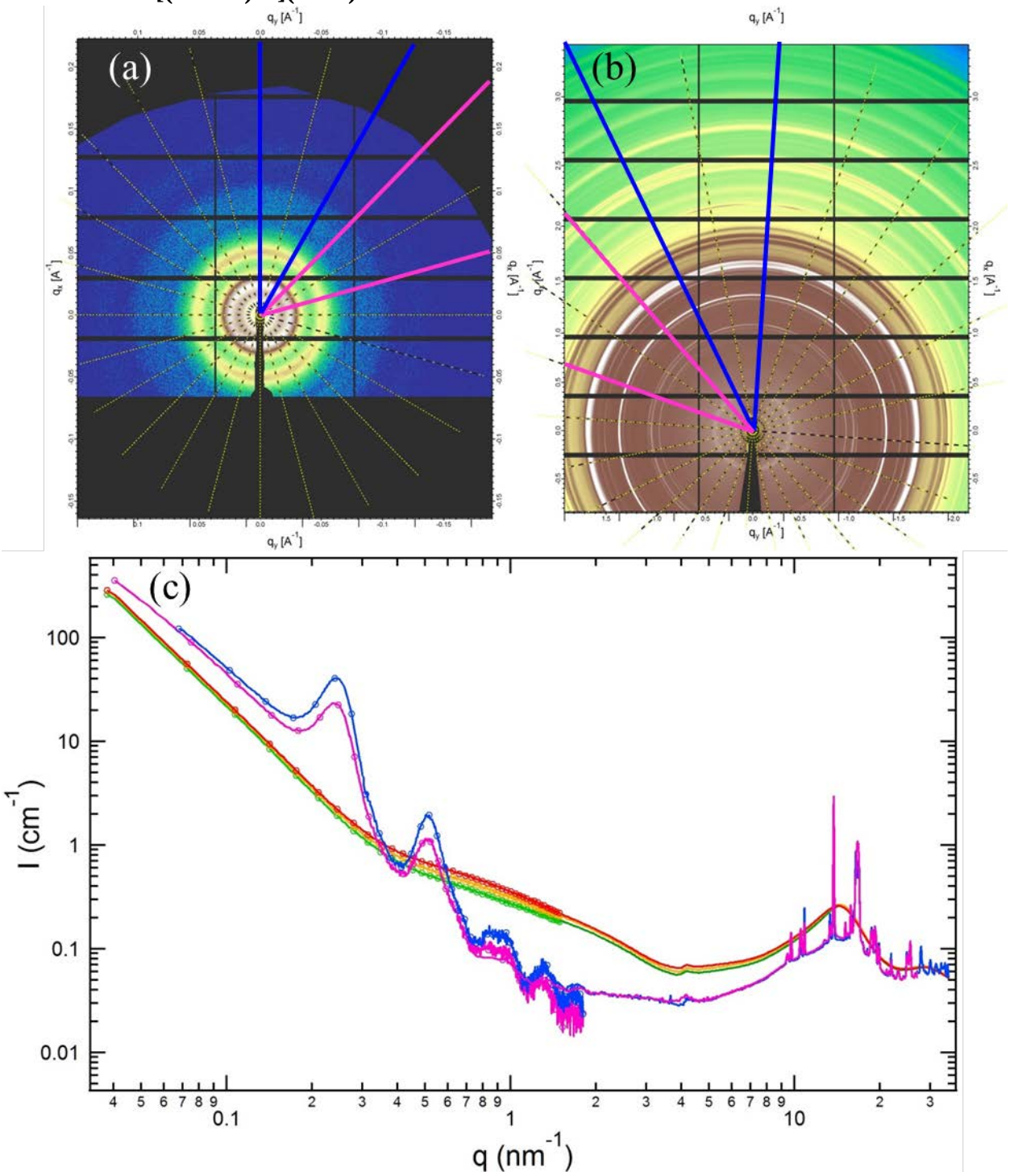

Figure A2.5: 2D (a) SAXS and (b) WAXS scattering images from PEO-P[(STFSI)Li](5-2.0) at 30 °C. The blue and pink lines indicate regions where the sector averages of intensity were computed to yield the corresponding blue and pink 1D profiles in (c). (c) also provides the amorphous scattering from PEO-P[(STFSI)Li](5-2.0) at 90 °C (green), 110 °C (gold), and 130 °C (red).

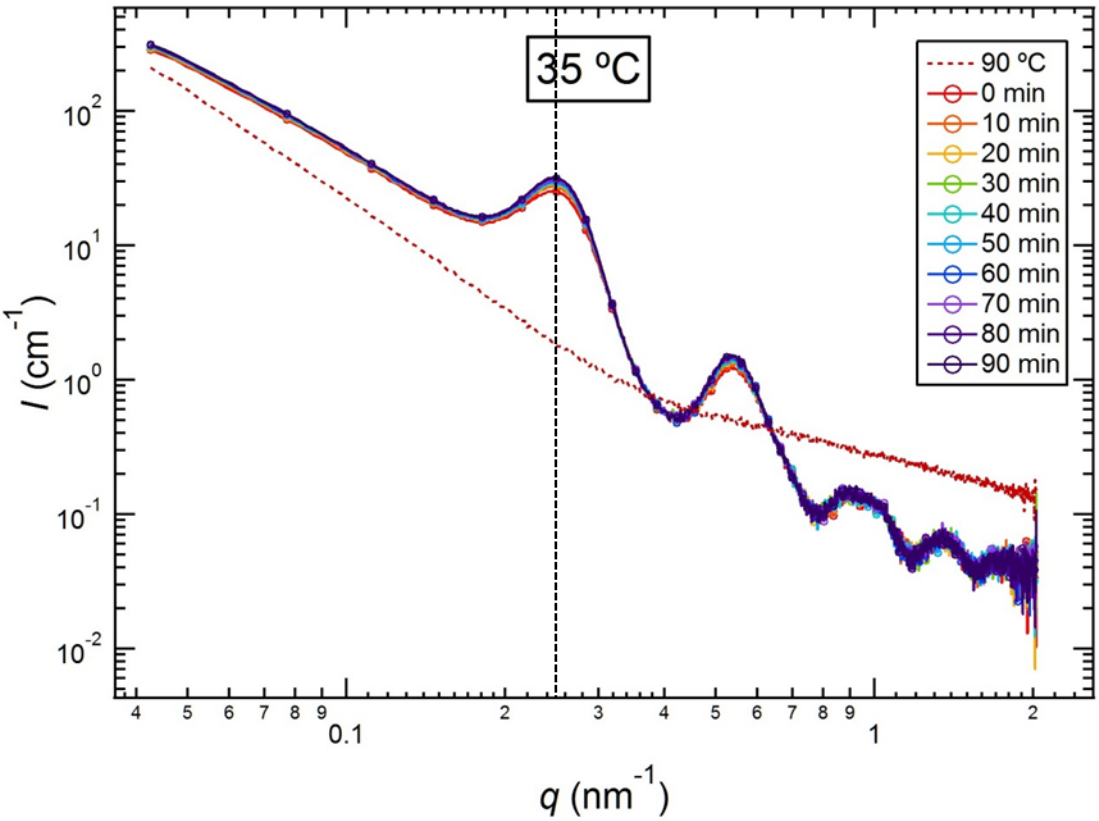

Figure A2.6: *in situ* 1D SAXS profiles for PEO-P[(STFSI)Li](5-2.0) during isothermal crystallization at 35 °C. For reference, the dark red dashed curve represents the scattering from PEO-P[(STFSI)Li](5-2.0) at 90 °C, and the black dashed vertical line indicates where I_{peak} was evaluated.

A2.2.4 PEO-P[(STFSI)Li](5-3.2)

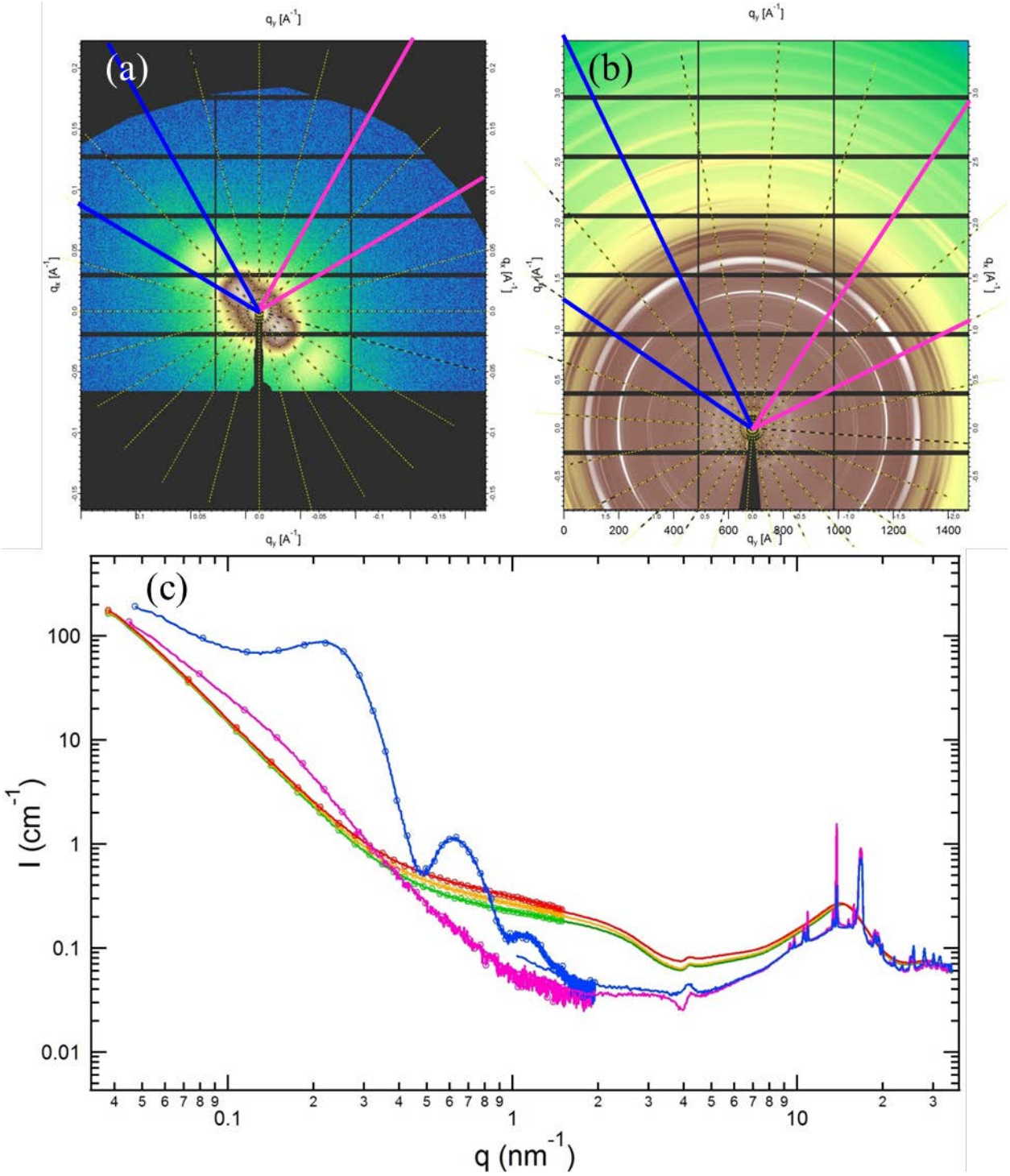

Figure A2.7: 2D (a) SAXS and (b) WAXS scattering images from PEO-P[(STFSI)Li](5-3.2) at 30 °C. The blue and pink lines indicate regions where the sector averages of intensity were computed to yield the corresponding blue and pink 1D profiles in (c). (c) also provides the amorphous scattering from PEO-P[(STFSI)Li](5-3.2) at 90 °C (green), 110 °C (gold), and 130 °C (red).

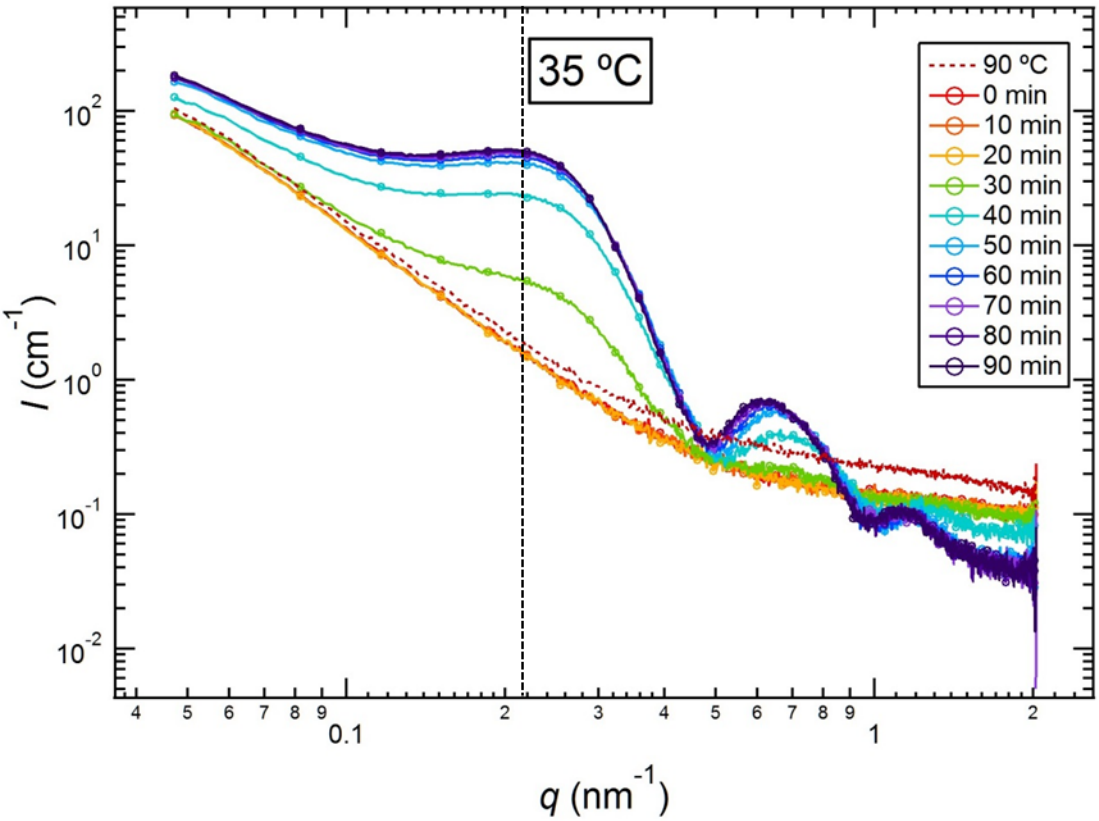

Figure A2.8: *in situ* 1D SAXS profiles for PEO-P[(STFSI)Li](5-3.2) during isothermal crystallization at 35 °C. For reference, the dark red dashed curve represents the scattering from PEO-P[(STFSI)Li](5-3.2) at 90 °C, and the black dashed vertical line indicates where I_{peak} was evaluated.

A2.2.5 PEO-P[(STFSI)$_2$Mg](5-1.1)

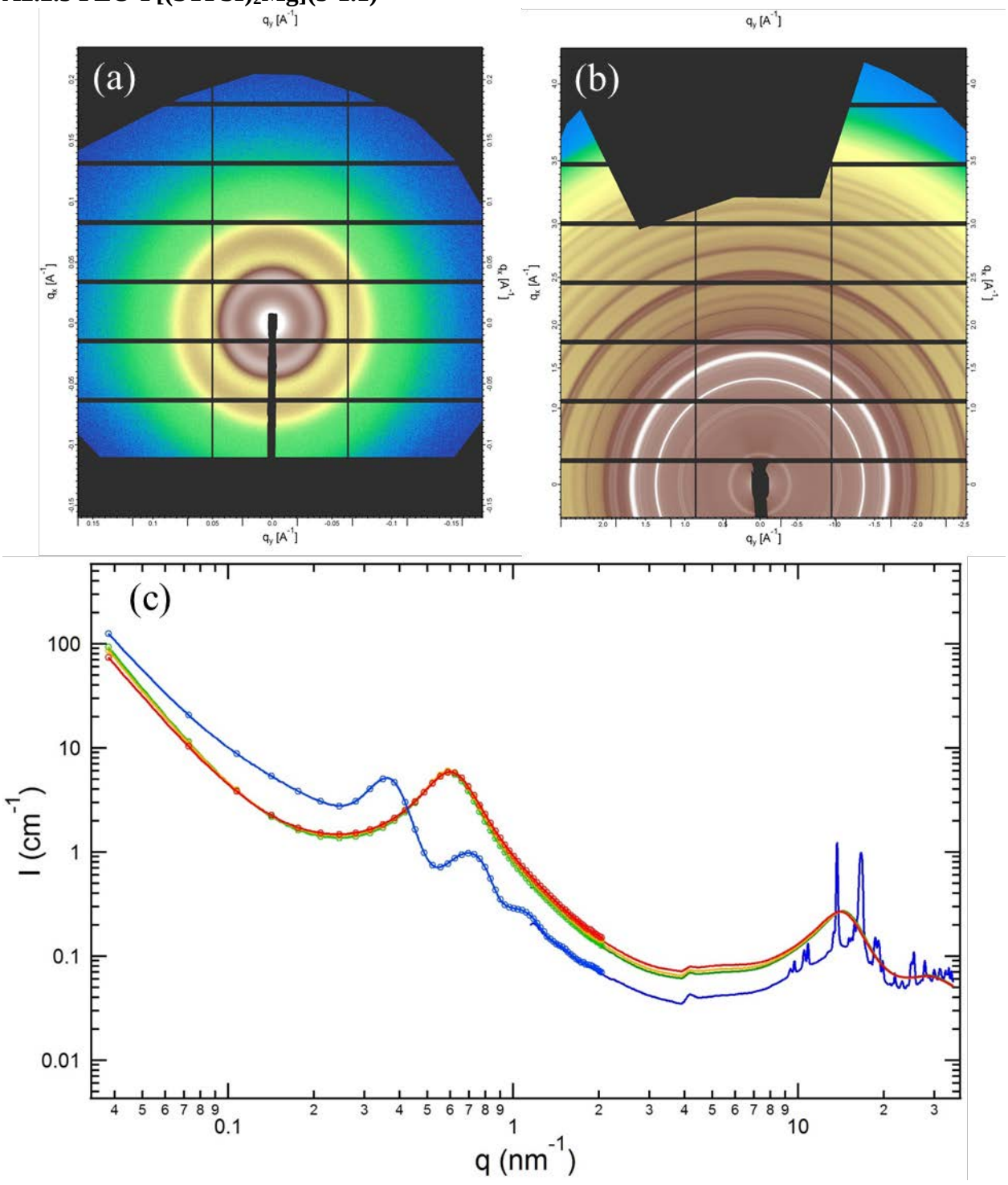

Figure A2.9: 2D (a) SAXS and (b) WAXS scattering images from PEO-P[(STFSI)$_2$Mg](5-1.1) at 35 °C. The 2D images were azimuthally averaged to yield the blue 1D profile in (c) along with the amorphous scattering profiles from PEO-P[(STFSI)$_2$Mg](5-1.1) at 90 °C (green), 110 °C (gold), and 130 °C (red).

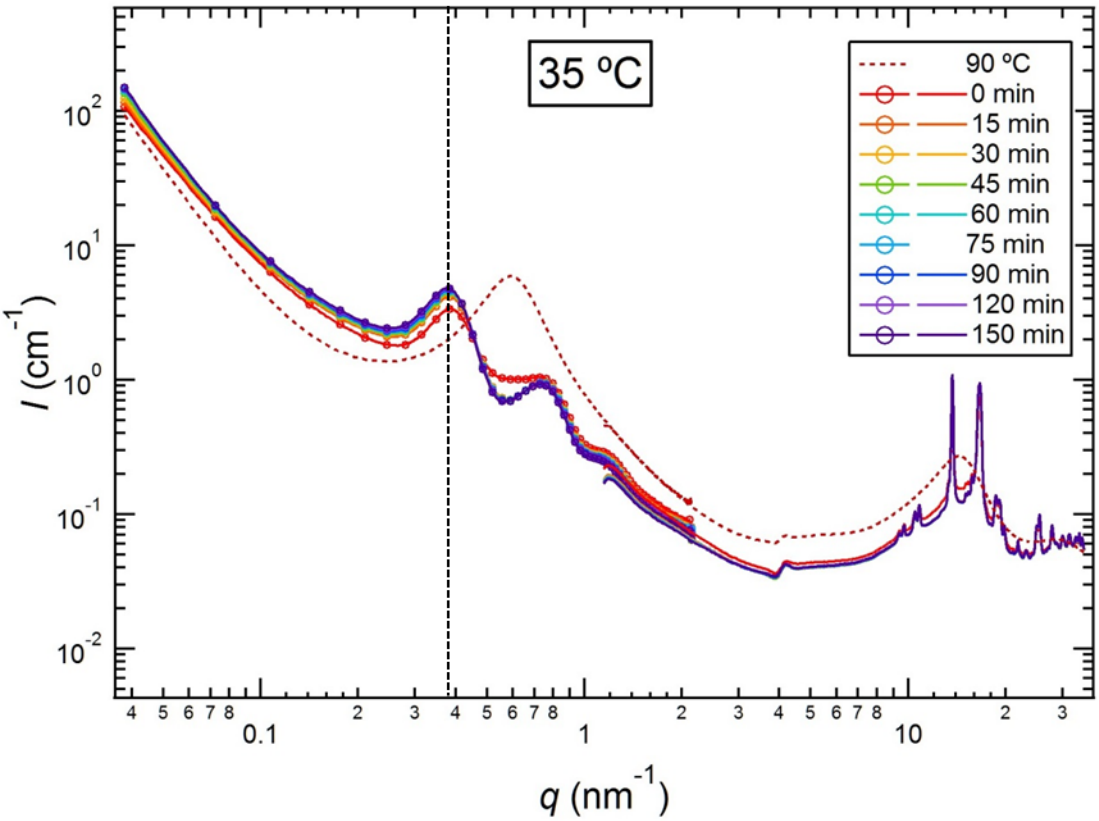

Figure A2.10: *in situ* 1D SAXS/WAXS profiles for PEO-P[(STFSI)$_2$Mg](5-1.1) during isothermal crystallization at 35 °C. For reference, the dark red dashed curve represents the scattering from PEO-P[(STFSI)$_2$Mg](5-1.1) at 90 °C, and the black dashed vertical line indicates where I_{peak} was evaluated.

A2.2.6 PEO-P[(STFSI)$_2$Mg](5-2.0)

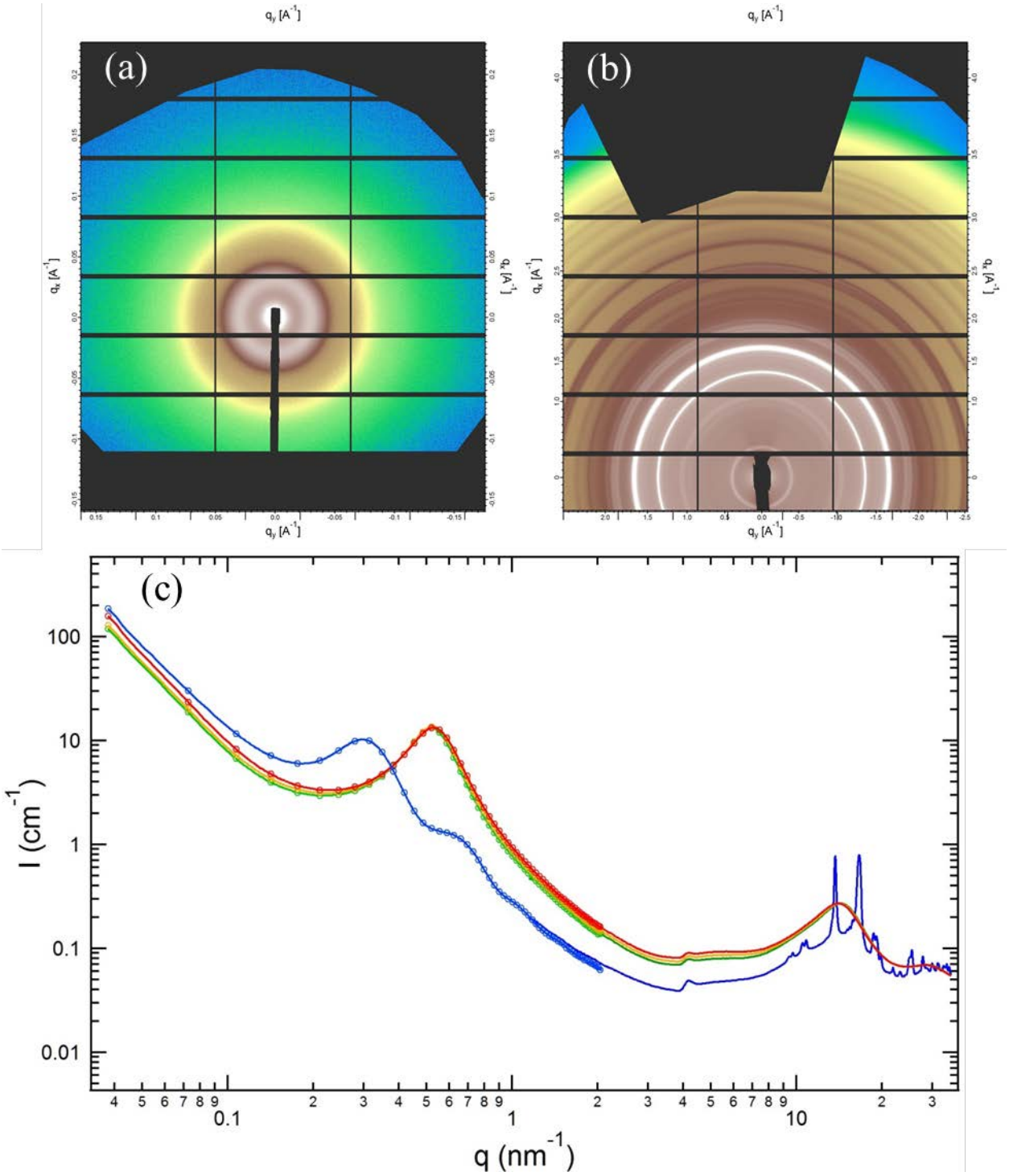

Figure A2.11: 2D (a) SAXS and (b) WAXS scattering images from PEO-P[(STFSI)$_2$Mg](5-2.0) at 35 °C. The 2D images were azimuthally averaged to yield the blue 1D profile in (c) along with the amorphous scattering profiles from PEO-P[(STFSI)$_2$Mg](5-2.0) at 90 °C (green), 110 °C (gold), and 130 °C (red).

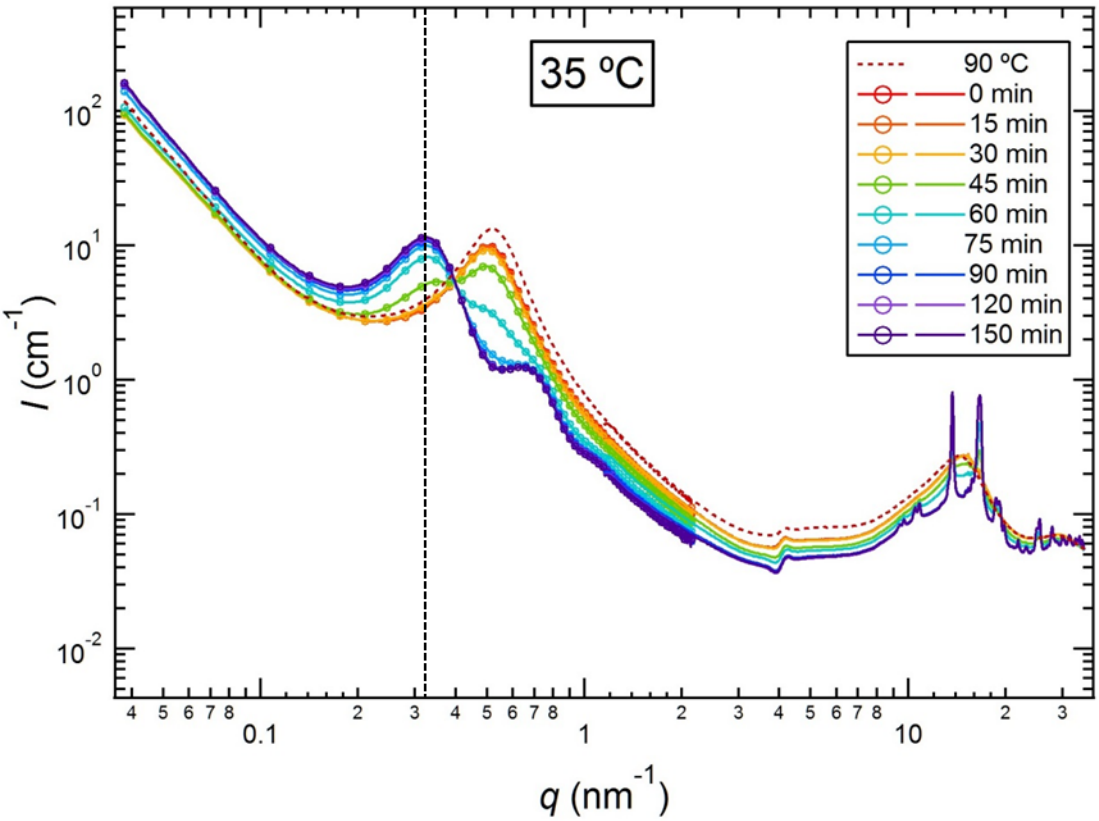

Figure A2.12: *in situ* 1D SAXS/WAXS profiles for PEO-P[(STFSI)$_2$Mg](5-2.0) during isothermal crystallization at 35 °C. For reference, the dark red dashed curve represents the scattering from PEO-P[(STFSI)$_2$Mg](5-2.0) at 90 °C, and the black dashed vertical line indicates where I_{peak} was evaluated.

A2.2.7 PEO-P[(STFSI)$_2$Mg](5-3.2)

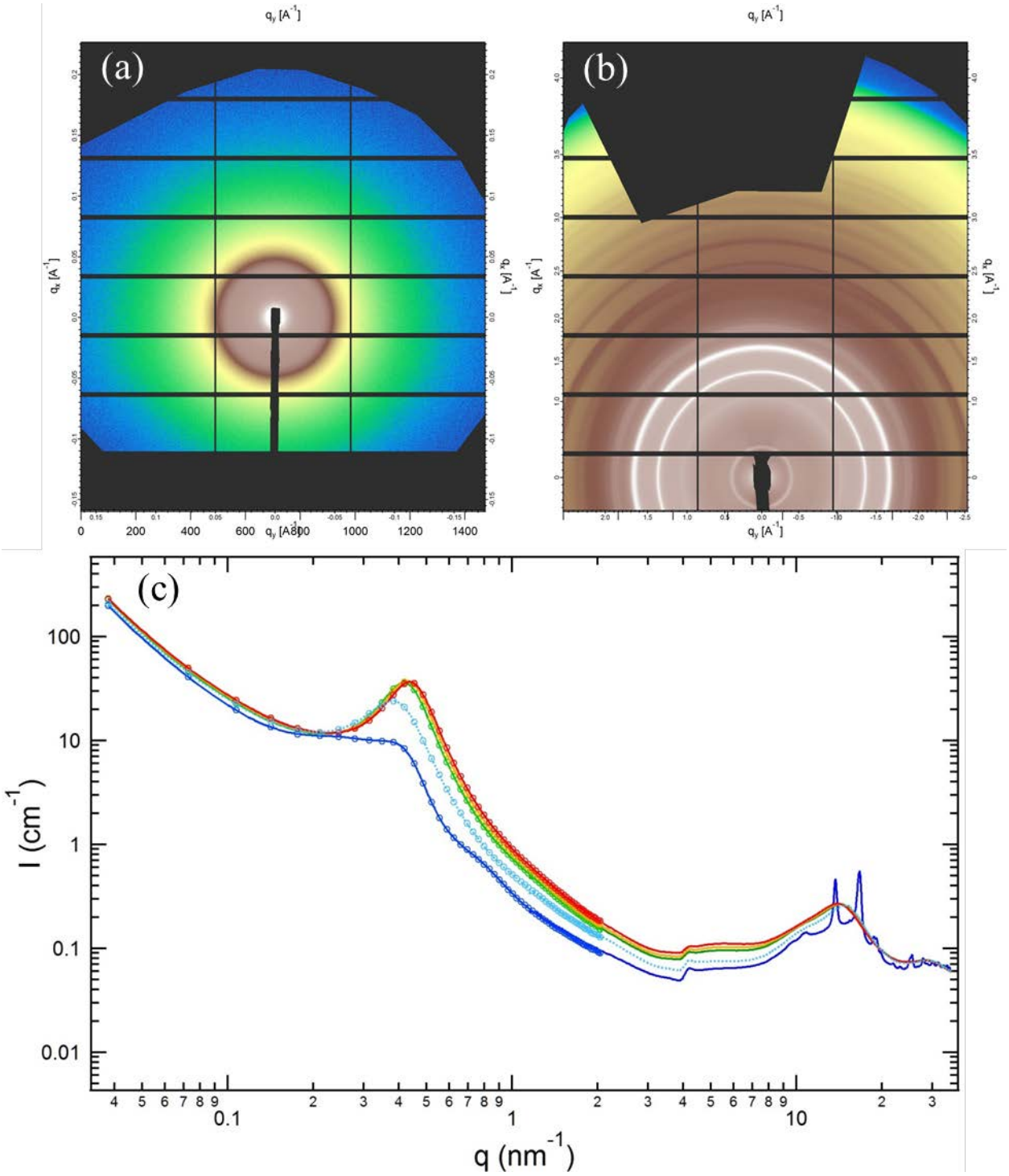

Figure A2.13: 2D (a) SAXS and (b) WAXS scattering images from PEO-P[(STFSI)$_2$Mg](5-3.2) at 35 °C. The 2D images were azimuthally averaged to yield the blue 1D profile in (c) along with the amorphous scattering profiles from PEO-P[(STFSI)$_2$Mg](5-3.2) at 90 °C (green), 110 °C (gold), and 130 °C (red). The dashed (cyan) profile in (c) is amorphous PEO-P[(STFSI)$_2$Mg](5-3.2) at 35 °C obtained before PEO crystallization after quenching from 90 °C.

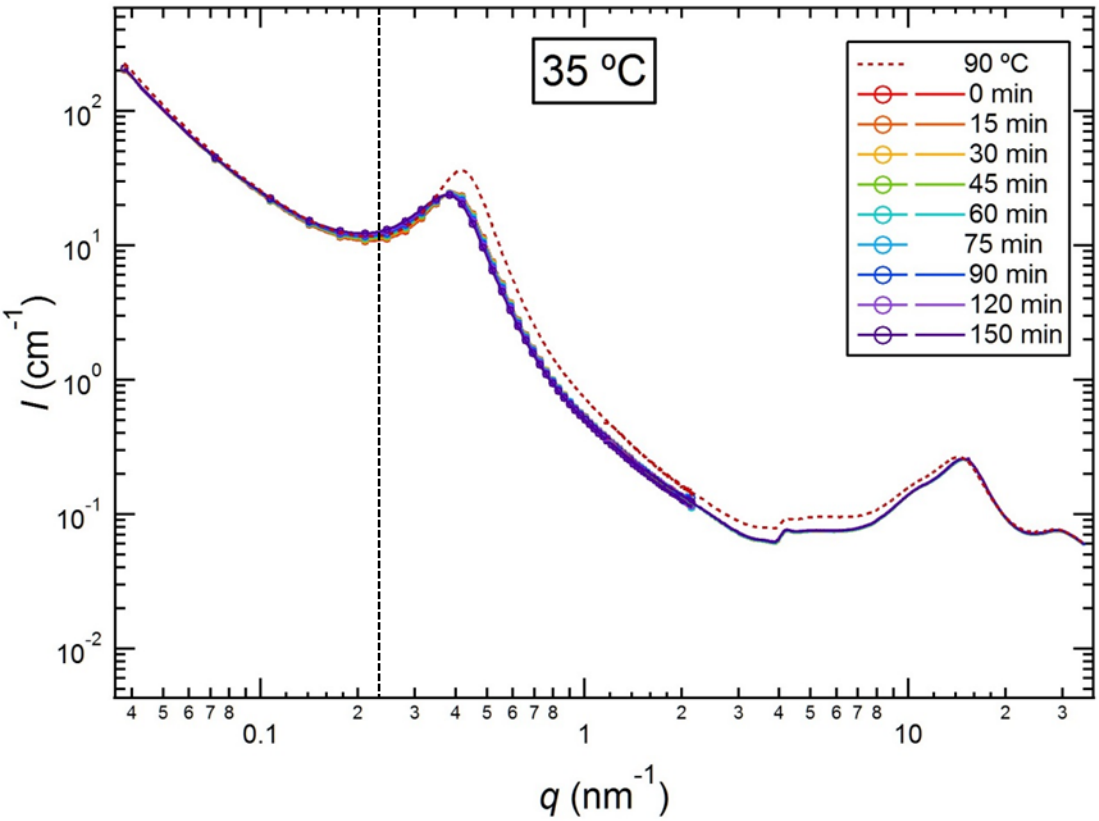

Figure A2.14: *in situ* 1D SAXS/WAXS profiles for PEO-P[(STFSI)$_2$Mg](5-3.2) during isothermal crystallization at 35 °C. For reference, the dark red dashed curve represents the scattering from PEO-P[(STFSI)$_2$Mg](5-3.2) at 90 °C, and the black dashed vertical line indicates where I_{peak} was evaluated.